POLYPUBLIE
Polytechnique Montréal

POLYTECHNIQUE MONTRÉAL
UNIVERSITÉ D'INGÉNIERIE

Titre: Title:	Modèles non linéaires pour l'interaction tube-support
Auteur: Author:	Abdallah Hadji
Date:	2016
Type:	Mémoire ou thèse / Dissertation or Thesis
Référence: Citation:	Hadji, A. (2016). Modèles non linéaires pour l'interaction tube-support [Thèse de doctorat, École Polytechnique de Montréal]. PolyPublie. https://publications.polymtl.ca/2228/

Document en libre accès dans PolyPublie
Open Access document in PolyPublie

URL de PolyPublie: PolyPublie URL:	https://publications.polymtl.ca/2228/
Directeurs de recherche: Advisors:	Njuki W. Mureithi
Programme: Program:	Génie mécanique

Ce fichier a été téléchargé à partir de PolyPublie, le dépôt institutionnel de Polytechnique Montréal
This file has been downloaded from PolyPublie, the institutional repository of Polytechnique Montréal

https://publications.polymtl.ca

UNIVERSITÉ DE MONTRÉAL

MODÈLES NON LINÉAIRES POUR L'INTERACTION TUBE-SUPPORT

ABDALLAH HADJI

DÉPARTEMENT DE GÉNIE MÉCANIQUE

ÉCOLE POLYTECHNIQUE DE MONTRÉAL

THÈSE PRÉSENTÉE EN VUE DE L'OBTENTION

DU DIPLÔME DE PHILOSOPHIAE DOCTOR

(GÉNIE MÉCANIQUE)

AOÛT 2016

© Abdallah Hadji, 2016.

UNIVERSITÉ DE MONTRÉAL

ÉCOLE POLYTECHNIQUE DE MONTRÉAL

Cette thèse intitulée :

MODÈLES NON LINÉAIRES POUR L'INTERACTION TUBE-SUPPORT

présentée par : HADJI Abdallah

en vue de l'obtention du diplôme de : Philosophiae Doctor

a été dûment acceptée par le jury d'examen constitué de :

M. BALAZINSKI Marek, Docteur ès sciences, président
M. MUREITHI Njuki William, Ph. D., membre et directeur de recherche
M. LAKIS Aouni A., Ph. D., membre
M. HASSAN Marwan, Ph. D., membre externe

DÉDICACE

Je dédie ce travail à mon grand-père, Souilah HADJI pour leur espérance en moi, ma mère et ma femme pour leurs passions.

REMERCIEMENTS

J’aimerais saisir cette occasion pour remercier chaleureusement mon directeur de recherche, le professeur Njuki Mureithi pour son soutien, ses encouragements, son inspiration tout au long de ce doctorat et de m’avoir partagé avec moi sa très riche expérience dans l’analyse des problèmes technologiques. Je leur suis reconnaissant pour m’avoir offert l’opportunité d’apprendre au sein du laboratoire d’Interaction Fluide-Structure (IFS) de l’École Polytechnique de Montréal. Je remercie également tous les professeurs de chaire de recherche industrielle IFS, Stéphane Étienne et Michel Pettigrew pour les discussions utiles sur le sujet étudié dans cette thèse.

J’aimerais aussi remercier le personnel de la Chaire de Recherche en Interaction Fluide-Structure (IFS) pour leur assistance technique dans la réalisation de ce projet. Où, je remercie Thierry Lafrance pour m’avoir fait profiter de son expérience dans la conception et le montage de banc d’essai, je remercie aussi Bénédict Besner et Nour Aimène pour leurs aidés. J’aimerais aussi remercier aussi tous les étudiants de chaire de recherche industrielle IFS et en particulier Stephen Olala pour leur aide précieuse.

J’aimerais aussi remercier tous les étudiants de section mécanique appliquée pour les discussions sur les différents sujets scientifiques utiles dans notre développement.

Enfin, J’aimerais remercier le Conseil de Recherches en Sciences Naturelles et en Génie du Canada (CRSNG) et les partenaires industriels de la Chaire IFS, Babcock & Wilcox Canada (BWC) et Énergie Atomique du Canada Limité (ÉACL) pour leur soutien financier.

RÉSUMÉ

L’usure par frottement de tubes de générateur de vapeur due aux vibrations induites par l’écoulement de fluide demeure un problème important dans l’industrie nucléaire. Azizian et Mureithi ont récemment développé le modèle de frottement Hybride (Azizian & Mureithi, 2013) pour simuler tous les comportements de frottement pour l’interaction tube/support. Cependant, l'identification des paramètres du ce modèle demeure non résolue.

Pour identifier les paramètres des modèles de frottement, tous les éléments suivants sont nécessaires : les forces de contact (force tangentielle (frottement) et force normale (impact)), la vitesse et le déplacement de glissement dans la zone de contact. La mesure directe de ces éléments par l’utilisation d’un tube de générateur de vapeur en interaction avec ces supports est difficile à réaliser. Pour simplifier ce problème, on a construit un nouveau banc d’essai, où on a utilisé une poutre encastrée d'un côté et simple appui avec le pris en considération de l’effet de frottement dans l’autre. Cette poutre agit comme un amplificateur mécanique des effets de frottement à l'échelle microscopique. L'utilisation de ce problème simplifié, les forces de contact, la vitesse et le déplacement de glissement peuvent être calculés en utilisant la mesure de réponse de la poutre.

La méthode de balance harmonique inversée est une nouvelle méthode basée sur l'analyse modale non linéaire qui a été développée dans ce travail pour calculer les forces de contact. Cette méthode est basée également sur le principe de superposition modale et le développement en série de Fourier. Deux formulations sont possibles, celle de la forme harmonique et celle de la forme sous-harmonique. Ces deux formulations peuvent être combinées avec deux méthodes de lissage de la forme modale, le lissage par série trigonométrique et le lissage par de spline. L'approche basée sur les formes sous-harmoniques combinée à la méthode de lissage par de spline a donné de meilleurs résultats pour la reconstruction des signaux des accéléromètres. La reconstruction des signaux a permis d'identifier avec précision les paramètres du modèle de frottement Hybride avec une approche à plusieurs étapes. Cinq paramètres du modèle de frottement Hybride ont étés identifiés en utilisant des modèles de frottement Dahl et LuGre. Certains de ces paramètres sont les mêmes que ceux du modèle de frottement de Coulomb et du modèle de frottement de decay (Stribeck).

Dans le présent travail, la simulation par la méthode des éléments finis (MEF) sera réalisée en prenant en considération une poutre encastrée à une extrémité et un simple appui avec l'effet de frottement à l'autre extrémité. Cette poutre est modélisée en utilisant l'élément 2D shell et elle sert à valider les paramètres des modèles de frottement identifiés à l'aide des résultats de la méthode de balance harmonique inversée et des modèles de base du modèle de frottement hybride.

Deux modèles statiques de frottement, le modèle Coulomb et le modèle Stribeck (seulement des résultats préliminaires) ont été testés. Les deux modèles produisent des forces de frottement, la force normale et le déplacement de glissement de l'ordre de grandeur similaire à la force de frottement calculée à l'aide de la méthode de la balance harmonique inverse (BHI) à la fréquence de résonance. Cependant, les valeurs de bande passante sont évidemment différentes de celles des résultats expérimentaux. Par ailleurs, les modèles de frottement de Coulomb et de decay (Stribeck) donnent des paramètres modaux (fréquence de résonance et modes normaux non linéaires (MNNs)) qui sont plus proches de ceux des expériences. De plus, le modèle de frottement de decay (Stribeck) donne des résultats plus proches du résultat expérimental.

Le présent travail démontre que les deux modèles de frottement statique: le modèle de frottement de Coulomb et celui de decay sont incapables de représenter avec précision tous les comportements de frottement, en particulier dans le régime collage, conduisant finalement à de mauvaises estimations du taux de travail à toutes les fréquences.

Dans des travaux futurs, une analyse plus approfondie du comportement du modèle Stribeck sera nécessaire pour être en mesure de valider leurs paramètres. Ensuite, les paramètres des deux modèles de frictions dynamiques (modèles Dahl et LuGre) seront validés et suivis de la validation du modèle de frottement hybride en passant par l'identification de leurs paramètres.

ABSTRACT

Fretting wear of steam generator tubes due to vibration induced by fluid flow remains a serious problem in the nuclear industry. Azizian and Mureithi (2013) have recently developed a hybrid friction model to simulate the friction behavior of tube-support interaction. However, identification of the model parameters remains unresolved.

To identify the parameters of the friction model, the following quantities are required: contact forces (tangential force (friction) and normal force (impact)), the slip velocity and displacement in the contact region. Simultaneous direct measurement of these quantities by using a steam generator tube interacting with its supports is difficult. To simplify the problem, a newly built test rig, where a beam clamped at one end and simply supported with the consideration of friction at the other is used as a mechanical amplifier of the friction effects at the microscopic level. Using this simplified approach, the contact forces, the sliding velocity and the displacement can be indirectly obtained from the beam's vibration response measurements.

The inverse harmonic balance method is a new method based on nonlinear modal analysis which is developed in this work to calculate the contact forces. The method is based on the modal superposition principle and Fourier series expansion. Two formulations are possible, a harmonic form formulation and a sub-harmonic form formulation. These two formulations can be combined with two mode shape form fitting methods, a trigonometric series and spline methods. The approach based on sub-harmonic forms coupled with spline fitting gave the best results for the accelerometer signal reconstruction. Signal reconstruction made it possible to accurately identify the parameters of the hybrid friction model with a multiple step approach. Five parameters of the hybrid friction model were identified using Dahl and LuGre friction models. Some of these parameters are the same as those of the Coulomb and decay (Stribeck) friction models.

In further work, the simulation by the finite element method (FEM) of a beam clamped at one end and simply supported with the consideration of friction effect at the other is conducted. This beam is modeled using 2D shell FEM element and is used to validate the parameters of the

friction models identified using inverse harmonic balance method results and the basic models of the Hybrid friction model.

Two static friction models, the Coulomb model and Stribeck model (preliminary result), are tested. The two models produce friction forces, normal force and slip displacement of the correct order of magnitude compared to the friction force calculated using the inverse harmonic balance method at the resonance frequency. However, their FRF bandwidth values are significantly far from the experimental results. Furthermore, Coulomb and decay friction models yield modal parameters (resonance frequency and the nonlinear normal modes (NNMs)) that are close to those of the experiments. The decay friction model yields the closest to the experimental result for the NNMs and resonance frequency.

The analysis demonstrates that both static friction models: Coulomb friction model and decay friction model are incapable of accurately representing all the behaviors of friction, especially in the sticking regime, ultimately leading to incorrect work rate estimates in all frequency.

In recommended future work, more analysis of the Stribeck model behaviour is necessary to be able to validate their parameters. The parameters of the two dynamic friction models (Dahl and LuGre models) can be validated followed by the validation of the hybrid friction model through their parameters identification.

TABLE DES MATIÈRES

DÉDICACE III

REMERCIEMENTS IV

RÉSUMÉ V

ABSTRACT VII

TABLE DES MATIÈRES IX

LISTE DES TABLEAUX XIII

LISTE DES FIGURES XV

LISTE DES SIGLES ET ABRÉVIATIONS XXII

LISTE DES ANNEXES XXV

CHAPITRE 1 INTRODUCTION 1

CHAPITRE 2 REVUE DE LITTÉRATURE 2

2.1 Interaction entre les tubes et leurs supports 2

2.1.1 Introduction 2

2.1.2 Modes de contact 3

2.1.3 Forces d'excitation 4

2.1.4 Mécanisme de défaillances 5

2.1.5 Zone de contact 5

2.1.6 Le modèle de contact ponctuel vs le modèle de contact segmentaire 7

2.2 Modèles d'impact 8

2.2.1 Introduction 8

2.2.2 Théorème de contact de Hertz 9

2.2.3 Problème de contact avec glissement : 14

2.2.4 Les autres modèles de contact 18

2.3 Modèles de frottement 19
2.3.1 Les effets du phénomène de frottement : 20
2.3.2 Modèles statiques de frottement 21
2.3.3 Modèles dynamiques de frottement 23
2.4 Identification des paramètres des modèles 30
2.4.1 Identification des paramètres du modèle de LuGre 32
2.4.2 Identification des paramètres dynamiques 32
2.4.3 Identification des paramètres statiques 34
2.4.4 Identification des paramètres par l'approche de Borsotto : 34
2.4.5 Identification des paramètres du modèle d'Azizian-Mureithi 35
CHAPITRE 3 PRÉSENTATION DE LA THÈSE 37
3.1 Introduction 37
3.2 La problématique 37
3.3 Objectifs de la recherche : 38
3.4 Méthodologie 38
3.5 Présentation de la thèse : 40
CHAPITRE 4 MÉTHODE EXPÉRIMENTALE 42
4.1 Introduction 42
4.2 Banc d'essai 42
4.3 La méthode NNMs 46
4.4 Conclusion 49
CHAPITRE 5 ARTICLE 1: IDENTIFICATION OF FRICTION MODEL PARAMETERS USING THE INVERSE HARMONIC METHOD 50
5.1 Abstract 50
5.2 Introduction 51

5.3 The test rig and theoretical consideration 52
5.4 The nonlinear normal modes 54
5.5 Experimental Results and Discussion 61
5.5.1 Slip regimes 61
5.5.2 The non-linear effects of friction 62
5.5.3 Nonlinear normal modes versus linear normal modes 64
5.5.4 Reconstruction of accelerometer signals 66
5.5.5 Friction force 68
5.5.6 Friction model parameters identification 72
5.5.7 Friction model simulation results 77
5.6 CONCLUSION 80
CHAPITRE 6 ARTICLE 2: VALIDATION OF FRICTION MODEL PARAMETERS IDENTIFIED USING THE IHB METHOD USING FINITE ELEMENT METHOD 81
6.1 Abstract 81
6.2 Introduction 82
6.3 Principle of the inverse harmonic balance (IHB) method 83
6.4 Numerical simulation 87
6.4.1 Coulomb friction model 87
6.4.2 Decay friction model (Stribeck friction model) 89
6.4.3 Finite element modeling 90
6.4.4 PARAMETER VALIDATION 94
6.4.5 PARAMETER SENSITIVITY ANALYSIS 101
6.5 CONCLUSION 109
CHAPITRE 7 DISCUSSION GÉNÉRALE 111
7.1 Résultats complémentaires de Chapitre 5 111

7.2 L’approche multi étapes : 117
7.3 Conclusion 118
CHAPITRE 8 CONCLUSION ET RECOMMANDATIONS 119
BIBLIOGRAPHIE 123
ANNEXES 133

LISTE DES TABLEAUX

Tableau 2-1 : Formulations et caractéristiques des modèles statiques de frottement 22

Tableau 2-2 : Méthodes d'identification des paramètres par l'approche de Borsotto 35

Tableau 2-3 : Les paramètres du modèle d'Azizian-Mureithi trouvés pour le test de Baumberger 36

Tableau 4-1 : Dimension exacte de la poutre et paramètres de la zone de contact 44

Tableau 7-1 : Erreur d'amplitude de la FFT (niveau d'excitation de 8 N).....114

Tableau 7-2 : Erreur de phase de la FFT (niveau d'excitation de 8 N) 114

Tableau 7-3 : Rapport de l'amplitude de la FFT sur la limitation de linéarité des accéléromètres (niveau d'excitation de 8 N) 116

Tableau 8-1 : Bilan des modèles de frottement selon leurs propriétés et leur domaine d'application (Nuninger et al., 2006) 133

Table 5-1 : 1st natural frequency 62

Table 5-2 : The accelerometer signals reconstruction error (8 N excitation force level).....67

Table 5-3 : FFT expansion amplitude error (6.5 N excitation force level) 69

Table 5-4 : FFT expansion phase error (6.5 N excitation force level) 70

Table 5-5 : Ratio of the FFT expansion amplitude over the non-linear accelerometer limitation (6.5N excitation force level).....71

Table 5-6 : Friction model parameters (8 N).....78

Table 5-7 : Friction model parameters (6.5 N).....78

Table 6-1 : Abaqus plane strain elements type 91

Table 6-2 : Finite element beam model characteristic 92

Table 6-3 : Friction model parameters (6.5 N) (Hadji & Mureithi, 2016).....93

Table 6-4 : 1st resonance frequency.....94

Table B–1 : 1st natural frequency.....150

Table C–1 : The accelerometer signals reconstruction error.....171

Table C–2 : LuGre and Dahl friction model parameters.....176

Table D–1 : Finite element model.....193

Table D–2 : 1st resonance frequency.....195

LISTE DES FIGURES

Figure 2-1 : Modes des supports (mode active et mode inactif) (Chen, 1991) 3

Figure 2-2 : Réponse vibratoire d'un faisceau de tubes en fonction de la vitesse 4

Figure 2-3 : Type de contact tube/support : (a) contact ponctuel; (b) contact segmentaire (M. Hassan & Rogers, 2005).....6

Figure 2-4 : Modèle de contact tube/support : (a) contact ponctuel; (b) contact segmentaire (M. Hassan & Rogers, 2005).....6

Figure 2-5 : Contact tube/support ponctuel (M. Hassan & Rogers, 2005).....7

Figure 2-6 : L'effet de largeur de support sur la RMS de force d'impact : (a) contact ponctuel; (b) contact segmentaire (M. Hassan & Rogers, 2005) 7

Figure 2-7 : L'effet de largeur de support sur la RMS de force d'impact : (a) contact ponctuel; (b) contact segmentaire(M. Hassan & Rogers, 2005).....8

Figure 2-8 : Carte de modèles d'adhésion pour les sphères élastiques basé sur le modèle Maugis-Dugdale (K. L. Johnson, 1998) 9

Figure 2-9 : Zone de contact entre deux coups (Kenneth Langstreth Johnson, 1985).....10

Figure 2-10 : Distribution de la contrainte au niveau de la zone de contact : (gauche) pression uniforme ; (droite) pression de Hertz (Kenneth Langstreth Johnson, 1985).....12

Figure 2-11 : Contact cylindrique : a) Contrainte surfacique b) Contours de la contrainte principale de cisaillement (Kenneth Langstreth Johnson, 1985) 13

Figure 2-12 : Contraintes de cisaillements principales au niveau de la zone de contact (photoélastique) : a) charge ponctuelle, b) pression uniforme, c) Poinçon plat (rigide) et d) cylindre (contact linéaire) (Kenneth Langstreth Johnson, 1985) 13

Figure 2-13 : Contrainte de cisaillement principale durant un contact avec glissement (Kenneth Langstreth Johnson, 1985) 14

Figure 2-14 : Distribution de la contrainte tangentielle (théorème de Cattaneo et Mindlin (1949)). Le tracé rouge est une simplification de la modification de Ödfalk et Vingsbo (1992) 15

Figure 2-15 : Régions de contact selon le théorème de Cattaneo et Mindlin (Kenneth Langstreth Johnson, 1985; Mindlin, 1949) 16

Figure 2-16 : Contact circulaire avec une charge P_0 et une oscillation tangentielle d'amplitude Q_* 17

Figure 2-17 : Les principales caractéristiques des modèles de contact (Zeng, 2013).....18

Figure 2-18 : Les modèles de frottement statique (figure modifiée (Aizel, 2005; Armstrong-Hélouvry et al., 1994; Ronnie Herman Anna Hensen, 2002; Olsson, Astrom, De Wit, Gafvert, & Lischinsky, 1998)) 21

Figure 2-19 : Le modèle de Dahl (figure modifiée (Aizel, 2005; Olsson et al., 1998)).....24

Figure 2-20 : Vue microscopique entre deux surfaces en contact (modélisation de Bristles) (Aizel, 2005).....25

Figure 2-21 : Représentation de la fonction $\alpha(z,\dot{x})$ (Dupont et al., 2000).....27

Figure 2-22 : Régions de déplacement dans la zone de contact et le modèle hybride de ressort-amortisseur d'Azizian-Mureithi (2012) 28

Figure 2-23 : Comparaison entre le modèle de frottement d'Azizian-Mureithi et le modèle de LuGre (Azizian, 2012) 29

Figure 2-24 : Comparaison entre le modèle de frottement d'Azizian-Mureithi, le modèle d'Ozaki-Hashiguchi (2010) et l'expérience réalisée par Baumberger et al. (Azizian, 2012) 30

Figure 2-25 : Algorithme d'identification des paramètres statiques du modèle de LuGre (Couillard, 2008) 34

Figure 4-1 : Schéma d'une poutre non-linéaire.....43

Figure 4-2 : Les directions des forces appliquées au point de contact.....43

Figure 4-3 : Schéma du banc d'essai poutre non-linéaire 44

Figure 5-1 : Schematic of a nonlinear beam 52

Figure 5-2 : Direction of forces applied at the contact point 52

Figure 5-3 : Schematic of the test rig 53

Figure 5-4 : The effect of slip regime on the shaker (the sensitivity of the shaker slip regime) Zone I: Stable sticking (pre-sliding), Zone II: beginning slip (stick-slip) and Zone III: sliding regime. 61

Figure 5-5 : The effect of slip regime on the beam response Zone I: Stable sticking (pre-sliding), Zone II: unstable slip (stick-slip) and Zone III: stable sliding regime (large slip) 62

Figure 5-6 : FFT of the system response at the drive point (at 50Hz) 63

Figure 5-7 : The frequency response (FRF) of the system (first harmonic) 63

Figure 5-8 : The first non-linear mode depending on the level of excitement (F_{max} = 8 N) 64

Figure 5-9 : The first harmonic and sub-harmonic form at 8 N excitation level 64

Figure 5-10 : The second harmonic and sub-harmonic form at 8 N excitation level 65

Figure 5-11 : The evaluation of the 1^{st} and the 2^{nd} harmonic form in one period 66

Figure 5-12 : Accelerometer signal reconstruction (F_{max} = 8 N) 67

Figure 5-13 : Harmonic number effect in friction force calculation (decoupled harmonic) Firstly, we investigate the effect of the number of harmonics considered on the friction force level calculation 68

Figure 5-14 : Harmonic number effect in friction force calculation (coupled harmonic) 69

Figure 5-15 : Friction force (8N excitation force level) 71

Figure 5-16 : Friction force (IHB method at 8N excitation force level) 72

Figure 5-17 : Schematic of the hybrid friction model (Azizian, 2012) 73

Figure 5-18 : Friction force (Stribeck model simulation) 76

Figure 5-19 : Friction force (Dahl and LuGre models simulation) 77

Figure 5-20 : 1 DOF friction models simulation 79

Figure 6-1 : Schematic of a nonlinear beam (Hadji & Mureithi, 2014a) 84

Figure 6-2 : Forces acting at the contact point (Hadji & Mureithi, 2014a).....84

Figure 6-3 : Cantilever beam end deflection, (B) is the zoom of the superimposed lines in the figure (A).....90

Figure 6-4 : Beam meshing, (A) is the 1D model, (B) is the 2D model 91

Figure 6-5 : 1st natural frequency, (B) is the zoom of the superimposed lines in the figure (A) ...92

Figure 6-6 : 1st nonlinear normal mode, a- Lagrange formulation b- penalty formulation.....95

Figure 6-7 : Beam response envelope (deflection maximal), a- Lagrange formulation b- penalty formulation.....96

Figure 6-8 : FRF at driving point, Coulomb friction model (a- Lagrange formulation and b- penalty formulation), c- decay friction model.....97

Figure 6-9 : Slip displacement, a- Lagrange formulation b- penalty formulation 98

Figure 6-10 : Slip velocity, a- Lagrange formulation b- penalty formulation.....99

Figure 6-11: Friction force, a- Lagrange formulation b- penalty formulation 100

Figure 6-12 : Contact normal force, A- Lagrange formulation, B- penalty formulation 100

Figure 6-13 : Beam response envelope (deflation maximal), (A) Lagrange formulation, penalty formulation: (B) F_f sensitivity and (C) μ_c sensitivity).....101

Figure 6-14 : FRF at driving point, (A) Lagrange formulation, penalty formulation: (B) Ff sensitivity and (C) μ_c sensitivity.....102

Figure 6-15 **:** Slip displacement, (A) Lagrange formulation, penalty formulation: (B) Ff sensitivity and (C) μ_c sensitivity.....103

Figure 6-16 : Slip velocity, (A) Lagrange formulation, penalty formulation: (B) F_f sensitivity and (C) μ_c sensitivity 104

Figure 6-17 : Friction force obtained from: Lagrange formulation (a), penalty formulation (b- F_f sensitivity and c- μ_c sensitivity).....105

Figure 6-18 : Contact normal force, (A) Lagrange formulation, penalty formulation: (B) F_f sensitivity and (C) μ_c sensitivity.....106

Figure 6-19 : Schematic of the hybrid friction model (Azizian, 2012).....108

Figure 7-1 : Les formes harmoniques et sous harmoniques à niveau d'excitation de 8N 112

Figure 7-2 : Friction force (6.5N excitation force level).....113

Figure 7-3 : Force de frottement (la méthode IHB niveau d'excitation de 6,5N) 113

Figure 7-4 : L'évaluation dans une période pour des formes harmoniques (haute harmonique) .115

Figure 8-1 : Simulation de l'effet de broutage (Stribeck effect) (Aizel, 2005).....133

Figure 8-2 : Fonctions de réponse en fréquence (FRF) comportement de préglissement (Ron H. A. Hensen et al., 2002).....134

Figure 8-3 : Exemple schématique de la zone de contact d'un contact métal-métal avec lubrification (Armstrong & Qunyi, 2008). 134

Figure 8-4 : La dynamique de brins (Bristles) dans le test de Cattaneo-Mindlin. 135

Figure B–1 : Schematic of a nonlinear beam 142

Figure B–2 : Direction of forces applied at the contact point 142

Figure B–3 : Schematic of the test rig.....143

Figure B–4 : The effect of slip regime on the shaker (the sensitivity of the shaker slip regime) 148

Figure B–5 : FFT of the system response at the drive point (at 50Hz) 149

Figure B–6 : The frequency response (FRF) of the system (first harmonic) 149

Figure B–7 : The first non-linear mode depending on the level of excitement 150

Figure B–8 : The error between the first experimental NM, the NNMs and LMs.....151

Figure B–9 : The accelerometer signals reconstruction 151

Figure B–10 : The accelerometer signals reconstruction error 152

Figure B–11 : Friction force.....152

Figure B–12 : Schematic of the hybrid friction model (Azizian, 2012) 153

Figure B–13 : Friction force and Dahl model 156

Figure B–14 : The first non-linear mode depending on the level of excitement 160

Figure C–1 : Schematic of a nonlinear beam 164

Figure C–2 : Direction of forces applied at the contact point 164

Figure C–3 : The first harmonic and sub-harmonic form at 6.5 N excitation level 169

Figure C–4 : The second harmonic and sub-harmonic form at 6.5 N excitation level 170

Figure C–5 : The evaluation of the 1^{st} and the 2^{nd} harmonic form in one period 170

Figure C–6 : Friction force.....172

Figure C–7 : Schematic of the hybrid friction model (Azizian, 2012) 173

Figure C–8 : Friction force and LuGre model.....175

Figure C–9 : The high harmonic and sub-harmonic form at 6.5 N excitation level 181

Figure C–10 : The evaluation of high harmonic form in one period 182

Figure D–1 : Schematic of a nonlinear beam (Hadji & Mureithi, 2014a) 188

Figure D–2 : Forces acting at the contact point (Hadji & Mureithi, 2014a).....188

Figure D–3 : 1^{st} nonlinear normal mode 195

Figure D–4 : FRF at driving point experimental result.....196

Figure D–5: FRF at driving point simulation results 197

Figure D–6: Slip tolerance (fraction Ff) effect on the friction force (Coulomb) 198

Figure D–7 : Slip tolerance (fraction Ff) effect on the friction force (decay).....198

Figure D–8 : Slip tolerance (fraction Ff) effect on the system response at the driving point (Coulomb) 199

Figure D–9 : Slip tolerance (fraction Ff) effect on the system response at the driving point (decay) 199

Figure D–10 : Added proportional mass damping effect on the friction force (decay) 200

Figure D–11 : Added proportional mass damping effect on the system response at the driving point (decay) 200

Figure D–12 : Slip tolerance (fraction Ff) effect on the slipping displacement (decay) 201

Figure D–13 : Schematic of the hybrid friction model (azizian, 2012) 203

LISTE DES SIGLES ET ABRÉVIATIONS

A	Area of the cross section of the beam
E	Youngs modulus
F	Excitation force by a shaker
F_c	Kinetic friction force limitation
F_{ex}	Excitation force amplitude
F_f	Slip tolerance (fraction of characteristic contact surface length)
F_s	Static friction force limitation
I	Quadratic bending moment
L	Length of the beam
N	Resultant of the normal force
Obj	Optimization objective function
P	Static load to ensure a permanent contact between the beam and support
R	Support reaction (impact force)
RT	Resultant of the force at the contact point in the sliding direction
T	Frictional force
T_{crit}	Critical friction force
$T_{\text{exp.}}$	Experimental friction force
$T_{suml.}$	Simulated friction force
X_f	Position of the excitation point
$\dot{W}$	Work rate
c_p	Plastic damping
c_s	Pre-sliding damping
c_z	Stribeck damping
e	Thickness of the beam

$g(\dot{x})$	Stribeck function
k_e	Elastic stiffness
k_{ep}	Elastic-plastic stiffness
k_{ps}	Plastic-pre sliding stiffness
$\bar{l}_i$	Characteristic contact surface length
m	Half cylinder mass (contact element)
n	Mode index
q_i	Linear generalized coordinates
$\tilde{q}_i$	Nonlinear generalized coordinates
r	Radius of the contact element (half-cylinder)
(t)	Time dependence
u	Displacement at the contact zone
u_{crit}	Elastic slip
x_j	Position of the accelerometer j
(x)	Position dependence
y	System response (beam deflection)
y_j	System response of the accelerometer j
z_e	Elastic slip relative displacements
z_p	Plastic slip relative displacements
z_s	Partial slip relative displacements
α	Proportional mass damping
α_n	Proportional mass damping of mode n
δ	Stribeck exponent
ϕ_i	Linear normal modes
$\tilde{\phi}_i$	Nonlinear normal modes
μ_c	Kinetic friction coefficient

μ_s	Static friction coefficient
ρ	Density of the beam material
v	Velocity at the contact area
ω_n	Naturel pulsation of mode n
ζ	Damping ratio
ζ_n	Damping ratio of mode n

LISTE DES ANNEXES

Annexe A - LES MODÈLES DE FROTTEMENT 133

Annexe B – ARTICLE 3: NONLINEAR NORMAL MODES AND THE DAHL FRICTION MODEL PARAMETER IDENTIFICATION 138

Annexe C – ARTICLE 4: NONLINEAR NORMAL MODES AND THE LUGRE FRICTION MODEL PARAMETER IDENTIFICATION 161

Annexe D – ARTICLE 5: VALIDATION OF A FRICTION MODEL PARAMETERS IDENTIFIED USING THE INVERSE HARMONIC BALANCE METHOD 183

Annexe E – THESIS PRESENTATION.....207

Annexe F – GENERAL DISCUSSION 209

Annexe G – CONCLUSION AND RECOMMENDATIONS 213

CHAPITRE 1 INTRODUCTION

L'usure par frottement de tubes de générateur de vapeur due aux vibrations demeure un problème important dans l'industrie nucléaire. Dans le générateur de vapeur, l'eau s'écoule à l'intérieur de tubes du circuit primaire et autour de celui-ci à une vitesse d'environ 4 m/s, ce qui génère des vibrations et des frottements donc de l'usure (Marwan A. Hassan, Weaver, & Dokainish, 2002). Le bris d'un seul de ces tubes peut conduire à la fermeture complète de la centrale nucléaire et donc provoquer l'arrêt de production de l'énergie pour plusieurs jours. Il est donc primordial de comprendre et de résoudre les problèmes encourus à travers le design des générateurs de vapeur afin d'optimiser leur durée de vie et leur rendement. En général, durant la phase de design, les conditions aux limites sont considérées parfaites, mais en réalité il n'existe pas de conditions aux limites idéales.

Selon Chen (1991), quatre différents phénomènes peuvent causer la défaillance d'un des tubes d'un générateur de vapeur: l'impact et l'usure entre les tubes ; l'impact et l'usure entre les tubes et leurs supports ; la défaillance du joint de tube dans la plaque tubulaire et la fatigue de tube. Cependant, les causes les plus importantes d'usure sont le frottement et l'impact entre les tubes et leurs supports. De nombreux auteurs ont tenté de modéliser et de simuler ces phénomènes. Weaver et Schneider (1983) ont mis en œuvre des tests expérimentaux sur des tubes coudés en « U » avec des supports plats. Chen et al. (1985) ont effectué des essais expérimentaux pour comprendre l'efficacité du support de tube. Ce genre de tests expérimentaux fait suite aux travaux d'Axisa et al. (1984). Les travaux les plus récents ont été réalisés par Nowlan et al.(2009) et Lalonde et al. (2010). En parallèle, de nombreux auteurs ont essayé de simuler la réponse du tube en utilisant des techniques de simulations numériques (Rogers & Choisissez (1977), Rao et al. (1987), Fisher et al. (1989), Tan & Roger, (1996), Hassan et al. (2002) et Hassan et al.(2005) et Azizian (2012)). Ce projet s'inscrit dans la continuité des travaux d'Azizian (2012) où les paramètres des modèles de frottement sont identifiés expérimentalement et seront utilisés dans l'amélioration des modèles des frottement très basiques utilisées actuellement par l'industrie. À la fin, nous serons capables de prédire de manière précise la durée de vie d'un tube de générateur de vapeur.

.

CHAPITRE 2 REVUE DE LITTÉRATURE

2.1 Interaction entre les tubes et leurs supports

Hassan et Rogers (2005) ont caractérisé la zone d'interaction entre les tubes et leurs supports comme étant un contact ponctuel ou un contact linéaire. Mais leur modèle est basé sur le principe de Hertz et utilisation de la combinaison ressort-amortisseur. Plusieurs auteurs ont étudié les différents aspects de la modélisation du tube et de leur support pour estimer l'usure par frottement. Des codes de simulation ont déjà été mis au point pour simuler l'interaction tube-supports telle que : VIBIC (Rogers & Pick, 1977), H3DMAP (Sauve & Teper, 1987), Gerboise (Axisa, Antunes, & Villard, 1988), INDAP (M. A. Hassan, Weaver, & Dokainish, 2003) et FIVDYNA (Babcock & Wilcox (Toorani, Pan, Idvorian, & Vincent, 2009)).

2.1.1 Introduction

Les mécanismes des forces induites par l'écoulement de fluide dans l'échangeur de chaleur peuvent conduire à des amplitudes de vibration très élevées des tubes et provoquer un impact (Chen et al., 1985). Par conséquent, nous allons voir que des frottements et l'usure des tubes peuvent provoquer une défaillance des tubes sur une courte durée. Ce genre de défaillance pourrait être dû à la fatigue par frottement, à l'usure par frottement ou à la corrosion causée par la vibration et par l'impact (Axisa et al., 1984).

Pour avoir une bonne modélisation de l'interaction entre les tubes et leurs supports lors de la vibration induite par l'écoulement de fluide, nous devons avoir un bon modèle pour chaque type de composant du système (Chen, 1991) : 1- les forces d'excitation par l'écoulement de fluides, 2- le modèle dynamique tube-support, 3- le modèle de l'impact, 4- le modèle de frottement. Chen (1991) a aussi défini deux différents modes de support : support inactif et support actif. Généralement, il est possible de considérer que le support est actif lorsque la distance entre le tube et le support est relativement petite. Par contre, si la distance est importante, le mode de support devra être considéré comme inactif. Selon Moretti et Lowery (1973), les fréquences naturelles changent en fonction du mode de support, du niveau d'excitation et du jeu dans le support.

Price (1995) a classifié les mécanismes d'excitations de vibrations des structures soumises à des écoulements en trois catégories : 1- les forces de turbulences, 2- les forces périodiques ou les tourbillons alternés, 3- les forces fluidélastiques. De plus, Gorman (1976) a mis en évidence ces trois mécanismes d'excitations vibratoires lorsqu'il a présenté la réponse vibratoire d'une poutre de tubes en fonction de la vitesse de l'écoulement.

2.1.2 Modes de contact

Pour avoir une bonne simulation de la dynamique de tube avec ses supports en cas de vibration induite par l'écoulement de fluide dans le générateur de vapeur, nous devons avoir un bon modèle pour chacun des composants du système tel que décrit par Chen (1991):

1) Les forces d'excitation dues aux fluides;

2) Le modèle de dynamique du tube/support;

3) Le modèle d'impact tube/support;

4) Le modèle de frottement tube/support;

5) Les effets des différents paramètres du système.

Deux différents modes de support ont été définis par Chen (1991), support inactif et support actif. Le mode de support actif correspond à la réponse d'une poutre continue supportée par plusieurs appuis. Généralement, il est possible de considérer que le support est actif lorsque la distance entre le tube et le support est relativement petite. Par contre, si la distance est importante, le mode de support inactif devra être considéré, donc le tube est soumis à de petites oscillations dans le cadre de ce type de support.

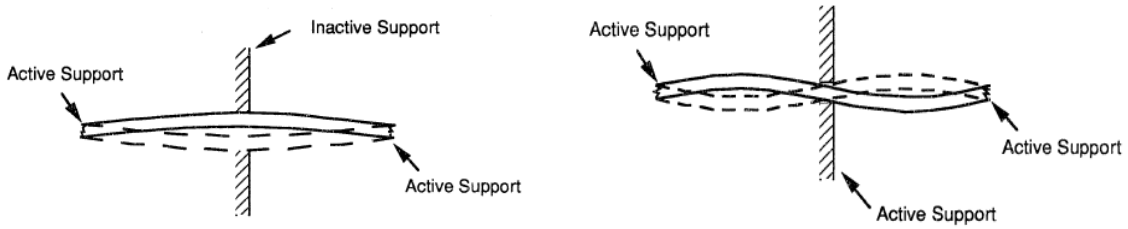

Figure 2-1 : Modes des supports (mode active et mode inactif) (Chen, 1991)

Pour de grandes et de petites oscillations, le mode de support actif et le mode de support inactif seront assumés respectivement. Mais dans la réalité, l'interaction entre les tubes et les supports dépendent de leurs conditions aux limites. Ainsi, une combinaison de ces deux modes devra être obtenue. Selon Moretti et Lowery (1973), les fréquences naturelles changent en fonction du mode de support, du niveau d'excitation et du jeu dans le support (Chen, 1991).

2.1.3 Forces d'excitation

Les forces d'excitation appliquées sur les tubes de générateur de vapeur sont induites par l'écoulement du fluide. Price (1995) classifie les mécanismes d'excitations des vibrations des structures soumises à des écoulements en trois catégories :

1- **Les forces de turbulences** : elles sont présentes dès que la vitesse de l'écoulement est non nulle;

2- **Les forces périodiques (les tourbillons alternés)** : ces forces dues aux tourbillons alternés ont des effets vibratoires importants lorsqu'il y a résonance;

3- **Les forces fluidélastiques** : elles sont prépondérantes à des vitesses très élevées de l'écoulement.

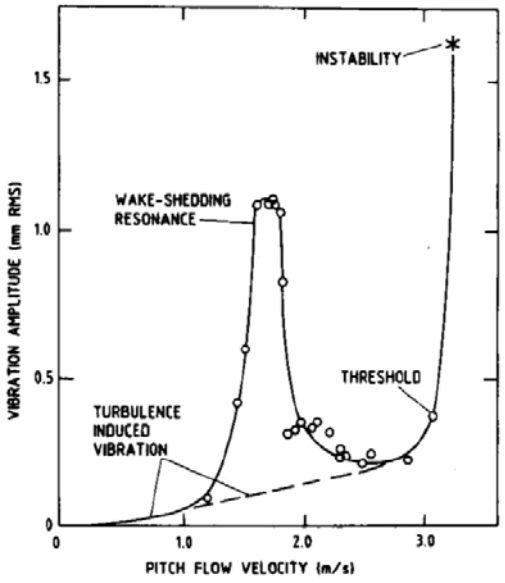

Figure 2-2 : Réponse vibratoire d'un faisceau de tubes en fonction de la vitesse de l'écoulement (Gorman, 1976)

Dans la Figure 2-2, Gorman (1976) a présenté la réponse vibratoire d'un faisceau de tubes en fonction de la vitesse de l'écoulement. Elle met en évidence les trois mécanismes d'excitations vibratoires.

2.1.4 Mécanisme de défaillances

Chen (1991) a divisé les causes de la défaillance du tube dans l'échangeur de chaleur en quatre catégories :

1) L'usure et l'impact entre les tubes;
2) L'impact et l'usure entre les tubes et leurs supports;
3) La défaillance du joint du tube dans la plaque tubulaire;
4) La fatigue du tube.

De plus, avec la présence de l'eau sous forme de vapeur à haute température et à haute pression, d'autres mécanismes peuvent provoquer aussi la défaillance des tubes (Hertzberg, 1996) :

5) La corrosion;
6) L'affaiblissement par hydrogène.

Les causes les plus importantes d'usure sont le frottement et l'impact entre le tube et leurs supports, ces causes feront l'objet d'une analyse approfondie ultérieurement.

2.1.5 Zone de contact

La zone de contact est un paramètre essentiel pour une bonne modélisation du frottement et de l'impact. Hassan et Rogers (2005) ont caractérisé la zone d'interaction entre les tubes et leurs supports comme suit :

1) Contact ponctuel (edge or point contact);
2) Contact linéaire (Line or segment contact).

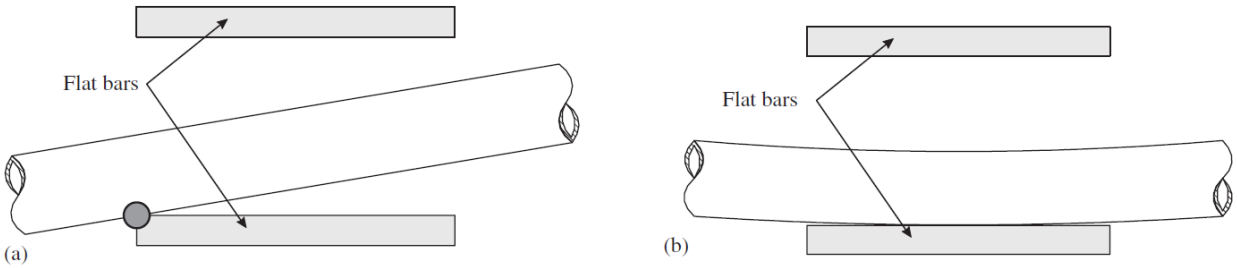

Figure 2-3 : Type de contact tube/support : (a) contact ponctuel; (b) contact segmentaire (M. Hassan & Rogers, 2005)

Dû à la difficulté d'estimer précisément la surface et la pression sur la zone de contact, on peut simplifier le mode de contact comme un contact ponctuel, où le support est considéré comme une arête de couteau (voir la Figure 2-4 (a)). Cependant, dès que le support a une largeur finie, un modèle de contact plus précis est nécessaire, comme par exemple le modèle de contact segmentaire (voir la Figure 2-4 (b)). Les points et les raideurs de ces deux modes du contact peuvent être modélisés avec un système de ressort comme indiqué sur la figure suivante (M. Hassan & Rogers, 2005) :

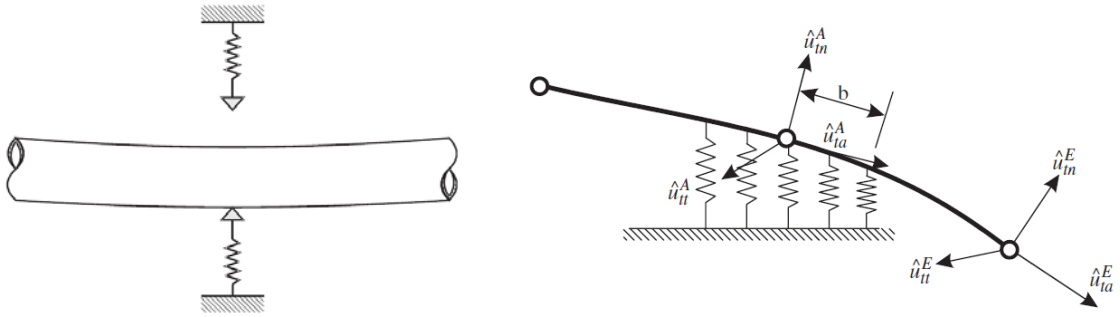

Figure 2-4 : Modèle de contact tube/support : (a) contact ponctuel; (b) contact segmentaire (M. Hassan & Rogers, 2005)

En réalité, la combinaison de ces deux modèles de contact peut se produire selon certains facteurs. La précharge au niveau de la zone du contact, le jeu et l'alignement de tubes vont influencer le type de contact. Par exemple, quand le jeu est petit avec une grande précharge, le modèle de contact approprié est le modèle de contact segmentaire. Par contre, avec un jeu important et petit ou une précharge intermittente, le modèle de contact approprié est le modèle ponctuel (M. Hassan & Rogers, 2005). Mais en réalité, d'autres cas sont possibles. Par exemple

même avec une grande précharge, il est possible de voir un contact entre le tube et l'arête vive du support dont l'usure est plus critique et que peut se produire. Pour cette raison, on a besoin d'un modèle de contact plus robuste qui peut présenter tous les cas possibles.

2.1.6 Le modèle de contact ponctuel vs le modèle de contact segmentaire

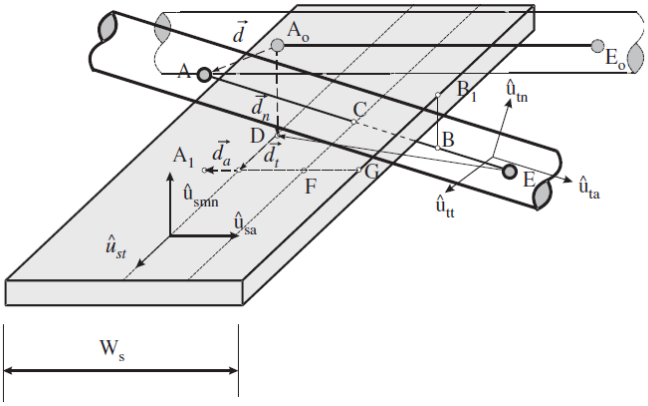

Figure 2-5 : Contact tube/support ponctuel (M. Hassan & Rogers, 2005)

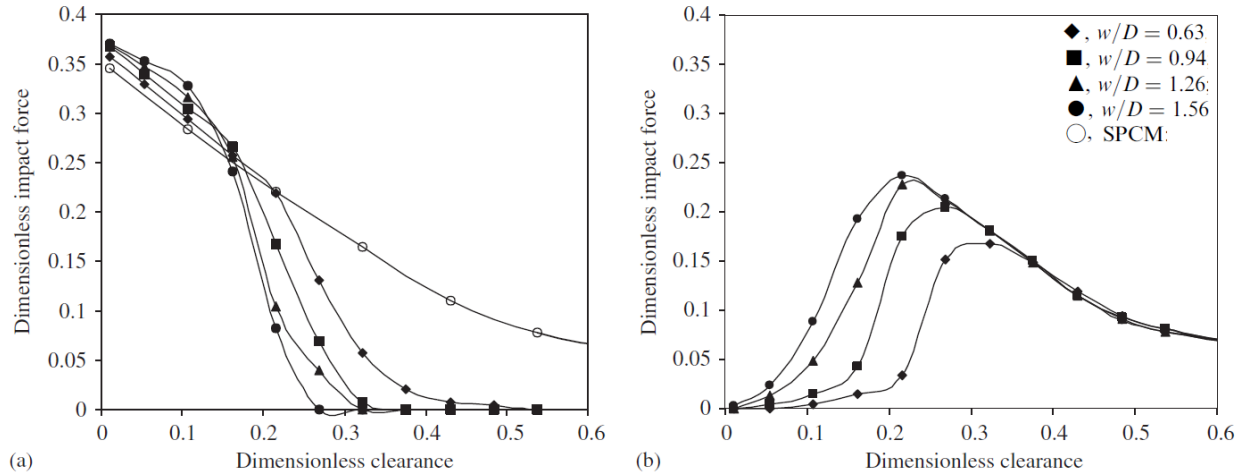

Figure 2-6 : L'effet de largeur de support sur la RMS de force d'impact : (a) contact ponctuel; (b) contact segmentaire (M. Hassan & Rogers, 2005)

Comme le montre la Figure 2-6 (a), pour le modèle de contact segmentaire, la force d'impact diminue linéairement avec l'augmentation du jeu adimensionnel d'environ 0,2. Après ce point, la moyenne quadratique « RMS » de la force d'impact diminue fortement. Pour le modèle de

contact ponctuel, la force d'impact augmente avec l'augmentation de jeu adimensionnel jusqu'à une distance adimensionnelle d'environ 0,2. Après ce point, la force efficace commence à diminuer et converge vers la même valeur indépendamment de la largeur du support (M. Hassan & Rogers, 2005). On peut trouver le même comportement pour la variation de la puissance d'usure en fonction du jeu entre le tube et le support, voir la figure suivante :

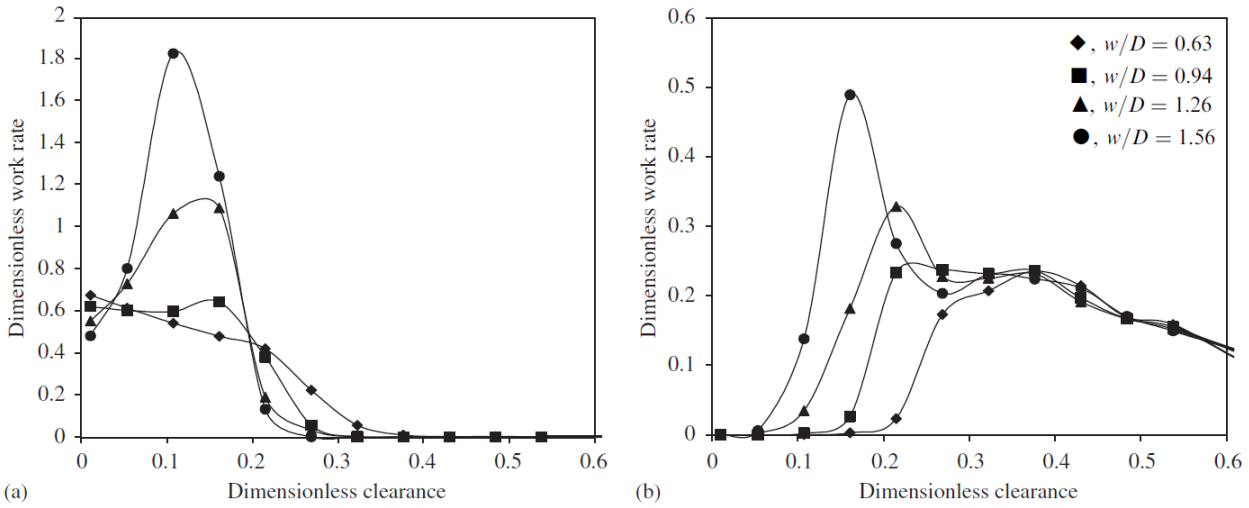

Figure 2-7 : L'effet de largeur de support sur la RMS de force d'impact : (a) contact ponctuel; (b) contact segmentaire(M. Hassan & Rogers, 2005)

2.2 Modèles d'impact

2.2.1 Introduction

Les modèles de contact ont été classifiés par Johnson et Greenwood (1998) (Figure 2-8). Les modèles Maugis-Dugdale, Bradley, DMT et JKR peuvent modéliser le contact par l'adhésion. Par contre, le modèle de Hertz est le plus utilisé pour la modélisation du contact entre des matériaux rigides (module de Young relativement grande), cependant il ne prend pas en compte le phénomène d'adhérence. Goyal et al. (1994) ont divisé les modèles d'impact en deux parties : la première étant la détection du contact entre les deux corps et la seconde, le calcul de la force due à l'interaction. Durant l'impact, il y a deux sources de dissipation d'énergie : par la force de frottement (tangentiel) et par la force d'impact (normal). Stevens et al. (2005) ont défini trois

mécanismes de dissipation de l'énergie durant l'impact : ondes élastiques, viscoélasticité et déformation plastique.

Il existe deux approches pour évaluer les forces de contact entre deux objets : la première approche, nommée contact dur « hard contact », suppose que les deux corps soient infiniment rigides (les déformations sont donc négligées). La seconde approche est nommée contact tendre « soft contact » où la déformation locale dans la zone de contact est prise en considération. La plupart des modèles développés utilisent l'une de ces approches et se basent sur le principe de la théorie de contact hertzienne (Goyal et al., 1994).

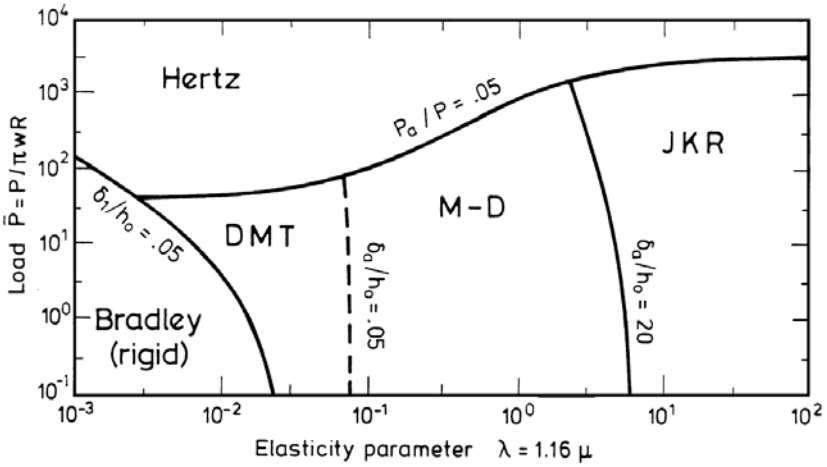

Figure 2-8 : Carte de modèles d'adhésion pour les sphères élastiques basé sur le modèle Maugis-Dugdale (K. L. Johnson, 1998)

2.2.2 Théorème de contact de Hertz

Le plupart des modèles de contact apparus dans la littérature ont été développés en se basant sur le théorème de contact de Hertz développé entre 1881 et 1895 (Geneviève, Tony, & Isabelle, 2011). Le théorème de contact de Hertz est basé sur les hypothèses suivantes (Kenneth Langstreth Johnson, 1985) :

1) Le contact sans frottement : la force normale est seule présente dans la zone de contact;
2) Les deux corps doivent être complètement élastiques;
3) Cette théorie ne tient pas compte de la force provoquée par la déformation;

4) La surface de contact doit être faible par rapport aux dimensions du corps ;
5) La surface de contact doit être continue;
6) Les forces d'adhérence de la zone de contact sont négligeables (K. L. Johnson, 1998).

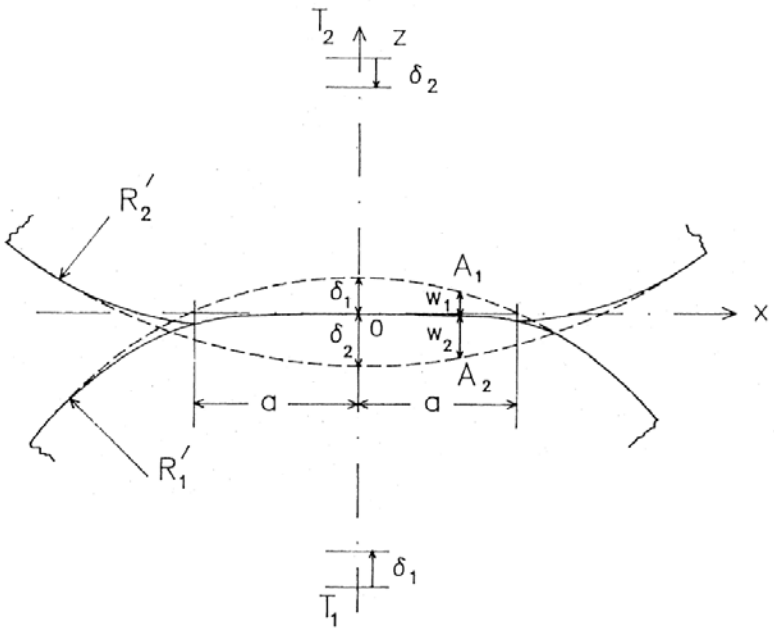

Figure 2-9 : Zone de contact entre deux coups (Kenneth Langstreth Johnson, 1985)

La Figure 2-9 montre un simple exemple de contact entre deux cylindres, leurs déplacements peuvent être calculés par (Kenneth Langstreth Johnson, 1985) :

$$u_{z1} + u_{2z} = \delta - (1/2R)r^2 \tag{2.1}$$

La courbure équivalente et le module d'élasticité peuvent être calculés par :

$$\frac{1}{R} = \frac{1}{R_1} + \frac{1}{R_2} \tag{2.2}$$

$$\frac{1}{E^*} = \frac{1-\nu_1^2}{E_1} + \frac{1-\nu_2^2}{E_2} \tag{2.3}$$

La répartition de la pression entre deux cylindres identiques peut être déterminée selon la théorie de Hertz, comme indiqué ci-dessous (Kenneth Langstreth Johnson, 1985) :

$$p = p_0\{1-(r/a)^2\}^{1/2} \tag{2.4}$$

En utilisant cette répartition de pression, le déplacement normal sera déterminé comme suit (Kenneth Langstreth Johnson, 1985) :

$$u_z = \frac{1-\nu^2}{E_{eff}}\frac{\pi p_0}{4a}(2a^2 - r^2), r \le a \tag{2.5}$$

Le demie largeur de surface de contact est calculée par (Kenneth Langstreth Johnson, 1985) :

$$a = \pi p_0 R/2E^* \tag{2.6}$$

La valeur maximale de pression peut-être calculée par (Kenneth Langstreth Johnson, 1985) :

$$P_0 = \frac{2Gu_{z,t}}{\pi(1-\nu)a} = \frac{4G\zeta_t}{\pi(1-\nu)a} \tag{2.7}$$

Donc, la charge de compression sera (Kenneth Langstreth Johnson, 1985) :

$$P = \int_0^a p(r)2\pi r dr = \frac{2}{3}p_0\pi a^2 \tag{2.8}$$

De la théorie de Hertz, la force entre deux cylindres identiques peut être déterminée avec les équations suivantes (Babitskii, 1998):

$$F = c_1 u_z^{3/2} \tag{2.9}$$

où :

$$c_1 = \frac{4\sqrt{2}}{3}c\frac{E}{1-\nu^2}\left(\frac{1}{R_1}+\frac{1}{R_2}\right)^{-1/2} \tag{2.10}$$

Comme les deux surfaces en interaction tentent à devenir des surfaces planes, l'équation de la force de contact sera formulée comme suit (Babitskii, 1998):

$$F = c_2 u_z^{\frac{2m+1}{2m}} \tag{2.11}$$

où $1 \le \frac{2m+1}{2m} \le 3/2$ et m=1, 2, 3…. Comme la surface de contact est plate (par différentes géométries de la zone de contact ou par la dégradation de la zone de contact par usure) m

converge vers l'infini. Le coefficient C_2 est de l'ordre de la valeur de C_1. c est une constante de proportionnalité et elle est déterminée expérimentalement. Mais, quand $c = \frac{1}{\pi\sqrt{8}}$, l'équation (2.11) prend la forme hertzienne.

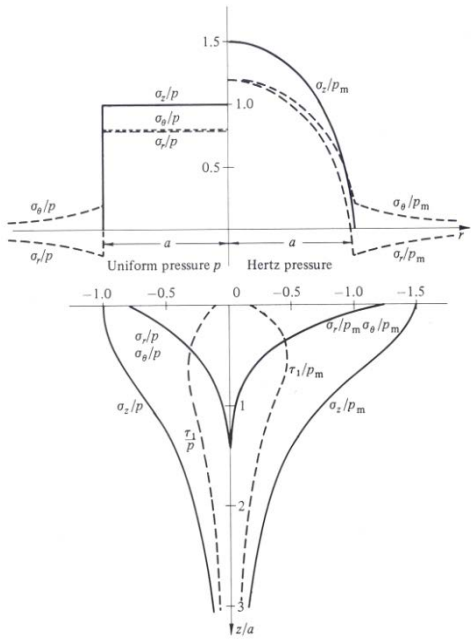

Figure 2-10 : Distribution de la contrainte au niveau de la zone de contact : (gauche) pression uniforme ; (droite) pression de Hertz (Kenneth Langstreth Johnson, 1985)

Comme le montre la Figure 2-10, les contraintes sur la surface de la zone de contact dans les directions $r, \theta \; et \; z$ peuvent être déterminées par (Kenneth Langstreth Johnson, 1985) :

$$\bar{\sigma}_r / p_0 = \frac{1-2\nu}{3}(a^2/r^2)\left\{1-(1-r^2/a^2)^{3/2}\right\} - (1-r^2/a^2)^{1/2} \tag{2.12}$$

$$\bar{\sigma}_\theta / p_0 = -\frac{1-2\nu}{3}(a^2/r^2)\left\{1-(1-r^2/a^2)^{3/2}\right\} - 2\nu(1-r^2/a^2)^{1/2} \tag{2.13}$$

$$\bar{\sigma}_z / p_0 = -(1-r^2/a^2)^{1/2} \tag{2.14}$$

La Figure 2-11 montre les contraintes dans la direction (z) que l'on peut calculer par (Kenneth Langstreth Johnson, 1985) :

$$\sigma_x = -\frac{p_0}{a}\left\{(a^2+2z^2)(a^2+z^2)^{-1/2} - 2z\right\} \tag{2.15}$$

$$\sigma_z = -p_0 a(a^2+z^2)^{-1/2} \tag{2.16}$$

$$\tau_1 = p_0 a\left\{z - z^2(a^2+z^2)^{-1/2}\right\} \tag{2.17}$$

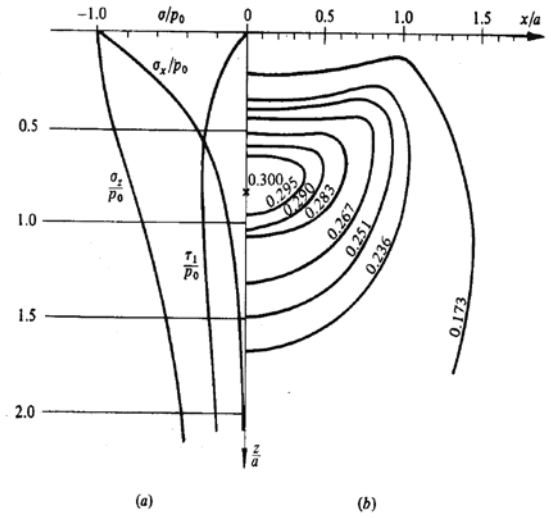

Figure 2-11 : Contact cylindrique : a) Contrainte surfacique b) Contours de la contrainte principale de cisaillement (Kenneth Langstreth Johnson, 1985)

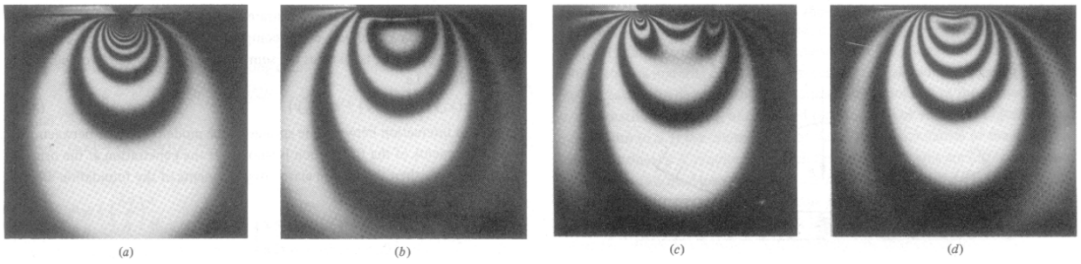

Figure 2-12 : Contraintes de cisaillements principales au niveau de la zone de contact (photoélastique) : a) charge ponctuelle, b) pression uniforme, c) Poinçon plat (rigide) et d) cylindre (contact linéaire) (Kenneth Langstreth Johnson, 1985)

La Figure 2-12 montre les contours de contrainte de cisaillement principale McEwen, que l'on peut calculer par (Kenneth Langstreth Johnson, 1985) :

$$\tau_{xz} = \frac{p_0}{a} n \left(\frac{m^2 - z^2}{m^2 + n^2} \right) \tag{2.18}$$

$$m^2 = \frac{1}{2}[\{(a^2 - x^2 + z^2)^2 + 4x^2 z^2\}^{1/2} + (a^2 - x^2 + z^2)] \tag{2.19}$$

$$n^2 = \frac{1}{2}[\{(a^2 - x^2 + z^2)^2 + 4x^2 z^2\}^{1/2} - (a^2 - x^2 + z^2)] \tag{2.20}$$

2.2.3 Problème de contact avec glissement :

Comme le montre la Figure 2-13, la contrainte de cisaillement principale pour différents types de charges peut être utilisée pour valider l'équation (2.18). La contrainte de cisaillement pour un contact cylindrique (Figure 2-12 (d)) est $(\tau_1)_{\max} = 0.30\, p_0$ à $z = 0.78a$. Cependant, il est important de noter que la distribution de la contrainte de cisaillement principale va changer dû à l'application d'une vitesse tangentielle comme montre la Figure 2-13.

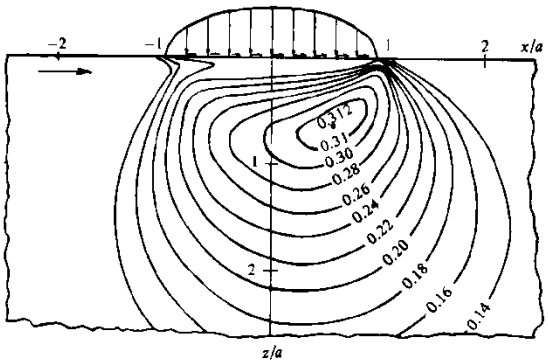

Figure 2-13 : Contrainte de cisaillement principale durant un contact avec glissement (Kenneth Langstreth Johnson, 1985)

La distribution de la contrainte tangentielle selon le théorème de Cattaneoet Mindlin (Kenneth Langstreth Johnson, 1985; Stachowiak & Batchelor, 2005) est donnée par les équations suivantes :

$$q(r)=\begin{cases}\mu p_0\left\{\left(1-\dfrac{r^2}{a^2}\right)^{1/2}-\left(1-\dfrac{r^2}{c^2}\right)^{1/2}\right\} & 0\le r<c\\ \mu p_0\left(1-\dfrac{r^2}{a^2}\right)^{1/2} & c\le r\le a\end{cases} \tag{2.21}$$

où μ est le coefficient de frottement, P_0 contrainte normale et a rayon de contact.

En se basant sur l'équation (2.21), la surface de contact est divisée en deux régions, une région avec un déplacement élastique et une région de glissement partiel. La Figure 2-14 montre la différence entre la distribution de la contrainte tangentielle dans les deux régions qui sont démarquées par le paramètre 'c'.

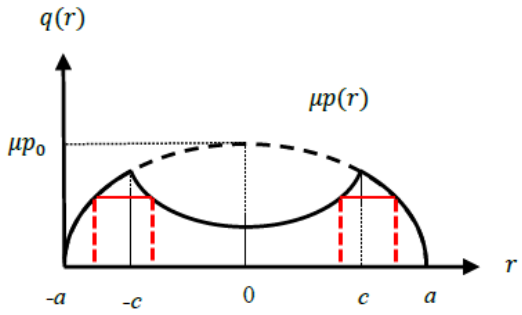

Figure 2-14 : Distribution de la contrainte tangentielle (théorème de Cattaneo et Mindlin (1949)). Le tracé rouge est une simplification de la modification de Ödfalk et Vingsbo (1992)

Dans la région $0 \le |r| \le c$, les points de l'interface de contact coïncident et se déplacent ensemble, représentant ainsi la région de collage comme il est indiqué sur la Figure 2-15 par le point 'A'. Cependant, pour la région $c \le |r| \le a$, les points de contact sur les deux corps ont un mouvement tangentiel relatif qui représente la région de glissement, comme représentée sur la Figure 2-15 par les points 'B' et 'C' (Kenneth Langstreth Johnson, 1985; Mindlin, 1949).

La valeur absolue du déplacement tangentiel relatif de la région de contact est déterminée comme suit (Kenneth Langstreth Johnson, 1985; Mindlin, 1949) :

$$\delta_x=\frac{3(2-\nu)\mu N}{8Ga}\left\{1-\left(1-\frac{F_T}{\mu N}\right)^{2/3}\right\} \tag{2.22}$$

où N est la force normale du contact, v le coefficient de Poisson, μ le coefficient de frottement et G est le module de cisaillement.

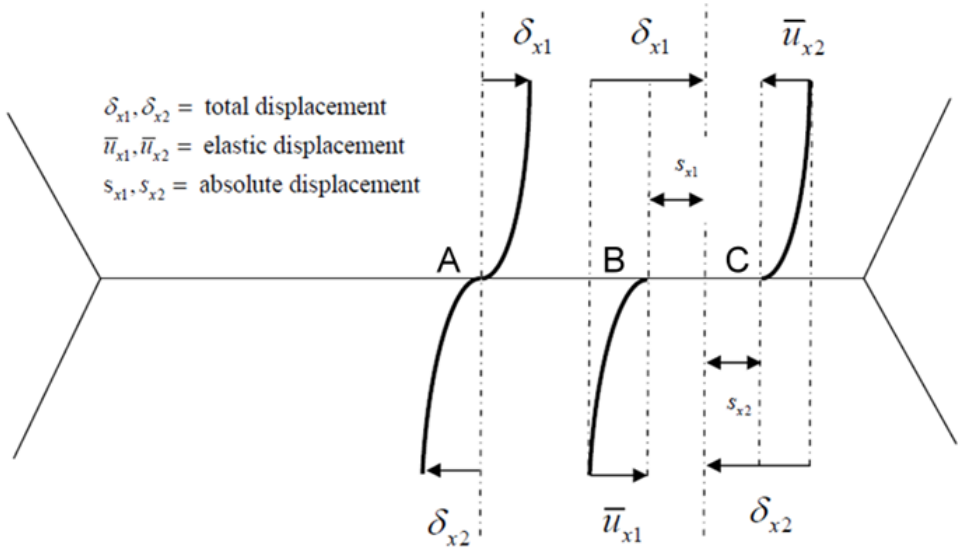

Figure 2-15 : Régions de contact selon le théorème de Cattaneo et Mindlin (Kenneth Langstreth Johnson, 1985; Mindlin, 1949)

Lors du développement des théories, Cattaneo-Mindlin, Mindlin et Deresiewicz (1953) , ont étudié l'effet de la variation de la force tangentielle sur la répartition des contraintes dans la zone de contact. Cette étude a déterminé l'énergie de dissipation par cycle lors d'un déplacement tangentiel oscillatoire, donnée par l'équation (2.23), par l'intégration de la courbe de force de déplacement pour un cycle.

$$\Delta E = \frac{9(2-v)\mu^2 N^2}{10Ga}\left\{1-\left(1-\frac{T^*}{\mu N}\right)^{5/3}-\frac{5T^*}{6\mu N}\left[1+\left(1-\frac{T^*}{\mu N}\right)^{2/3}\right]\right\} \qquad (2.23)$$

où T^* est l'amplitude de la force d'oscillation tangentielle et « a » est le rayon de contact.

En 1992 Ödfalk et Vingsbo (1990) ont mesuré le déplacement de préglissement δ en fonction de la fréquence d'excitation. Les résultats indiquent une sous-estimation du déplacement de préglissement par la théorie élastique de Cattaneo-Mindlin (1953). Pour corriger cette sous-estimation, Ödfalk et Vingsbo (1992) ont développé un modèle plastique en considérant la limite d'élasticité de la zone de contact sur la base des équations (2.24)-(2.27).

$$\delta_p = \beta\left[\gamma\frac{(F_T - \alpha F_{Ty})}{k_p} - \alpha\frac{(T^* - F_{Ty})}{2k_p}\right] \tag{2.24}$$

où F_T, k_p, F_{Ty} sont la force tangentielle, le coefficient d'écrouissage et la limite de frottement élastique respectivement. δ_p est le déplacement de préglissement associé à la limite d'élasticité. Les paramètres α β et γ peuvent être déterminés par (Ödfalk & Vingsbo, 1992):

$$\alpha = \begin{cases} 1 & \frac{d\delta}{dt} > 0 \\ -1 & \frac{d\delta}{dt} < 0 \end{cases} \tag{2.25}$$

$$\beta = \begin{cases} 1 & T > F_{Ty} \\ 0 & T <= F_{Ty} \end{cases} \tag{2.26}$$

$$\gamma = \begin{cases} 1 & |F_T| > F_{Ty} \text{ et } \frac{dF_T}{dt}F_T > 0 \\ 0 & \text{si non} \end{cases} \tag{2.27}$$

où δ est le déplacement de préglissement total.

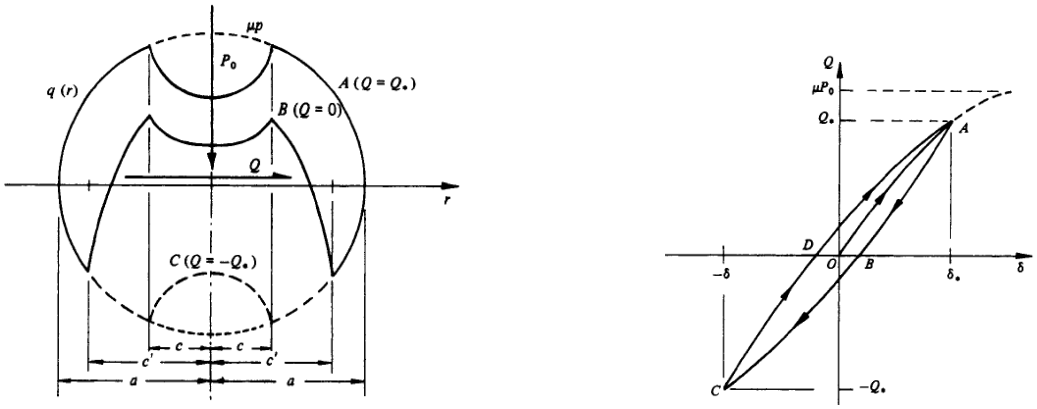

(a) (b)

Figure 2-16 : Contact circulaire avec une charge P_0 et une oscillation tangentielle d'amplitude Q_* (a) changement de distribution de la contrainte de cisaillement en fonction des trois cas d'excitations (A, B et C), (b) cycle de chargement en fonction du déplacement (Kenneth Langstreth Johnson, 1985)

2.2.4 Les autres modèles de contact

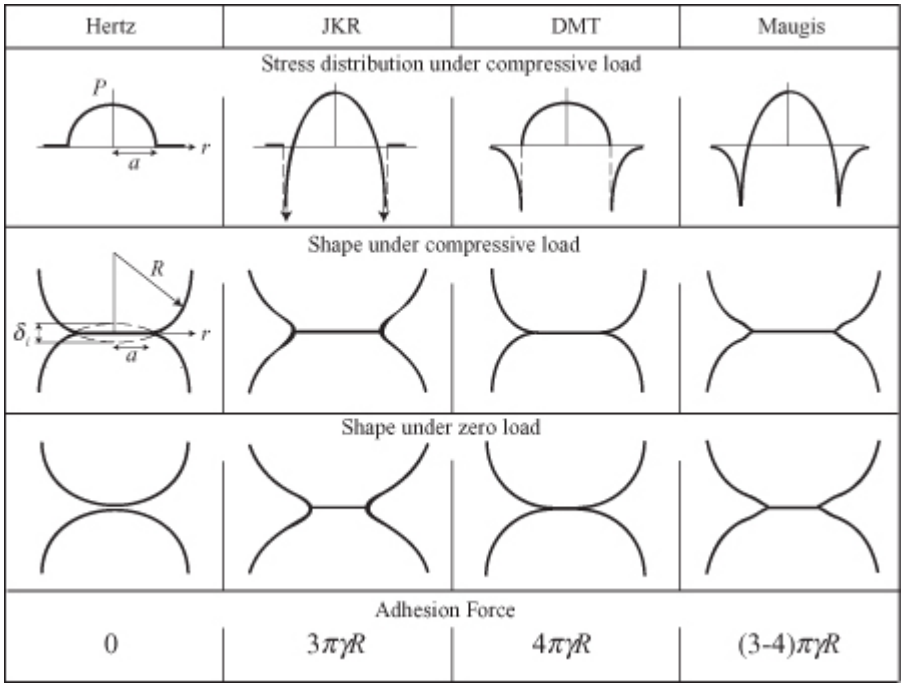

Figure 2-17 : Les principales caractéristiques des modèles de contact (Zeng, 2013)

Comme cité précédemment, la principale différence entre le modèle de contact de Hertz et les autres modèles est l'incapabilité de modèle de Hertz de modéliser l'adhésion entre les deux corps. Par contre, Johnson (1998) a classifié aussi dans la Figure 2-8 le domaine d'utilisation des différents modèles de contact selon l'élasticité des matériaux et la charge appliquée entre les deux corps en contact. Le modèle de Hertz est applicable à tous les matériaux pour un grand niveau de chargement. Les autres modèles ont été développés comme suit : le modèle de Bradly (1931) en 1931, le modèle JKR par Johnson, Kendall et Roberts (1971), le modèle DMT par Derjaguin, Muller et Toporov (1983) et le modèle de Maugis-Dougdal par Maugis (1992). Zeng (2013) (cf. Figure 2-17) a résumé les différentes caractéristiques des quatre principaux modèles de contact. Ce résumé est une modification de celui présenté par Horn et al.(1987).

2.3 Modèles de frottement

Plusieurs revues bibliographiques classifient le modèle de frottement. Par exemple : La revue proposée par Armstrong et al. (Armstrong-Hélouvry, Dupont, & De Wit, 1994) ont classé les modèles de frottement du point de vue tribologique, lubrification et physique. Berger (2002) a classé les modèles de frottement selon la modélisation dynamique pour des fins numériques et de simulation. Quant à la revue donnée par Shih et al. (2003), les modèles de frottement ont été classés selon un aspect topographique et selon les surfaces de glissement. Pour l'interaction tube-support, Hassan et al. (2005) ont classé les modèles de frottement selon le système utilisé pour détecter les régions de glissement et d'adhérence. D'après les travaux récents de Nuninger et al. (2006), les modèles de frottement ont été classifiés selon leurs propriétés et leur domaine d'application ; voir Annexe A Tableau 8-1.

L'historique de l'évolution des modèles de frottement est présenté en détail dans plusieurs références. En voici un aperçu (Aizel, 2005; Armstrong-Hélouvry et al., 1994) : Leonard de Vinci (1452-1519) fonda les premiers concepts de base du frottement des modèles classiques (le frottement est proportionnel au poids). Par la suite, le deuxième modèle de frottement a été créé par Charles Augustin Coulomb en 1785. Après, plusieurs travaux ont été faits pour améliorer le modèle statique de frottement selon l'ordre suivant (Armstrong-Hélouvry et al., 1994): Morin en (1833), le modèle de de Coulomb-Viscous, Reynolds en (1886), le modèle de Coulomb-Viscous-Static, Stribeck en (1903), le modèle de Coulomb-Viscous-Static-Stribeck, Karnopp en (1985) et finalement le modèle statique le plus complet et le plus complexe; c'est le modèle d' Armstrong en (1993). Par contre, les modèles dynamiques ont été développés à cause de l'incapacité des modèles statiques de frottement cités précédemment de présenter tout le comportement et les effets de frottement. Le premier modèle dynamique de frottement a été développé par Dahl (1976) en 1960, ensuite ce modèle a été généralisé par Bliman en (1993) dans son nouveau modèle. Haessig en (1991) a développé un autre type de modèle de frottement nommé modèle de Bristles. Le modèle le plus utilisé actuellement dans le domaine de contrôle est le modèle LuGre (Lund-Grenoble) développé en 1994 par (Canudas, Olsson, Astrom, & Lischinsky, 1995). Ce modèle présente la majorité des effets de frottement. Dupont, Armstrong et Hayward en (2000) ont proposé leur modèle élasto-plastique, qui est une extension du modèle LuGre. Ce modèle permet de modéliser la propriété de préglissement en plus des phénomènes déjà représentés dans le modèle de LuGre. En plus, ils ont introduit une fonction non linéaire dans la fonction

dynamique du modèle de LuGre qui dépend de la limite de déflexion moyenne de Bristles en régime de préglissement. Le modèle le plus récent est celui d'Azizian-Mureithi (le modèle de frottement Hybride) en (2012). Ils ont utilisé le principe du modèle de LuGre avec la prise en considération des distributions des contraintes dans la zone de contact selon le principe de Cattaneo-Mindlin (Kenneth Langstreth Johnson, 1985) dans le but de représenter la propriété de préglissement. Il existe aussi d'autres modèles de frottements utilisés dernièrement dans le domaine de contrôle, comme le modèle de Leuven développé par Leuven et al. en (2000) (qui est considéré comme une extension du modèle LuGre) et le modèle GMS (Lampaert, Al-Bender, & Swevers, 2003) paru en 2003 qui est considéré comme une généralité du modèle générique de Maxwell (Aizel, 2005).

2.3.1 Les effets du phénomène de frottement :

Le frottement est un phénomène naturel qui joue un rôle essentiel dans une grande majorité des phénomènes physiques de notre vie courante. En effet, sans frottement, plusieurs mécanismes ne peuvent pas fonctionner comme la marche, le roulement ou l'arrêt des voitures et la transmission de mouvement ou de puissance. Ceci étant, le frottement engendre des conséquences indésirables comme l'usure, le réchauffement, la perte d'énergie et la dégradation des performances des systèmes mécaniques. Pour pallier à ces états désagréables, plusieurs chercheurs essaient de modéliser le phénomène de frottement afin de trouver de nouvelles solutions de conception qui amélioreraient l'efficacité et la longévité des systèmes.

Il est possible de résumer les différents comportements du phénomène dénommé le frottement comme suit (Azizian, 2012; Berger, 2002) :

L'effet visqueux : où la force de frottement augmente avec l'augmentation de la vitesse une fois le mouvement initié.

L'effet de collage ou de séparation (stick effect or break-away forces) : La force nécessaire pour initier le mouvement, ou « break-away force»; elle est reliée au coefficient de frottement statique supérieur au coefficient de frottement dynamique.

L'effet de Stribeck : Cet effet est caractérisé par une baisse subite et continue de la force de frottement une fois le mouvement initié.

Comportement hystérétique : Variation en fonction du déplacement x (distances parcourues) avec asymétrie en dissipation d'énergie.

L'effet du petit déplacement au cours du collage : Des déplacements relatifs au niveau de la zone de contact (une région de glissement et une région de collage au même instant).

La somme des modèles de frottement dans la littérature est énorme, mais ces modèles peuvent être classés en deux catégories principales : les modèles statiques et les modèles dynamiques.

2.3.2 Modèles statiques de frottement

En général le modèle de Coulomb continu est le plus utilisé à cause de la discontinuité d'autres modèles statiques; il a été développé sur la base du modèle de Karnopp (1985) et de celui de Coulomb-Viscous-Static-Stribeck (1903). La forme du modèle d'Armstrong (1994) est semblable à celui de Coulomb continu, voir la Figure 2-18.

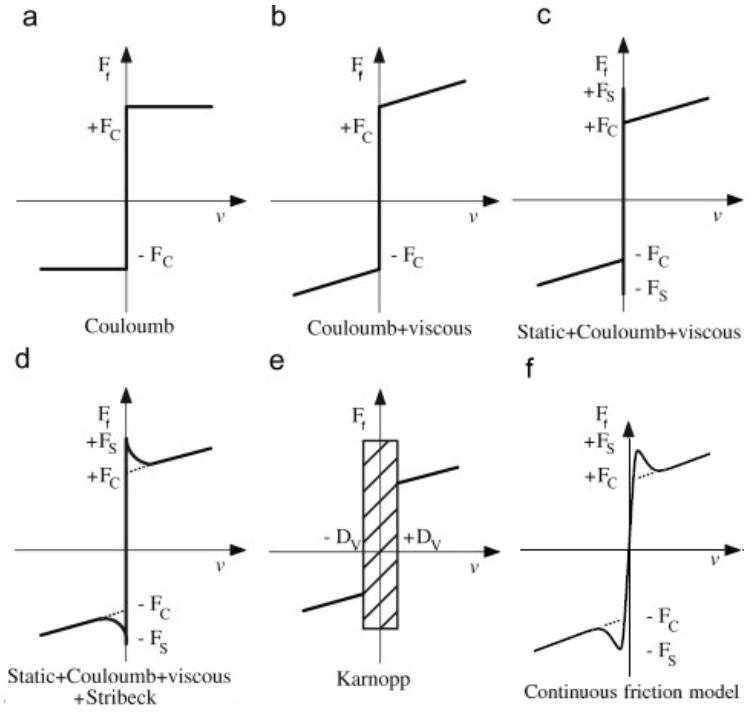

Figure 2-18 : Les modèles de frottement statique (figure modifiée (Aizel, 2005; Armstrong-Hélouvry et al., 1994; Ronnie Herman Anna Hensen, 2002; Olsson, Astrom, De Wit, Gafvert, & Lischinsky, 1998))

Tableau 2-1 : Formulations et caractéristiques des modèles statiques de frottement

Modèle de	Formulation	**Caractéristique**
Coulomb	$F_f(\dot{x}) = \begin{cases} F_{Co} & si\ \dot{x} \neq 0 \\ T & si\ \dot{x} = 0\ et\ \lvert T\rvert > F_s \\ F_s sgn(T)\ \ pour\ le\ autre\ cas \end{cases}$ Avec : $F_{Co} = \left(F_c + (F_s - F_c)e^{-\left(\frac{\dot{x}}{v_s}\right)^{\delta_s}}\right) sgn(\dot{x}) + F_v\dot{x}$ $F_c = \mu_c * N$ $F_s = \mu_s * N$ $F_v = \mu_v * N$	$\mu_s = \mu_c, \quad \mu_v = 0$ et $v_s = \infty$
Coulomb-Viscous		$\mu_s = \mu_c \quad , \quad \mu_v \neq 0$ et $v_s = \infty$
Coulomb-Viscous-Static		$\mu_s \neq \mu_c \quad , \quad \mu_v \neq 0$ et $v_s = \infty$
Coulomb-Viscous-Static-Stribeck		$\mu_s \neq \mu_c \quad , \quad \mu_v \neq 0$ et $v_s \neq \infty$ N : force normale. δ_s : exposant de Stribeck en général égale à 2.
Karnopp	$F_f(\dot{x}, T) = \begin{cases} -sgn(\dot{x})F_{Co} & \lvert\dot{x}\rvert > D_{\dot{x}} \\ -sgn(T)\max(T, F_h) & \lvert\dot{x}\rvert \leq D_{\dot{x}} \end{cases}$	F_h : force d'adhérence maximale. $D_{\dot{x}}$: petite vitesse au voisinage de zéro
Coulomb continue	$F_f(\dot{x}) = \begin{cases} F_{Co} & si \quad \lvert\dot{x}\rvert \geq V_{th} \\ \frac{\dot{x}}{V_{th}} F_s & si \quad \lvert\dot{x}\rvert < V_{th} \end{cases}$	T : force tangentielle. V_{th} : vitesse limite au début du glissement
Armstrong	$F_f(\dot{x}) = \begin{cases} F_A(\dot{x}) & en\ ca\ de\ glissement \\ \sigma_0 x & en\ cas\ de\ collage \end{cases}$ $F_A(\dot{x}) = \left(F_c + F_{sA}\frac{1}{1 + \left(\frac{\dot{x}(t-\tau_L)}{\dot{x}}\right)^2}\right) sgn(\dot{x}) + F_v\dot{x}$ $F_{sA} = F_{s,a}\left(F_{s,\infty} - F_{s,a}\right)\frac{t_d}{t_d + \gamma}$ γ : paramètre temporel de hausse de frottement statique, σ_0 : raideur de collage	avec : $F_{s,a}$: force de friction de Stribeck à la fin de période de préglissement, $F_{s,\infty}$: force de friction de Stribeck à après une longue période de repos, τ_L : constant temporel de mémoire de friction, t_d : temps de pause (temps de vitesse nulle)

où

μ_c : est le coefficient de frottement cinétique,

μ_s : est le coefficient de frottement statique,

μ_v : est le coefficient de frottement visqueux,

v_s : est la vitesse de Stribeck,

Les modèles de frottement utilisés pour modéliser l'interaction tube-support citée par Hassan et Rogers (2005) sont des cas particuliers des modèles de frottement statique mentionnés précédemment. Le modèle de frottement à vitesse limitée (VLFM)[1] est un modèle de Coulomb continu sans les effets de Stribeck et de la viscosité. Cependant, les deux autres modèles, le modèle de force équilibrée (FBFM)[2] et le modèle d'amortisseur-ressort (SDFM)[3], sont basés sur la modélisation des frottements par des ressorts et des amortisseurs. Quant au modèle (FBFM), celui-ci utilise le principe du modèle de Karnopp. Enfin, pour le modèle (SDFM), les auteurs ont utilisé un autre concept pour utiliser ces éléments. Les équations de ces modèles sont présentées dans l'Annexe A.

2.3.3 Modèles dynamiques de frottement

Les modèles dynamiques de frottement modélisent les effets macroscopiques ou microscopiques de frottement. À cause de l'incapacité des modèles statiques de frottement de présenter tous les comportements et les effets de frottement, les modèles dynamiques de frottement ont été développés pour résoudre ces problèmes.

Dans les points à suivre, nous donnerons de plus amples détails sur les principaux modèles dynamiques de frottement :

2.3.3.1 Modèle de Dahl

Le modèle de Dahl est inspiré des caractéristiques de la courbe contrainte-tension de la mécanique des solides (Figure 2-19), la courbe de force peut être modélisée par l'équation différentielle suivante (Aizel, 2005) :

$$\frac{dF}{dx} = \sigma_0 \left(1 - \frac{F}{F_c} sgn(\dot{x})\right)^{\alpha} \tag{2.28}$$

[1] En anglais : Velocity-limited friction models

[2] En anglais : Force balance friction models

[3] En anglais : Spring damper friction models

où x, F, F_c, σ_0 et ẋ représentent respectivement le déplacement, la force de frottement, la force dynamique de Coulomb, le coefficient de rigidité et la vitesse. Le paramètre « α » détermine la forme de la courbe contrainte-déformation, généralement $(\alpha = 1)$; cependant, pour des valeurs plus élevées de « α », on aura une courbe avec une courbure plus forte.

Dans le domaine temporel, le modèle peut être réécrit sous la forme suivante (Dahl, 1976):

$$\frac{dF}{dt} = \frac{dF}{dx}\frac{dx}{dt} = \frac{dF}{dx}\dot{x} = \sigma_0 \left(1 - \frac{F}{F_c} sgn(\dot{x})\right)^{\alpha} \dot{x} \tag{2.29}$$

Si on prends$(\alpha = 1)$, le modèle peut s'écrire sous la forme (Dahl, 1976):

$$\frac{dF}{dt} = \sigma_0 \dot{x} - \frac{F}{F_c}\sigma_0 |\dot{x}| \tag{2.30}$$

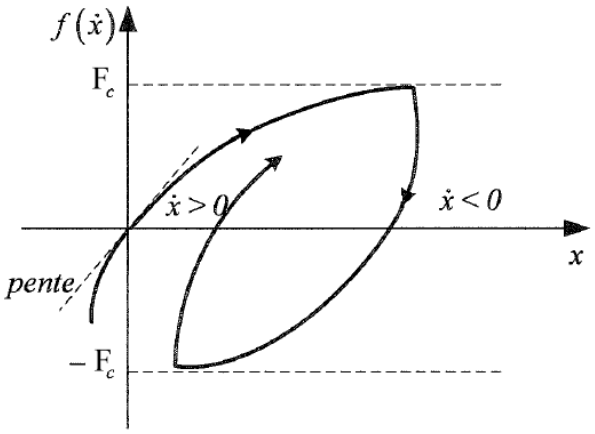

Figure 2-19 : Le modèle de Dahl (figure modifiée (Aizel, 2005; Olsson et al., 1998))

2.3.3.2 Modèle de Bristles

Haessig et al. (1991) prennent en considération les aspérités irrégulières (état de surface) du contact au niveau microscopique comme un ensemble de brins (Bristles) flexibles élastiquement d'une raideur σ_0, avec n brins localisés aléatoirement en b_i. La force appliquée entraîne une tension des brins qui génère une force de frottement sans amortissement « σ_1 ». Pour une valeur suffisante de la force appliquée, la distance relative ($z=x_i-b_i$) atteint une valeur limite z_0 et il y a une brusque rupture du contact avec détente et mise en glissement, voir la Figure 2-20.

$$F = \sum_{i=1}^{n} \sigma_0 (x_i - b_i) \tag{2.31}$$

2.3.3.3 Modèle de LuGre

Le modèle de LuGre est un modèle qui représente un grand nombre de phénomènes de frottement. Il est basé sur le modèle de Dahl d'une part et sur le modèle de Bristles d'autre part. Le modèle de LuGre introduit une variable interne qui représente la déflexion moyenne des brins (Bristles), voir la Figure 2-20. Il modélise plusieurs phénomènes de frottement comme le déplacement de préglissement, la variation de la force de décrochage, l'effet de Stribeck et celui de l'adhérence (Aizel, 2005; Canudas et al., 1995).

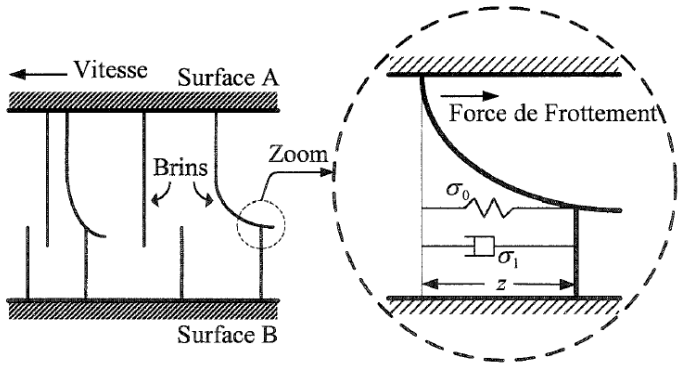

Figure 2-20 : Vue microscopique entre deux surfaces en contact (modélisation de Bristles) (Aizel, 2005)

La force de frottement selon le modèle de LuGre est donnée par (Canudas et al., 1995) :

$$F = \sigma_0 z + \sigma_1 \frac{dz}{dt} + \sigma_2 \dot{x} \tag{2.32}$$

où σ_0, σ_1, σ_2, ẋ et z représentent respectivement : le coefficient de raideur de brins, le coefficient d'amortissement de brins, le coefficient de frottement visqueux « $\sigma_2 = \mu_v$ », la vitesse relative entre les deux surfaces et la déformation moyenne de brins. La vitesse de la déformation « z » moyenne peut être calculée avec la formule suivante (Canudas et al., 1995) :

$$\frac{dz}{dt} = \dot{x} - \frac{|\dot{x}|}{g(\dot{x})} z \tag{2.33}$$

L'équation ci-dessus est équivalente à l'équation (2.30) du modèle de Dahl si on remplace $F\sigma_0$ par z.

La fonction $g(\dot{x})$ est la fonction de Stribeck, c'est une fonction positive qui varie en fonction des propriétés du matériau, de la lubrification et de la température. Elle est donnée comme suit (Canudas et al., 1995) :

$$\sigma_0 g(\dot{x}) = N\left(\mu_C + (\mu_s - \mu_C)e^{-(\dot{x}/v_s)^2}\right) \tag{2.34}$$

2.3.3.4 Modèle élasto-plastique d'Armstrong et al. (EP-DAH model) :

Le modèle élasto-plastique, proposé par Dupont, Armstrong et Hayward (2000), est une extension du modèle LuGre. Il permet de modéliser la propriété de préglissement en plus des phénomènes déjà représentés dans le modèle de LuGre. Armstrong et al. ont introduit une fonction $\alpha(z,\dot{x})$ dans la fonction dynamique du modèle de LuGre (équation (2.33)). Cette fonction dépend d'une nouvelle variable z_{ba} (la limite de déflexion moyenne de Bristles en régime de préglissement), donc l'équation (2.33) peut être réécrite sous la forme suivante :

$$\frac{dz}{dt} = \dot{x} - \alpha(z,\dot{x})\frac{|\dot{x}|}{g(\dot{x})}z \tag{2.35}$$

avec :

$$\alpha(z,\dot{x}) = \begin{cases} 0 & \text{si } \operatorname{sgn}(\dot{x}) \neq \operatorname{sgn}(z) \\ \begin{cases} 0 & si\,|z| \le z_{ba} \\ \dfrac{1}{2}\sin\left(\pi\dfrac{z - \frac{z_{\max}+z_{ba}}{2}}{z_{\max}+z_{ba}}\right) & si\ z_{ba} \le |z| < z_{\max} = \dfrac{F_s}{\sigma_0} \\ 1 & si\,|z| \ge z_{\max} = \dfrac{F_s}{\sigma_0} \end{cases} & \text{si } \operatorname{sgn}(\dot{x}) = \operatorname{sgn}(z) \end{cases} \tag{2.36}$$

ou :

z_{ba} : La limite de déplacement de préglissement ou la limite du décrochage (breakaway displacement), elle correspond aussi à la limite de déflexion élastique de brins (Bristles).

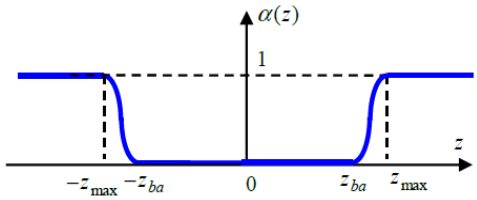

Figure 2-21 : Représentation de la fonction $\alpha(z,\dot{x})$ (Dupont et al., 2000)

La figure ci-dessus présente l'évaluation de la fonction $\alpha(z,\dot{x})$ en fonction du déplacement moyen de Bristles z. $z_{\max}$ est la limite de déflexion plastique de brins (Bristles).

2.3.3.5 Modèle d'Azizian-Mureithi (hybrid spring-damper friction model)

Le modèle le plus récent est le modèle d'Azizian-Mureithi (2012) qui utilise le principe du modèle de LuGre. Toutes les propriétés et les avantages des modèles cités précédemment sont inclus dans celui-ci, à savoir : la dynamique du modèle de Dahl (donc l'effet hystérétique), la dynamique de brins (Bristles) du modèle de Bristles et l'effet de Stribeck du modèle d'Armstrong d'une manière plus robuste. Azizian et Mureithi (2012) ont pris en considération la distribution des contraintes dans la zone de contact selon le principe de Cattaneo-Mindlin (Kenneth Langstreth Johnson, 1985), où il serait possible de présenter tout le comportement de frottement dans les différentes zones de contact.

Ce modèle est basé sur le théorème de la distribution de la contrainte tangentielle au niveau de la zone de contact de Cattaneo-Mindlin présenté dans le chapitre précédent. La zone de contact peut être divisée en trois régions principales : élastique au centre, glissement au bord et plastique entre les deux. La zone plastique a été introduite par le théorème de Ödfalk-Vingsbo (1992). De plus, il y a une zone de transition entre chaque couple de régions : la région de transition de l'élasticité vers la plasticité et la région de transition de la plasticité vers le glissement. Azizian et Mureithi (2012) se sont inspirés du théorème de Ödfalk-Vingsbo (1992) en interprétant chaque zone par un ressort et chaque région de transition par un amortissement (Figure 2-22).

La formulation du modèle d'Azizian-Mureithi est présentée dans les équations suivantes :

$$F_f = k_e z_e + c_p \dot{z}_p + c_s \dot{z}_s \tag{2.37}$$

$$z = z_e + z_p + z_s \tag{2.38}$$

où z_e , z_p et z_s sont des déplacements relatifs respectivement : élastique, plastique et glissement partiel, k_e , c_p, c_s sont respectivement les coefficients de la rigidité élastique, de l'amortissement plastique et de l'amortissement de préglissement.

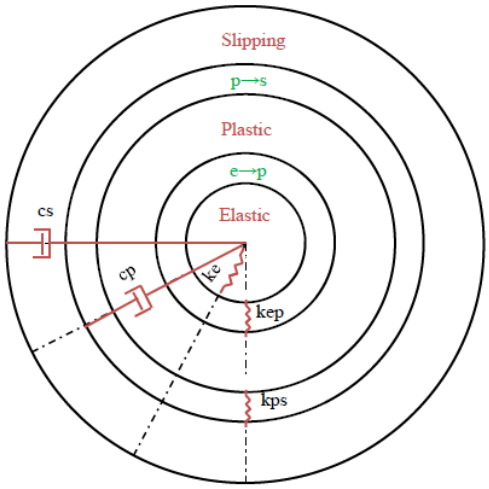

Figure 2-22 : Régions de déplacement dans la zone de contact et le modèle hybride de ressort-amortisseur d'Azizian-Mureithi (2012)

Pour simplifier l'utilisation et la compréhension de leur modèle, Azizian et Mureithi (2012) ont utilisé une combinaison des ressorts et d'amortisseurs. La Figure 2-23 représente une comparaison entre cette simplification et la simplification du modèle de LuGre. On peut remarquer trois différences entre les deux modèles : la première différence est la rigidité moyenne de brins σ_0 dans le modèle de LuGre (C. Canudas, Olsson, Astrom, & Lischinsky, 1995) considérée constante. Par contre, dans le modèle d'Azizian-Mureithi (2012), la rigidité est considérée variable et est fonction du déplacement élastique de glissement z_e et de deux autres rigidités (la rigidité élastique k_e et la rigidité de transition élastique-plastique $k_{ep.}$). La deuxième différence est l'effet de la viscosité, elle est fonction de la vitesse absolue $\dot{x}$ entre le deux corps dans le modèle de LuGre (C. Canudas et al., 1995) et fonction de la vitesse relative de préglissement $\dot{z}_s$ dans le modèle d'Azizian-Mureithi (2012). La troisième différence est l'introduction de la rigidité relative entre la zone plastique et la zone de préglissement k_{ps}.

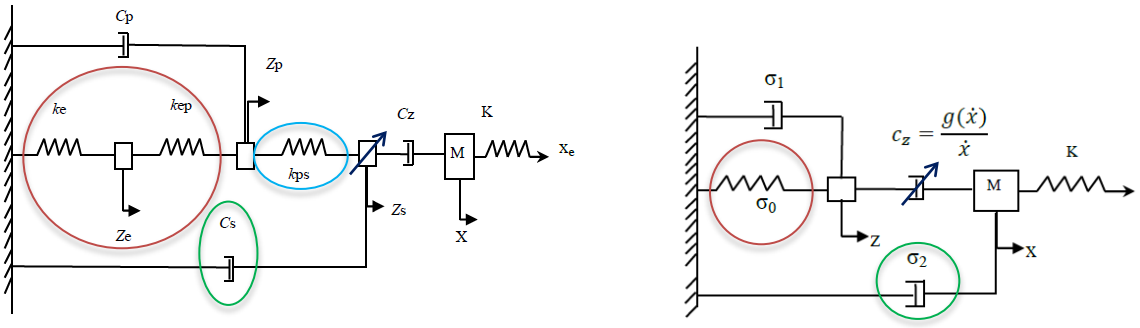

a) Le modèle d'Azizian-Mureithi b) Modèle de LuGre

Figure 2-23 : Comparaison entre le modèle de frottement d'Azizian-Mureithi et le modèle de LuGre (Azizian, 2012)

$$\underbrace{k_e z_e}_{\text{élastique}} + \underbrace{k_{ep}(z_e - z_p)}_{\text{transition } e \to p} = 0 \tag{2.39}$$

$$\underbrace{k_{ep}(z_p - z_e)}_{\text{transition p}\to e} + \underbrace{k_{ps}(z_p - z_s)}_{\text{transition p}\to s} + \underbrace{c_p \dot{z}_p}_{\substack{\text{dissipation} \\ \text{plastique}}} = 0 \tag{2.40}$$

$$\underbrace{k_{ps}(z_p - z_s)}_{\text{transitiont s}\to p} + \underbrace{c_z(\dot{z}_s - \dot{x})}_{\substack{\text{transitiont} \\ \text{préglissement}\to\text{glissement}}} + \underbrace{c_s \dot{z}_s}_{\substack{\text{dissipation} \\ \text{de préglissement}}} = 0 \tag{2.41}$$

où c_z est l'amortissement de Stribeck qui peut être calculé par :

$$c_z = \frac{\sigma_0 g(\dot{x})}{\dot{x}} \tag{2.42}$$

où $g(\dot{x})$ est la même fonction de Stribeck utilisée dans le modèle de LuGre équation (2.34).

Ce modèle, qui a été présenté schématiquement dans la Figure 2-23 (a), considère quatre effets importants : le premier est la prise en considération de la rigidité moyenne des brins, du déplacement inspiré par la théorie de Cattaneo-Mindlin (équation (2.22)) par l'introduction du paramètre k_e. Le second est la prise en considération du déplacement plastique inspiré par le théorème d'Odfalk-Vignsbo (1992) qui est basé sur la relation d'intégration force-déplacement (équation (2.24)) et l'introduction de l'amortissement et de la rigidité de la zone plastique équivalente par les paramètres c_p et k_{ep} respectivement. Le troisième effet considéré est le déplacement de préglissement inspiré par la théorie de Mindlin-Deresiewicz (1953) (équation

(2.23)) et par l'introduction des paramètres c_s et k_{ps}. Finalement, le phénomène de Stribeck apparaît dans la majorité des modèles dynamiques de frottement (équation (2.34)).

Un premier test de performance de ce modèle a été fait. Les auteurs ont comparé à l'expérience réalisée par Baumberger et al. (1994) et le modèle de Ozaki-Hashiguchi (2010). Cette expérience consiste à tirer un ressort attaché à une masse (m) qui glisse sur un support avec une vitesse constate v_p comme le montre la Figure 2-24. Le modèle d'Azizian-Mureithi (2012) présente le plus fidèlement le résultat de test, et il donne le même nombre d'états de collage, contrairement au modèle d'Ozaki-Hashiguchi (2010).

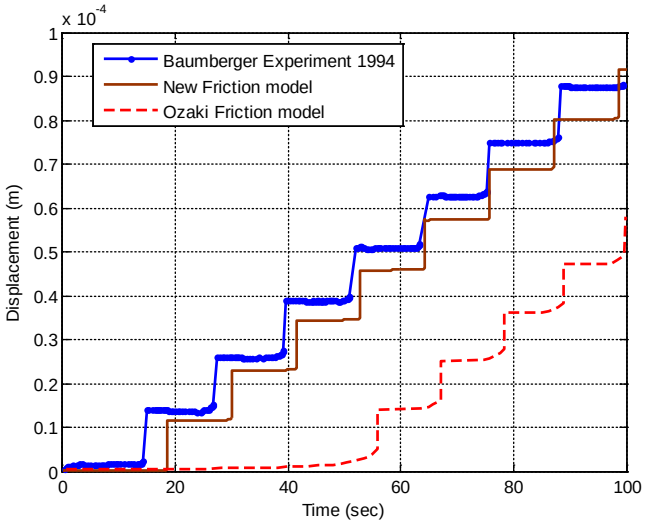

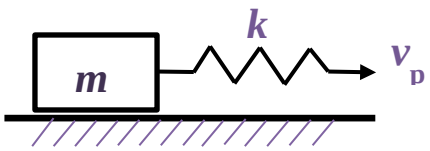

Système masse-ressort

Tableau de valeurs des paramètres

M (kg)	K (Nm^{-1})	Vp (μms^{-1})
0.8	58000	1

Figure 2-24 : Comparaison entre le modèle de frottement d'Azizian-Mureithi, le modèle d'Ozaki-Hashiguchi (2010) et l'expérience réalisée par Baumberger et al. (Azizian, 2012)

2.4 Identification des paramètres des modèles

Il est très important d'identifier les paramètres du modèle de frottement pour qu'ils puissent être utilisés efficacement pour la simulation de systèmes mécaniques. Dans la littérature, les méthodes d'identification des paramètres du frottement ont évolué en harmonie avec ceux de la modélisation. En effet, plusieurs chercheurs tentent de résumer les méthodes utilisées pour identifier les paramètres du frottement, comme la revue réalisée par Grami (2009), en citant la majorité des méthodes développées. Il a classé les différentes méthodes selon la même classification que celles pour les modèles de frottement : méthodes d'identification des modèles statiques et les méthodes d'identification des modèles dynamiques. De plus, il cite aussi

l'existence d'autres types de classifications utilisés dans le domaine de contrôle: les méthodes d'identification en ligne et les méthodes d'identifications hors ligne.

Les méthodes d'identification en ligne (Commande adaptative) : aussi appelées les méthodes d'identifications adaptatives, où l'estimateur de paramètres des modèles de frottement est intégré dans la commande de contrôle en temps réel; ces types de méthodes ne sont pas applicables dans notre cas.

Les méthodes d'identifications hors ligne : selon Grami (2009), ces types de méthodes sont plus robustes et parfois très efficaces, mais elles demandent de réaliser une série d'expériences et l'estimation des paramètres se fait hors ligne par une combinaison de plusieurs techniques. Les différents résultats accumulés seront intégrés dans la commande. Cependant, les paramètres du modèle de frottement peuvent varier selon les conditions de travail (précharge, état de surface, géométrie et les propriétés mécaniques des organes du système (élasticité, dureté … etc.)), les variations de l'environnement (température, pression, humidité, lubrification) ainsi que selon l'état de service (usure).

Par contre, Borsotto (2008) a proposé d'autres approches, où il cite pour chaque paramètre les méthodes d'identification qui peuvent être utilisées. On peut résumer le principe de cette approche par les points suivants :

- **Les essais :** il a cité quatre types de tests avec différents niveaux d'excitation : test à vitesse constante (statique), test avec excitation sinusoïdale (dynamique), test en rampe et test à une consigne de position impulsionnelle.
- **La mesure :** On mesure le frottement en fonction de la vitesse $F_f(v)$, le frottement en fonction du déplacement $F_f(x)$ et par la mesure de la fonction de transfert $\frac{X(wj)}{F_e(Wj)}$.
- **Les méthodes d'identification :** On peut utiliser la mesure directe (pour certains paramètres avec des tests spécifiques) ou la résolution d'un problème d'optimisation avec la méthode de régression (linéaire ou non linéaire).

2.4.1 Identification des paramètres du modèle de LuGre

Canudas et al. (1997) ont proposé une méthode d'identification des paramètres du modèle de LuGre basée sur plusieurs étapes. La première étape comporte deux méthodes hors ligne, la première méthode consiste à faire une série d'expériences avec une vitesse constante afin de tracer la courbe de frottement en fonction de la vitesse pour identifier les paramètres statiques à l'aide de l'algorithme d'optimisation Simplex (fminu (Matlab® optimization toolbox)). La deuxième méthode est utilisée pour identifier les paramètres dynamiques en se basant sur la connaissance des paramètres statiques. Cette méthode est basée sur un algorithme d'optimisation non linéaire nommé programme d'intégration numérique (numerical intégration routine). Finalement, la deuxième étape consiste à proposer un observateur adaptatif pour estimer la variable interne du modèle de frottement. Par contre, Couillard (2008) a proposé une méthode d'identification des paramètres du modèle de LuGre complètement hors ligne établie sur deux étapes. La première consiste à identifier les paramètres dynamiques par la mesure de la fonction de transfert FRF (domaine fréquentiel). La deuxième étape consiste à identifier les paramètres statiques avec la même approche proposée par Canudas et al. (1997). Dans la suite, on va démontrer les détails de cette méthode pour un système à 1DDL

2.4.2 Identification des paramètres dynamiques

La difficulté entourant l'identification des paramètres dynamiques vient du fait que la déformation de brins (z) n'est pas directement mesurable. De cette façon, on peut considérer que l'interface de frottement (la dynamique de brins) se comporte essentiellement comme une simple raideur avec un amortissement visqueux. L'équation du mouvement du système en régime de préglissement peut s'écrire à partir de l'équation du mouvement du système à 1 DDL (Éq. (2.43)) et des équations du modèle de LuGre (voir Éqs. (2.47) a (2.50)), et en considérant z = x, comme montre l'équation (2.44):

$$m\ddot{x} + c\dot{x} + kx + F_f = F_{ex} \tag{2.43}$$

$$F_{ex} = m\ddot{x} + \big(c + N(\sigma_1 + \sigma_2)\big)\dot{x} + (k + N\sigma_0)x \tag{2.44}$$

où F_f et F_{ex} sont respectivement : la force de frottement et la force d'excitation. Avec l'absence de capteur de force normale (N) dans son cas, il a utilisé la normalisation suivante $\widehat{\sigma_i} = N\sigma_i$ avec i=0,1, et 2. Donc la fonction de transfert du système est écrite comme suit :

$$\frac{X(j\omega)}{F_{ex}(j\omega)} = \frac{1}{-m\omega^2+(c+\hat{\sigma}_1+\hat{\sigma}_2)j\omega+(k+\hat{\sigma}_0)} \quad (2.45)$$

Selon la littérature, le coefficient visqueux est négligeable devant l'amortissement des brins $\hat{\sigma}_2 \ll \hat{\sigma}_1$. On obtient aussi :

$$\frac{X(j\omega)}{F_{ex}(j\omega)} = \frac{1}{-m\omega^2+(c+\hat{\sigma}_1)j\omega+(k+\hat{\sigma}_0)} \quad (2.46)$$

À partir des données expérimentales (test FRF du système) et l'outil d'identification de Matlab® (System Identification Toolbox), les paramètres dynamiques du modèle de LuGre peuvent être déterminés.

Il existe d'autres méthodes d'identification des paramètres dynamiques, qui ont été proposées par Hensen et al (2002). Ils ont utilisé une méthode d'identification dans le domaine fréquentiel, l'interface de frottement (la dynamique de brins) est considérée comme étant en régime de préglissement. Ils ont utilisé un modèle de LuGre à ordre réduit (linéarisation) (Éq. (2.47)) pour déterminer le paramètre σ_0 avec les conditions suivantes : force d'excitation très faible (F_{ex} < RMS (F_s)) et déplacement de préglissement très petit. Quand la limite du gain de FRF s'approche de zéro, $H(j\omega)$ est égale à C_m/σ_0, donc σ_0 peut être calculé facilement (voir la Figure 8-2 Annexe A). Par contre, pour les ordres les plus élevés, ils ont utilisé une procédure itérative à étapes de combinaison convexe semblable au SK-Iteration (une méthode d'identification des paramètres modale utilisée dans le domaine de contrôle).

$$\frac{A(j\omega)}{U(j\omega)} = H(j\omega) = \frac{C_m}{-\omega^2+(\sigma_1+\sigma_2)j\omega+\sigma_0} \quad (2.47)$$

où :

C_m : constant de moteur

u : tension d'alimentation de moteur

J : moment d'inertie de l'ensemble le rotor formé par de moteur et le bras rotatif.

2.4.3 Identification des paramètres statiques

Typiquement, les paramètres statiques du modèle de frottement de LuGre sont obtenus en effectuant une série de mesures de la force de frottement à vitesse constante (Canudas & Lischinsky, 1997). Ceci s'explique par le fait que pour une vitesse constante, et donc une variation de la déflexion des brins nulle, on obtient une valeur de déflexion des brins constants, tel que :

$$\frac{dz}{dt} = 0 \Rightarrow z = \frac{\dot{x}g(\dot{x})}{|\dot{x}|} = g(\dot{x})sgn(\dot{x}) \tag{2.48}$$

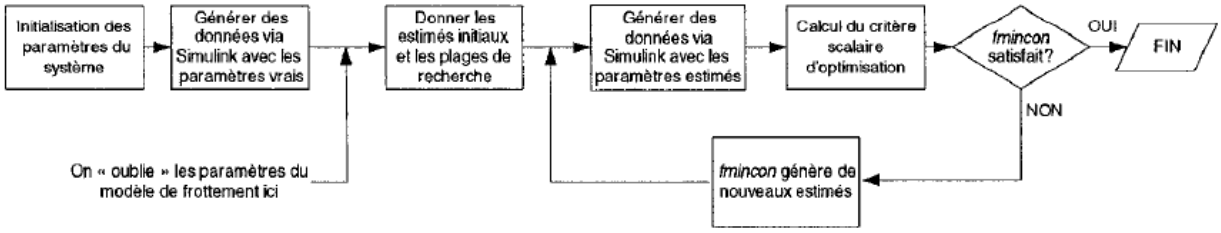

Figure 2-25 : Algorithme d'identification des paramètres statiques du modèle de LuGre (Couillard, 2008)

La force de frottement selon le modèle de LuGre se réduit à :

$$F_f = N\left[\left(\mu_C + (\mu_s - \mu_C)e^{-(\dot{x}/v_s)^2}\right)\text{sgn}(\dot{x}) + \sigma_2\dot{x}\right] \tag{2.49}$$

À partir des mesures des forces de frottement pour différentes valeurs de vitesse, les paramètres statiques des modèles vont être déterminés avec l'algorithme d'optimisation tel que la fonction lsqcurvefit (régression par les moindres carrés) de Matlab®. Cette méthode a été présentée par Canudas (1997). Cependant, elle est applicable seulement aux systèmes qui peuvent être soumis à des tests à vitesse constante. Par contre, pour le cas où la réalisation de ce type de test est impossible, Couillard (2008) a proposé une autre méthode, en utilisant une fonction d'optimisation non-linéaire de Matlab® nommée fmincon utilisée avec une réponse temporelle du système.

2.4.4 Identification des paramètres par l'approche de Borsotto :

On peut résumer l'approche de Borsotto (2008) dans le tableau suivant :

Tableau 2-2 : Méthodes d'identification des paramètres par l'approche de Borsotto

Paramètre	**Test**	**Mesure**	**Méthode d'identification**	**Équation**
F_s	Rampe croissante	$\begin{cases} F_f(t) \\ x(t) \end{cases}$	Directe	$F_s = F_f(t)$ où début de déplacement
	Sinusoïdale	$F_f(t)$	Régression non-linéaire	Tous les paramètres identifiés en même temps
F_c	Sinusoïdale	$F_f(t)$	Régression non-linéaire	
v_s	Sinusoïdale	$F_f(t)$	Régression non-linéaire ou linéaire	
σ_0	Sinusoïdale et réduction de la complexité de modèle	$F_f(x)$	Directe en fixe $sig(\dot{x})$	$F_c = F_f(t)$ *finale* (*ou* max) $\sigma_0\left(1-\frac{F_f(t)}{F_c}\right)=\frac{dF_f(t)}{dx}$
		$F_f(x)$	Directe, Pour de faible déplacement.	$F_f(t) \cong \sigma_0 x$
σ_v	Choisi suffisamment petit			En pratique $\sigma_v=10^{-3}$ m/s
σ_1	Mesure de la fonction de transfert	Il a utilisé la même méthode d'identification que celle des paramètres dynamiques présentée précédemment		

En ce qui concerne le paramètre z_{ba} du modèle élasto-plastique d'Armstrong, celui-ci doit être choisir arbitrairement en fonction de la déflexion maximale z_{max}.

$$z_{ba} = a \cdot z_{\max} \quad a < 1$$
$$z_{\max} = \frac{F_c}{\sigma_0} \tag{2.50}$$

2.4.5 Identification des paramètres du modèle d'Azizian-Mureithi

Le modèle de frottement d'Azizian-Mureithi (2012) a été développé que très récemment. Une seule méthode a été proposée par Azizian et Mureithi (2012) pour identifier leurs paramètres. Un

des objectifs de cette thèse sera de développer une nouvelle méthode pour identifier les paramètres du ce modèle.

Azizian et Mureithi (2012) ont identifié les paramètres de leur modèle par une méthode d'optimisation des moindres carrés non linéaire. Ils ont divisé les paramètres en deux catégories. La première catégorie (k_e, F_s, F_c et v_s) représente le comportement général de stick-slip, la deuxième concerne principalement le comportement de préglissement.

L'optimisation a été réalisée en deux étapes. La première étape consiste à définir le comportement général du frottement par l'optimisation des paramètres k_e, F_s, F_c et v_s. Dans cette étape, la fonction objective est la différence entre la quadratique du déplacement expérimental et la simulation numérique de l'ensemble du mouvement de stick-slip. La deuxième étape d'optimisation comprend l'identification des paramètres qui sont plus sensibles au déplacement de préglissement K_{ep} k_{ps}, C_S et C_P. Dans cette étape, la fonction objective est la différence quadratique entre le déplacement expérimental et la simulation numérique du mouvement de préglissement. Dans le tableau ci-dessous, l'ensemble des paramètres optimisés sont présentés. (Voir Figure 2-22)

Tableau 2-3 : Les paramètres du modèle d'Azizian-Mureithi trouvés pour le test de Baumberger

Paramètres	Paramètres du comportement général				Paramètres du préglissement			
	k_e *(N/m)*	F_s *(N)*	F_c *(N)*	v_s *(m/s)*	k_{ep} *(N/m)*	k_{ps} *(N/m)*	C_s *(N.s/m)*	C_p *(N.s/m)*
Valeurs	5.2e+7	1.07	0.707	1e-6	1.9e+7	8.5e+7	2.3e+3	6.3e+2

Azizian et Mureithi (2012) ont trouvé que la première étape de l'optimisation est la plus coûteuse puisque la fonction objective est très sensible aux paramètres. La deuxième étape, quant à elle, a permis de capturer le déplacement de préglissement. Cela a été rendu possible en utilisant le pas de temps le plus petit possible. Le pas de temps choisi est de 1e-6 seconde (Azizian, 2012).

CHAPITRE 3 PRÉSENTATION DE LA THÈSE

3.1 Introduction

Dans le chapitre précédent, on a revu la littérature sur la modélisation de l'interaction des tubes de générateur de vapeur avec leurs supports. On a aussi revu les différents éléments reliés à ces problèmes tels que les modèles de frottement et de contact, etc. De cet état de l'art, seront dégagés la problématique et les objectifs de recherche :

3.2 La problématique

La prédiction de la durée de vie d'un tube du générateur de vapeur est présentement estimée avec 50% de précision. L'objectif final de cette recherche est donc d'améliorer cette prédiction à travers une meilleure modélisation du contact entre les tubes du générateur de vapeur et de ses différents types de supports. Les modèles de frottement et d'impact devront être validés et ses paramètres devront être déterminés expérimentalement. Enfin, on sera capable de simuler numériquement avec une meilleure précision la durée de vie du tube de générateur de vapeur.

Dans cette recherche, nous allons essayer de modéliser et de simuler l'interaction tube- support de manière théorique et expérimentale. Le but de ce travail est donc, dans un premier temps, le développement d'un nouveau modèle d'impact et de frottement de l'interaction entre le tube et ses supports et, dans un second temps, la détermination de la puissance d'usure pour être en mesure de donner une meilleure estimation de l'usure par frottement du tube.

La puissance d'usure est un paramètre utile pour prédire la durée de vie des composantes usées par frottement. L'équation (2.1) montre que le calcul de la puissance d'usure est une fonction de la force normale de la zone de contact et de la distance de glissement dans un délai donné. Ces deux paramètres sont obtenus à partir du modèle de frottement et d'impact. Pour cette raison, on a besoin de modèles de frottement et d'impact plus réalistes pour afin d'être capable de calculer la durée de vie d'un tube de générateur de vapeur de façon plus précise (Azizian, 2012). Dans ce but, le modèle de frottement Hybride a été récemment développé par Azizian-Mureithi (2012). Par contre, leurs paramètres n'ont pas encore été identifiés.

$$\dot{W} = \frac{\int_0^t N(t).\dot{u}(t)dt}{\int_0^t dt} \qquad (3.1)$$

Où :

$\dot{W}$: La puissance d'usure

$N(t)$: Force normale

$u(t)$: Vitesse de glissement

t : Durée de contact.

3.3 Objectifs de la recherche :

Avant d'arriver au but final de ce projet, plusieurs objectifs devront être atteints à l'aide du développement d'une méthodologie permettant de modéliser et de simuler les conditions aux limites réelles. Comme mentionné précédemment, vu l'état actuel des choses, pour arriver au but final de ce projet, plusieurs objectifs doivent être atteints par le développement d'une méthodologie permettant de modéliser et de simuler les conditions aux limites réelles. Aussi, nous devons :

1- Réaliser un banc d'essai fonctionnel;
2- Développer une méthode pour obtenir de meilleurs résultats expérimentaux, nécessaires dans l'identification des paramètres des modèles de contact;
3- Développer une méthodologie d'identification des paramètres des modèles de frottement Hybride (Azizian, 2012);
4- Valider et améliorer les modèles de contact (modèles de frottement et modèles d'impact).

En fin de compte, nous serons en mesure de simuler le problème de contact et de déterminer la puissance d'usure par frottement avec précision.

3.4 Méthodologie

Les objectifs de recherche énumérés précédemment seront poursuivis en utilisant les méthodes suivantes :

Pour arriver à ces objectifs, une méthodologie pour modéliser et simuler les conditions aux limites réelles doit être élaborée. Les modèles de contact (frottement et impact) entre les tubes du générateur de vapeur et les différents types de supports développés par Azizian (2012) vont être validés et améliorés. Leurs paramètres seront déterminés expérimentalement. Pour cela, il est nécessaire de réaliser un banc d'essai fonctionnel. Enfin, la base des données de paramètres sera utilisée pour simuler, précisément, le contact et, ainsi, calculer la puissance d'usure par frottement avec précision.

Les points principaux de cette méthodologie peuvent être définis comme suit :

1- **Les bancs d'essai :** Les bancs d'essai vont être construits pour tester et analyser toutes les conditions (le niveau d'excitation, la précharge, la géométrie, l'environnement et les matériaux de zone de contact). Par l'inspiration du banc d'essai réalisé par Jalali et al. (2011) pour construire le nôtre. Dans notre design, on doit prendre en considération les contraintes suivantes : 1- la possibilité de changement du niveau d'excitation et la précharge dans la zone de contact, avec et sans lubrification et avec moins d'interaction avec les différents supports (par exemple le support de pot vibrant) ;

2- **Méthode expérimentale** : Développement d'une méthode basée sur l'analyse modale non-linéaire pour déterminer tous les éléments de la dynamique non-linéaire comme les NNMs, les fréquences naturelles et les forces de contact : (tangentielles (frottement) et normales (impact)), et le développement d'une nouvelle méthode pour identifier les paramètres des modèles de contact. La méthode expérimentale proposée est basée sur les hypothèses suivantes :

3- **Identification des paramètres des modèles de frottement Hybride (Azizian, 2012) :** une méthodologie d'identification doit être développée, ou elle va être réalisée en plusieurs étapes, en se basant sur l'intensification des différents paramètres pour certains modèles de base du modèle de frottement Hybride (Azizian, 2012), comme le modèle de Coulomb et le celui de LuGre. Les paramètres peuvent être identifiés directement par l'utilisation des résultats expérimentaux ou par l'inspiration de toutes les méthodes citées précédemment pour développer une nouvelle méthodologie.

4- **Validation et amélioration des modèles :** Le modèle développé par Azizian (2012) doit être validé expérimentalement et numériquement après la caractérisation et l'analyse de ses

paramètres. Donc, ce modèle peut être amélioré selon la sensibilité des paramètres et des différentes conditions de contact.

3.5 Présentation de la thèse :

Le contenu du travail réalisé durant le doctorat est présenté dans les prochains chapitres sous forme d'articles. Le banc d'essai a été conçu, fabriqué, testé et amélioré pour réduire l'interaction avec le système d'excitation (pot vibrant) en premier. L'idée et quelques détails sur le banc d'essai ont été présentés dans le Chapitre 4. Ensuite, des résultats expérimentaux ont été obtenus avec ce banc d'essai et ont été utilisés pour obtenir tous les résultats présentés dans les cinq articles exposés dans cette thèse. L'ordre chronologique et le contenu des articles sont présentés comme suit :

Dans le premier article réalisé (Article 3), tel que présenté dans l'Annexe B, nous retrouvons la première formulation (forme harmonique) de la nouvelle méthode de balance harmonique inversée (BHI) avec la première méthode de lissage (par série trigonométrique) et l`approche d'orthogonalité harmonique. Dans cet article, deux paramètres d'un modèle de frottement Hybride ont été identifiés en utilisant le modèle de frottement de Dahl.

La première amélioration de la méthode BHI est présentée dans le deuxième article réalisé (Article 4 présenté dans l'Annexe C), par l'introduction de la deuxième formulation (forme sous-harmonique) et la deuxième méthode de lissage (par Spline naturelle). Dans cet article, cinq paramètres d'un modèle de frottement Hybride ont été identifiés en utilisant le modèle de frottement de LuGre.

Ensuite, les paramètres du modèle de frottement Hybride identifiés dans le premier et le deuxième article, Article 3 (Annexe B) et Article 4 (Annexe C), ont été validés par les modèles de frottement de Coulomb et de Stribeck en utilisant la méthode des éléments finis. Un modèle 1D (élément poutre) a été utilisé pour modéliser notre poutre et les éléments de contact sous le logiciel Abaqus. Ce travail est présenté dans le troisième article réalisé (Article 5) présenté dans l'Annexe D.

La deuxième amélioration de la méthode BHI est présentée dans le quatrième article réalisé (Article 1 présenté dans Chapitre 5). Celle-ci concerne l'utilisation de l'approche de non-orthogonalité harmonique pour calculer la force de frottement. Dans cet article, on présente aussi

l’approche utilisée (approche à étapes multiples) pour identifier les cinq paramètres des modèles de frottement Hybride, lesquels ont été identifiés en utilisant les modèles de frottement de Coulomb, de Stribeck, de Dahl et de LuGre.

Finalement, les paramètres des modèles de frottement Hybride identifiés dans le quatrième article réalisé (Article 1 présenté dans Chapitre 5) ont été validés par les modèles de Coulomb et de Stribeck (résultat préliminaire) en utilisant la méthode des éléments finis. Un modèle 2D (élément Shell avec déformation plane) a été développé sous le logiciel Abaqus. Ce travail est présenté dans le cinquième article réalisé (Article 2) présenté dans Chapitre 6.

De plus, quelques résultats et discussions complémentaires du Chapitre 5 (article 1) sont présentés dans le Chapitre 7 avec la discussion générale. Les conclusions et des recommandations pour un travail futur seront présentées au Chapitre 8. Quelques graphiques et des informations complémentaires de revues de littérature (reliés au Chapitre 2) sont présentés dans l’Annexe A.

Une traduction anglaise de la présentation de la thèse présentée dans le Chapitre 3, de la discussion générale (Chapitre 7) et de la conclusion (Chapitre 8) est proposée dans les Annexes E, F et G, respectivement.

CHAPITRE 4 MÉTHODE EXPÉRIMENTALE

4.1 Introduction

La réalisation d'un banc d'essai capable de mesurer tous les éléments nécessaires (force de frottement, force d'impact, déplacement et vitesse du glissement) permettant l'étude du phénomène d'usure par frottement des tubes du générateur de vapeur est nécessaire. Nowlan (2009), Lalonde (2010) et Azizian (2012) ont fabriqué un banc d'essai comportant un des tubes d'un générateur de vapeur réel. Malgré la résolution de plusieurs problèmes de design, il reste quelques problèmes à solutionner à savoir : la complexité de la modélisation de la dynamique du tube, la faible précision des capteurs de position et l'incertitude sur la nature des conditions aux limites réelles. C'est pour cette raison que nous nous sommes inspirés du banc d'essai réalisé par Jalali et al. (2011) pour construire le nôtre. Nous pouvons maintenant l'utiliser pour caractériser les paramètres et valider les modèles de frottement.

4.2 Banc d'essai

Le banc d'essai a été conçu comme montre la Figure 4-1. Il s'agit d'un concept simple, l'éprouvette est une poutre encastrée d'un côté et simplement appuyée (avec l'effet de frottement non négligeable) sur l'autre, la poutre est excitée par un pot vibrant et sa réponse est mesurée par des accéléromètres (Figure 5-3 chapitre 5).

La poutre est modélisée par le théorème d'Euler-Bernoulli équation suivante :

$$\rho A\ddot{y}(x,t)+EIy''''(x,t)-T(t)y''(x,t)=F(t)\delta\left(x-X_f\right) \tag{4.1}$$

avec les conditions aux limites suivantes :

$$\begin{cases} x=0:\begin{cases} y(0,t)=0 \\ y'(0,t)=0 \end{cases} \\ x=L:\begin{cases} EIy''(L,t)=\left(r+e/2\right)T(t) \\ EIy'''(L,t)=-N(t)+m\ddot{y}(L,t)+T(t)y'(L,t) \end{cases} \end{cases} \tag{4.2}$$

Jalali et al. (2011) ont considéré que l'effet de $y'(L,t)$ est relativement négligeable dans l'équation (4.2). Par contre, dans notre modèle, tous les termes ont été utilisés. Pour que nous soyons capables d'avoir de bons résultats avec une analyse simple des données expérimentales, la poutre sera excitée avec leur première fréquence propre (en résonance). Donc, une analyse modale adéquate est nécessaire.

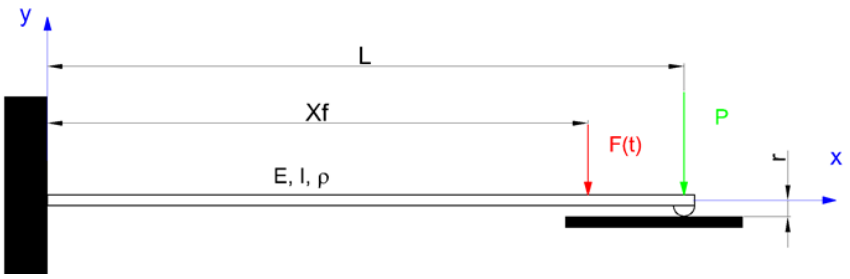

Figure 4-1 : Schéma d'une poutre non-linéaire

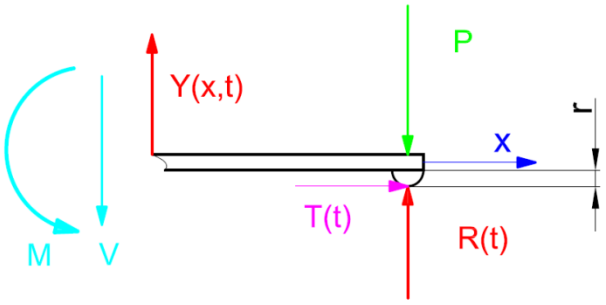

Figure 4-2 : Les directions des forces appliquées au point de contact

Avec les forces *F(t)*, *P*, *T(t)* et *R(t)* sont respectivement, la force d'excitation par un pot vibrant, la charge statique pour assurer un contact permanent entre la poutre et l'appui, la force de frottement et la réaction de l'appui (force d'impact). Les dimensions de la poutre sont : *L* la longueur, *e* l'épaisseur, A la surface de la section transversale, r le rayon de l'élément de contact (demi-cylindre) et X_f c'est la position du point d'excitation. On définit aussi les paramétrées physiques de poutre comme : le module de Yong *E*, la masse volumique ρ et le moment quadratique en flexion *I*. Certaines valeurs de ces paramètres sont présentées dans le Tableau 4-1.

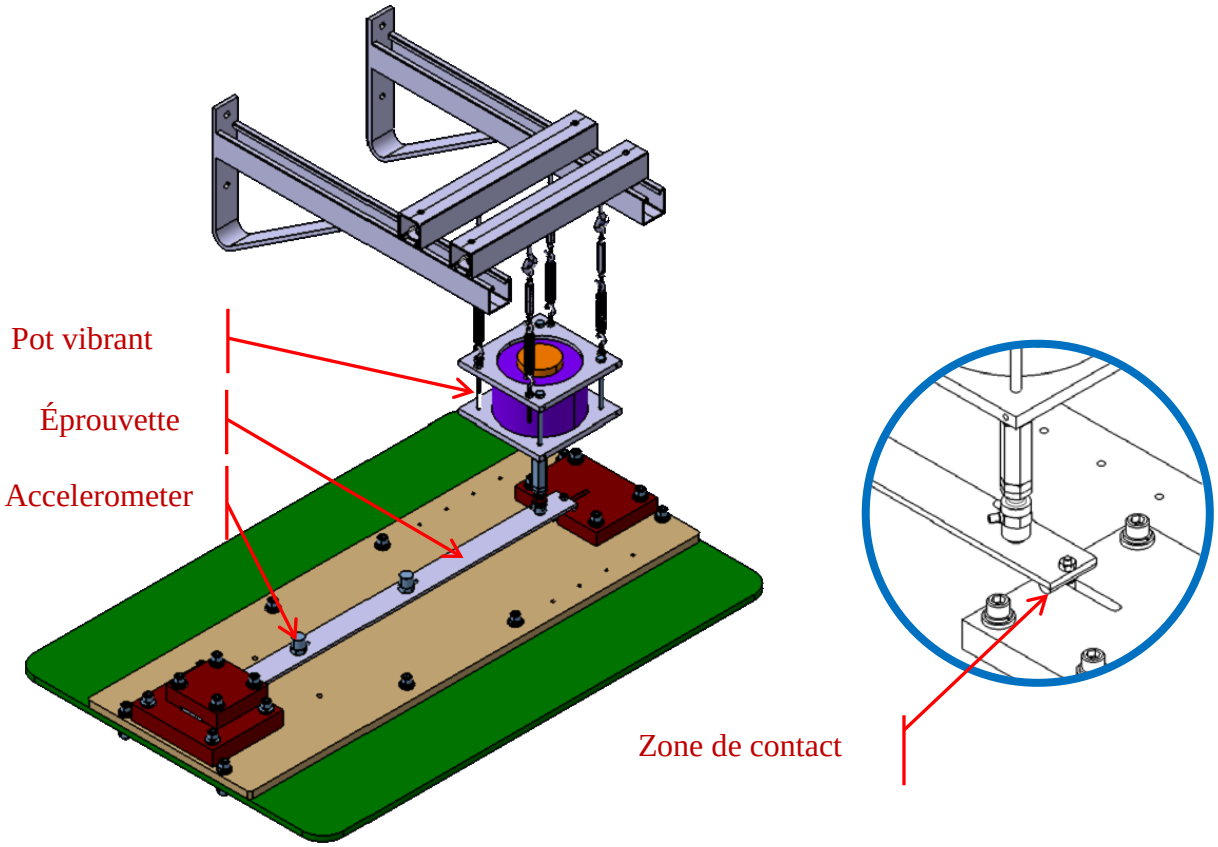

Figure 4-3 : Schéma du banc d'essai poutre non-linéaire

Tableau 4-1 : Dimension exacte de la poutre et paramètres de la zone de contact

Longueur L (mm)	Largeur b (mm)	Épaisseur e (mm)	Précharge P (kg)	Rayon r (mm)
606	38.88	4.76	8.5	5

Le montage a été conçu d'une manière telle que la géométrie et le matériau de la zone de contact peuvent être changés facilement. Une modification a été effectuée pour pouvoir échanger la géométrie et le matériau de l'appui. Il est même possible de modifier l'environnement de contact (avec ou sans lubrification).

$$y(x,t)=\sum_{i=1}^{n}\phi_i(x)q_i(t) \tag{4.3}$$

où :

$q_i(t)$ (i=1,2,...n) sont les coordonnées généralisées

$\varphi_i(x)$ (i=1,2,...n) sont les modes linéaires de base du système

En utilisant le principe de superposition modale (équation (4.3)) et la méthode de Galerkin sur l'équation du mouvement (4.1), cette dernière peut être réécrite comme suit :

$$\ddot{q}_i(t)+\omega_i^2 q_i(t)-F(t)\tilde{\phi}_i(Xf,a)=$$
$$\left[r\tilde{\phi}_i{}'(L,a)+\sum_{j=1}^{n}q_j(t)\left(\int_0^L \tilde{\phi}_j''(x,a)\tilde{\phi}_i(x,a)dx-\tilde{\phi}_i'(L,a)\tilde{\phi}_j(L,a)\right)\right]T(t)-N(t)\tilde{\phi}_i(L,a),\ \text{i=1-n} \quad (4.4)$$

où :

$N(t)=P-R(t)$: La force d'impact (ou la force normale dans la zone du contact)

Avec les conditions d'orthogonalité modales suivantes :

$$\rho A\int_0^L \tilde{\varphi}_i(x,a)\tilde{\varphi}_j(x,a)dx+m\tilde{\varphi}_i(L,a)\tilde{\varphi}_j(L,a)=\delta_{ij} \quad (4.5)$$

$$EI\int_0^L \tilde{\varphi}_i''(x,a)\tilde{\varphi}_j''(x,a)dx=\omega_i^2\delta_{ij} \quad (4.6)$$

Le déplacement et la vitesse dans la zone de contact peuvent être calculés par les équations suivantes :

$$u(t)=-\frac{1}{2}\int_0^L\left(\frac{\partial y(x,t)}{\partial x}\right)^2 dx+r\left.\frac{\partial y(x,t)}{\partial x}\right|_{x=L}+\frac{T(t)L}{AE} \quad (4.7)$$

$$u(t)=-\frac{1}{2}\sum_{i=1}^{n}q_i^2(t)\int_0^L\left(\frac{\partial\phi_i(x)}{\partial x}\right)^2 dx+r\sum_{i=1}^{n}q_i(t)\phi_i'(L)+\frac{T(t)L}{AE} \quad (4.8)$$

$$v(t)=-\frac{1}{2}\sum_{i=1}^{n}\dot{q}_i^2(t)\int_0^L\left(\frac{\partial\phi_i(x)}{\partial x}\right)^2 dx+r\sum_{i=1}^{n}\dot{q}_i(t)\phi_i'(L)+\frac{\dot{T}(t)L}{AE} \quad (4.9)$$

où :

$u(t)$: déplacement au niveau de la zone de contact,

$v(t)$: vitesse au niveau de la zone de contact.

4.3 La méthode NNMs

Comme notre équation du mouvement est non linéaire et que la poutre va être excitée à la résonance, une analyse modale adéquate est nécessaire pour déterminer tous les paramètres modaux (fréquences, modes normaux, fonction de transfert et leurs paramètres). La méthode d'analyse des modes normaux non linéaires (NNMs) est un outil d'analyse modale pour un système non linéaire capable de fournir, expérimentalement, les modes normaux non linéaires. Le terme NNMs a été introduit pour la première fois dans la littérature par Rosenberg (1966). D'autres chercheurs ont tenté de mesurer le NNMs d'une poutre, expérimentalement. Par exemple, Jalali et al. (2011) ont utilisé les LNMs de base pour construire le NNMs d'une poutre encastrée- avec appui simple.

Dans la littérature, il existe deux hypothèses utilisées pour modéliser la dynamique de système non linéaire. La première hypothèse LNMs est l'hypothèse la plus usitée, qui consiste à utiliser seulement les modes normaux linéaires (LNMs). Les effets de la non-linéarité recueillent donc, dans les coordonnées généralisées (GCs). Par contre, la deuxième hypothèse NNMs consiste à tenir compte de l'effet de la non-linéarité qui se manifeste aussi dans la déformation des modes normaux. Jalali et al. (2011) ont proposé une approche pour identifier les NNMs expérimentalement. Ils n'ont considéré que les trois premières harmoniques de la réponse comme les GCs. Ils ont ainsi construit le NNMs à partir de LNMs de base.

Dans les prochains points, il vous sera présenté les étapes utilisées pour identifier les NNMs :
L'équation du mouvement d'un système continu non linéaire peut s'écrire sous la forme suivante :

$$\frac{\partial^2 y(x,t)}{\partial t^2} + L\left(y(x,t)\right) + NL\left(y(x,t)\right) = f(x,t) \tag{4.10}$$

Avec :

$L\left(y(x,t)\right)$ est la partie linéaire de l'équation du mouvement;

$NL\left(y(x,t)\right)$ est la partie non linéaire ;

$f(x,t)$ est la force d'excitation.

La réponse du système peut s'écrire si l'effet de la non-linéarité n'est pas présent sous la forme :

$$y(x,t)=\sum_{i=1}^{n}\varphi_i(x)q_i(t) \tag{4.11}$$

Mais si l'effet de la non-linéarité est présent, la réponse du système devient :

$$y(x,t)=\sum_{i=1}^{n}\tilde{\phi}_i(x)\tilde{q}_i(t) \tag{4.12}$$

D'où :

$q_i(t)$ et $\tilde{q}_i(t)$ (i=1,2,...n) sont les LGCs et les NGCs respectivement.

$\phi_i(x)$ et $\tilde{\phi}_i(x)$ (i=1,2,...n) sont, respectivement, les LNMs et les NNMs du système.

Les formes de $q_i(t)$ et de $\phi_i(x)$ sont connues, par contre, celles de $\tilde{q}_i(t)$ et de $\tilde{\phi}_i(x)$ doivent être déterminées.

On détermine les (n) coordonnées généralisées à partir de l'équation suivante :

$$\ddot{y}(x,t)=\begin{Bmatrix}\ddot{y}_1(x_1,t)\\ \ddot{y}_2(x_2,t)\\ \vdots\\ \ddot{y}_n(x_n,t)\end{Bmatrix}=\begin{bmatrix}\varphi_1(x_1) & \varphi_2(x_1) & \cdots & \varphi_n(x_1)\\ \varphi_1(x_2) & \varphi_2(x_1) & \cdots & \varphi_n(x_2)\\ \vdots & \vdots & \ddots & \vdots\\ \varphi_1(x_n) & \varphi_2(x_n) & \cdots & \varphi_n(x_n)\end{bmatrix}\begin{Bmatrix}\ddot{q}_1(t)\\ \ddot{q}_2(t)\\ \vdots\\ \ddot{q}_n(t)\end{Bmatrix} \tag{4.13}$$

Avec $\ddot{y}(x,t)$ c'est la réponse du système au point de mesure (i). Cependant, la présence de l'effet de non-linéarité dans le système nous oblige à écrire l'équation (4.13) sous la forme suivante :

$$\ddot{\tilde{q}}(t)=\begin{Bmatrix}\ddot{\tilde{q}}_1(t)\\ \ddot{\tilde{q}}_2(t)\\ \vdots\\ \ddot{\tilde{q}}_n(t)\end{Bmatrix}=\begin{bmatrix}\tilde{\varphi}_1(x_1) & \tilde{\varphi}_2(x_1) & \cdots & \tilde{\varphi}_n(x_1)\\ \tilde{\varphi}_1(x_2) & \tilde{\varphi}_2(x_1) & \cdots & \tilde{\varphi}_n(x_2)\\ \vdots & \vdots & \ddots & \vdots\\ \tilde{\varphi}_1(x_n) & \tilde{\varphi}_2(x_n) & \cdots & \tilde{\varphi}_n(x_n)\end{bmatrix}^{-1}\begin{Bmatrix}\ddot{y}_1(x_1,t)\\ \ddot{y}_2(x_2,t)\\ \vdots\\ \ddot{y}_n(x_n,t)\end{Bmatrix} \tag{4.14}$$

Jalali et al. (2011) ont proposé une méthode de calculs pour identifier les NNMs.

On utilise les LNMs pour calculer les NCGs purement non linéaires avec l'équation suivante :

$$\ddot{\tilde{q}}_{PN}(t)=\begin{Bmatrix}\ddot{\tilde{q}}_{PN.1}(t)\\ \ddot{\tilde{q}}_{PN.2}(t)\\ \vdots\\ \ddot{\tilde{q}}_{PN.n}(t)\end{Bmatrix}=\begin{bmatrix}\tilde{\varphi}_1(x_1) & \tilde{\varphi}_2(x_1) & \cdots & \tilde{\varphi}_n(x_1)\\ \tilde{\varphi}_1(x_2) & \tilde{\varphi}_2(x_1) & \cdots & \tilde{\varphi}_n(x_2)\\ \vdots & \vdots & \ddots & \vdots\\ \tilde{\varphi}_1(x_n) & \tilde{\varphi}_2(x_n) & \cdots & \tilde{\varphi}_n(x_n)\end{bmatrix}^{-1}\begin{Bmatrix}\ddot{y}_1(x_1,t)\\ \ddot{y}_2(x_2,t)\\ \vdots\\ \ddot{y}_n(x_n,t)\end{Bmatrix} \tag{4.15}$$

On utilise les séries de Fourier pour lisser les signaux des coordonnées généralisées.

$$\tilde{\ddot{q}}_{PN.i}(t) = \sum_{j=1}^{M}\left(A_{ji}\cos\left(j\omega t + \psi_{ji}\right)\right) \tag{4.16}$$

On intègre l'équation (4.16) pour trouver les équations des coordonnées généralisées.

$$\tilde{q}_{NP.i}(t) = \sum_{j=1}^{M}\left(\frac{A_{ji}}{(j\omega)^2}\cos\left(j\omega t + \psi_{ji}\right)\right) \tag{4.17}$$

On remplace ensuite l'équation (4.12) dans l'équation (4.17) et on trouve :

$$y(x,t) = -\sum_{i=1}^{n}\left(\varphi_i(x)\sum_{j=1}^{M}\left(\frac{A_{ji}}{(j\omega)^2}\sin\left(j\omega t + \psi_{ji}\right)\right)\right) \tag{4.18}$$

Avec l'hypothèse : la réponse est dominée par le premier mode, les ψ_{1i} sont presque égaux ($\psi_1 = \psi_{1i}$), donc, l'équation précédente peut s'écrire comme suit:

$$y(x,t) \cong -\sum_{j=1}^{n}\left[\sum_{i=1}^{n}\left(\frac{A_{ji}\phi_i(x)}{(j\omega)^2}\right)\sin\left(j\omega t + \psi_j\right)\right] \tag{4.19}$$

On multiplie la somme de (j) par $|A_j|$ et divise la somme de (i) par la même valeur et on trouve :

$$y(x,t) \cong -\sum_{j=1}^{n}\left[\sum_{i=1}^{n}\left(\frac{A_{ji}\phi_i(x)}{|A_j|(j\omega)^2}\right)|A_j|\sin\left(j\omega t + \psi_j\right)\right] \tag{4.20}$$

avec :

$$|A_j| = \sqrt{\sum_{i=1}^{n} A_{ji}^2} \tag{4.21}$$

On définit les modes normaux non linéaires comme suit :

$$\tilde{\phi}_j(x, F_{\max}) \cong -\frac{1}{|A_j|}\sum_{i=1}^{n}\left(\frac{A_{ji}\phi_i(x)}{(j\omega)^2}\right) \tag{4.22}$$

où $|A_j|$ est la norme du vecteur formé par les coefficients A_{ji} et $F_{\max}$: est l'amplitude maximale de force d'excitation.

4.4 Conclusion

Le banc d'essai a été conçu, fabriqué, testé et amélioré pour réduire l'interaction avec le système d'excitation (pot vibrant) et avec leur support. Tous les résultats présentés dans cette thèse ont été obtenus par ce banc d'essai.

Dans ce chapitre on a présenté seulement l'approche de Jalali et al. (2011) utilisée pour identifier les modes normaux non-linéaires (MNNs). Par la suite les MNNs ont été utilisés dans le calcul des forces de contact (frottement et impact). Les résultats de cette approche et des autres approches développées durant ce doctorat sont présentés dans les prochains chapitres et dans les annexes.

CHAPITRE 5 ARTICLE 1: IDENTIFICATION OF FRICTION MODEL PARAMETERS USING THE INVERSE HARMONIC METHOD

Hadji, A., & Mureithi, N. (2016)

Accepted for publication in “Journal of Pressure Vessel Technology (Transactions of the ASME)”. DOI: 10.1115/1.4034441

5.1 Abstract

A Hybrid friction model has been developed by Azizian and Mureithi (*2013, “A Hybrid Friction Model for Dynamic Modeling of Stick–Slip Behavior,” ASME Paper No. PVP2013-97249*) to simulate the general friction behavior between surfaces in contact. However, identification of the model parameters remains an unresolved problem.

To identify the parameters of the friction model, the following quantities are required: contact forces (normal and tangential or friction forces), the slip velocity and the displacement in the contact region. Simultaneous direct measurement of these quantities is difficult. In the present work, a beam clamped at one end and simply supported with the consideration of friction at the other is used as a mechanical amplifier of the friction effects at the microscopic level. Using this simplified approach, the contact forces, the sliding velocity and the displacement can be indirectly obtained by measuring the beam vibration response.

The inverse harmonic balance method is a new method based on nonlinear modal analysis which is developed in this work to calculate the contact forces. The method is based on the modal superposition principle and Fourier series expansion. Two formulations are possible, a harmonic form formulation and a sub-harmonic form formulation. The approach based on sub-harmonic forms coupled with spline fitting gave the best results for signal reconstruction. Signal reconstruction made it possible to accurately identify the parameters of the hybrid friction model with a multiple step approach.

5.2 Introduction

The problem under study is that of the accurate modeling of tube-support interaction in steam-generators and more specifically contact friction modeling (Hadji & Mureithi, 2014a, 2014b). The tube-support interaction friction models cited by (M. Hassan & Rogers, 2005) are special cases of static friction models. The velocity limited friction model (VLFM) (Rogers & Pick, 1977) is a continuous Coulomb model without Stribeck effects and with velocity dependence in the sticking regime. The force balance friction model (FBFM) (Xi & Rogers, 1996) and the spring-damper friction model (SDFM) (Antunes, Axisa, Beaufils, & Guilbaud, 1988) are based on the modeling of friction by springs and dampers. The principle of the Karnopp friction model (Karnopp, 1985) is used in the FBFM friction model. A hybrid friction model (Azizian, 2012; Azizian & Mureithi, 2013) has also recently been developed. The authors used the basic approach of the Dahl (1976) and LuGre (Canudas et al., 1995) models with additional consideration of the stress distribution in the contact area in accordance with the principle of Cattaneo-Mindlin (Kenneth Langstreth Johnson, 1985) and Ödfalk-Vingsbo (1992).

In the authors' previous work (Hadji & Mureithi, 2014a, 2014b), the parameters of the Dahl (1976) and LuGre (Canudas et al., 1995) friction models were identified experimentally at 6.5N excitation level (the test setup is described below). These two models are, respectively, based on the Coulomb and the Stribeck friction models. In the work presented here we analyze these two friction models to identify their coefficients at 6.5 and 8 (N) excitation levels, taking into consideration the conclusions of our recent results (Hadji & Mureithi, 2015).

To identify the friction model parameters experimentally using the proposed indirect method, accurate nonlinear normal modes (NNMs) are needed. Nonlinear normal modes and the principle of inverse harmonic balance (IHB) based on the harmonic balance (HB) method (Gilmore & Steer, 1991) were developed and presented in previous work (Hadji & Mureithi, 2014a, 2014b).

Nonlinear normal modes (NNMs) have increasingly been used in the analysis of nonlinear systems, as revealed by the works of Rosenberg (1966) and Pierre and co-workers (Boivin, Pierre, & Shaw, 1994; Pesheck, Boivin, Pierre, & Shaw, 2001; Shaw & Pierre, 1992). Other methods used in the analysis of nonlinear systems include the harmonic balance (HB) method (Gilmore & Steer, 1991) which is also widely used in the electronics field.

5.3 The test rig and theoretical consideration

The test rig (Figure 5-1) is based on a simple concept. The specimen is a simply supported beam on one side (but also including friction effects) and clamped on the other. Figure 5-2 represents all the forces acting at the contact point. The beam is excited by a shaker and its response measured by six accelerometers; as shown in Figure 5-3.

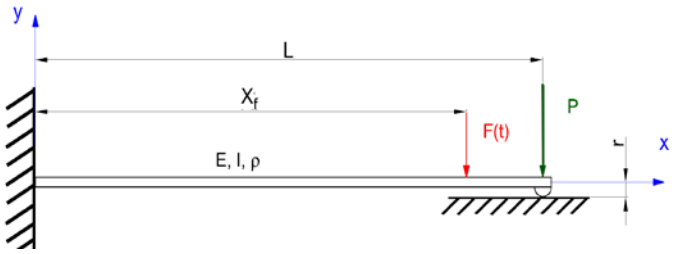

Figure 5-1 : Schematic of a nonlinear beam

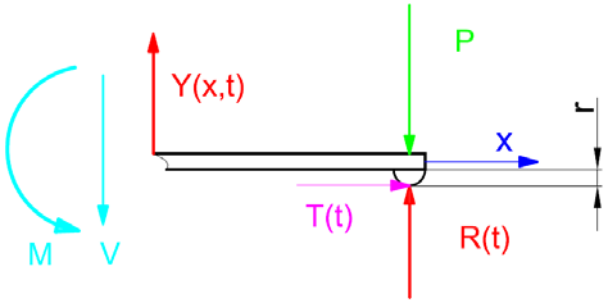

Figure 5-2 : Direction of forces applied at the contact point

The beam equation of motion is:

$$\rho A\ddot{y}(x,t)+EIy''''(x,t)-T(t)y''(x,t)=F(t)\delta(x-X_f) \tag{5.1}$$

with the following boundary conditions:

$$\begin{cases} x=0:\begin{cases} y(0,t)=0 \\ y'(0,t)=0 \end{cases} \\ x=L:\begin{cases} EIy''(L,t)=\left(r+e/2\right)T(t) \\ EIy'''(L,t)=-N(t)+m\ddot{y}(L,t) \end{cases} \end{cases} \tag{5.2}$$

The characteristics of the beam are as follows: length L = 606 mm, width b = 38.88 mm, thickness e = 4.76 mm and the radius r = 5 mm. The six accelerometers (3 acc. PCB 352C33, 2

acc. PCB 353B33 and an impedance head PCB 288D01) used in the test were positioned at 83 mm, 153mm, 268 mm, 408 mm, 499 mm and 555 mm, respectively, and the driving point (impedance head) at 555 mm from the clamped end.

The response of the system may be written in the following form, based on modal superposition:

$$y_j\left(x_j,t\right)=\sum_{i=1}^{n}\phi_i\left(x_j\right)q_i\left(t\right) \tag{5.3}$$

where:

$q_i\left(t\right)$ (i=1,2,...n) are the generalized coordinates

$\phi_i\left(x_j\right)$ (i=1,2,...n) are the normal modes of the system, and j is the accelerometer position index (j=1,2,...6).

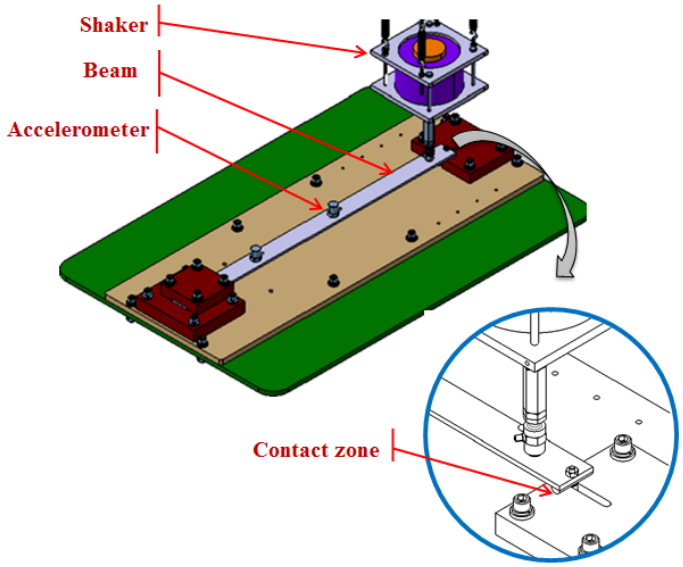

Figure 5-3 : Schematic of the test rig

Using the modal superposition principle, Eq. (5.3), the boundary condition equations, Eq. (5.2), and the Galerkin method, Eq. (5.1), can be rewritten as follows:

$$\ddot{q}_i\left(t\right)+\omega_i^2q_i\left(t\right)-F(t)\tilde{\phi}_i\left(X_f\right)=-N(t)\tilde{\phi}_i\left(L\right)+$$
$$\left[r\tilde{\phi}_i{}'\left(L\right)+\sum_{j=1}^{n}q_j\left(t\right)\left(\int_0^L\tilde{\phi}_j''\left(x\right)\tilde{\phi}_i\left(x\right)dx-\tilde{\phi}_i'\left(L\right)\tilde{\phi}_j\left(L\right)\right)\right]T(t)\ ,\quad i\text{=}1\text{-}n \tag{5.4}$$

where $N(t) = P - R(t)$ is the impact force (or the resultant of the normal force in the contact zone). Modal orthogonality may be expressed as follows:

$$\begin{cases} \rho A \int_0^L \tilde{\phi}_i(x,a)\tilde{\phi}_j(x,a)\,dx + m\tilde{\phi}_i(L,a)\tilde{\phi}_j(L,a) = \delta_{ij} \\ EI \int_0^L \tilde{\phi}_i''(x,a)\tilde{\phi}_j''(x,a)\,dx = \omega_i^2 \delta_{ij} \end{cases} \tag{5.5}$$

The reader is referred to (Jalali et al., 2011) for the derivation of Eq.(5.4). In the analysis the term $\tilde{\phi}_i'(L,a)\tilde{\phi}_j(L,a)$ is considered negligible. The displacement and velocity in the contact area can be calculated as follows. The displacement:

$$u(t) = -\frac{1}{2}\int_0^L \left(\frac{\partial y(x,t)}{\partial x}\right)^2 dx + r\frac{\partial y(x,t)}{\partial x}\bigg|_{x=L} + \frac{T(t)L}{AE} \tag{5.6}$$

This equation can be rewritten as:

$$u(t) = -\frac{1}{2}\int_0^L \left(\frac{\partial y(x,t)}{\partial x}\right)^2 dx + r\frac{\partial y(x,t)}{\partial x}\bigg|_{x=L} + \frac{T(t)L}{AE} \tag{5.7}$$

By differentiating Eq.(7) we obtain the following velocity equation:

$$v(t) = -\frac{1}{2}\sum_{i=1}^{n}\dot{q}_i^2(t)\int_0^L \left(\frac{\partial \phi_i(x)}{\partial x}\right)^2 dx + r\sum_{i=1}^{n}\dot{q}_i(t)\phi_i'(L) + \frac{\dot{T}(t)L}{AE} \tag{5.8}$$

Since the beam is excited at its first natural frequency (resonance), adequate modal analysis is necessary.

5.4 The nonlinear normal modes

Nonlinear normal modes (NNMs) were first introduced by Rosenberg (1966) who proposed a definition applicable only for a discrete and conservative system. However, the NNMs description proposed by Pierre and co-workers (Boivin et al., 1994; Jiang, Pierre, & Shaw, 2005; Pesheck et al., 2001; Shaw & Pierre, 1992) is the most general and applicable to all systems;

including continuous systems. Researchers have also attempted to identify the NNMs of a beam experimentally. For example, Jalali et al. (2011) used basic linear normal modes to rebuild the NNMs of a frictional clamped-simply supported beam.

In our recent work (Hadji & Mureithi, 2014a, 2014b), different approaches used to model nonlinear dynamical systems were presented. In the modal analysis of a nonlinear system, the nonlinear effects may be accounted for either in the normal modes, in the generalized coordinates, or in both the normal modes and the generalized coordinates. The assumption most commonly used is the linear normal modes and nonlinear generalized coordinates (Linear approach).

Jalali et al. (2011) proposed a second approach: nonlinear normal modes (NNMs) coupled with linear generalized coordinates (Jalali et al. (2011) approach). Below we present the main steps used to determine NNMs according to this approach. The nonlinear response of the system can be written in the following form:

$$y_j\left(x_j,t\right)=\sum_{i=1}^{n}\tilde{\phi}_i\left(x_j\right)\tilde{q}_i\left(t\right) \tag{5.9}$$

where

$\tilde{q}_i\left(t\right)$ (i=1,2,...n) are the N generalized coordinates

$\tilde{\phi}_i\left(x\right)$ (i=1,2,...n) are the NNMs of the system.

j is the accelerometer position index.

The quantities $q_i\left(t\right)$ and $\phi_i\left(x\right)$ are known, however, $q_i\left(t\right)$ and $\tilde{\phi}_i\left(x\right)$ must be determined.

The second derivative of the *n* generalized coordinates can be determined from the following equation:

$$\ddot{q}\left(t\right)=\begin{Bmatrix}\ddot{q}_1\left(t\right)\\ \ddot{q}_2\left(t\right)\\ \vdots\\ \ddot{q}_n\left(t\right)\end{Bmatrix}=\begin{bmatrix}\phi_1\left(x_1\right) & \phi_2\left(x_1\right) & \cdots & \phi_n\left(x_1\right)\\ \phi_1\left(x_2\right) & \phi_2\left(x_1\right) & \cdots & \phi_n\left(x_2\right)\\ \vdots & \vdots & \ddots & \vdots\\ \phi_1\left(x_n\right) & \phi_2\left(x_n\right) & \cdots & \phi_n\left(x_n\right)\end{bmatrix}^{-1}\begin{Bmatrix}\ddot{y}_1\left(x_1,t\right)\\ \ddot{y}_2\left(x_2,t\right)\\ \vdots\\ \ddot{y}_n\left(x_n,t\right)\end{Bmatrix} \tag{5.10}$$

$\ddot{y}_i = (x_i, t)$ being the system response at the measurement point *i*. A Fourier series is used torepresent the signal of the second derivative of generalized coordinates.

$$\ddot{q}_i(t) = \sum_{j=1}^{M} \left(A_{ji} \cos\left(j\omega t + \psi_{ji} \right) \right) \tag{5.11}$$

On integration, we obtain the equations of the generalized coordinates as:

$$q_i(t) = \sum_{j=1}^{M} \left(\frac{A_{ji}}{(j\omega)^2} \cos\left(j\omega t + \psi_{ji} \right) \right) \tag{5.12}$$

Substituting Eq. (12) into Eq. (9) yields:

$$y(x,t) = -\sum_{i=1}^{n} \left(\phi_i(x) \sum_{j=1}^{M} \left(\frac{A_{ji}}{(j\omega)^2} \sin\left(j\omega t + \psi_{ji} \right) \right) \right) \tag{5.13}$$

Assuming the system response to be dominated by the first mode and the ψ_{j1} equal $(\psi_j = \psi_{j1})$, the above equation can be rewritten as follows:

$$y(x,t) \cong -\sum_{j=1}^{n} \left[\sum_{i=1}^{n} \left(\frac{A_{ji}\phi_i(x)}{|A_j|(j\omega)^2} \right) |A_j| \sin\left(j\omega t + \psi_j \right) \right] \tag{5.14}$$

with

$$|A_j| = \sqrt{\sum_{i=1}^{n} A_{ji}^2} \tag{5.15}$$

The NNMs are then defined as:

$$\tilde{\phi}_j(x, F_{\max}) \cong -\frac{1}{|A_j|} \sum_{i=1}^{n} \left(\frac{A_{ji}\phi_i(x)}{(j\omega)^2} \right) \tag{5.16}$$

where $F_{\max}$ is the maximum amplitude of the excitation force.

According to Ewins (2000) the modal analysis of a nonlinear system is performed for a constant level of response (approach used by Jalali et al. (2011)) or a constant level of excitation force. The latter approach is the more relevant for displaying the non-linearity effect and the experimental system frequency response function (FRF). Since the level of excitation of the fluid force in practice is known and the final objective is to determine the tube wear rate corresponding to each force level, the latter approach is used in the current work. The theory of Jalali et al. and underlying assumptions are presented in detail in (Hadji & Mureithi, 2014a) and (Hadji & Mureithi, 2014b).

In the new approach we propose, nonlinear normal modes and nonlinear generalized coordinates are obtained using the inverse harmonic balance (IHB) method. The IHB analysis is performed based on two methods, the harmonic form approach (H-form) or the combined average phase approach plus sub-harmonic form approach (Sub-H-form), as described next.

The harmonic form approach (H-form) is based on the principal of modal superposition and utilizes all the (significant) harmonics that appear in the system response signal. The nonlinear response of the system can be written in the following form:

$$y_j\left(x_j,t\right)=\sum_{r=1}^{n}\tilde{\tilde{\phi}}_{ir}\left(x_j\right)\tilde{\tilde{q}}_{ir}\left(t\right) \tag{5.17}$$

where

$\tilde{\tilde{q}}_{ir}(t)$ (r=1,2,...n) are the Harmonic generalized coordinates

$\tilde{\tilde{\phi}}_{i1}\left(x\right)$ is the ith nonlinear normal mode of the system and $\tilde{\tilde{\phi}}_{ir}\left(x\right)$ (r=2,...n) are his harmonic form.

The NNMs are calculated in the following manner:

STEP 1: The Fourier series of the response signal is written as follows:

$$y_j\left(x_j,t\right)=\sum_{r=1}^{n}A_{rj}\left(x_j\right)\cos\left(r\cdot\omega_{ext}t+\psi_{rj}\left(x_j\right)\right) \tag{5.18}$$

STEP 2: Eq.(5.18) can also be written as:

$$y_j\left(x_j,t\right)=\sum_{r=1}^{n}\tilde{\tilde{\phi}}_{ir}\left(x_j\right)C_r\cos\left(r\cdot\omega_{ext}t+\psi_r\right) \tag{5.19}$$

$$\ddot{\tilde{\tilde{q}}}_{ir}(t) = C_{ir}\cos\left(r\cdot\omega_{ext}t+\varphi_r\right) \tag{5.20}$$

where x_j is the position of the accelerometer *j*.

The transition from Eq. (5.18) to Eq. (5.19) requires the calculation of ψ_r by the minimization of the error in the reconstruction of the accelerometer signals (which yields ψ_{rj} optimal) and C_{ir} by the normalization of $\tilde{\tilde{\phi}}_{ir}(x_j)$ from $A_{rj}\left(x_j\right)$ using the modal orthogonality equation Eq. (5.5) if we suppose that the harmonic forms are orthogonal. In the previous work (Hadji & Mureithi, 2014a, 2014b), it was assumed (for simplicity) that the harmonic forms are orthogonal, but in reality they are not. Where, they are slightly coupled with a low level of excitation force this assumption holds; however, the coupling increases as the level of the excitation force increases.

For both approaches, coupled and decoupled harmonic forms, the modal equation, Eq. (5.4), and modal orthogonality equations Eq. (5.5) are reformulated as:

$$\begin{aligned}&\sum_{s=1}^{n} a_{rs}\ddot{\tilde{\tilde{q}}}_{is}(t)+\sum_{s=1}^{n} b_{rs}\tilde{\tilde{q}}_{is}(t)-F(t)\tilde{\tilde{\phi}}_{ir}\left(X_f,a\right)=-N(t)\tilde{\tilde{\phi}}_{ir}\left(L,a\right)+\\&\left[r\tilde{\tilde{\phi}}_{i}'\left(L,a\right)+\sum_{s=1}^{n}\tilde{\tilde{q}}_{is}(t)\left(\int_0^L \tilde{\tilde{\phi}}_{is}''(x,a)\tilde{\tilde{\phi}}_{ir}(x,a)dx-\tilde{\tilde{\phi}}_{ir}'\left(L,a\right)\tilde{\tilde{\phi}}_{is}\left(L,a\right)\right)\right]T(t),\quad r=1\text{-}n\end{aligned} \tag{5.21}$$

$$\begin{cases}\rho A\int_0^L \tilde{\tilde{\phi}}_{is}(x,a)\tilde{\tilde{\phi}}_{ir}(x,a)dx+m\tilde{\tilde{\phi}}_{ir}\left(L,a\right)\tilde{\tilde{\phi}}_{is}\left(L,a\right)=a_{rs}\\ EI\int_0^L \tilde{\tilde{\phi}}_{ir}''(x,a)\tilde{\tilde{\phi}}_{is}''(x,a)dx=b_{rs}\end{cases} \tag{5.22}$$

where

$$\begin{cases}a_{rs}=\delta_{rs} & \text{coupled harmonic forms}\\ a_{rr}=1 & \text{decoupled harmonic forms}\end{cases} \tag{5.23}$$

STEP 3: $\tilde{\tilde{\phi}}_{ir}(x)$ are represented by a series of trigonometric functions, Eq. (5.24). To reduce the smoothing error, an intermediate step (natural smoothing spline) must be used to predict the natural deformed form of the beam and improve the fitting result.

$$\tilde{\tilde{\phi}}_{ir}(x)=\sum_{k=1}^{n}\left(a_{ik1}\sin\left(\beta_{ik}x\right)+a_{ik2}\sinh\left(\beta_{ik}x\right)+a_{ik3}\cos\left(\beta_{ik}x\right)+a_{ik4}\cosh\left(\beta_{ik}x\right)\right) \tag{5.24}$$

n equal to 3 minimizes the fitting error.

The Sub-harmonic form approach (Sub-H-form) is also based on the principal of modal superposition and utilizes all the harmonics that appear in the system response signal but without phase averaging. The NNMs are calculated in the following manner:

STEP 1

The Fourier series of the response signal is written as follows:

$$y_j\left(x_j,t\right)=\sum_{r=1}^{n}\alpha_{rj}\left(x_j\right)\cos\left(r\cdot\omega_{ext}t\right)+\sum_{r=1}^{n}\beta_{rj}\left(x_j\right)\sin\left(r\cdot\omega_{ext}t\right) \tag{5.25}$$

STEP 2

This equation can also be written as:

$$y_j\left(x_j,t\right)=\sum_{r=1}^{n}\tilde{\tilde{\phi}}_{ir1}\left(x_j\right)\gamma_{r1}\cos\left(r\cdot\omega_{ext}t\right)+\sum_{r=1}^{n}\tilde{\tilde{\phi}}_{ir2}\left(x_j\right)\gamma_{r2}\sin\left(r\cdot\omega_{ext}t\right) \tag{5.26}$$

$$\begin{cases}\tilde{\tilde{q}}_{ir1}\left(t\right)=\gamma_{r1}\cos\left(r\cdot\omega_{ext}t\right)\\ \tilde{\tilde{q}}_{ir2}\left(t\right)=\gamma_{r2}\sin\left(r\cdot\omega_{ext}t\right)\end{cases} \tag{5.27}$$

$$\begin{cases}\tilde{\tilde{\phi}}_{ir1}\left(x_j\right)=\dfrac{\alpha_{rj}\left(x_j\right)}{\gamma_{r1}}\\ \tilde{\tilde{\phi}}_{ir2}\left(x_j\right)=\dfrac{\beta_{rj}\left(x_j\right)}{\gamma_{r2}}\end{cases} \tag{5.28}$$

where, $\tilde{\tilde{\phi}}_{ir1}$ is the first sub-harmonic form (or cosines sub-harmonic form) and $\tilde{\tilde{\phi}}_{ir2}$ is the second sub-harmonic form (or sines sub-harmonic form). The modal equation of motion (Eq.(5.21)) becomes:

$$\sum_{s=1}^{n}\left(a_{rsk}\ddot{\tilde{\tilde{q}}}_{isk}(t)+a_{rsl}\ddot{\tilde{\tilde{q}}}_{isl}(t)\right)+\sum_{s=1}^{n}\left(b_{rsk}\tilde{\tilde{q}}_{isk}(t)+b_{rsl}\tilde{\tilde{q}}_{isl}(t)\right)-F(t)\tilde{\tilde{\phi}}_{irk}(X_f)=$$

$$-N(t)\tilde{\tilde{\phi}}_{irk}(L)+\begin{pmatrix}\sum_{s=1}^{n}\tilde{\tilde{q}}_{is1}(t)\int_0^L\tilde{\tilde{\phi}}''_{is1}(x)\tilde{\phi}_{irk}(x)dx\\+\sum_{s=1}^{n}\tilde{\tilde{q}}_{is2}(t)\int_0^L\tilde{\phi}''_{is2}(x)\tilde{\phi}_{irk}(x)dx\\-\left(\sum_{s=1}^{n}\tilde{\tilde{\phi}}'_{is1}(L)\tilde{\tilde{q}}_{is1}(t)+\sum_{s=1}^{n}\tilde{\tilde{\phi}}'_{is2}(L)\tilde{\tilde{q}}_{is2}(t)\right)\tilde{\tilde{\phi}}_{irk}(L)\\+\left(r+e/2\right)\tilde{\tilde{\phi}}'_{irk}(L)\end{pmatrix}T(t)\quad,\ r=1\text{-}n;\quad(5.29)$$

with k and l chosen as follows: k=1, l=2 or k=1, l=2. In the present work, k=1 and l=2 were chosen. The modal orthogonality equations Eq. (5.22) become:

$$\begin{cases}\rho A\int_0^L\tilde{\tilde{\phi}}_{isk}(x,a)\tilde{\tilde{\phi}}_{irk}(x,a)dx+m\tilde{\tilde{\phi}}_{irk}(L,a)\tilde{\tilde{\phi}}_{isk}(L,a)=a_{rsk}\\ EI\int_0^L\tilde{\tilde{\phi}}''_{irk}(x,a)\tilde{\tilde{\phi}}''_{isk}(x,a)dx=b_{rsk}\end{cases}\qquad(5.30)$$

and

$$\begin{cases}\rho A\int_0^L\tilde{\tilde{\phi}}_{isk}(x,a)\tilde{\tilde{\phi}}_{irl}(x,a)dx+m\tilde{\tilde{\phi}}_{irk}(L,a)\tilde{\tilde{\phi}}_{isl}(L,a)=a_{rsl}\\ EI\int_0^L\tilde{\tilde{\phi}}''_{irk}(x,a)\tilde{\tilde{\phi}}''_{isl}(x,a)dx=b_{rsl}\end{cases}\qquad(5.31)$$

where

$$\begin{cases}\begin{cases}a_{rsk}=\delta_{rs}\\ a_{rsl}=\delta_{rs}\end{cases}&\text{coupled harmonic forms}\\ \begin{cases}a_{rrk}=\delta_{rs}\\ a_{rrl}=\delta_{rs}\end{cases}&\text{decoupled harmonic forms}\end{cases}\qquad(5.32)$$

Equations (5.27) and (5.28) are used to calculate γ_{r1} and γ_{r2} by the normalization of $\tilde{\tilde{\phi}}_{irk}(x_j)$ via α_{rj} or β_{rj}.

STEP 3: $\tilde{\tilde{\phi}}_{ir1}(x)$ and $\tilde{\tilde{\phi}}_{ir2}(x)$ can be represented by a natural smoothing spline or a series of trigonometric functions (Eq.(5.24)).

5.5 Experimental Results and Discussion

In the previous papers (Hadji & Mureithi, 2014a, 2014b) some experimental results were presented. In this part we summarize these results including the improvement of the friction force result and the friction model identified parameters.

5.5.1 Slip regimes

To detect the different slip regimes at constant frequency, several tests were performed with different levels of the excitation force. Figure 5-4 presents the beam excitation force as a function of the shaker input voltage or the shaker sensitivity to the slip regime change. Zone II, presented in a previous paper (Hadji & Mureithi, 2014a) as unstable slip can also be considered as the beginning of the slip regime; Figure 5-5 confirms this conclusion. The figure presents the effect of the friction regime on the beam response. Zone I is similar to that in Figure 5-4, contrary to zone II and III. The results of Figure 5-5 thus confirm and complete the information and conclusions obtained from Figure 5-4.

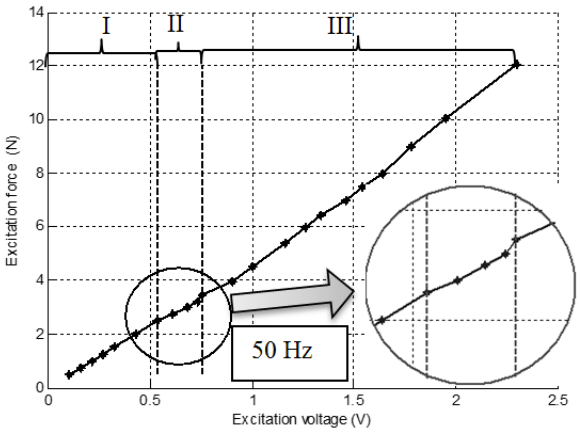

Figure 5-4 : The effect of slip regime on the shaker (the sensitivity of the shaker slip regime) Zone I: Stable sticking (pre-sliding), Zone II: beginning slip (stick-slip) and Zone III: sliding regime.

The variation of the reaction force of the vibrating beam is linear in both stable regimes (pre-sliding and stable sliding). This variation is, however, non-linear in the regime of unstable slip

(stick-slip regime), especially at the beginning of slipping regime and the beginning of large slip regime. This result will be useful in the identification of the friction parameters, especially in the identification of the critical velocity (or Stribeck velocity v_s or v_{th}) and the critical displacement $\gamma_{crit.}$ in the Stribeck Model (Stribeck & Schröter, 1903).

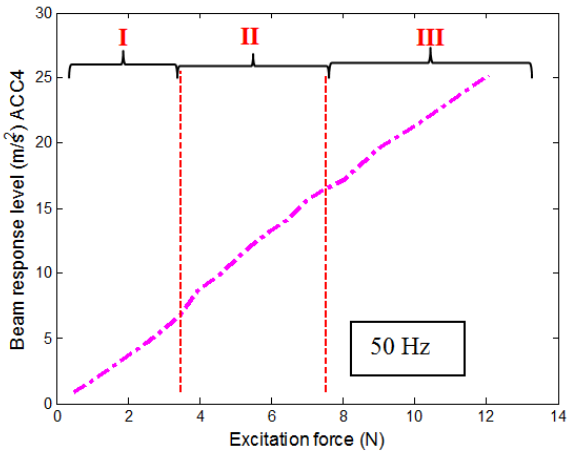

Figure 5-5 : The effect of slip regime on the beam response Zone I: Stable sticking (pre-sliding), Zone II: unstable slip (stick-slip) and Zone III: stable sliding regime (large slip)

5.5.2 The non-linear effects of friction

The non-linear friction effects are illustrated next. Firstly, the fast Fourier transform (FFT) of the response at the driving point of the same test shown in Figure 5-4 and Figure 5-5 is computed. As seen in Figure 5-6 several harmonics appear in the response and their amplitudes change according to the level of excitation. The amplitude of the third harmonic is greater than the second and the higher harmonics. This is because this harmonic is close to the second natural frequency of the system. The harmonics are therefore caused by the cross-coupling between the first mode and the higher modes.

Table 5-1 : 1st natural frequency

excitation F_{max} ***(N)***	***1st natural frequency (Hz)***
1	53
3	52
6.5	50
8	49.1

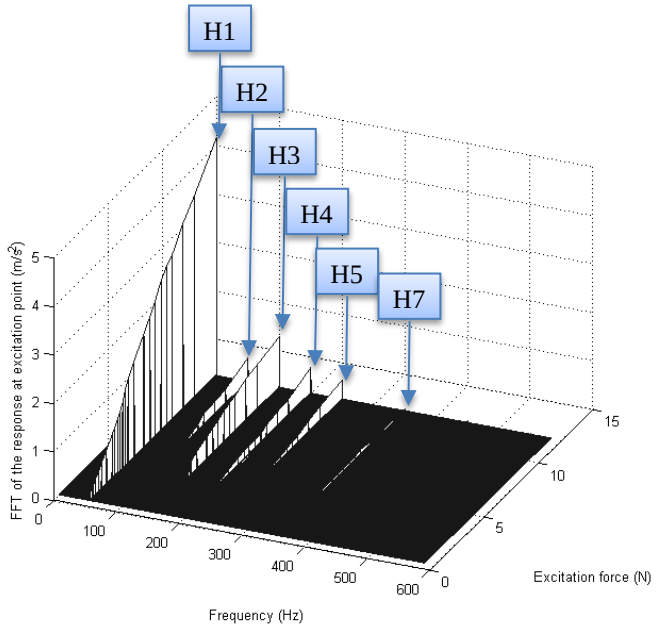

Figure 5-6 : FFT of the system response at the drive point (at 50Hz)

The frequency response of the system is obtained by a manual frequency sweep with the excitation force level values of 1 N, 3 N, and 8 N. In Figure 5-7 we can clearly see the effect of the non-linearity in the change of the first natural frequency (tabulated in Table 5-1) and the damping dependence on the excitation level. Figure 5-7 will also be useful for the identification of the hybrid friction model (Azizian, 2012; Azizian & Mureithi, 2013) parameters.

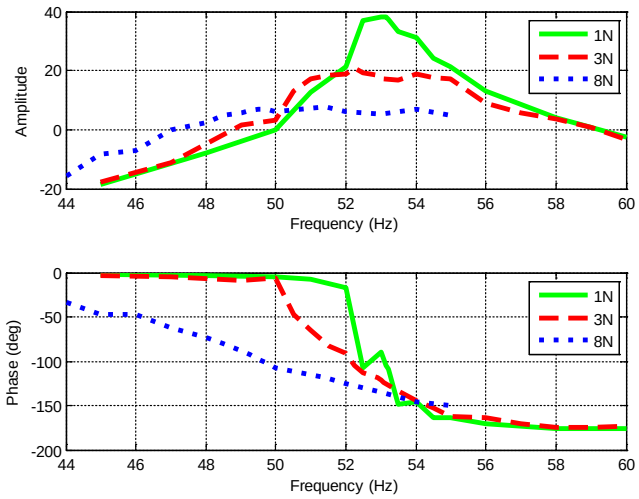

Figure 5-7 : The frequency response (FRF) of the system (first harmonic)

5.5.3 Nonlinear normal modes versus linear normal modes

The first deformed mode varies depending on the excitation level, and may be represented as a combination of several harmonic forms. Figure 5-8 represents the first harmonic at 8N excitation level. In general, the form is between that of a clamped-clamped beam and a simply-supported beam. This is due to the normal force applied at the contact point and the resulting friction effects. It can also be seen in this graph that the approach proposed by Jalali et al. (2011) produces a mode shape closer in form to the linear mode than IHB method mode shape.

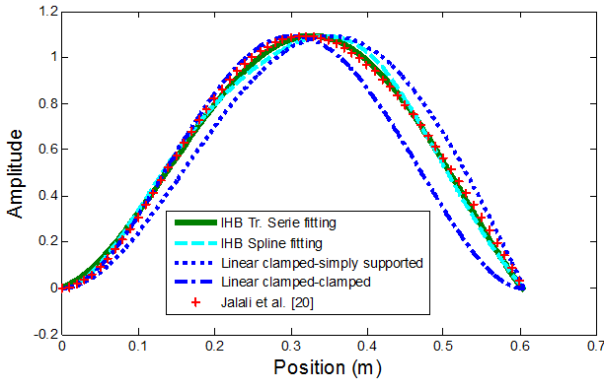

Figure 5-8 : The first non-linear mode depending on the level of excitement (F_{max} = 8 N)

In the previous works (Hadji & Mureithi, 2014a, 2014b), we have shown that the first NNM shape is closer to a clamped-simply supported beam mode for very high excitation levels, and closer to a clamped-clamped beam mode for low excitation levels. But at this level of excitation the IHB method with different approaches and the Jalali et al.'s approach give the same first NNM shape.

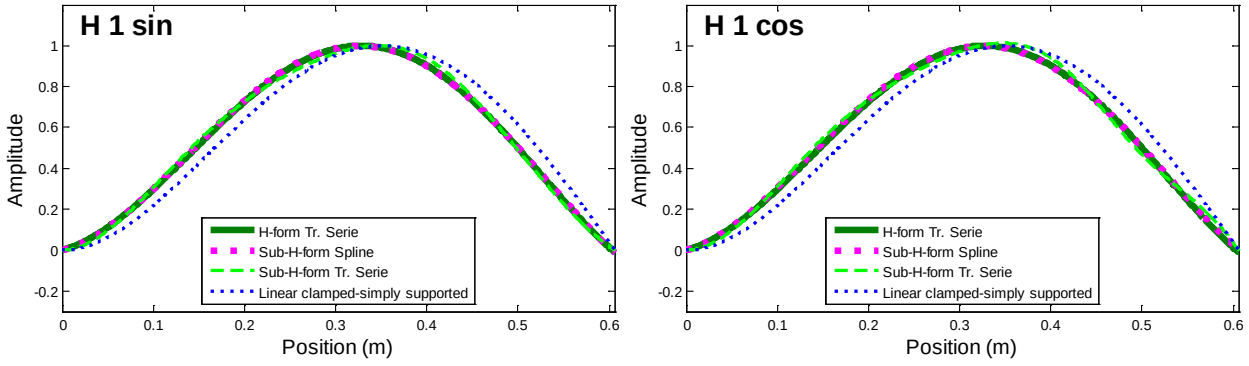

Figure 5-9 : The first harmonic and sub-harmonic form at 8 N excitation level

Figure 5-9 and Figure 5-10 present the first and second harmonic forms and the two sub-harmonic forms at the 8 N excitation level fitted using natural splines and trigonometric series. The linear normal modes (clamped-simply supported) are also plotted. The fitting using the trigonometric series of the harmonic form and the natural spline fitting of the sub-harmonic forms have the same form which is different from trigonometric series fitting of sub-harmonic form. However, in the previous works (Hadji & Mureithi, 2014a, 2014b) and at 6.5N excitation level, The fitting using the trigonometric series of the first harmonic gives the same harmonic form and sub-harmonic form which is different from that obtained with sub-harmonic form fitting using the natural spline.

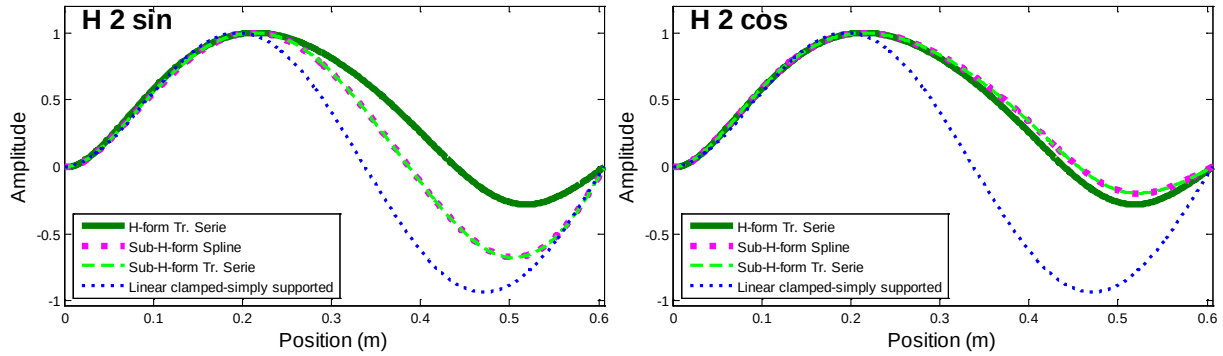

Figure 5-10 : The second harmonic and sub-harmonic form at 8 N excitation level

For the second harmonic, Figure 5-10, the fitting using the trigonometric series gives the same result as the natural spline fitting. On the other hand, the harmonic form and sub-harmonic form are different and give two different sub-harmonic forms, where this harmonic form seems equal to the average of the two sub-Harmonic forms. Similar results are also observed for the other harmonics.

Figure 5-11 presents the first and second harmonic forms in one period. This representation is useful in explaining the nonlinear behavior. For the first harmonic, it is difficult to distinguish the difference between the linear and the nonlinear behaviors. However, for the second harmonic the difference between the linear and the nonlinear behavior is clearly visible.

The evolution of the linear mode in one period is homogeneous and symmetric; conversely, both the nonlinear forms (NL sub H. form, NL H. form) are none homogeneous but have some symmetry in the time axes (vertical axes) in the harmonic form and asymmetry in the sub-harmonic form.

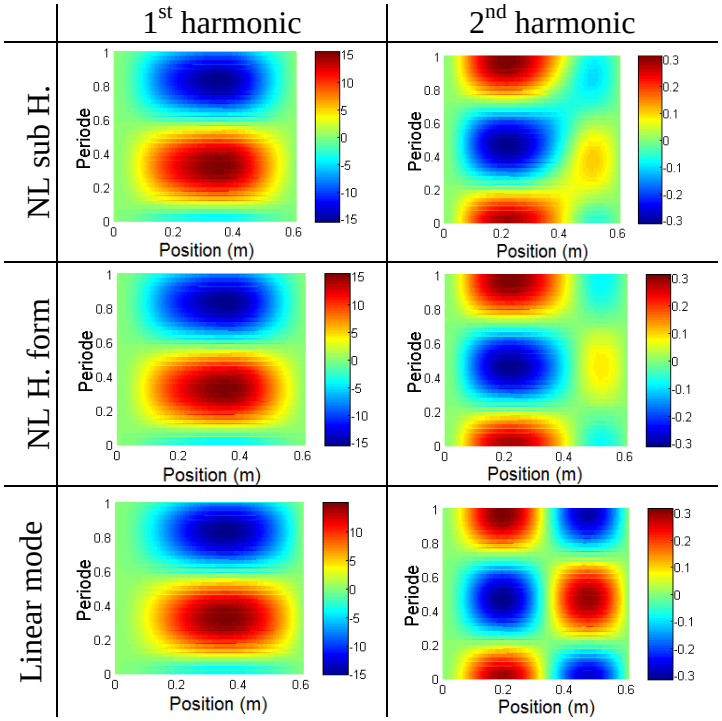

Figure 5-11 : The evaluation of the 1st and the 2nd harmonic form in one period

5.5.4 Reconstruction of accelerometer signals

Using the normal modes and the generalized coordinates it is possible to rebuild the accelerometer signals using equation (5.9), (5.17) or (5.26). In Figure 5-12, we show the response of the beam and the reconstruction of the accelerometer signals at the driving point. Compared to the approach proposed by Jalali et al. (2011), the present approaches can much better reconstruct the accelerometer signals at all levels of excitation and for all accelerometer positions.

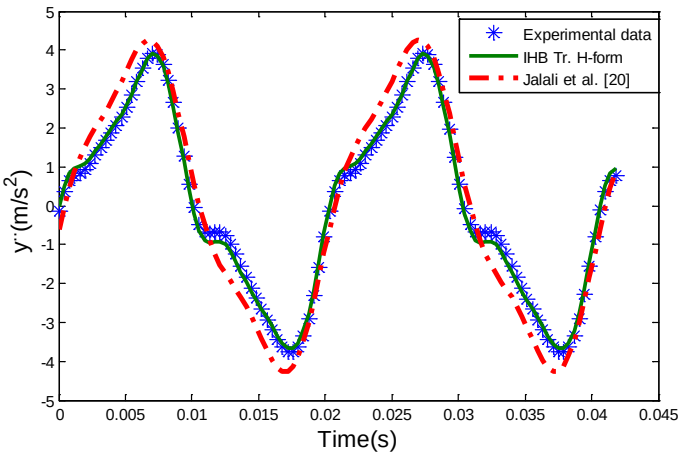

Figure 5-12 : Accelerometer signal reconstruction (F_{max} = 8 N)

In our previous works (Hadji & Mureithi, 2014a, 2014b), the signals reconstruction error of the accelerometers at the driving point and the average for all accelerometers are presented as functions of the excitation levels. Table 5-2 presents the error of the accelerometer signal reconstruction at 8N excitation force level. The inverse harmonic balance (IHB) method gives the best results in the reconstruction of the accelerometer signals in comparison with the linear approach and the Jalali et al. (2011) approach. The sub-harmonic form approach, in general, gives better results. The spline fit method gives also better result relative to the trigonometry series fit. However, the sub-harmonic form approach with the spline fitting method improves the reconstruction of the accelerometer signals with an error less than 1E-11 % (machine error).

Table 5-2 : The accelerometer signals reconstruction error (8 N excitation force level)

Specification		***Error (%)***	
		Driving point	**All Acc.**
Linear approach		12.38	4.97
Jalali et al. approach		13.88	7.96
IHB H. form	spline	5.51	2.30
	Tr. series	4.58	2.32
IHB sub-H. form	spline	5.95E-12	5.22E-12
	Tr. series	2.94	1.16

5.5.5 Friction force

Using the results of the NNMs (Figure 5-9 and Figure 5-10) and the generalized coordinates (Eqs. (5.11), (5.20) or (5.27)) together with Eqs ((5.4),(5.21) or (5.29), (5.7) and (5.8)) the friction force, velocity and the displacement at the contact point can be calculated. It is noteworthy that Jalali et al. (2011) used only the first harmonic ($i=1$ in Eq. (5.11)) in their calculations while in our previous works (Hadji & Mureithi, 2014a, 2014b), all the harmonics have been used; where it was assumed that the friction force is the average of all the harmonic effects. In more recent work (Hadji & Mureithi, 2015), it was found that any value of friction coefficient, μ_c, used produced the same friction force level. This led to a review of our previous approach.

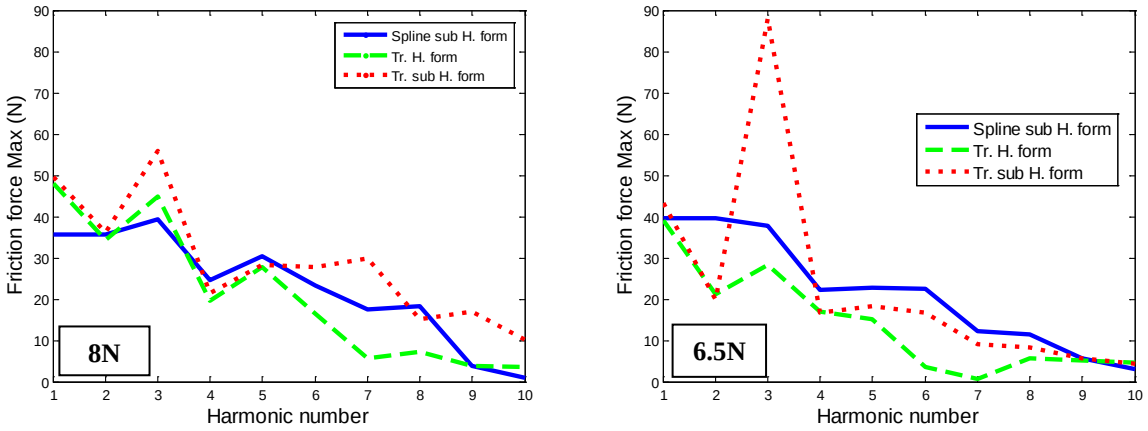

Figure 5-13 : Harmonic number effect in friction force calculation (decoupled harmonic) Firstly, we investigate the effect of the number of harmonics considered on the friction force level calculation

We observe from Figure 5-14 that the sub-harmonic approach with coupled harmonics assumption and spline fitting method is the most stable, where information from all accelerometer signals is used to calculate the friction force.

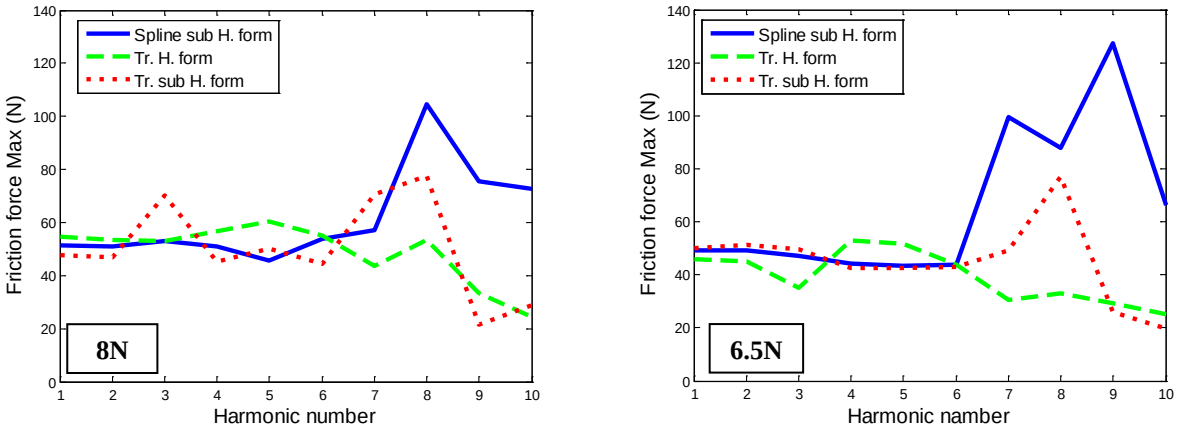

Figure 5-14 : Harmonic number effect in friction force calculation (coupled harmonic)

Table 5-3 : FFT expansion amplitude error (6.5 N excitation force level)

	Amplitude error (%)						
H.	Acc. 1	Acc. 2	Acc. 3	Acc. 4	Acc. 5	Acc. 6	Av.
H1	0,13	0,10	0,09	0,08	0,07	0,08	0,09
H2	2,04	2,45	1,73	5,71	54,16	35,46	16,92
H3	0,97	1,15	2,00	1,11	1,41	1,19	1,30
H4	21,94	22,48	20,50	21,69	21,85	19,91	21,39
H5	3,12	1,90	1,78	6,73	1,26	2,19	2,83
H6	5,83	5,09	8,49	19,82	11,25	12,71	10,53
H7	9,12	5,36	9,02	10,15	5,74	4,57	7,33
H8	41,53	87,36	58,17	64,49	71,01	39,90	60,41
H9	4,91	4,72	8,89	32,28	4,81	12,33	11,32
H10	20,55	44,13	25,37	5,26	30,22	11,90	22,91

We have next analyzed the FFT results presented in Table 5-3 and Table 5-4 for 6.5N excitation level The FFT calculations are done for different intervals of the accelerometer signals. For both excitation levels the amplitude error is around 0.1% for the first harmonic and less than 3% for the third and the forth harmonics. However, for the other harmonics the average amplitude error is larger than 8 %. The FFT phase errors are of the same order as the FFT amplitude errors. Where, the phase error is around 0.1 degree for 6.5N excitation level and 2 degrees for the 8N excitation level. This explains the harmonic number effect (error) presented previously.

Table 5-4 : FFT expansion phase error (6.5 N excitation force level)

H.	Phase error (degree)						
	Acc. 1	Acc. 2	Acc. 3	Acc. 4	Acc. 5	Acc. 6	Av.
H1	0,10	0,12	0,10	0,10	0,10	0,09	0,10
H2	18,73	20,08	17,95	7,14	42,03	39,80	24,29
H3	0,48	0,47	0,28	0,50	0,46	0,32	0,42
H4	9,57	9,09	12,92	8,86	2,58	9,16	8,70
H5	1,82	2,74	1,29	5,95	1,67	2,24	2,62
H6	17,65	20,62	19,32	22,48	22,01	20,12	20,37
H7	1,17	2,26	2,10	1,61	2,41	0,59	1,69
H8	91,33	66,25	69,10	83,00	90,53	96,40	82,77
H9	2,43	4,32	6,59	4,34	3,01	7,51	4,70
H10	48,75	31,30	8,28	33,61	46,21	13,76	30,32

Analyzing the ratio of the FFT expansion amplitude over the non-linear accelerometers limitation (FFT A_N.L.A.L) presented in Table 5-5, we observe that, if the FFT A_N.L.A.L is bigger than 0.4 the FFT errors are small; while if this ratio is between 0.4 and 0.2 the FFT errors are acceptable, but the errors are unacceptable below this value. We can conclude that if the FFT harmonic amplitude expansion is below than 20% of the non-linear accelerometers limitation the FFT expansion may contain errors even if the global signal amplitude is higher than this limitation. In this condition and with the Figure 5-13 and Figure 5-14 observations discussed above, we can use only the first three harmonics as a maximum for the decoupled harmonics method, and the first six harmonics for the coupled harmonics method. For this reason, the first five harmonics have been taken into consideration in the results that follow. In addition, the more stable approach (sub-harmonic approaches with decoupled assumption and spline fitting method) was used to identify the friction model parameters.

In Figure 5-15 and Figure 5-16, we present the friction force as a function of the speed and displacement at the contact point for 8N excitation level (at a frequency of 49.25 Hz). Corresponding results for 6.5 N excitation are excluded for brevity.

Table 5-5 : Ratio of the FFT expansion amplitude over the non-linear accelerometer limitation (6.5N excitation force level)

H.	Ratio Amplitude /N.L.A.L					
	Acc. 1	Acc. 2	Acc. 3	Acc. 4	Acc. 5	Acc. 6
N.L.A.L (m/s2)	2,94	5,88	5,88	5,88	2,94	5,88
H1	1.074	1.370	2.079	2.278	2.310	1.074
H2	0.029	0.029	0.028	0.012	0.017	0.029
H3	0.414	0.318	0.100	0.314	0.471	0.414
H4	0.171	0.124	0.016	0.123	0.018	0.171
H5	0.065	0.031	0.026	0.008	0.055	0.065
H6	0.018	0.008	0.009	0.003	0.018	0.018
H7	0.078	0.054	0.041	0.037	0.102	0.078
H8	0.004	0.000	0.002	0.002	0.001	0.004
H9	0.011	0.009	0.004	0.002	0.019	0.011
H10	0.007	0.002	0.001	0.002	0.007	0.007

N.L.A.L is Non-Linear Accelerometer Limitation

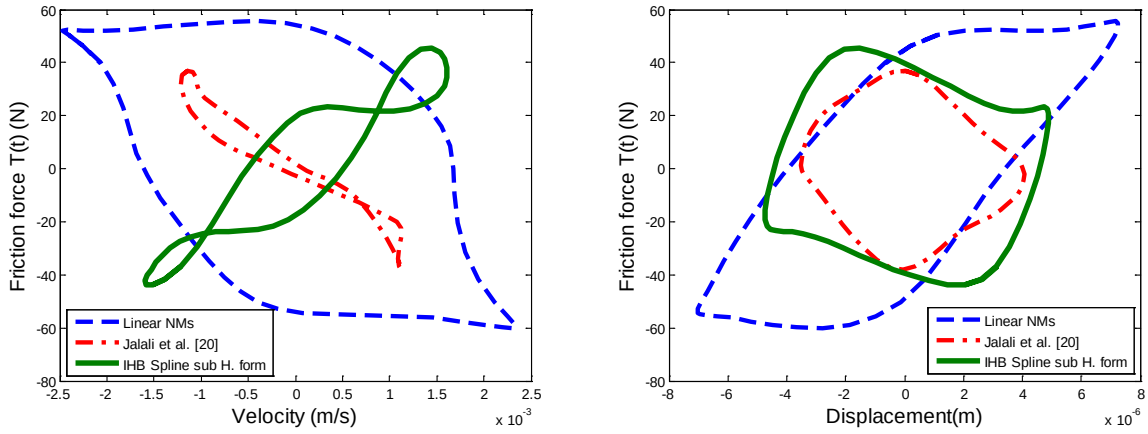

Figure 5-15 : Friction force (8N excitation force level)

In Figure 5-15, we compare the friction force calculated by IHB method with trigonometric fitting, linear normal modes and the Jalali et. al (2011) approach. The level of the friction force calculated by the conventional approach (LNMs) is the largest at all excitation force levels, by around 50N at 6.5N excitation level and 60N at 8N excitation level. The IHB method with trigonometric series fitting yields a higher friction force level than the approach proposed by

Jalali et. al (2011) at 8N excitation force level. Contrarily, at 6.5N excitation force level both approaches lead to approximately the same level of friction force around 40N.

For the IHB method result presented in Figure 5-16, the sub-harmonic form approach leads to much smaller calculated friction force levels than other approaches. This is due to the inability of the trigonometric series and the harmonic form approaches to represent all the harmonic forms accurately, specifically the first harmonic and sub-harmonic forms. This underestimation leads to poor results for this approach.

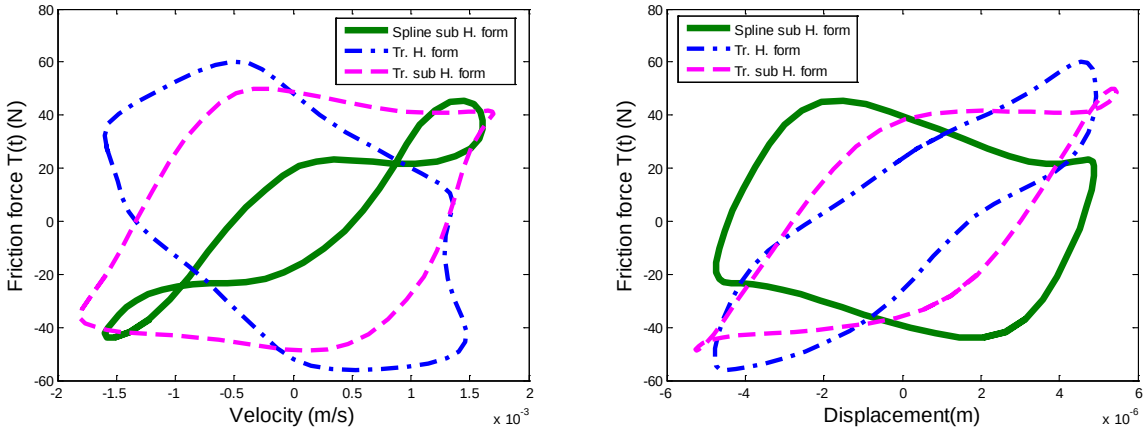

Figure 5-16 : Friction force (IHB method at 8N excitation force level)

5.5.6 Friction model parameters identification

The hybrid friction model (Azizian, 2012; Azizian & Mureithi, 2013), presented in Figure 5-17, is recently developed to model tube-support interaction, is based on the principle of the LuGre friction model (Canudas et al., 1995). All properties and benefits of other friction models are included, namely the dynamics of the Dahl friction model (Dahl, 1976) (i.e. hysteresis effect), the dynamics of bristles (Haessig Jr & Friedland, 1991) and the Stribeck effect (Stribeck & Schröter, 1903). This model also takes into account the distribution of the stresses in the contact area according to the principle of Cattaneo-Mindlin (1953).

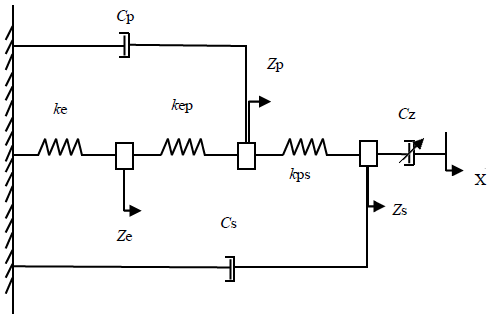

Figure 5-17 : Schematic of the hybrid friction model (Azizian, 2012)

The formulation for the friction force T in the hybrid friction model (Azizian & Mureithi, 2013) is presented in the following equations:

$$T = k_e z_e + c_p \dot{z}_p + c_s \dot{z}_s \tag{5.33}$$

$$z = z_e + z_p + z_s \tag{5.34}$$

$$k_e z_e + k_{ep}(z_e - z_p) = 0 \tag{5.35}$$

$$k_{ep}(z_p - z_e) + k_{ps}(z_p - z_s) + c_p \dot{z}_p = 0 \tag{5.36}$$

$$k_{ps}(z_p - z_s) + c_z(\dot{z}_s - \dot{x}) + c_s \dot{z}_s = 0 \tag{5.37}$$

where z_e, z_p and z_s are, respectively, the elastic, plastic and partial slip relative displacements. k_e, c_p and c_s are the coefficients of the elastic stiffness, plastic damping and pre-sliding damping, respectively. The authors considered two transition stiffness coefficients: elastic-plastic k_{ep} and plastic-pre-sliding k_{ps}. c_z is the Stribeck damping which is given by:

$$c_z = \frac{Ng(\dot{x})}{\dot{x}} \tag{5.38}$$

$$g(\dot{x}) = \left(\mu_c + (\mu_s - \mu_c)e^{-(\dot{x}/v_s)^2}\right) \tag{5.39}$$

where $g(\dot{x})$ is the Stribeck function (or Stribeck friction model (1903)), μ_c is the kinetic friction coefficient, μ_s the static friction coefficient and v_s the Stribeck velocity.

The identification of the hybrid friction model parameters is done in multiple steps using a basic friction model for each parameter; where, in general, the result of each step will be used as initial value of the optimization program in the next step. The steps of the hybrid friction model parameters identification follow:

Step 1 (Coulomb friction model): The Coulomb friction model is the most basic friction model. The classical formulation of this model is:

$$F_c = \mu_C \times R \tag{5.40}$$

$$R = N + P \tag{5.41}$$

where F_c is the kinetic friction force, P the static load to ensure permanent contact between the beam and support and R the support reaction (impact force).

The identification of the kinetic friction coefficient μ_c is obtained by direct calculation using Eq. (5.42)for the next step and by Eq. (5.43) for the 1 DOF system simulations (will be presented in the next section). The kinetic friction coefficient μ_c of Coulomb friction model is the equivalent of the static friction coefficient μ_s in the other models; only the Dahl friction model uses the same coefficient as the Coulomb friction model.

$$\mu_C = \max(T) / \max(|\mathrm{R}|) \tag{5.42}$$

or

$$\mu_C = \max(T) / |P| \tag{5.43}$$

In most of finite element method (FEM) formulations, Coulomb friction is modeled as an elastic slip in the sticking regime Eq. (5.44).; to do this one must also identify the critical displacement u_{crit} to calculate the elastic stiffness k_S from Eq. (5.45).

$$T = \begin{cases} k_s u & if \quad u \le u_{crit} \quad (\text{sticking}) \\ \mu_C N(-sig(v)) & if \quad u > u_{crit} \quad (\text{slipping}) \end{cases} \tag{5.44}$$

and

$$k_s = \frac{\mu_c N}{u_{crit}} \tag{5.45}$$

where u_{crit} is the critical displacement and k_S the elastic stiffness.

Step 2 (Dahl friction model): The Dahl friction model (Dahl, 1976) is used to identify two hybrid friction model (Azizian & Mureithi, 2013) parameters, k_e (the equivalent of the σ_0 in Dahl friction model) and μ_c . This model can be written as:

$$\frac{dT}{dt} = \sigma_0 \dot{x} - \frac{T}{F_c}\sigma_0 \left|\dot{x}\right| \tag{5.46}$$

where σ_0 is the slope of the friction force versus slip displacement curve.

Step 3 (Stribeck friction model): The Stribeck Model (Stribeck & Schröter, 1903) (Eq.(5.47)) is the second friction model used in finite element method (FEM) simulations. The general form is presented in Eq. (5.47) with the elastic slip in the sticking regime (the elastic stiffness k_S calculation by Eq. (5.48)). In this equation, δ is the Stribeck exponent equal to two in the Stribeck function used in the LuGre friction model Eq. (5.39) while it is equal to one for the decay friction model also found in FEM codes. This model is used to identify the critical displacement u_{crit} and for the Coulomb and decay friction models since it is difficult to identify this parameter using the Coulomb friction model. The Stribeck velocity v_s is identified as the critical velocity (equal to the velocity at the instant of reaching the critical displacement u_{crit}).

The friction force in the Stribeck friction mode is given by:

$$T = \begin{cases} k_s u & if\ u \le u_{crit}\ (\text{sticking}) \\ \left(\mu_c + (\mu_s - \mu_c)e^{-(v/v_s)^{\delta}}\right) N\left(-sig\left(v\right)\right)\ if\ u > u_{crit}\ (\text{slipping}) \end{cases} \tag{5.47}$$

where

$$k_s = \frac{\mu_s N}{u_{crit}} \tag{5.48}$$

and δ is the Stribeck exponent.

Step 4 (LuGre friction model): The LuGre friction model (Canudas et al., 1995), widely used in the control domain, is also based on the principal of the Dahl friction model (Dahl, 1976). This model is used to identify the three other hybrid friction model (Azizian & Mureithi, 2013) parameters. k_e and c_s which are the equivalent of σ_0 and σ_1, respectively, in the LuGre friction model (Canudas et al., 1995). μ_c, μ_s and v_s are used to identify c_z. This model can be expressed as:

$$T = \sigma_0 z + \sigma_1 \frac{dz}{dt} + \sigma_2 \dot{x} \tag{5.49}$$

$$\frac{dz}{dt} = \dot{x} - \frac{|\dot{x}|}{g(\dot{x})} z \tag{5.50}$$

where σ_0 and σ_1 are, respectively, the stiffness and damping coefficients of the bristles, σ_2 is the viscous friction coefficient and $g(\dot{x})$ is defined in Eq.(5.39).

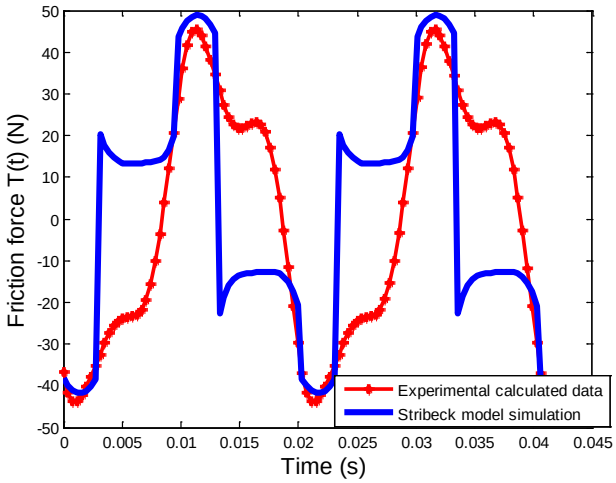

Figure 5-18 : Friction force (Stribeck model simulation)

The objective function for parameter estimation is that given in Eq.(5.51). This objective function is more useful to compare signals with different behaviors (with or without beating phenomena, offset problems or phase problems):

$$Obj = \left(\left| \max\left(T_{\exp.}\right) - \min\left(T_{\exp.}\right) \right| - \left| \max\left(T_{simul.}\right) - \min\left(T_{simul.}\right) \right| \right) / 2 \tag{5.51}$$

where Obj is the objective function, $T_{\exp.}$ the experimental friction force and $T_{simul.}$ the simulated friction force.

5.5.7 Friction model simulation results

Using the different steps presented above, the friction force model parameters are determined with the Matlab® (MathWorks, 2011) Optimization function FMINSEARCH where the objective function is that given in Eq.(51). The friction model parameters are presented in Table 6 and Table 7. The simulations results of the friction models using the identified parameters are presented in Figure 5-18, Figure 5-19 and Figure 5-20. In Figure 5-18 we present the simulation results of the Stribeck friction model (Stribeck & Schröter, 1903). While differences between the simulation and the experimental calculated forces are observed, the behavior of the friction force is similar near the maximum and the minimum levels, (slip regime only). However, for the sticking regime the behavior is completely different. This means that the Stribeck friction model (Stribeck & Schröter, 1903) only correctly represents the slip regime behavior while the elastic stiffness modification during sticking is incorrect.

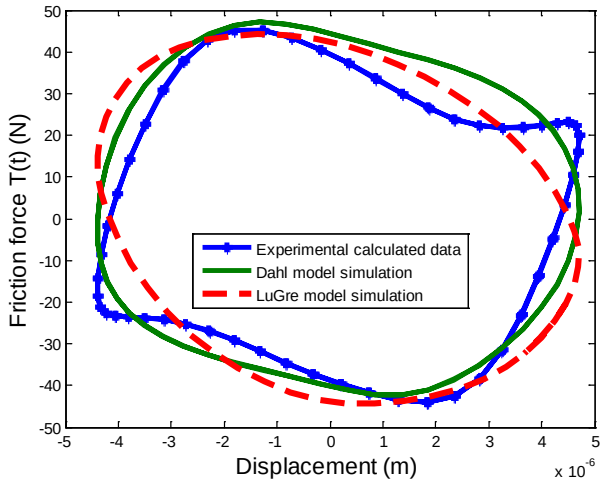

Figure 5-19 : Friction force (Dahl and LuGre models simulation)

From Figure 5-19, the LuGre friction model (Canudas et al., 1995) is seen to better represents the behavior of the friction force than the Dahl model with best offset representation. In general, however, both models have nearly the same behavior; where they both approach the experiment result. More detailed comparison between the models will be done using the Finite elements method in future work.

Table 5-6 : Friction model parameters (8 N)

Parameter	*Coulomb friction model*	*Dahl friction model*	*Stribeck friction model*	*LuGre friction model*
μ_c	0.546	0.511	0.155	0.197
μ_s	-	-	0.479	0.463
v_s (m/s)	-	-	6.797E-4	4.728E-4
u_{crit} (m)	-	-	3.845E-6	4.464E-6
σ_0 *(N/m)*	-	9.581E+6	-	1.220E+5
σ_1 *(N.s/m)*	-	-	-	27.750
σ_2 *(N.s/m)*	-	-	-	0.000

Figure 5-20 presents the simulation of the friction models using an equivalent one degree-of-freedom system model of our beam and the identified parameters presented in Table 5-7. Despite the differences in the displacement generated by the friction models, we obtain an accurate maximum value of the friction force. This result can be considered as the first validation of the friction parameters and the approaches used in the parameter identification.

Table 5-7 : Friction model parameters (6.5 N)

Parameter	*Coulomb friction model*	*Dahl friction model*	*Stribeck friction model*	*LuGre friction model*
μ_c	0.520	0.500	0.161	0.160
μ_s	-	-	0.477	0.492
v_s (m/s)	-	-	6.101E-4	7.152E-4
u_{crit} (m)	-	-	4.146E-6	4.060E-6
σ_0 *(N/m)*	-	1.003E+7	-	1.140E+4
σ_1 *(N.s/m)*	-	-	-	347.030
σ_2 *(N.s/m)*	-	-	-	0.000

Using the experimental velocity and displacement to generate the friction force is a low cost procedure for identifying the friction model parameters. Even though the behavior of the friction models in the time domain is not perfectly accurate (e.g. Figure 5-18) and despite the differences in the displacement generated by the friction models compared to experiments (Figure 5-20), using the objective function Eq.(5.51), we obtain a good agreement with the experimental results in the phase plane Figure 5-19 and an accurate maximum value of the friction force, Figure 5-20. This is an encouraging first step and a confirmation of the feasibility of the proposed approach.

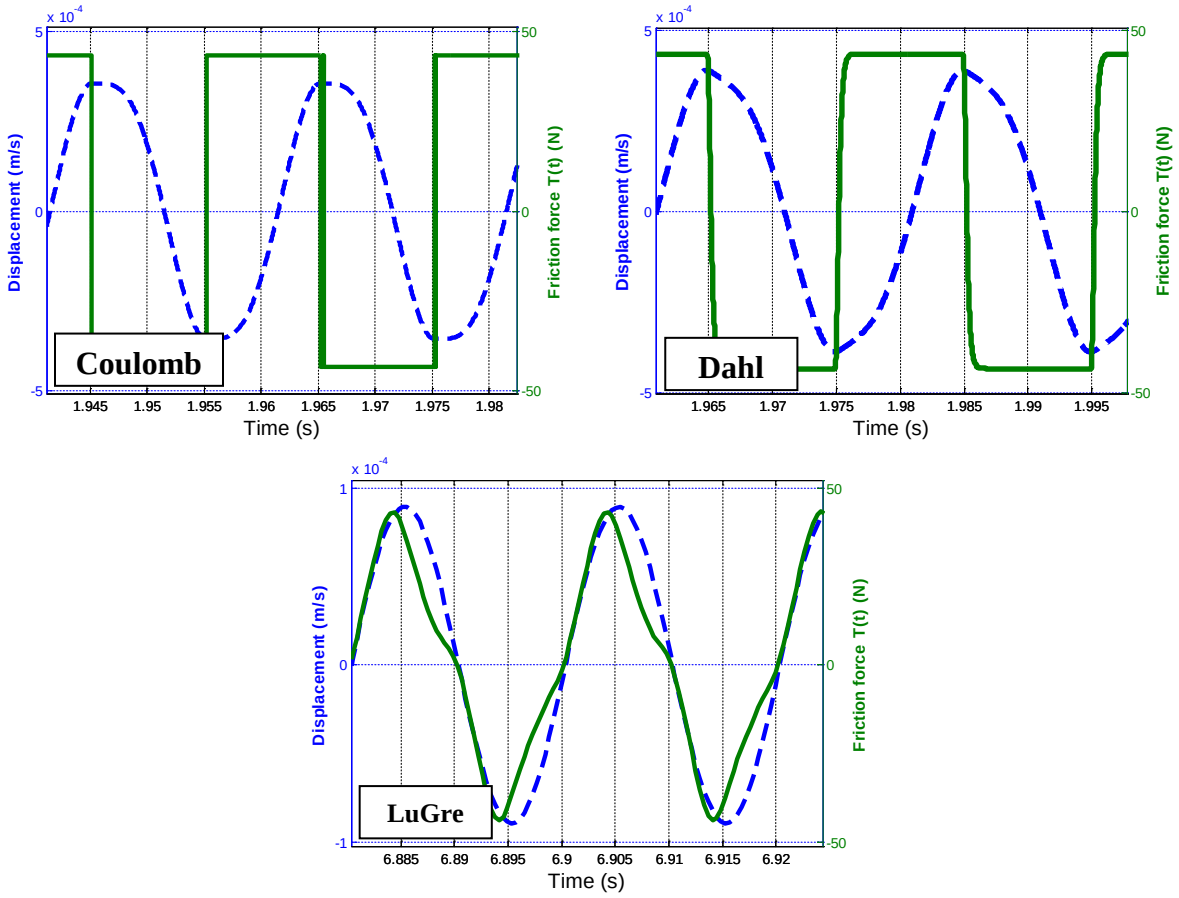

Figure 5-20 : 1 DOF friction models simulation

The identified friction model parameters for 8 N and 6.5N excitation force levels are presented in Table 5-6 and Table 5-7, respectively. For the Coulomb friction model the difference between the kinetic friction coefficients μ_c is 5% and the maximum is not far from the usual value of

$\mu_c = 0.56$ (Jalali et al., 2011). From the Coulomb friction model to the Dahl friction model the kinetic friction coefficient μ_c is reduced by 6% at 8N excitation force level and by 6% at 6.5N excitation force level; we make the same observation going from the Stribeck friction model (Stribeck & Schröter, 1903) to the LuGre friction model (Canudas et al., 1995).

5.6 CONCLUSION

The inverse harmonic balance (IHB) method is a new method based on nonlinear modal analysis developed to calculate the contact forces and the displacement at the contact point between two bodies. The method is based on the modal superposition principle and Fourier series expansion.

A coupled harmonic form was also introduced to improve the IHB method. A harmonic number analysis has been proposed to enable the choice of the optimal number of harmonics to accurately calculate the friction force. The approach based on sub-harmonic forms with spline fitting method gave the best results.

Using the experimental velocity and displacement to generate the friction force is a low cost procedure to identify the friction model parameters.

Five parameters (k_e, c_s and c_z (μ_s, and v_s)) of the Hybrid friction model (Azizian & Mureithi, 2013) have been determined using Coulomb, Stribeck (1903), Dahl (1976) and LuGre (Canudas et al., 1995) friction models. The three other parameters (c_p, k_{ep} and k_{ps}) will be determined in future work.

CHAPITRE 6 ARTICLE 2: VALIDATION OF FRICTION MODEL PARAMETERS IDENTIFIED USING THE IHB METHOD USING FINITE ELEMENT METHOD

Hadji, A., & Mureithi, N. (2016).

Submitted to “Journal of Pressure Vessel Technology” on 2016-07-20

6.1 Abstract

A hybrid friction model was recently developed by Azizian and Mureithi (Azizian & Mureithi, 2013) to simulate the friction behavior of tube-support interaction. However, identification of the model parameters remains unresolved.

In previous work, the friction model parameters were identified using the reverse harmonic method, where the following quantities were indirectly obtained by measuring the vibration response of a beam: friction force, sliding speed of the force of impact and local displacement at the contact point.

In the present work, the numerical simulation by the finite element method (FEM) of a beam clamped at one end and simply supported with the consideration of friction effect at the other is conducted. This beam is used to validate the inverse harmonic balance method and the parameters of the friction models identified previously.

Two static friction models (the Coulomb model and Stribeck model) are tested. The two models produce friction forces of the correct order of magnitude compared to the friction force calculated using the inverse harmonic balance method. However, the models cannot accurately reproduce the beam response; the Stribeck friction model is shown to give the response closest to experiments.

The results demonstrate some of the challenges associated with accurate friction model parameter identification using the inverse harmonic balance method. The present work is an intermediate

step toward identification of the hybrid friction model parameters and, longer term, improved analysis of tube-support dynamic behavior under the influence of friction.

6.2 Introduction

The friction model is an essential element in the detailed analysis of the dynamics of steam generator tubes in the nuclear industry. Most of the friction models currently used to simulate tube-support interaction are cited by (M. Hassan & Rogers, 2005). These are special cases of static friction models. The velocity limited friction model (VLFM) (Rogers & Pick, 1977) is a continuous Coulomb model without Stribeck effects (Stribeck & Schröter, 1903). The force balance friction model (FBFM) (Xi & Rogers, 1996) and the spring damper friction model (SDFM) (Antunes et al., 1988) are two models based on springs and dampers. The principle of the Karnopp friction model (Karnopp, 1985) is used in the FBFM friction model. Recently a hybrid friction model (Azizian, 2012; Azizian & Mureithi, 2013) has been developed to model tube-support interaction. In the hybrid model all the properties and benefits of other friction models are included, namely the dynamics of the Dahl model (Dahl, 1976) (i.e. hysteresis effect), the dynamics of bristles (Haessig Jr & Friedland, 1991) and the Stribeck effect (Stribeck & Schröter, 1903) (transition from the static friction limitation to the kinetic friction limitation). This model also indirectly takes into account the distribution of the stresses in the contact area according to the principle of Cattaneo-Mindlin (1953) to model the pre-sliding phenomenon.

In finite element modeling (FEM) codes, the Coulomb friction model and the decay friction model are widely used; these are combined with the principle of the velocity limit (Rogers & Pick, 1977) to model the pre-sliding (sticking) regime (ABAQUS-User's-Manual, 2013). Most of the numerical algorithms for analyzing dynamic friction in FEM codes are presented by Oden and Martins (1985). Diehl (1995) has also numerically investigated the friction effect of a circular rigid body in sliding contact with a flexible beam.

In present work, we validate the friction coefficient identified experimentally in previous work (Hadji & Mureithi, 2016) using the finite element method (FEM) by Abaqus Software.

Four standard friction model parameters have been identified by direct friction force measurement. In the present ongoing work an indirect approach, based on acceleration

measurement, has been proposed (Hadji & Mureithi, 2014a, 2014b, 2016). To identify the friction model parameters experimentally using this indirect method, accurate nonlinear normal modes are needed. Nonlinear normal modes (NNMs) and the principle of inverse harmonic balance (IHB) based on the harmonic balance (HB) method (Gilmore & Steer, 1991) were developed and presented in previous work (Hadji & Mureithi, 2014a, 2014b, 2016).

In the previous work (Hadji & Mureithi, 2014a, 2014b, 2016), the parameters of the Dahl (1976) and LuGre (Canudas et al., 1995) friction models, which are, respectively, based on Coulomb and Stribeck friction models were reported. In this paper, therefore, we analyze these two friction models to validate their friction coefficients identified also in the work (Hadji & Mureithi, 2016), where the basic friction model identified parameters have been used to identify the parameters of the more complex models.

6.3 Principle of the inverse harmonic balance (IHB) method

Figure 6-1 shows a schematic of the test rig used to extract the contact force (friction and impact) and displacement. The specimen is a beam simply supported at one end (but allowing sliding hence friction effects) and clamped at the other. In Figure 6-2 all the forces acting at the contact point are represented; for more details see (Hadji & Mureithi, 2014a, 2014b, 2016).

The beam equation of motion is:

$$\rho A\ddot{y}\left(x,t\right)+EIy''''\left(x,t\right)-T\left(t\right)y''\left(x,t\right)=F\left(t\right)\delta\left(x-X_f\right) \tag{6.1}$$

with the following boundary conditions:

$$\begin{cases} x=0:\begin{cases} y\left(0,t\right)=0 \\ y'\left(0,t\right)=0 \end{cases} \\ x=L:\begin{cases} EIy''\left(L,t\right)=\left(r+e/2\right)T\left(t\right) \\ EIy'''\left(L,t\right)=-N\left(t\right)+m\ddot{y}\left(L,t\right) \end{cases} \end{cases} \tag{6.2}$$

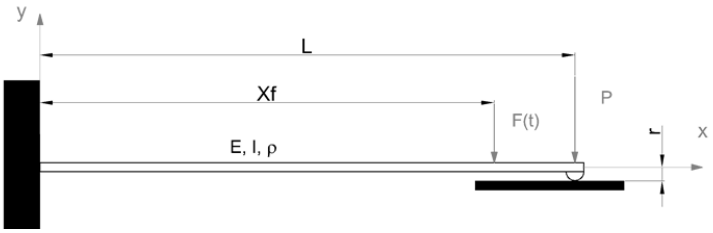

Figure 6-1 : Schematic of a nonlinear beam (Hadji & Mureithi, 2014a)

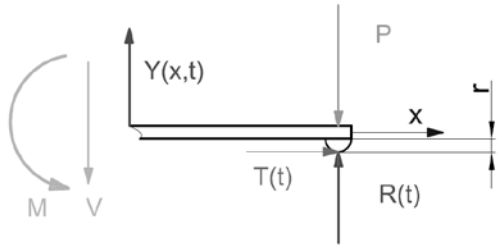

Figure 6-2 : Forces acting at the contact point (Hadji & Mureithi, 2014a)

The characteristics of the beam are presented in Table 1 below. The beam response is measured by six accelerometers, where their type and position are cited in the previous works (Hadji & Mureithi, 2014a, 2014b, 2016).

Based on modal superposition, the response of the system may be written in the following form:

$$y_j\left(x_j,t\right)=\sum_{i=1}^{n}\phi_i\left(x_j\right)q_i\left(t\right) \tag{6.3}$$

where:

$q_i\left(t\right)$ (i=1,2,...n) are the generalized coordinates

$\phi_i\left(x\right)$ (i=1,2,...n) are the normal modes of the system.

Using the modal superposition principle, Eq. (6.3), the boundary conditions equations, Eqs. (6.2) and the Galerkin method, Eq. (6.1)(1) can be rewritten as follows:

$$\ddot{q}_i\left(t\right)+\omega_i^2 q_i\left(t\right)-F(t)\tilde{\phi}_i\left(X_f\right)=-N(t)\tilde{\phi}_i\left(L\right)+$$
$$\left[r\tilde{\phi}_i{}'\left(L\right)+\sum_{j=1}^{n}q_j\left(t\right)\left(\int_0^L\tilde{\phi}_j''\left(x\right)\tilde{\phi}_i\left(x\right)dx-\tilde{\phi}_i'\left(L\right)\tilde{\phi}_j\left(L\right)\right)\right]T(t),\quad i\text{=1-}n \tag{6.4}$$

where:

$N(t) = P - R(t)$

Modal orthogonality may be expressed as follows:

$$\begin{cases} \rho A \int_0^L \tilde{\phi}_i(x,a)\tilde{\phi}_j(x,a)dx + m\tilde{\phi}_i(L,a)\tilde{\phi}_j(L,a) = \delta_{ij} \\ EI \int_0^L \tilde{\phi}_i''(x,a)\tilde{\phi}_j''(x,a)dx = \omega_i^2 \delta_{ij} \end{cases} \tag{6.5}$$

and *m* is the half cylinder mass (contact element)

In our previous work, different methods were proposed to identify the nonlinear normal modes (NNMs). Here, we present only a summary of the most accurate method, where the NNMs are computed based on the coupled sub-harmonic approach. The NNMs are calculated in the following manner:

Firstly, the Fourier series of the response signal is written as follows:

$$y_j(x_j,t) = \sum_{r=1}^{n} \alpha_{rj}(x_j)\cos(r\cdot\omega_{ext}t) + \sum_{r=1}^{n} \beta_{rj}(x_j)\sin(r\cdot\omega_{ext}t) \tag{6.6}$$

Next this equation is written as:

$$y_j(x_j,t) = \sum_{r=1}^{n} \tilde{\tilde{\phi}}_{ir1}(x_j)\gamma_{r1}\cos(r\cdot\omega_{ext}t) + \sum_{r=1}^{n} \tilde{\tilde{\phi}}_{ir2}(x_j)\gamma_{r2}\sin(r\cdot\omega_{ext}t) \tag{6.7}$$

$$\begin{cases} \tilde{\tilde{q}}_{ir1}(t) = \gamma_{r1}\cos(r\cdot\omega_{ext}t) \\ \tilde{\tilde{q}}_{ir2}(t) = \gamma_{r2}\sin(r\cdot\omega_{ext}t) \end{cases} \tag{6.8}$$

$$\begin{cases} \tilde{\tilde{\phi}}_{ir1}(x_j) = \dfrac{\alpha_{rj}(x_j)}{\gamma_{r1}} \\ \tilde{\tilde{\phi}}_{ir2}(x_j) = \dfrac{\beta_{rj}(x_j)}{\gamma_{r2}} \end{cases} \tag{6.9}$$

where, $\tilde{\tilde{\phi}}_{ir1}$ is the first sub-harmonic form (or cosines sub-harmonic form) and $\tilde{\tilde{\phi}}_{ir2}$ is the second sub-harmonic form (or sine sub-harmonic form). The modal equation of motion (Eq.(5.4)) becomes:

$$\sum_{s=1}^{n}\left(a_{rsk}\ddot{\tilde{\tilde{q}}}_{isk}(t)+a_{rsl}\ddot{\tilde{\tilde{q}}}_{isl}(t)\right)+\sum_{s=1}^{n}\left(b_{rsk}\tilde{\tilde{q}}_{isk}(t)+b_{rsl}\tilde{\tilde{q}}_{isl}(t)\right)-F(t)\tilde{\tilde{\phi}}_{irk}\left(X_f\right)=$$

$$-N(t)\tilde{\tilde{\phi}}_{irk}(L)+\begin{pmatrix}\sum_{s=1}^{n}\tilde{\tilde{q}}_{is1}(t)\int_0^L\tilde{\tilde{\phi}}''_{is1}(x)\tilde{\phi}_{irk}(x)\,dx\\+\sum_{s=1}^{n}\tilde{\tilde{q}}_{is2}(t)\int_0^L\tilde{\tilde{\phi}}''_{is2}(x)\tilde{\phi}_{irk}(x)\,dx\\-\left(\sum_{s=1}^{n}\tilde{\tilde{\phi}}'_{is1}(L)\tilde{\tilde{q}}_{is1}(t)+\sum_{s=1}^{n}\tilde{\tilde{\phi}}'_{is2}(L)\tilde{\tilde{q}}_{is2}(t)\right)\tilde{\tilde{\phi}}_{irk}(L)\\+\left(r+e/2\right)\tilde{\tilde{\phi}}'_{irk}(L)\end{pmatrix}T(t)\quad r=1\text{-}n;\qquad(6.10)$$

with *k* and *l* chosen as follows (*k*=1, *l*=2 or *k*=1, *l*=2). In the present work, *k*=1 and *l*=2 were chosen. The modal orthogonality equations Eq. (5.5) become:

$$\begin{cases}\rho A\int_0^L\tilde{\tilde{\phi}}_{isk}(x,a)\tilde{\tilde{\phi}}_{irk}(x,a)\,dx+m\tilde{\tilde{\phi}}_{irk}(L,a)\tilde{\tilde{\phi}}_{isk}(L,a)=a_{rsk}\\ EI\int_0^L\tilde{\tilde{\phi}}''_{irk}(x,a)\tilde{\tilde{\phi}}''_{isk}(x,a)\,dx=b_{rsk}\end{cases}\qquad(6.11)$$

and

$$\begin{cases}\rho A\int_0^L\tilde{\tilde{\phi}}_{isk}(x,a)\tilde{\tilde{\phi}}_{irl}(x,a)\,dx+m\tilde{\tilde{\phi}}_{irk}(L,a)\tilde{\tilde{\phi}}_{isl}(L,a)=a_{rsl}\\ EI\int_0^L\tilde{\tilde{\phi}}''_{irk}(x,a)\tilde{\tilde{\phi}}''_{isl}(x,a)\,dx=b_{rsl}\end{cases}\qquad(6.12)$$

where

$$\begin{cases}a_{rrk}=\delta_{rs}\\ a_{rrl}=\delta_{rs}\end{cases}\qquad(6.13)$$

Equations (5.27) and (5.28) are used to calculate γ_{r1} and γ_{r2} by the normalization of ϕ_{irk} from α_{rj} and β_{rj}. Equation (6.13) is used in the harmonic forms normalization.

Finally, the nonlinear normal modes $\tilde{\tilde{\phi}}_{ir1}(x)$ and $\tilde{\tilde{\phi}}_{ir2}(x)$ can be represented by a natural smoothing spline or a series of trigonometric functions (Eq.(5.24)).

$$\tilde{\tilde{\phi}}_{ir}(x) = \sum_{k=1}^{n} \begin{pmatrix} a_{ik1}\sin(\beta_{ik}x) + a_{ik2}\sinh(\beta_{ik}x) \\ +a_{ik3}\cos(\beta_{ik}x) + a_{ik4}\cosh(\beta_{ik}x) \end{pmatrix} \tag{6.14}$$

n equal to 3 minimizes the fitting error.

6.4 Numerical simulation

Coulomb and decay friction models are widely used in the finite element (FEM) software. In previous work (Hadji & Mureithi, 2015), we analyzed these two friction models and validated the friction coefficient identified experimentally in the works (Hadji & Mureithi, 2014a, 2014b) using a 1D element. The results showed that the 1D element is not a capable of modeling the contact problem with friction. But after the improvement of the inverse harmonic balance method (Hadji & Mureithi, 2016), five new parameters of the Hybrid friction model were re-identified using the new calculated experimental results. In this work, we analyze the different implementations of these models to validate the friction coefficient identified experimentally in (Hadji & Mureithi, 2016) using a plane stress element. Firstly, we present the principles and formulation of FEM friction models.

6.4.1 Coulomb friction model

In the Coulomb friction model the friction force is computed in an analytical formulation:

$$T = \begin{cases} \mu_c N\left(-sig\left(v\right)\right) & if \quad v \neq 0 \\ RT & if \quad v = 0 \end{cases} \tag{6.15}$$

where μ_c is the kinetic friction coefficient, N is the resultant of the normal forces at the contact point, v the velocity at the contact point and RT the resultant of the tangential force at the contact point in the sliding direction.

Generally, in the sticking regime, the resultant of the tangential force RT is less than the kinetic friction force $\mu_c N$. The sliding regime begins when the resultant of the tangential force reaches this limit ($RT >= \mu_c N$). This formulation is computed using Lagrange method in Abaqus (ABAQUS-User's-Manual, 2013; HKS-Inc., May 29. 2001b) (FEM software). The formulation of the Coulomb friction model using the penalty method in Abaqus is similar in form to the Karnopp friction model (Karnopp, 1985) or the velocity-limited friction model (Rogers & Pick, 1977). The latter is used to model the sticking (or pre-sliding) regime (called the "elastic slip" regime in Abaqus (ABAQUS-User's-Manual, 2013; HKS-Inc., May 29. 2001a)). The Coulomb friction model with FEM penalty formulation is given by:

$$T = \begin{cases} k_s u & if \quad u \le u_{crit} \\ \mu_c N\left(-sig\left(v\right)\right) & if \quad u > u_{crit} \end{cases} \tag{6.16}$$

and

$$k_s = \frac{T_{crit}}{u_{crit}} \tag{6.17}$$

$$T_{crit} = \mu_c N \tag{6.18}$$

where T_{crit} is the critical friction force and u_{crit} the critical elastic slip.

In general k_s or u_{crit} is defined by the user in most of FEM software. However in Abaqus there are two options to define the limiting values: Abaqus uses the same option (k_s or u_{crit} is defined by the user) or by the automatic u_{crit} calculation during the simulations using the formula:

$$u_{crit} = F_f \bar{l}_i \tag{6.19}$$

where $\bar{l}_i$ is the characteristic contact surface length and F_f is the slip tolerance (default value, $F_f = 0.005$ (ABAQUS-User's-Manual, 2013)).

The slip tolerance F_f is defined also as the maximum allowable 'elastic slip' (pre-sliding displacement), expressed as a fraction of a characteristic length. The characteristic length is the average length of the contact surface elements (half cylinder). The value of 0.5% is considered typical and used by default in the code. Alternatively, an absolute value (e.g. based on known experimental values) of the characteristic length may be specified. Note that 'elastic slip' is, strictly, not slip at all but rather refers to pre-sliding relative displacement between the contact surfaces. The relative surface displacement is possible due the contact area asperities which deform elastically without breaking. Gross slip occurs when the asperities break.

6.4.2 Decay friction model (Stribeck friction model)

The decay friction model is a special case of the Stribeck friction model (Stribeck & Schröter, 1903) (Eq.(6.20)), with the exponent δ is equal to one. Equation (6.20) represents the general Stribeck friction model (Stribeck & Schröter, 1903) in the slip regime. However, in the pre-sliding (or elastic slip) regime, the friction force takes the same value in the Eqs. (6.16) to (6.18) with the replacement of μ_c by μ_s in these equations (6.16) and (6.18).

$$T = N\left(\mu_C + (\mu_s - \mu_C)e^{-(v/v_s)^{\delta}}\right)\left(-sig\left(v\right)\right) \tag{6.20}$$

where μ_s is the static friction coefficient, v_s is the Stribeck velocity and δ is Stribeck exponent.

To validate the friction model parameters using the FEM code, we must validate the other parameters used as well as the contact algorithms (surface to surface or nodes to surface) and the slip tolerance F_f. In the present work the surface-to-surface contact algorithm with the hard contact model is considered. One of the important parameters investigated is the slip tolerance F_f.

6.4.3 Finite element modeling

In the previous work (Hadji & Mureithi, 2015) a 1D FEM model (Figure 6-4-A) was used to validate the friction coefficient identified experimentally in the works (Hadji & Mureithi, 2014a, 2014b), where this model was compared and validated using the 2D and 3D models. However, in this work, the beam of Figure 6-1 is modelled by 2D elements FEM model (Figure 6-4-B). Then, in conjunction with the friction models presented above it is used to validate the friction coefficient identified experimentally in the previous work (Hadji & Mureithi, 2016). The beam is discretized using 2D plane strain elements. The validation of this model is done using a different mesh stages analysis. In the first stage, a cantilever beam end deflection, a modal analysis and a calculation times (model size) have used to choose the element type and size. However, only the modal analysis and the calculation times (model size) have used in the mesh method and the elements size choice of the half cylinder element (contact element). The results of this analysis are presented in Figure 6-3 and Figure 6-5. The description of the elements presented in legend of those figures is defined in Table 6-1.

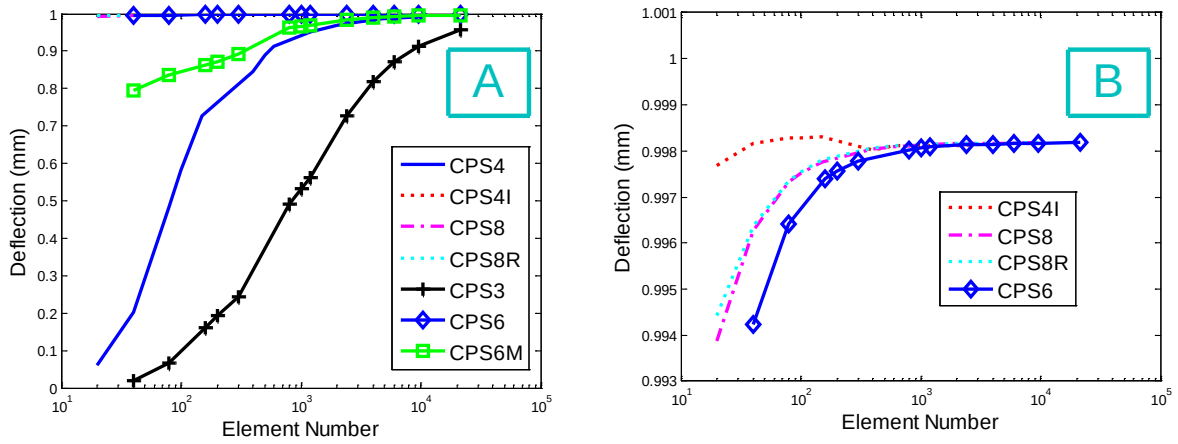

Figure 6-3 : Cantilever beam end deflection, (B) is the zoom of the superimposed lines in the figure (A)

In general, the triangular elements are the most used to mesh the cylindrical form because geometrically is the most appropriate form. On the other hand, we have solved the problem of the quadrilateral elements incompatibility of this type of geometry by dividing the circular section of the cylinder by four. That signifies that, for our contact element (half cylinder) it should be dividing in two parts (two quarter of cylinder), see Figure 6-4-B.

Those analyses are necessary in this work to optimize our model mesh to reduce the simulation time. For example, using our optimal mash (Figure 6-4-B), the time simulation for each iteration (one frequency excitation of 1.2 second using direct implicit dynamic integration) take 90 minutes using PC of (CPU of Intel i7 3GHz, 24Gb of memory). That mean, to obtain one case of parameters analysis result take 30 hours.

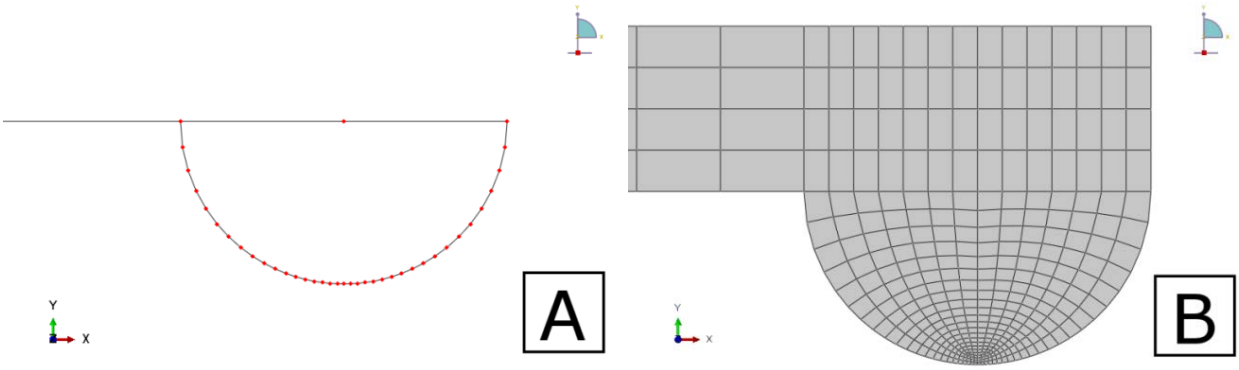

Figure 6-4 : Beam meshing, (A) is the 1D model, (B) is the 2D model

Table 6-1 : Abaqus plane strain elements type

Element symbol	***descriptions***
CPS4	4-node bilinear quadrilateral element
CPS4R	4-node bilinear quadrilateral element with reduced integration
CPS4I	4-node bilinear quadrilateral with incompatible modes
CPS8	8-node biquadratic quadrilateral element
CPS8R	8-node quadrilateral biquadratic element with reduced integration
CPS3	3-node triangle bilinear
CPS6	6-node triangle biquadratic
CPS6M	6-node modified biquadratic triangle element

From the Figure 6-3 and Figure 6-5 we can see the quadrilateral elements gave best result then triangular elements. In both case (cantilever beam end deflection, a modal analysis), the CPS4I (4-node bilinear quadrilateral with incompatible modes) is the best of all other element for both objectives. For that we this element type has chosen to model the beam and the half cylinder (the

contact element). The tringle element form is the most used to model the cylindrical structure. In the half cylinder element (contact element) meshing analysis, the solutions adopted to get the best results are: 1- divide the half cylinder in to part to be able to use the CPS4I element in this geometry, 2- the space ratio must be less than two to optimize the number of element with bias mesh controller concentered in the contact zone.

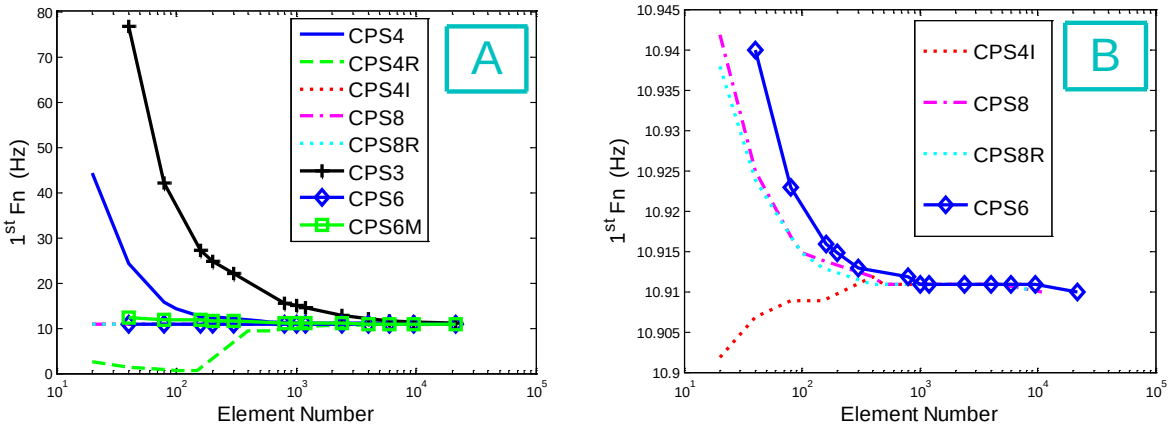

Figure 6-5 : 1st natural frequency, (B) is the zoom of the superimposed lines in the figure (A)

The characteristic of the finite element beam model are presented in Table 6-2.

Table 6-2 : Finite element beam model characteristic

Property	*Symbol*	*Quantity*	*units*
Young's modulus	E	210	GPa
Density	ρ	7800	kg/m^3
Length	L	606	mm
Width	l	38.88	mm
Thick	e	4.78	mm
Radius	r	5	mm
Damping ratio	ζ_1	0.01	%
Proportional mass damping	α_1	0.06	
Normal force	N	83	N
Excitation force amplitude	F_{ex}	6.5	N

The friction model parameters are presented in Table 6-3. The parameters μ_c, μ_s and v_s were identified experimentally using the Dahl friction model (Dahl, 1976) and LuGre friction model (Canudas et al., 1995). These models are detailed in the previous works (Hadji & Mureithi, 2014a, 2014b, 2016). The objective function previously used for parameter identification is that given in Eq.(6.21). Optimization based on an objective function is used to validate the simulation results here as well.

Table 6-3 : Friction model parameters (6.5 N) (Hadji & Mureithi, 2016)

Parameter	*Coulomb friction model*	*Dahl friction model*	*Stribeck friction model*	*LuGre friction model*
μ_c	0.520	0.500	0.161	0.160
μ_s	-	-	0.477	0.492
v_s (m/s)	-	-	6.101E-4	7.152E-4
u_{crit} (m)	-	-	4.146E-6	4.060E-6
σ_0 *(N/m)*	-	1.003E+7	-	1.140E+4
σ_1 *(N.s/m)*	-	-	-	347.030
σ_2 *(N.s/m)*	-	-	-	0.000

All the results are obtained at the excitation force amplitude of 6.5 N.

$$Obj = \left(\left| \max\left(T_{\text{exp.}}\right) - \min\left(T_{\text{exp.}}\right) \right| - \left| \max\left(T_{suml.}\right) - \min\left(T_{suml.}\right) \right| \right) / 2 \tag{6.21}$$

where Obj is the objective function, $T_{\text{exp.}}$ the experimental friction force and $T_{suml.}$ the simulated friction force.

A proportional (Rayleigh) damping is used to simulate the beam structural damping. The mass proportional damping coefficient α_n is given by the following equation:

$$\alpha_n = 2\omega_n \zeta_n \tag{6.22}$$

where ω_n is the angular natural frequency of mode n and ζ_n the corresponding damping ratio.

The value of the damping ratio ζ in Table 6-2 is identified experimentally using an impact test and the logarithmic decrement method.

6.4.4 PARAMETER VALIDATION

All the results of the simulation are obtained using Abaqus software version 6.12-3, with 1.2 second simulation time, 1E-4 second fixed time step using the implicit integration method. 8E-4 increment save time has chosen to optimize the simulation time. Which mean, only one value of eight time increment are saved in database file to reduce his size. Two models were tested; the Coulomb friction model with two different formulations, Lagrange and Penalty formulations, and the decay friction model. We begin by presenting the modal analysis results.

Table 6-4 presents the first resonance frequency. The simulations using the two Coulomb (Lagrange and penalty) models give approximately equal first resonance frequencies (difference of 0.2 Hz); the predicted frequencies are around 3Hz higher than the experimental result. However, the decay friction model is closest to the experimental results when compared to the Coulomb models. For the resonance frequency, the Lagrange formulation is better than penalty formulation, while the decay friction model frequencies are the closest to the experimental values.

Table 6-4 : 1st resonance frequency

Test	***1st resonance frequency(Hz)***
Experimental	50
Coulomb – Lagrange formulation	52.8
Coulomb – penalty formulation	53
Decay friction model	51.6

In the following figures, from Figure 6-6 to Figure 6-12, the simulations of two cases for each Coulomb friction model formulation are presented. For the Lagrange formulation the simulation

of the two friction coefficients identified via Coulomb and LuGre friction models (Table6-3) are presented. However, for the penalty formulation we present the simulation results obtained using the friction coefficient identified via Coulomb model with two values of the slip tolerance (Ff): the default value (0.005) and the optimal value (0.0015) identified during this analysis using the beam response envelope validation criteria.

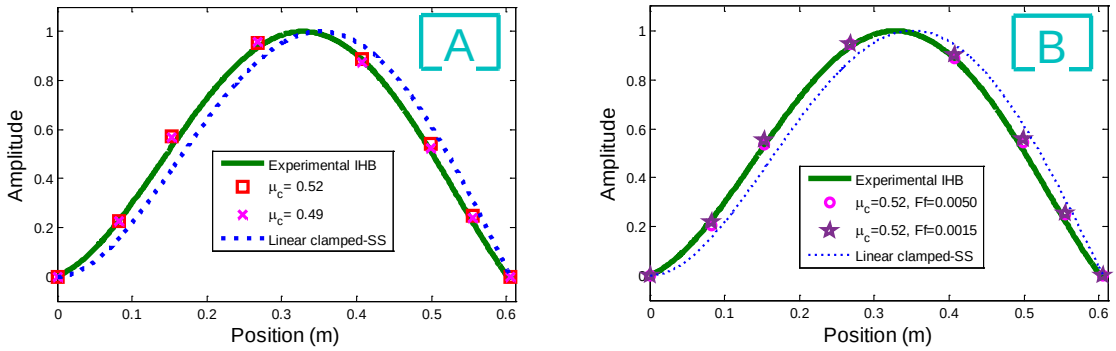

Figure 6-6 : 1st nonlinear normal mode, a- Lagrange formulation b- penalty formulation

Figure 6-6 presents the first nonlinear normal mode (NNM). Simulation results are compared with the experimental normal modes identified using the inverse harmonic balance method (IHB) and the linear normal mode (LNM) of the clamped-simply supported beam. The simulation results of both friction models have approximately the same NNMs; the NNM form is also very close to the first NNM identified experimentally using the IHB. However, the NNM of the simulation results using the penalty formulation are even closer to the experiments NNM compared to the Lagrange formulation results.

Note that while the simulated 1st nonlinear modes (NNMs) appears similar to the experimental NNM, the small difference is important; the mode spatial derivatives are particularly critical for accurate determination of the friction dynamics at the contact point; this is evident in Eq. (5.29). Hence, even though the NNMs look similar; these slight differences lead to significantly different responses (see Figure 6-7).

To better compare the results, we can use data showing in the Figure 6-7. In this figure, the beam response envelopes (maximal deflection) using both formulations of the Coulomb friction model are presented. From Figure 6-7-A, Coulomb friction model with Lagrange formulation, we find

that the friction coefficient identified using LuGre model $\mu_c = 0.49$ yields the closer result to experiment than the value identified using the Coulomb friction model. Contrary wise, for the penalty formulation (Figure 6-7-B), the value identified using the Coulomb friction model ($\mu_c = 0.52$) gave the best results but with the optimal value of the slip tolerance $\left(F_f = 0.0015\right)$. The default value of the slip tolerance is unable to produce the correct results.

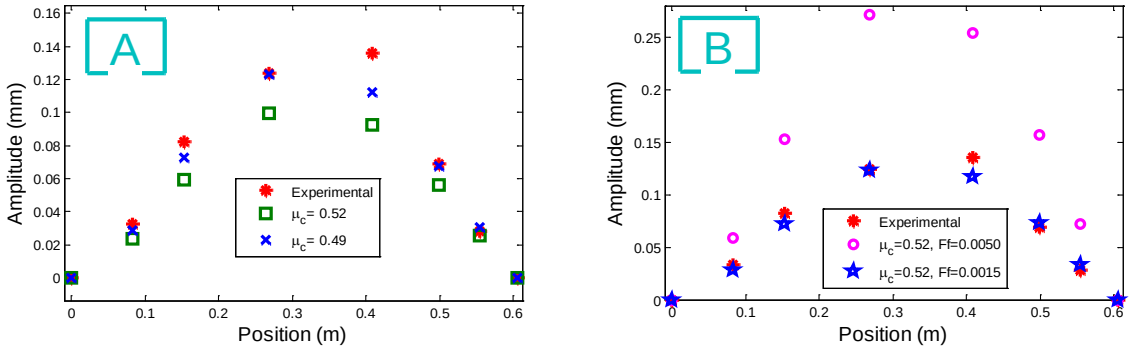

Figure 6-7 : Beam response envelope (deflection maximal), a- Lagrange formulation b- penalty formulation

For more details for the beam response, the frequency response (FRF) of the system at the driving point (position 555 mm from the clamped end) are presented in Figure 6-8 for the Coulomb and decay friction models. Similarly to Figure 6-7 observations, where the case with $\mu_c = 0.49$ for Coulomb friction model with Lagrange formulation (Figure 6-8-A) and the case with $\left(\mu_c = 0.52,\ F_f = 0.0015\right)$ for penalty formulation (Figure 6-8-B) are the closest results to the experimental response, where those two cases can be considered as the optimal cases (optimal parameters) for each model formulation.

From Figure 6-8, we can also observe that the penalty formulation gives smooth system response (without multiple-resonance peaks), in the interval 45-56 Hz, comparatively to the Lagrange formulation, where this phenomenon is not observed experimentally in the 45Hz interval up to the second naturel frequency (160 Hz). However, for both formulations there are other resonances above 56 Hz (while not presented in the results, we can see the beginning of a second possible resonance after the 1st natural frequency in Figure 6-8-B. Furthermore, the experimental

response occurs over a wider frequency bandwidth. The large response predicted by the Coulomb friction model with both formulations shows that the models do not correctly capture the energy dissipation due to friction. This is partly expected due to the known inadequacies of the Coulomb friction model.

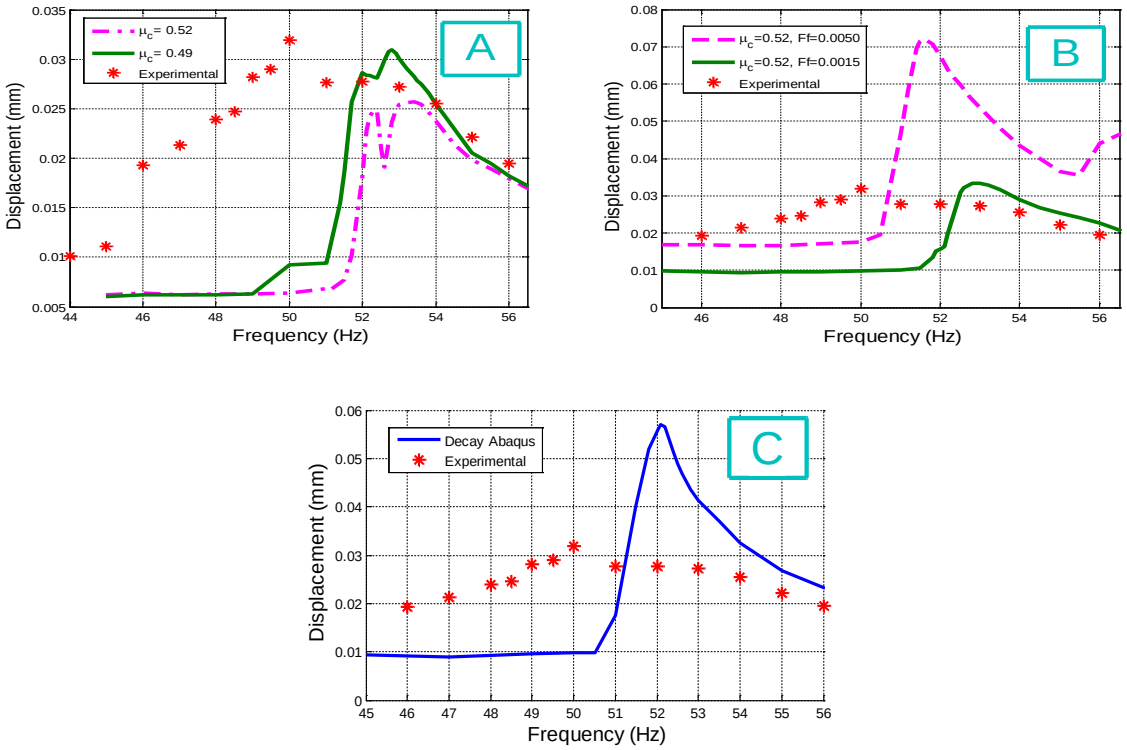

Figure 6-8 : FRF at driving point, Coulomb friction model (a- Lagrange formulation and b-penalty formulation), c- decay friction model

Note, however, that there is gradual improvement in the predictive behavior between the more basic Coulomb and the improved decay friction model. The preliminary result of decay friction model peak frequency is closer to the experimental value than Coulomb model (Table6-3); however the beam response amplitude (Figure 6-8-C) is higher than the experimental result. The results of Figure 6-8-C are obtained using the optimal parameters of the penalty formulation $\left(\mu_s = 0.52,\ F_f = 0.0015\right)$ and the optimal value of $\mu_c = 0.16$ presented in Table6-3 from the previous work (Hadji & Mureithi, 2016) with Abaqus decay friction model. In the next step, a complete analysis of the decay and Stribeck models must be done to improve our decay user subroutine.

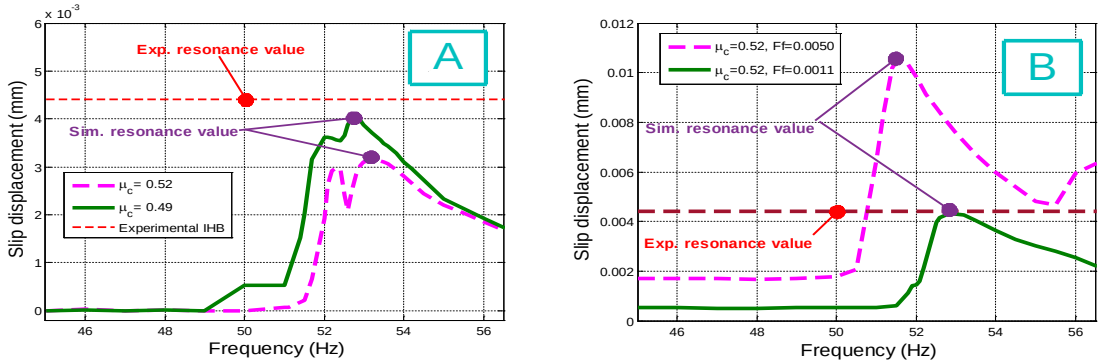

Figure 6-9 : Slip displacement, a- Lagrange formulation b- penalty formulation

Figure 6-9 and Figure 6-10 present the Slip displacement and slips velocity at the contact point. For both formulations, the simulated resonance slip displacement (Figure 6-9) of the optimal parameters defined above: $\left(\mu_c = 0.49\right)$ for Lagrange formulation and $\left(\mu_c = 0.52,\ F_f = 0.0015\right)$ for penalty formulation, leads to the closest values to experimental results. However, all the simulated resonance slip velocity at the contact point (Figure 6-9), for both formulations, are bigger than the experimental value. This may come from the integration and the derivative methods used in Abaqus and/or due the inability of the Coulomb friction model to represent the real behavior of friction especially in the sticking condition. Thus for both formulations at low frequencies below the resonance, the system is in the sticking condition (zero slip displacement for the Lagrange formulation and slip displacement equal to the critical displacement for the penalty formulation). For the higher frequencies above the 1st resonance frequency, the slip displacement (Figure 6-9) values are closer to the experimental value. The slip velocity (as shown in Figure 6-10) for the Lagrange formulation results is higher than the penalty formulation results. Both formulations thus give higher results with the penalty formulation being 1.5 times the experimental value.

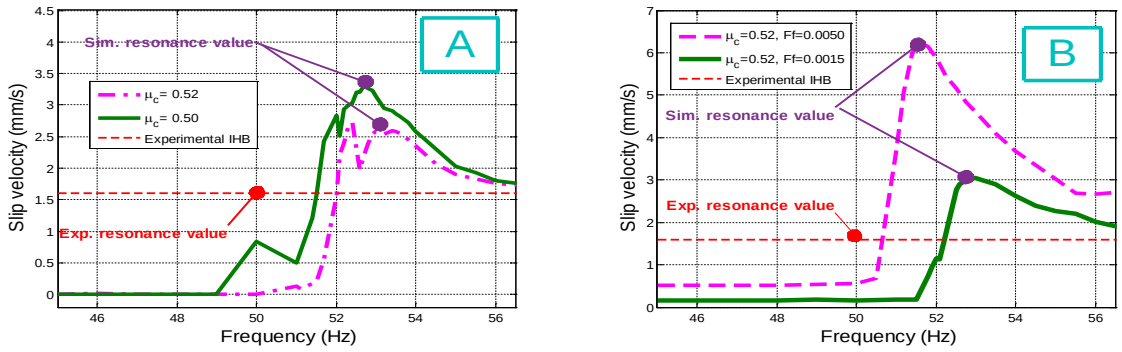

Figure 6-10 : Slip velocity, a- Lagrange formulation b- penalty formulation

We can also make the same observations in Figure 6-7, where for the beam frequency response at the driving point, for the low frequencies, the different between the simulations and the experimental results are quite large. However, for the higher frequencies (above the resonance frequency), there is a good match between the simulations and the experimental results. We conclude that, the Coulomb friction model is valid and applicable only for the cases with slipping conditions. Despite the penalty formulation improvement of the Coulomb friction model accuracy remains insufficient to represent the real behavior of the sticking or pre-sliding condition.

Figure 6-11 and Figure 6-12 present the contact force, tangential (friction force) and normal results. The friction force results, Figure 6-11, support the conclusion above for both formulations. The simulated friction force levels at the resonance frequency have closest values to the experimental results when the optimal parameters defined above are used. However, the simulated normal force levels obtained using the optimal parameters (Figure 6-12) at the resonance frequency are slightly higher than the experimental values, with an error of 4.39N (4.93%) for the Lagrange formulation and 3.56 N (4%) for the penalty formulation. Thus, even when the results of the friction force, the system response and the slip displacement are close to the experimental values, both formulations of the Coulomb model lead to slightly difference values for the normal force. The continuity of the penalty formulation slightly improves the normal force result compared to the discontinuity of the Lagrange formulation.

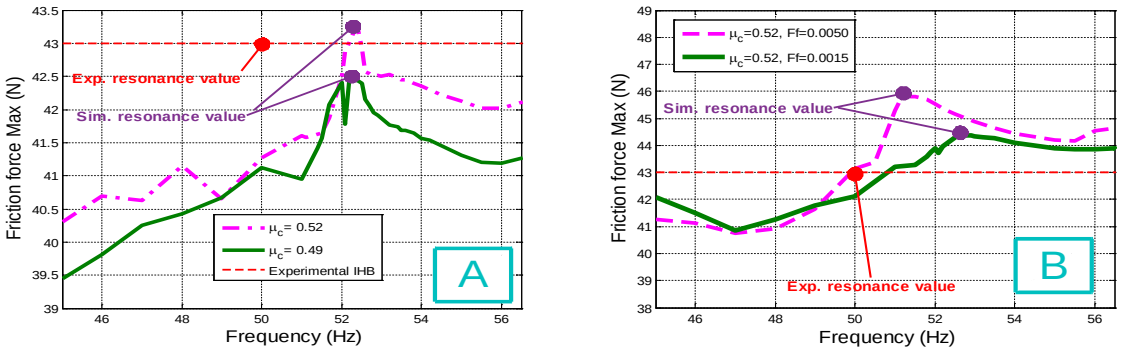

Figure 6-11: Friction force, a- Lagrange formulation b- penalty formulation

Finally, we can use these results (Figure 6-8, Figure 6-9 and Figure 6-11) to obtain the optimal Coulomb friction model parameters for the FEM model. The optimal parameters are (F_f between 0.0015 - 0.005 with $\mu_c = 0.52$) for the penalty formulation. For the Lagrange formulation and is μ_c less than 0.49 for the response system validation criteria and between 0.52 - 0.49 for the others validation criteria. Note, in conclusion, the accurate optimal parameters of the different Coulomb friction model formulation affect the system response, the friction force and the slip displacement with the same manner differently to the normal force.

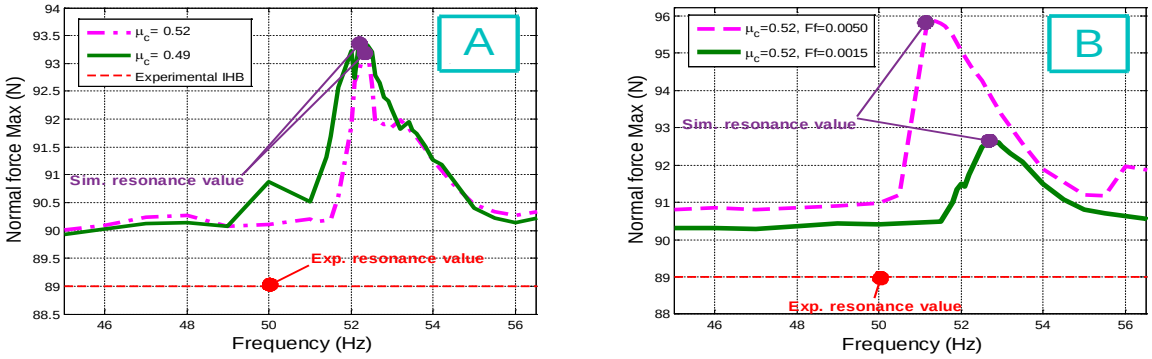

Figure 6-12 : Contact normal force, A- Lagrange formulation, B- penalty formulation

6.4.5 PARAMETER SENSITIVITY ANALYSIS

In this section we investigate the parameter sensitivity of both Coulomb friction model formulations. In Figure 6-13 to Figure 6-18, we present the simulation results using the parameters of the two cases presented in Figure 6-6 to Figure 6-12 plus other cases near the optimal parameters of both formulations. However, we present only the figures (or the validation criteria) where the parameters variation effect is clear. Furthermore, the sensitivity of the two parameters in the penalty formulation is presented separately: figure B for the slip tolerance F_f analysis and figure C for the friction coefficient μ_c analysis.

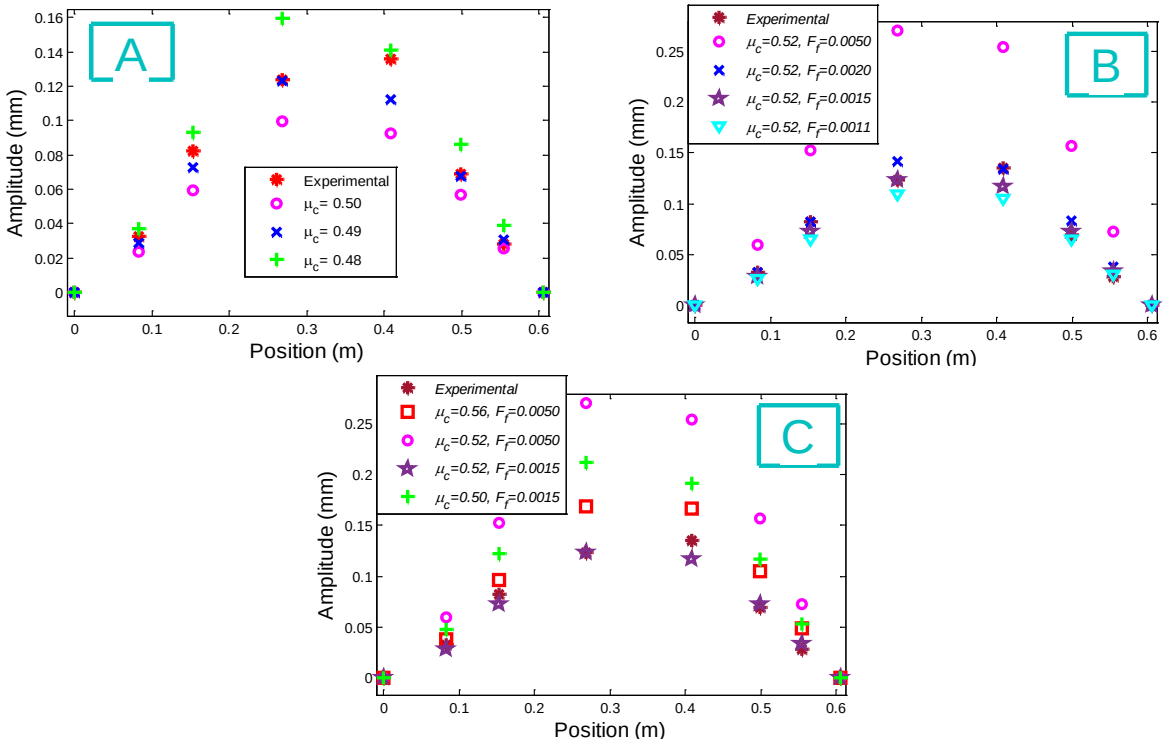

Figure 6-13 : Beam response envelope (deflation maximal), (A) Lagrange formulation, penalty formulation: (B) F_f sensitivity and (C) μ_c sensitivity)

In the Lagrange formulation (Figure 6-13-A), when the optimal parameter ($\mu_c = 0.49$) is increased by 2%, the beam response envelope decreases by 17% relative to the optimal parameter

response. However, the beam response envelope increases by 28% of the optimal parameters response when μ_c is decreased by 2% below the optimal value $\mu_c = 0.49$.

For the penalty formulation (Figure 6-13-B and C), firstly, the slip tolerance F_f sensitivity was tested by fixing the friction coefficient μ_c at 0.52 (Figure 6-13-B). It was found that the beam response envelope increased with increasing slip tolerance F_f (while means with increasing critical displacement u_{crit}). Additionally, it was noted that the optimal slip tolerance F_f could be improved within the interval (0.0011 to 0.0015) by using the experimentally identified $\mu_c = 0.52$. The friction coefficient μ_c sensitivity was also tested (Figure 6-13-C) by fixing the slip tolerance F_f to two values: by the default value $(Ff = 0.0050)$ and the optimal value $(Ff = 0.0015)$. These two cases are analyzed to understand the behavior of the μ_c variation. It was found that the beam response envelope increased by decreasing μ_c for both cases.

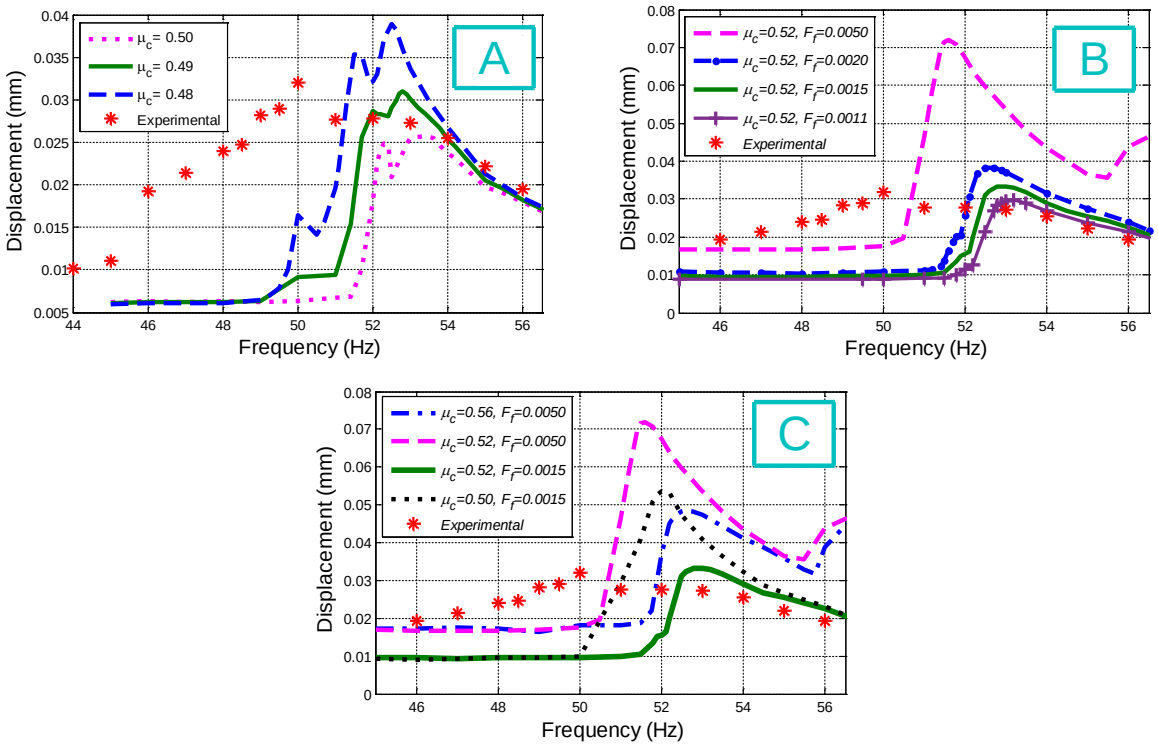

Figure 6-14 : FRF at driving point, (A) Lagrange formulation, penalty formulation: (B) Ff sensitivity and (C) μ_c sensitivity

The same approach was used to analyse the other criteria presented in the Figure 6-13 to Figure 6-18.

For the following two criteria: FRF at driving point (Figure 6-14) and slip displacement (Figure 6-15), the observations of the parameters sensitivity are similar to the beam response envelope (Figure 6-13) where, the simulation result values increase with decreasing μ_c for both criteria using both formulations (figures A and C in Figure 6-14 and Figure 6-15) and the simulated values increase with increasing F_f for the penalty formulation. Furthermore, for the penalty formulation, using the slip tolerance optimal value $F_f = 0.0015$, the simulation result approaches the experimental value, unlike the case using the default value $\left(F_f = 0.0050\right)$, with the appearance of a multi resonance, confirming the stability response of the slip tolerance F_f optimal value.

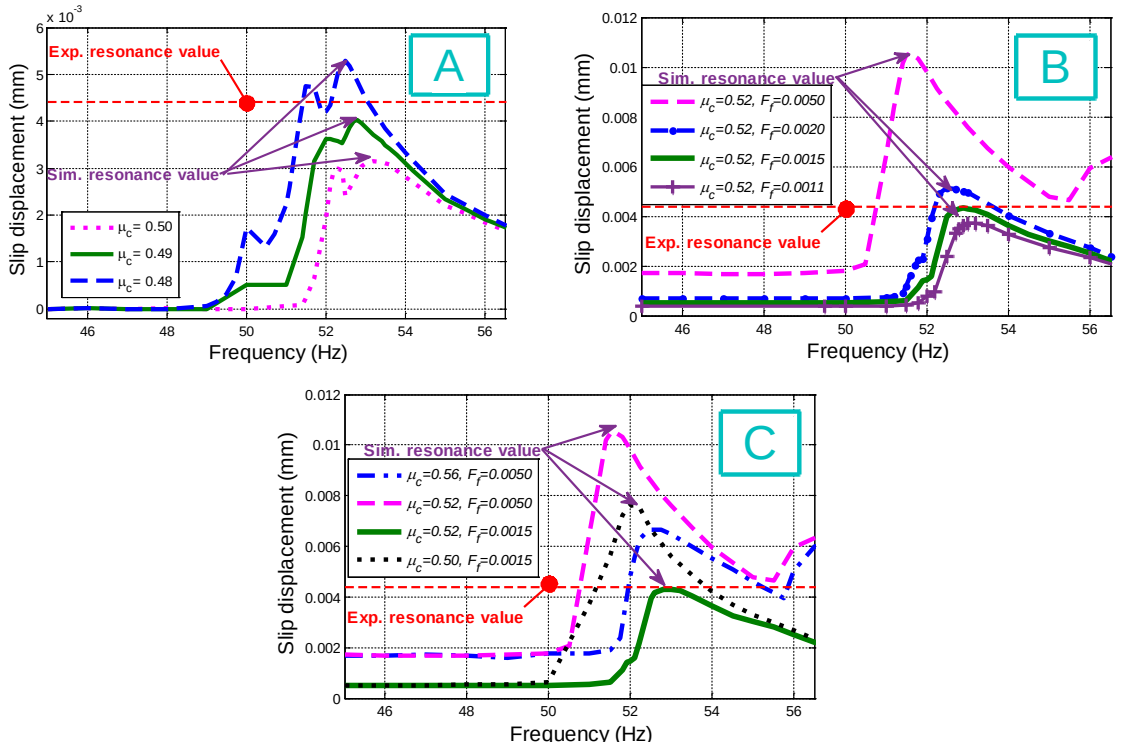

Figure 6-15 **:** Slip displacement, (A) Lagrange formulation, penalty formulation: (B) *Ff* sensitivity and (C) μ_c sensitivity

For the slip velocity criteria (Figure 6-16), the observations of the parameters sensitivity are similar as the FRF at driving point (Figure 6-14) and slip displacement (Figure 6-15) for the penalty formulation (Figure 6-16 B and C). However, for the Lagrange formulation the simulated slip tolerance (Figure 6-16-A) behaves differently around the optimal friction coefficient value $(\mu_c = 0.49)$. The simulated value increas away from the experiment at value for increasing or decreasing friction coefficient μ_c. This is another confirmation that $\mu_c = 0.49$ is the optimal value for the Lagrange formulation.

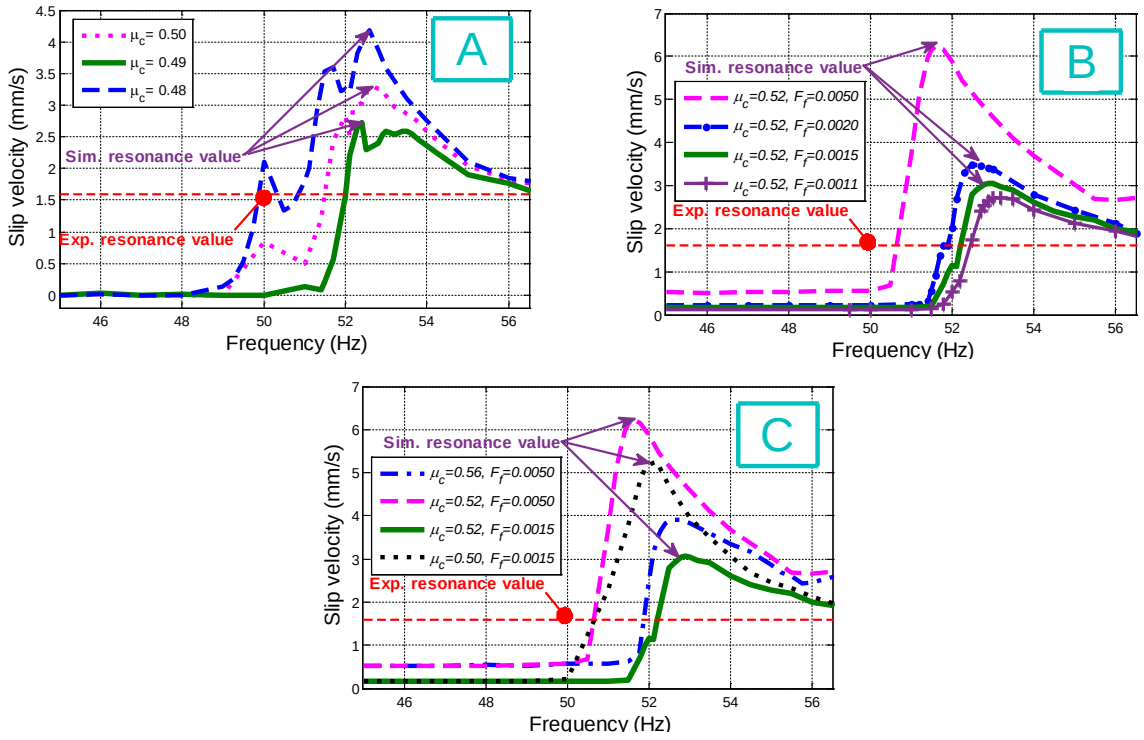

Figure 6-16 : Slip velocity, (A) Lagrange formulation, penalty formulation: (B) F_f sensitivity and (C) μ_c sensitivity

For the following two criteria: the friction force (Figure 6-17) and the normal force (Figure 6-18), the simulation values decrease for decreasing μ_c in the Lagrange formulation (figures A in Figure 6-17 and Figure 6-18) and also by decreasing F_f using the penalty formulation (figures B in Figure 6-17 and Figure 6-18). Furthermore, for the penalty formulation using default slip

tolerance F_f leads to values far from the experiments, there is small different for the values around the optimal value $F_f = 0.0015$. For the penalty formulation, the friction force (Figure 6-17-C) increase with decreasing the friction coefficient μ_c. However, the normal force (Figure 6-18-C) decrease with decreasing μ_c using the optimal value $\mu_c = 0.52$ lead to get the closest value to experiment for both criteria.

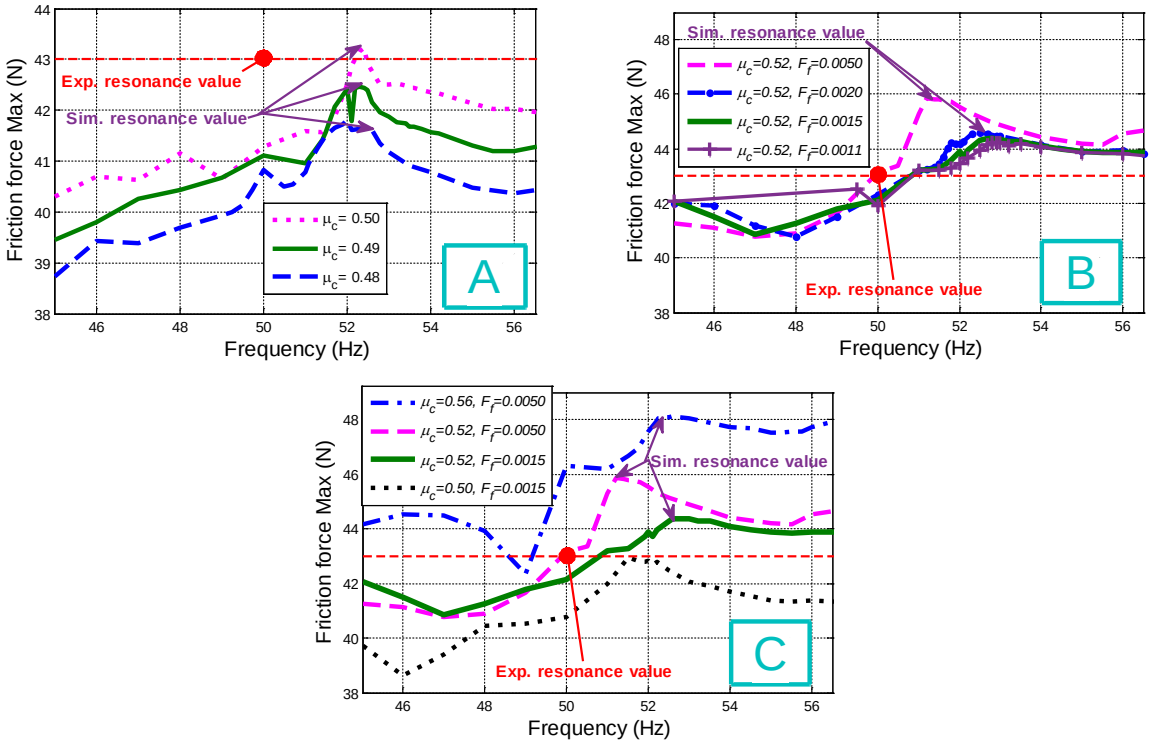

Figure 6-17 : Friction force obtained from: Lagrange formulation (a), penalty formulation (b- F_f sensitivity and c- μ_c sensitivity)

Finally, we conclude from this analysis that, using the optimal parameter values, ($\mu_c = 0.49$ for the Lagrange formulation and $F_f = 0.0015$ with $\mu_c = 0.52$ for the penalty formulation, yields the smoothest (the most stable) simulated results and the closest to experimental values for the six validation criteria presented above. This validates and confirms the accuracy of the friction model parameters identified using the inverse harmonic balance method IHB with LuGre model for Lagrange formulation and with Coulomb friction model for the penalty formulation. We can

conclude also that, the accurate optimal parameters of the different Coulomb friction model formulations affect the system response, the slip displacement and the slip velocity in the same manner. The friction force and normal forces are affected differently.

We can use the results of Figures (Figure 6-7 to Figure 6-18) to obtain the best (optimal) Coulomb friction model parameters for the FEM model. The optimal parameters are for F_f between 0.0015 - 0.0020 with $\mu_c = 0.52$ for penalty formulation and μ_c between 0.48 - 0.49 for the Lagrange formulation.

The friction coefficient identified experimentally using Coulomb model is the optimal value for the penalty formulation of Coulomb model. However for the optimal value for the Coulomb model with Lagrange formulation is the friction coefficient identified experimentally using LuGre friction model. This can be generalised only after testing different cases in future work.

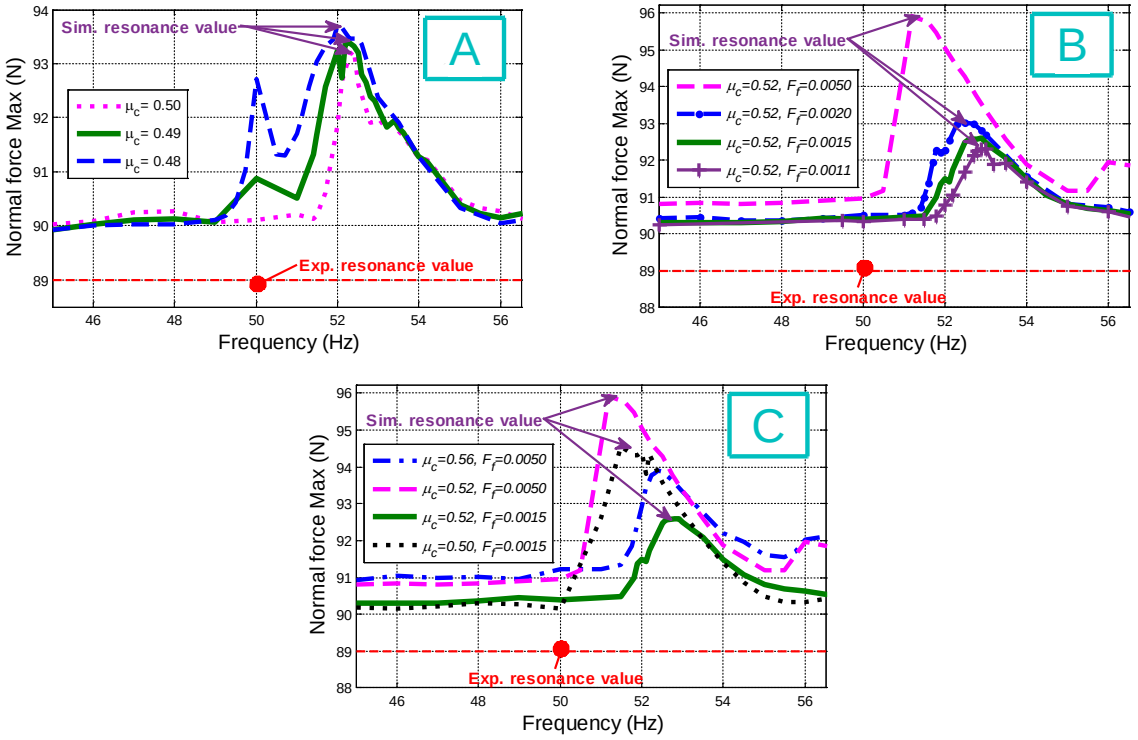

Figure 6-18 : Contact normal force, (A) Lagrange formulation, penalty formulation: (B) F_f sensitivity and (C) μ_c sensitivity

Modeling the Stribeck effect also significantly improves the resonance frequency prediction. The next step involves moving to more sophisticated models – the Dahl, LuGre and eventually the

Hybrid friction models. Prior to this, the role played by the numerical implementation of these models in the FEM codes needed to be verified. This is important because the implementation of the friction models in FEM codes is not mathematically trivial and involves adjustments and additional parameters.

Finally, a word concerning the slip displacement; this displacement is an important quantity used to calculate the work rate, Eq.(6.23). The slip displacement value at the contact point is plotted versus frequency in Figure 6-9 and Figure 6-15 for the Coulomb model. The values of the slip displacement generated by the Coulomb friction model are close to the experiment at resonance and too small (even equal to zeros for the Lagrange formulation) for the frequencies lower than the resonance frequency. This leads to smaller computed work rates compared to the experimental values in this frequency interval.

$$\dot{W} = \frac{\int_0^t N(t).\dot{u}(t)d\tau}{\int_0^t d\tau} \tag{6.23}$$

where

$\dot{W}$ is work rate,

$N(t)$ is normal force,

$\dot{u}(t)$ is sliding velocity,

t is duration of contact.

This paper presents intermediate results in a longer term project on hybrid friction model parameter identification and validation using the friction models used to create this friction model.

As presented in the previous works (Hadji & Mureithi, 2016), five parameters of the hybrid friction model are identified using Dahl (1976) and LuGre friction models (Canudas et al., 1995). Some of these parameters are the same as those of the Coulomb and decay (Stribeck) friction model. Starting then with these simpler models, some of the challenges associated with FEM

based parameter identification have been highlighted. Importantly, it is clear that friction models, as implemented in commercial FEM codes, should be used with caution. When quantities intimately related to the details of the friction model are considered, the resulting physical outputs maybe significantly affected and far from true values. The slip tolerance is an adjustable parameter that is found in the numerical friction models. This parameter has, however, been found to have little effect on the computed friction force and displacement when physically realistic values are used.

The Hybrid friction model (Azizian, 2012; Azizian & Mureithi, 2013) Figure 6-19 is based on the principle of the LuGre model (Canudas et al., 1995). All properties and benefits of other friction models are included, namely the dynamics of the Dahl model (Dahl, 1976) (i.e. hysteresis effect), the dynamics of bristles (Haessig Jr & Friedland, 1991) and the Stribeck effect (Stribeck & Schröter, 1903). This model also takes into account the distribution of the stresses in the contact area according to the principle of Cattaneo-Mindlin (1953) to model the pre-sliding phenomenon.

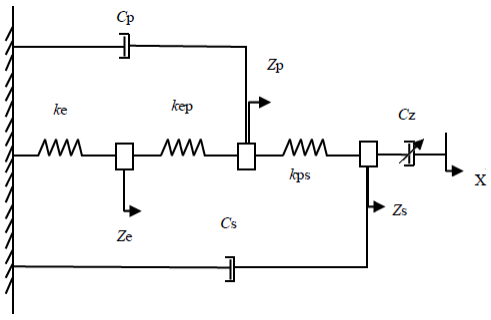

Figure 6-19 : Schematic of the hybrid friction model (Azizian, 2012)

The formulation of the hybrid friction model (Azizian, 2012) is represented in the following equations:

$$T = k_e z_e + c_p \dot{z}_p + c_s \dot{z}_s \tag{6.24}$$

$$z = z_e + z_p + z_s \tag{6.25}$$

$$k_e z_e + k_{ep}(z_e - z_p) = 0 \tag{6.26}$$

$$k_{ep}(z_p - z_e) + k_{ps}(z_p - z_s) + c_p \dot{z}_p = 0 \tag{6.27}$$

$$k_{ps}(z_p - z_s) + c_z(\dot{z}_s - \dot{x}) + c_s \dot{z}_s = 0 \tag{6.28}$$

where z_e, z_p and z_s are, respectively, the elastic, plastic and partial slip relative displacements. The pre-sliding or the sticking regime is modeled by elastic stiffness k_e, plastic damping c_p and pre-sliding damping c_s and two transition stiffness coefficients: elastic-plastic k_{ep} and plastic-pre sliding k_{ps} the slip regime is modeled by the coefficients of the Stribeck damping c_z which is given by:

$$c_z = \frac{\sigma_0 g(\dot{x})}{\dot{x}} \tag{6.29}$$

$$\sigma_0 g(\dot{x}) = N\left(\mu_C + (\mu_s - \mu_C)e^{-(\dot{x}/v_s)^2}\right) \tag{6.30}$$

where

$g(\dot{x})$ is Stribeck function (or Stribeck friction model (Stribeck & Schröter, 1903))

μ_c is kinetic friction coefficient

μ_s is static friction coefficient

v_s is Stribeck velocity

6.5 CONCLUSION

This paper presents the first step to validate, using 2D shell FEM elements, the parameters identified in previous work (Hadji & Mureithi, 2016) using the inverse harmonic balance method results and the basic models of the Hybrid friction model.

The accuracy of the friction model parameters identified using the inverse harmonic balance method (IHB) with the LuGre model are validated using Lagrange formulation. The parameters identified with Coulomb friction model are validated using the penalty formulation. The accuracy of the optimal parameters of the different Coulomb friction model formulations affect the system response, the slip displacement and the slip velocity in the same manner but differently from the friction and normal forces.

Both models produce friction forces, normal forces and slip displacements of the correct order of magnitude compared to the friction force calculated using the inverse harmonic balance method at the resonance frequency. However, their FRF bandwidths are significantly far from the experimental results. Furthermore, Coulomb and decay friction models yield modal parameters (resonance frequency and NNMs) that are close to those of the experiments. The decay friction model yields the result closest to experiments for the NNMs and resonance frequency.

The Coulomb friction model is valid and applicable only for cases with slipping conditions. Despite the improvement gained using the penalty formulation in the Coulomb friction model, it remains insufficiently accurate to represent the real physical behavior for sticking or pre-sliding condition.

The present work demonstrates that both static friction models produce results closest to the experiments at the resonance in the slipping regime, but are incapable of accurately representing all the behaviors of friction, especially in the sticking regime, ultimately leading to incorrect work rate estimates in the complete frequency range. The results presented here represent a part of ongoing work aimed at modeling the detailed physics underlying friction.

CHAPITRE 7 DISCUSSION GÉNÉRALE

(An english translation of this chapter is provided in the appendix Annexe F)

Dans ce chapitre, on présente quelques résultats et discussions complémentaires du Chapitre 5. On y présente les nouveaux résultats obtenus suite à l'amélioration de la méthode de balance harmonique inversée (IBH) avec l'utilisation de l'approche de non-orthogonalité de forme et sous-forme harmonique. À la fin, on présente quelques remarques avec la discussion générale.

7.1 Résultats complémentaires de Chapitre 5

Dans le Chapitre 5 (1er article), on présente les trois premières formes harmoniques (Figure 5-9 et Figure 5-10) et leurs évaluations dans une période (Figure 5-11) pour le niveau d'excitation de 8N utilisé dans le calcul de la force de frottement présenté dans la Figure 5-15 et la Figure 5-16.

De la Figure 7-1, nous pouvons voir des résultats similaires que aux trois premières formes harmoniques (Figure 5-9 et Figure 5-10), où, les formes harmoniques sont proches de l'une des formes de sous-harmoniques (les deux sous-harmoniques formes égales) si les fréquences harmoniques sont proches des fréquences naturelles, par exemple (H4 = 200Hz et la seconde fréquence naturelle F_{n2} = 160 Hz, H6 = 300 Hz et la troisième fréquence naturelle F_{n3} = 319 Hz). L'évolution des modes linéaires dans une période (Figure 7-4) est homogène et symétrique, contrairement pour aux deux formes harmoniques pour la réponse non-linéaire. Les formes harmoniques et les formes sous-harmoniques ne sont pas homogènes, mais il y a une symétrie légère dans l'axe de temps (axe vertical) pour les formes harmoniques avec une asymétrie pour les formes sous-harmoniques.

Ce comportement est le même que celui des formes harmoniques (Figure 7-1) et leur évaluation dans une période pour (Figure 7-2) pour le niveau d'excitation de 6.5N est présentée dans l'Annexe C. Donc, on peut conclure que ce comportement est général pour toutes les réponses non linéaires indépendamment des niveaux d'excitation.

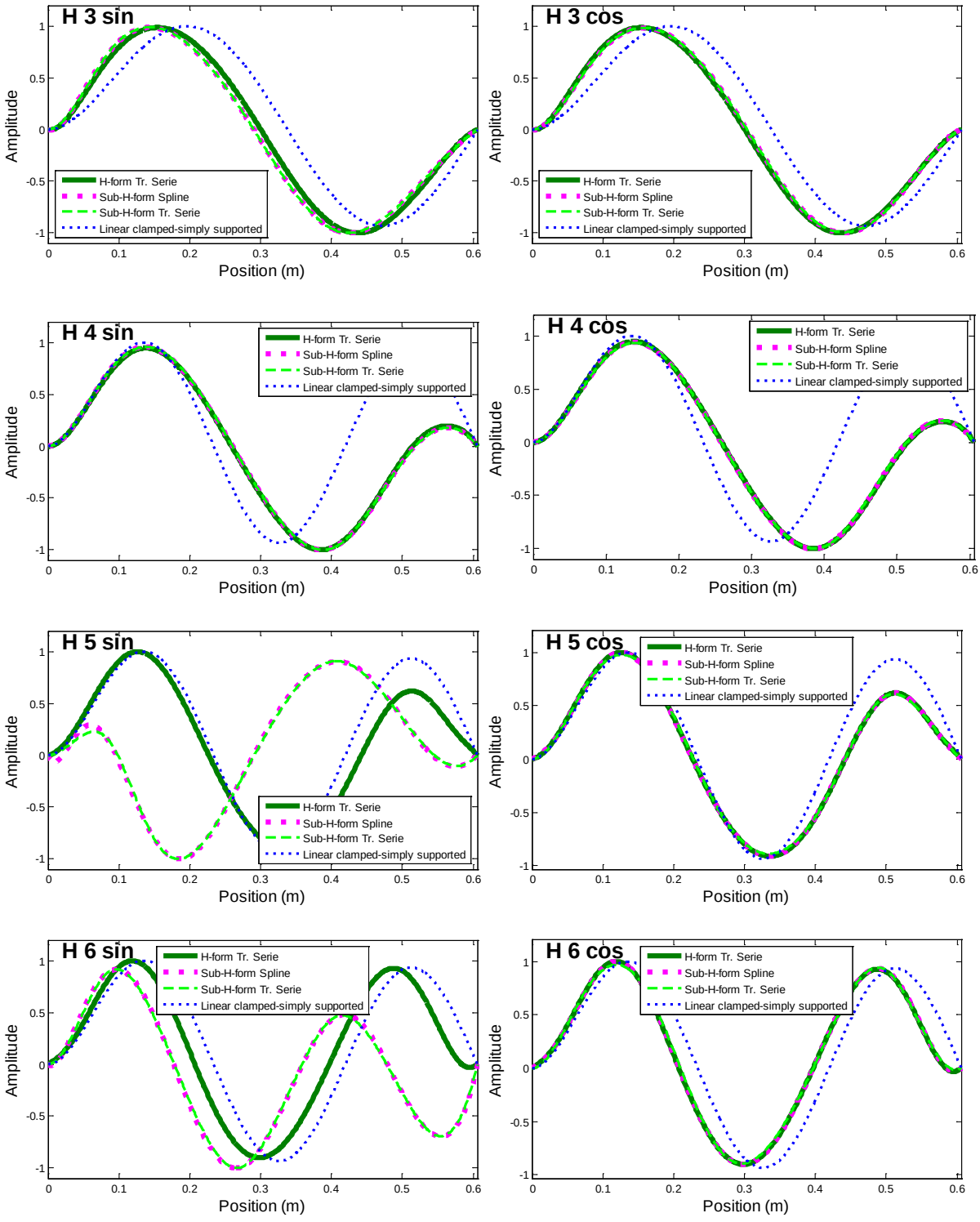

Figure 7-1 : Les formes harmoniques et sous harmoniques à niveau d'excitation de 8N

Pour le niveau d'excitation de 6.5N, la force de frottement en fonction de la vitesse et le déplacement présenté dans la Figure C–7 Annexe C (obtenu par l'application de la méthode BHI avec l'approche des formes harmoniques découplées) ont été recalculés en appliquant la méthode BHI avec l'approche des formes harmoniques couplées. Le nouveau résultat est présenté dans la Figure 7-2 et la Figure 7-3 et a été utilisés pour la réidentification des paramètres de modèles de frottement présentés dans le Table 5-7.

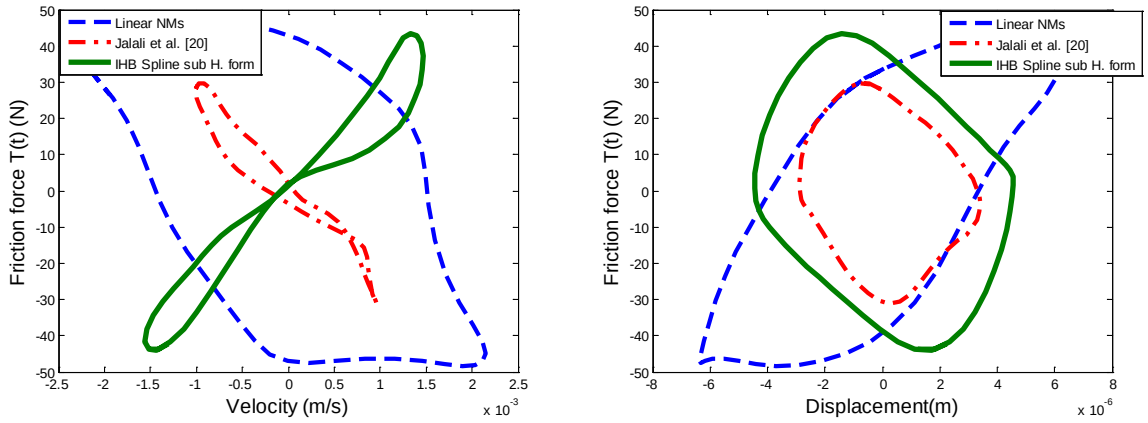

Figure 7-2 : Friction force (6.5N excitation force level)

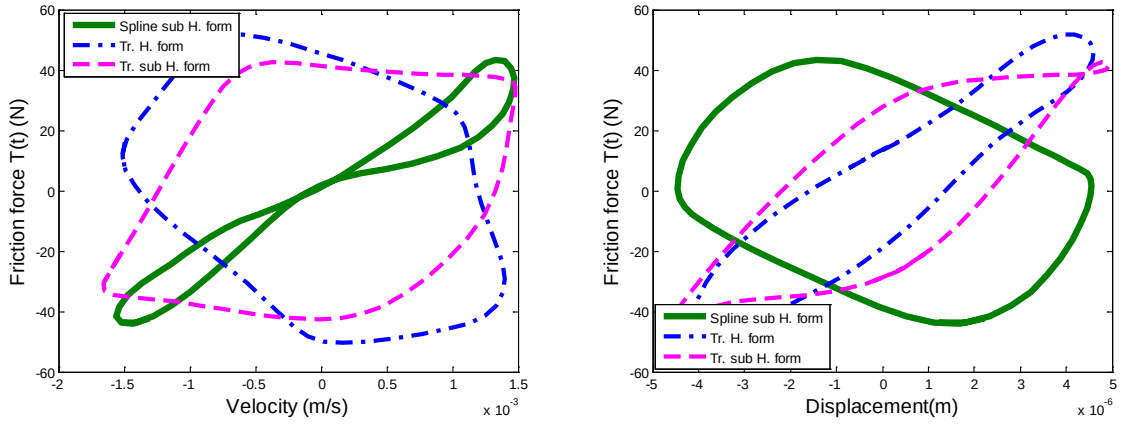

Figure 7-3 : Force de frottement (la méthode IHB niveau d'excitation de 6,5N)

L'analyse des résultats de la FFT sont présentés dans les tableaux (Table 5-3, Table 5-4 et Table 5-5) pour le niveau d'excitation de 6,5N. Pour compléter et généraliser cette analyse, les résultats pour le niveau d'excitation de 8N sont présentés dans les tableaux (Tableau 7-1,

Tableau 7-2 et Tableau 7-3). On peut dire que, pour les deux niveaux d'excitation, l'erreur d'amplitude est de l'ordre de 0,1% pour la première harmonique et inférieure à 3% pour le troisième et le quatrième harmoniques. Cependant, pour les autres harmoniques, l'erreur d'amplitude moyenne est supérieure à 8%. Les erreurs de phase de la FFT sont du même ordre que les erreurs d'amplitude de la FFT. Cela explique l'effet de nombre harmonique sur la précision de calcul de la force de frottement en utilisant la méthode de BHI présentée précédemment dans les figures (Figure 5-13 et Figure 5-14).

Tableau 7-1 : Erreur d'amplitude de la FFT (niveau d'excitation de 8 N)

H.	Amplitude error (%)						
	Acc. 1	Acc. 2	Acc. 3	Acc. 4	Acc. 5	Acc. 6	Av.
H1	0,32	0,32	0,32	0,33	0,33	0,32	0,32
H2	11,35	11,94	10,41	3,40	24,20	21,43	13,79
H3	0,96	1,02	1,12	1,14	1,19	1,14	1,09
H4	7,99	7,80	11,01	7,67	5,71	8,35	8,09
H5	2,04	2,40	1,28	4,30	0,51	0,71	1,87
H6	17,16	15,53	16,87	42,11	19,98	17,57	21,54
H7	11,75	4,24	8,33	15,21	5,06	1,49	7,68
H8	18,24	12,73	17,09	20,89	22,73	19,23	18,49
H9	3,87	2,67	9,70	9,09	2,35	3,09	5,13
H10	23,80	29,00	29,85	14,21	28,46	51,03	29,39

Tableau 7-2 : Erreur de phase de la FFT (niveau d'excitation de 8 N)

H.	Phase error (degree)						
	Acc. 1	Acc. 2	Acc. 3	Acc. 4	Acc. 5	Acc. 6	Av.
H1	2,00	2,00	2,00	2,01	2,00	2,01	2,00
H2	4,42	4,51	4,63	9,35	6,64	4,56	5,68
H3	6,02	6,03	6,02	6,04	6,04	6,03	6,03
H4	9,18	9,20	9,36	9,17	10,29	8,93	9,35
H5	5,96	9,92	7,60	9,91	8,25	5,79	7,91
H6	10,75	8,14	12,67	14,67	7,38	12,00	10,93
H7	14,52	14,21	14,31	14,22	14,14	13,67	14,18
H8	15,21	14,68	15,32	15,01	15,09	15,81	15,19
H9	17,73	17,82	18,57	17,70	17,75	17,41	17,83
H10	20,11	20,10	14,21	19,95	20,14	21,37	19,31

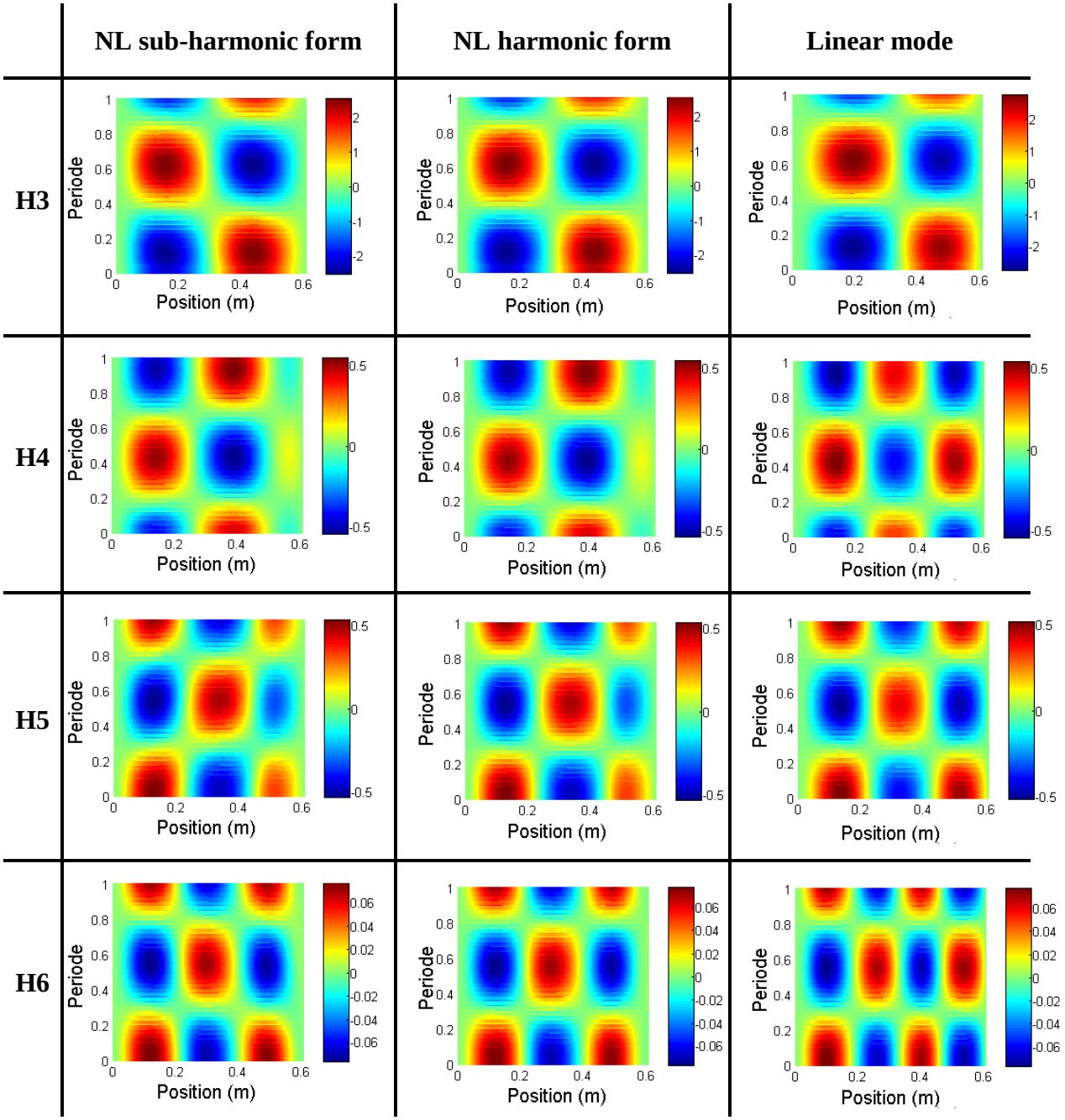

Figure 7-4 : L'évaluation dans une période pour des formes harmoniques (haute harmonique)

Tableau 7-3 : Rapport de l'amplitude de la FFT sur la limitation de linéarité des accéléromètres (niveau d'excitation de 8 N)

H.	Ratio Amplitude /N.L.A.L					
	Acc. 1	Acc. 2	Acc. 3	Acc. 4	Acc. 5	Acc. 6
N.L.A.L (m/s2)	2,94	5,88	5,88	5,88	2,94	5,88
H1	1.202	1.451	2.386	2.414	2.599	0.542
H2	0.048	0.046	0.049	0.015	0.034	0.014
H3	0.569	0.425	0.150	0.406	0.666	0.140
H4	0.126	0.087	0.010	0.089	0.026	0.018
H5	0.140	0.083	0.049	0.043	0.109	0.037
H6	0.021	0.011	0.011	0.002	0.025	0.004
H7	0.073	0.047	0.048	0.028	0.103	0.010
H8	0.014	0.003	0.006	0.007	0.001	0.002
H9	0.025	0.009	0.002	0.007	0.028	0.003
H10	0.012	0.003	0.002	0.003	0.012	0.000

N.L.A.L is Non-Linear Accelerometer Limitation

Le Code VIBIC de EACL (Rogers & Pick, 1977) est basé sur la méthode de superposition modale en utilisant les modes linéaires (méthode linéaire) ou des modes expérimentaux. Cette hypothèse est le plus utilisée dans l'industrie. D'après les figures (Figure 5-8 et Figure B–7 (Annexe B)), nous avons constaté que chaque hypothèse amène à obtenir différents modes normaux non linéaires. Les formes des modes normaux non linéaires sont également en fonction du niveau d'excitation et tout cela conduit à obtenir une réponse de système complètement différent. De plus, d'après la Figure 5-15, le niveau de la force de frottement calculée par la méthode conventionnelle (méthode linéaire) est trop élevé par rapport aux autres approches; et conduit à obtenir de coefficient de frottement très élevé (plus grand que la valeur couramment utilisée $(\eta_c = 0.74)$).

Les valeurs de la 1re fréquence naturelle, présentées dans Table 5-1, ont été obtenus à partir du graphique de phase non à partir du graphique d'amplitude (le pic), où les phases de la 1re mode sont égales à -90 degrés.

Figure 5-20 présente les résultats de simulation du modèle Stribeck de friction (Stribeck & Schröter, 1903) en utilisant un modèle l'équivalent a 1 DDL. Ce résultat est considéré comme la première étape de validation les paramètres identifiée du modèle de friction. De plus, les prédictions de l'amplitude de déplacement par les modèles de Coulomb et de Dahl sont presque trois fois plus grandes que seul perdure par le modèle de LuGre, où la prédiction par le modèle de LuGre est le résultat le plus proche à l'expérience. Cela signifie qu'en utilisant un modèle de frottement plus réaliste conduit à obtenir une production de réponse du système le plus proche à l'expérience, même en utilisant une simple approximation du système par un modèle équivalent à 1 DDL.

7.2 L'approche multi étapes :

L'approche multi étapes est une approche qui a été utilisée pour identifier les paramètres des modèles de frottements complexes en passant par l'identification de paramètres des modèles de base des modèles de frottement complexes pour chaque étape.

Par exemple, pour notre problème, l'identification du modèle de frottement Hybride a été réalisée comme suit:

Étape 1 : la force de frottement, la force normale, le déplacement de glissement et la vitesse de glissement ont été calculés en utilisant la méthode de balance harmonique inversée.

Étape 2 : l'utilisation des résultats de la 1ère étape pour identifier le coefficient de frottement cinématique μ_c en utilisant le modèle de frottement de Coulomb équation (5.42).

Étape 3 : l'utilisation du coefficient de frottement cinématique μ_c comme une valeur initiale pour identifier les deux paramètres (μ_c et σ_0 l'équivalent de k_e dans le modèle de frottement Hybride) du modèle de frottement de Dahl (1976) par la minimisation de l'erreur de force de frottement T équation (5.51) en utilisant la fonction FMINSEARCH de Matlab® avec l'équation (5.46).

Étape 4 : ensuit, en utilisant les paramètres du modèle de frottement de Dahl (1976) comme des valeurs initiales pour identifier les paramètres du modèle de frottement de Stribeck (Stribeck &

Schröter, 1903), équations (5.47) et (5.48). Les paramètres du modèle de Dahl μ_c et σ_0 sont l'équivalent de μ_s et k_s (équation (5.48)), respectivement.

Étape 5 : après, en utilisant les paramètres du modèle de frottement de Stribeck (Stribeck & Schröter, 1903) comme des valeurs initiales pour identifier les paramètres du modèle de frottement de LuGre (Canudas et al., 1995) équations (5.49) et (5.50).

Étape 6 : finalement, les paramètres du modèle de frottement de LuGre (Canudas et al., 1995) seront utilisés pour identifier les paramètres du modèle de frottement Hybride (Azizian & Mureithi, 2013) restants.

7.3 Conclusion

La méthode de balance harmonique inversée (BHI) est une nouvelle méthode développée pour calculer les forces de contact (frottement et impact). L'amélioration de cette méthode par l'utilisation de l'approche de non-orthogonalité de forme d'un côté et sous-forme harmonique d'un autre côté rend celle-ci plus précise et plus robuste, ainsi elle peut être utilisée avec différents niveaux d'excitation.

Le résultat obtenu par la méthode de balance harmonique inversée a permis d'identifier cinq paramètres (k_e, c_s et c_z (μ_s, μ_c et v_s)) du modèle de frottement Hybride (Azizian & Mureithi, 2013) à l'aide de l'approche à plusieurs étapes avec précision. Ces paramètres ont été validés par le modèle de frottement de Coulomb en utilisant la méthode des éléments finis.

CHAPITRE 8 CONCLUSION ET RECOMMANDATIONS

(An english translation of this chapter is provided in the appendix Annexe G)

Une bonne prévision de la dynamique de la structure nécessite une modélisation précise de ses conditions aux limites, des forces et des mécanismes d'excitation. Les effets majeurs de non-linéarité, de non-comparabilité et de non-reproductibilité des résultats proviennent des conditions aux limites « imparfaites ». Le présent travail a démontré que l'approche classique de la modélisation des conditions aux limites réelles (approche avec des conditions aux limites parfaites et modes normaux linéaires (MNLs)) donne de mauvaises productions de réponse du système.

Avec un faible niveau d'excitation, les éléments des conditions aux limites réelles (par exemple, le frottement) ne sont pas encore provoqués, donc la réponse du système est linéaire. Par contre, pour des niveaux d'excitation plus élevés, les éléments non-linéaires du système provoquent une divergence entre la réalité et la simulation.

Dans ce projet, nous étudierons le comportement de l'interaction d'un tube du générateur de vapeur avec ses supports, qui est un bon exemple de conditions aux limites présentant des effets non-linéaires de contact (frottement et impact). Ce problème a été simplifié en utilisant une poutre avec support frottant.

La méthode de balance harmonique inversée est une nouvelle méthode basée sur l'analyse modale non linéaire qui a été développée dans ce travail pour calculer les forces de contact. Dans ce travail, on a comparé six approches pour identifier les modes normaux non-linéaires (MNLs) utilisés pour calculer les forces de contact, soit: l'approche classique utilisant les modes linéaires (MLs) de base, l'approche proposée par Jalali et al. (2011) et les quatre combinaisons possibles de la méthode de balance harmonique inversée BHI (deux formulations et deux méthodes de lissage). La méthode BHI avec l'approche basée sur la forme sous-harmonique couplée avec la méthode de lissage par de spline a donné les meilleurs résultats pour la reconstruction des signaux des accéléromètres dans les différents niveaux d'excitation. Par contre, l'approche classique utilisant les MLs donne de mauvais résultats.

Le calcul de la force de frottement en utilisant la méthode BHI a permis d'identifier avec précision cinq paramètres du modèle de frottement Hybride avec une approche à plusieurs étapes a permis d'identifier cinq paramètres (k_e, c_s and c_z (μ_s, μ_c and v_s)) du modèle de frottement Hybride (Azizian & Mureithi, 2013) en utilisant des modèles de frottement de Dahl (1976) et LuGre (C. Canudas et al., 1995)). Certains de ces paramètres sont les mêmes que ceux du modèle de frottement de Coulomb et du modèle de frottement et de decay (Stribeck). Les autres paramètres (c_p , k_{ep} et k_{ps}) seront identifié

Une simulation par la méthode des éléments finis (MEF) de notre poutre en utilisant l'élément 1D (élément poutre) et 2D (élément Shell avec déformation plane) sert à valider les paramètres des modèles de frottement identifiés à l'aide des résultats de la méthode de balance harmonique inversée. La modélisation de zone de contact par des éléments poutres (1D) je pense que c'est plutôt n'est pas appropriée pour ce type de problème.

Deux modèles statiques de frottement, le modèle Coulomb et le modèle Stribeck ont été testés. Les deux modèles produisent des forces de frottement, force normale et déplacement de glissement de l'ordre de grandeur similaire à la force de frottement calculée avec la méthode de la balance harmonique inverse (BHI) à la fréquence de résonance. Cependant, les valeurs de bande passante sont évidemment différentes des résultats expérimentaux. Par ailleurs, les modèles de frottement de Coulomb et de decay (Stribeck) donnent des paramètres modaux (fréquence de résonance et mode normale (MNNs)) qui sont plus proches de ceux des expériences. De plus, le modèle de frottement de decay (Stribeck) donne des résultats plus proches du résultat expérimental.

Le présent travail démontre que les deux modèles de frottement statique: le modèle de frottement Coulomb et celui de decay sont incapables de représenter avec précision tous les comportements de frottement, en particulier dans le régime collage, conduisant finalement à de mauvaises estimations du taux de travail à toutes les fréquences.

Originalités et contributions

Les trois points les plus importants de l'originalité et contribution de cette thèse sont:

1. Le développement d'une nouvelle méthode dite balance harmonique inversée (BHI). Cette méthode est applicable dans un large éventail de domaines au-delà de la modélisation du frottement.
2. Le développement d'une nouvelle approche des plusieurs étapes pour identifier les paramètres des modèles de frottement.
3. L'identification des cinq paramètres du modèle de frottement hybride et cela en tenant compte des détails physiques du phénomène de frottement.

Publications

Ce projet de doctorat a conduit à deux articles de revues scientifiques et trois articles de conférences évaluées par des pairs. La relation entre ces articles est abordée dans la section qui décrit la présentation de la thèse au Chapitre 3.

A- Liste des articles soumis aux revues :

Hadji, A., & Mureithi, N. (2016a). Identification of friction model parameters using the inverse harmonic method. *ASME Journal of Pressure Vessel Technology*. doi: 10.1115/1.4034441 (Paper accepted for publication)

Hadji, A., & Mureithi, N. (2016b). Validation of friction model parameters identified using the IHB method using finite element method. (Paper submitted to) *ASME Journal of Pressure Vessel Technology*.

B- Liste des articles de conférences évaluées par des pairs:

Hadji, A., & Mureithi, N. (2014a). *Nonlinear Normal Modes and the Dahl Friction Model Parameter Identification.* Paper presented at the ASME 2014 Pressure Vessels and Piping Conference, Anaheim, California, USA.

Hadji, A., & Mureithi, N. (2014b). *Nonlinear normal modes and the LuGre friction model parameter identification*. Paper presented at the Proc. ASME-IMAC Conference, Montreal, Quebec, Canada.

Hadji, A., & Mureithi, N. (2015). *Validation of friction model parameters identified using the inverse harmonic balance method.* Paper presented at the ASME 2015 Pressure Vessels and Piping Conference, PVP 2015, July 19, 2015 - July 23, 2015, Boston, Massachusetts, United states.

Perspective :

La méthode de balance harmonique inversée est une méthode prometteuse pour l'identification de modes normaux non-linéaires et le calcul des forces ou des éléments dynamiques d'une manière indirecte et moins dispendieuse avec une grande précision. Cette méthode est capable de nous donner des informations sur la nature réelle des conditions aux limites. Elle peut même être utilisée pour extraire d'autres informations utiles pour la simulation numérique telle que la déformation de modes normaux et la variation des fréquences propres en fonction du niveau d'excitation. Donc, cette méthode peut trouver plusieurs applications dans le présent domaine d'étude et également être appliquée dans à différents domaines.

Par exemple, la méthode IBH peut être utilisée pour identifier non seulement les modes normaux et les paramètres de modèles, mais aussi pour trouver les lois de comportement (création de nouveaux modèles) des phénomènes physiques si on les combine avec le variogramme utilisé dans le Krigeage.

Dans des travaux futurs, une analyse plus approfondie du comportement du modèle Stribeck sera nécessaire pour être en mesure de valider leurs paramètres. Ensuite, les paramètres des deux modèles de frictions dynamiques (modèles Dahl et LuGre) seront validés et suivis de la validation du modèle de frottement hybride en passant par l'identification de leurs paramètres.

La formulation de puissance d'usure (work rate) (Eq.(6.23)) a été développée sur la base du modèle de frottement de Coulomb. Pour cela, une nouvelle formulation de la puissance d'usure est nécessaire à réaliser pour les nouveaux modèles de friction dans les travaux futurs.

BIBLIOGRAPHIE

ABAQUS-User's-Manual. (2013). *Version 6.12* Vol. 5. *Abaqus Inc*

Aizel, N. (2005). *Comparaison de quatre methodes d'identification d'un modele statique de frottement: Simulations et experimentations.* (MR00437 M.Ing.), Ecole de Technologie Superieure (Canada), Ann Arbor. Available from ProQuest Dissertations & Theses Full Text

Antunes, J., Axisa, F., Beaufils, B., & Guilbaud, D. (1988). *Coulomb friction modelling in numerical simulations of vibration and wear work rate of multispan tube bundles.* Paper presented at the International Symposium on Flow-Induced Vibration and Noise: Flow-Induced Vibration in Heat-Transfer Equipment - 1988, November 27, 1988 - December 2, 1988, Chicago, IL, USA.

Armstrong-Helouvry, B. (1993). Stick slip and control in low-speed motion. *Automatic Control, IEEE Transactions on, 38*(10), 1483-1496. doi: 10.1109/9.241562

Armstrong-Hélouvry, B., Dupont, P., & De Wit, C. C. (1994). A survey of models, analysis tools and compensation methods for the control of machines with friction. *Automatica, 30*(7), 1083-1138. doi: http://dx.doi.org/10.1016/0005-1098(94)90209-7

Armstrong, B., & Qunyi, C. (2008). The Z-properties chart [friction]. *IEEE Control Systems Magazine, 28*(5), 79-89. doi: 10.1109/mcs.2008.928939

Axisa, F., Antunes, J., & Villard, B. (1988). Overview of numerical methods for predicting flow-induced vibration. *Journal of Pressure Vessel Technology, Transactions of the ASME, 110*(1), 6-14.

Axisa, F., Desseaux, A., & Gibert, R. J. (1984). *Experimental study of tube/support impact forces in multi-span pwr steam generator tubes.* Paper presented at the Symposium on Flow-Induced Vibrations, Volume 6: Computational Aspects of Flow-Induced Vibration. Presented at the 1984 ASme Winter Annual Meeting., New Orleans, LA, USA.

Azizian, R. (2012). *Dynamic Modeling of Tube-Support Interaction in Heat Exchangers*. (1027 Ph.D.), Université De Montréal, École Polytechnique De Montréal (Canada), Canada. Available from publications.polymtl.ca & Mémoires et thèses

Azizian, R., & Mureithi, N. (2013). *A hybrid friction model for dynamic modeling of stick-slip behavior*. Paper presented at the Proc. ASME-PVP Conference, Paris.

Babitskii, V. I. (1998). *Theory of vibro-impact systems and applications*. Berlin: Springer.

Baumberger, T., Heslot, F., & Perrin, B. (1994). Crossover from creep to inertial motion in friction dynamics. *Nature, 367*(6463), 544-546. doi: 10.1038/367544a0

Berger, E. J. (2002). Friction modeling for dynamic system simulation. *Applied Mechanics Reviews, 55*(6), 535-577.

Bliman, P., & Sorine, M. (1993). Friction modeling by hysteresis operators. Application to Dahl, sticktion and Stribeck effects. *PITMAN RESEARCH NOTES IN MATHEMATICS SERIES*, 10-10.

Boivin, N., Pierre, C., & Shaw, S. (1994). *Non-linear modal analysis of structural systems using multi-mode invariant manifolds*. Paper presented at the Dynamics Specialists Conference. http://dx.doi.org/10.2514/6.1994-1672

Borsotto, B. (2008). *Modélisation, Identification et commande d'un organe de friction Application au contrôle d'un système d'embrayage et au filtrage d'acyclismes par glissement piloté.* Université Paris Sud-Paris XI.

Bradley, R. S. (1931). Reaction rate in the system solid-solid-gas. *Philosophical Magazine, 12*, 290-296.

C. Canudas, d. W., Olsson, H., Astrom, K. J., & Lischinsky, P. (1995). New model for control of systems with friction. *IEEE Transactions on Automatic Control, 40*(3), 419-425. doi: 10.1109/9.376053

Canudas, C. d. W., & Lischinsky, P. (1997). Adaptive friction compensation with partially known dynamic friction model. *International Journal of Adaptive Control and Signal*

Processing, 11(1), 65-80. doi: 10.1002/(sici)1099-1115(199702)11:1<65::aid-acs395>3.0.co;2-3

Canudas, C. d. W., Olsson, H., Astrom, K. J., & Lischinsky, P. (1995). New model for control of systems with friction. *IEEE Transactions on Automatic Control, 40*(3), 419-425. doi: 10.1109/9.376053

Chen, S. S. (1991). Dynamic tube/support interaction in heat exchanger tubes (pp. 28p). United States.

Chen, S. S., Jendrzejczyk, J. A., & Wambsganss, M. W. (1985). Dynamics of tubes in fluid with tube-baffle interaction. *Transactions of the ASME. Journal of Pressure Vessel Technology, 107*(1), 7-17.

Couillard, M. (2008). *Controle vibratoire semi-actif par frottement sec: Developpement d'une strategie de controle et etude de la modelisation du frottement.* (MR42945 M.A.Sc.), Universite de Sherbrooke (Canada), Ann Arbor. Available from ProQuest Dissertations & Theses Full Text

Dahl, P. R. (1976). Solid friction damping of mechanical vibrations. *AIAA Journal, 14*(12), 1675-1682.

Diehl, T. (1995). *Methods of Improving ABAQUS/Standard Predictions for Problems Involving Sliding Contact.* Paper presented at the ABAQUS User's Conference Proceedings, Paris, France.

Dupont, P., Armstrong, B., & Hayward, V. (2000, 2000). *Elasto-plastic friction model: contact compliance and stiction.* Paper presented at the American Control Conference, 2000. Proceedings of the 2000.

Ewins, D. J. (2000). *Modal testing : theory, practice, and application* (2nd ed.). Baldock, Hertfordshire, England ; Philadelphia, PA: Research Studies Press.

Fisher, N. J., Olesen, M. J., Rogers, R. J., & Ko, P. L. (1989). Simulation of tube-to-support dynamic interaction in heat exchange equipment. *Journal of Pressure Vessel Technology, Transactions of the ASME, 111*(4), 378-384.

Geneviève, I., Tony, D. S. B., & Isabelle, L. C. (2011). Théorie du contact de Hertz Contacts ponctuels ou linéiques. *Techniques de l'ingénieur Surfaces et thermomécanique du contact, base documentaire : TIB463DUO*(ref. article : tri200).

Gilmore, R. J., & Steer, M. B. (1991). Nonlinear circuit analysis using the method of harmonic balance. A review of the art. Part I. Introductory concepts. *International journal of microwave and millimeter-wave computer-aided engineering, 1*(1), 22-37.

Gorman, D. J. (1976). Experimental development of design criteria to limit liquid cross-flow-induced vibration in nuclear reactor heat exchange equipment. *Nuclear Science and Engineering, 61*(3), 324-336.

Goyal, S., Pinson, E. N., & Sinden, F. W. (1994). Simulation of dynamics of interacting rigid bodies including friction I: General problem and contact model. *Engineering with Computers, 10*(3), 162-174.

Grami, S. (2009). *Identification non lineaire du modele de frottement GMS pour l'amelioration de la commande des systemes mecaniques.* (Ph.D. NR54731), Ecole de Technologie Superieure (Canada), Canada. Available from Dissertations & Theses @ Ecole Polytechnique de Montreal; ProQuest Dissertations & Theses (PQDT)

Hadji, A., & Mureithi, N. (2014a). *Nonlinear Normal Modes and the Dahl Friction Model Parameter Identification.* Paper presented at the ASME 2014 Pressure Vessels and Piping Conference, Anaheim, California, USA.

Hadji, A., & Mureithi, N. (2014b). *Nonlinear normal modes and the LuGre friction model parameter identification*. Paper presented at the Proc. ASME-IMAC Conference, Montreal, Quebec, Canada.

Hadji, A., & Mureithi, N. (2015). *Validation of friction model parameters identified using the inverse harmonic balance method.* Paper presented at the ASME 2015 Pressure Vessels and Piping Conference, PVP 2015, July 19, 2015 - July 23, 2015, Boston, Massachusetts, United states.

Hadji, A., & Mureithi, N. (2016). Identification of friction model parameters using the inverse harmonic method. *ASME Journal of Pressure Vessel Technology*. doi: doi: 10.1115/1.4034441

Haessig Jr, D., & Friedland, B. (1991). On the modeling and simulation of friction. *Journal of Dynamic Systems, Measurement and Control, Transactions of the ASME*, *113*(3), 354-362.

Hassan, M., & Rogers, R. J. (2005). Friction modelling of preloaded tube contact dynamics. *Nuclear Engineering and Design*, *235*(22), 2349-2357. doi: 10.1016/j.nucengdes.2005.05.004

Hassan, M. A., Weaver, D. S., & Dokainish, M. A. (2002). A simulation of the turbulence response of heat exchanger tubes in lattice-bar supports. *Journal of Fluids and Structures, 16*(8), 1145-1176. doi: http://dx.doi.org/10.1006/jfls.2002.0468

Hassan, M. A., Weaver, D. S., & Dokainish, M. A. (2003). *A new tube/support impact model for heat exchanger tubes in loose supports.* Paper presented at the 2003 ASME Pressure Vessels and Piping Conference, July 20, 2003 - July 24, 2003, Cleveland, OH, United states.

Hassan, M. A., Weaver, D. S., & Dokainish, M. A. (2005). A new tube/support impact model for heat exchanger tubes. *Journal of Fluids and Structures, 21*(5-7 SPEC. ISS.), 561-577. doi: 10.1016/j.jfluidstructs.2005.07.016

Hensen, R. H. A. (2002). *Controlled mechanical systems with friction.* (C810350 Dr.), Technische Universiteit Eindhoven (The Netherlands), Ann Arbor. Available from ProQuest Dissertations & Theses Full Text

Hensen, R. H. A., Van De Molengraft, M. R. J. G., & Steinbuch, M. (2002). Frequency domain identification of dynamic friction model parameters. *IEEE Transactions on Control Systems Technology*, *10*(2), 191-196. doi: 10.1109/87.987064

Hertzberg, R. W. (1996). *Deformation and fracture mechanics of engineering materials* (4th ed.). New York ; Toronto: Wiley.

HKS-Inc. (May 29. 2001a). *Coulomb Friction in User Subroutine FRIC Using the Penalty Method*. HKS technical note #2.

HKS-Inc. (May 29. 2001b). *Lagrange Implementation of Coulomb Friction Using User Subroutine FRIC*. HKS technical note #1.

Horn, R. G., Israelachvili, J. N., & Pribac, F. (1987). Measurement of the deformation and adhesion of solids in contact. *Journal of Colloid and Interface Science, 115*(2), 480-492. doi: 10.1016/0021-9797(87)90065-8

Jalali, H., Ahmadian, H., & Pourahmadian, F. (2011). Identification of micro-vibro-impacts at boundary condition of a nonlinear beam. *Mechanical Systems and Signal Processing, 25*(3), 1073-1085. doi: http://dx.doi.org/10.1016/j.ymssp.2010.09.007

Jiang, D., Pierre, C., & Shaw, S. W. (2005). Nonlinear normal modes for vibratory systems under harmonic excitation. *Journal of Sound and Vibration, 288*(4–5), 791-812. doi: http://dx.doi.org/10.1016/j.jsv.2005.01.009

Johnson, K. L. (1985). *Contact mechanics*. Cambridge [Cambridgeshire] ; New York: Cambridge University Press.

Johnson, K. L. (1998). Mechanics of adhesion. *Tribology International, 31*(8), 413-418. doi: 10.1016/s0301-679x(98)00060-7

Johnson, K. L., Kendall, K., & Roberts, A. D. (1971). Surface energy and the contact of elastic solids. *Proceedings of the Royal Society of London, Series A (Mathematical and Physical Sciences), 324*(1558), 301-313.

Karnopp, D. (1985). Computer simulation of stick-slip friction in mechanical dynamic systems. *Journal of Dynamic Systems, Measurement and Control, Transactions of the ASME, 107*(1), 100-103.

Lalonde, V., Ross, A., Pettigrew, M. J., & Nowlan, I. (2010). *Experimental study of dynamic interaction between a steam generator tube and an anti-vibration bar*. Paper presented at the ASME 2010 3rd Joint US-European Fluids Engineering Summer Meeting, FEDSM 2010 - ASME 2010 7th International Symposium on Fluid-Structure Interactions, Flow-

Sound Interactions, and Flow-Induced Vibration and Noise, FSI2 and FIV+N, August 1, 2010 - August 5, 2010, Montreal, QC, Canada.

Lampaert, V., Al-Bender, F., & Swevers, J. (2003). *A generalized Maxwell-slip friction model appropriate for control purposes.* Paper presented at the 2003 International Conference Physics and Control. Proceedings, 20-22 Aug. 2003, Piscataway, NJ, USA.

Lim, Y. F., & Kan, C. (1998). Dynamics of dry friction: A numerical investigation. *Physical Review E (Statistical Physics, Plasmas, Fluids, and Related Interdisciplinary Topics), 58*(5), 5637-5642. doi: 10.1103/PhysRevE.58.5637

MathWorks. (2011). MATLAB Optimization Toolbox Release 2011a *2011A, The MathWorks, Inc., Natick, MA.*

Maugis, D. (1992). Adhesion of spheres: The JKR-DMT transition using a dugdale model. *Journal of Colloid and Interface Science, 150*(1), 243-269. doi: http://dx.doi.org/10.1016/0021-9797(92)90285-T

Mindlin, R. D. (1949). Compliance of elastic bodies in contact. *American Society of Mechanical Engineers -- Transactions -- Journal of Applied Mechanics, 16*(3), 259-268.

Mindlin, R. D., & Deresiewicz, H. (1953). Elastic spheres in contact under varying oblique forces. *American Society of Mechanical Engineers -- Transactions -- Journal of Applied Mechanics, 20*(3), 327-344.

Moretti, P., & Lowery, R. (1973). Heat Exchanger Tube Vibration Characteristics in a'No Flow, Condition. *Final Report: Tubular Exchanger Manufacturers Association Experimental Program, Oklahoma State University*.

Morin, A. (1833). New friction experiments carried out at Metz in 1831–1833. *Proceedings of the French Royal Academy of Sciences, 4*, 1-128.

Muller, V. M., Derjaguin, B. V., & Toporov, Y. P. (1983). On two methods of calculation of the force of sticking of an elastic sphere to a rigid plane. *Colloids and Surfaces, 7*(3), 251-259. doi: 10.1016/0166-6622(83)80051-1

Nowlan, I., Ross, A., & Pettigrew, M. J. (2009). *Dynamic interaction between a straight tube and an anti-vibration bar.* Paper presented at the 2009 ASME Pressure Vessels and Piping Conference 2009. Fluid-Structure Interaction, 26-30 July 2009, New York, NY, USA.

Nuninger, W., Perruquetti, W., & Richard, J. P. (2006). *Bilan et enjeux des modèles de frottements: tribologie et contrôle au service de la sécurité des transports*. Paper presented at the JEF'06, 5th European Conference on Braking (5e Journées Européennes du Freinage), Lille : France (2006). http://hal.inria.fr/docs/00/19/24/25/PDF/Nuninger_jef2006_id037_4.pdf

Oden, J. T., & Martins, J. A. C. (1985). Models and computational methods for dynamic friction phenomena. *Computer Methods in Applied Mechanics and Engineering, 52*(1–3), 527-634. doi: http://dx.doi.org/10.1016/0045-7825(85)90009-X

Odfalk, M., & Vingsbo, O. (1990). Influence of Normal Force and Frequency in Fretting©. *Tribology Transactions, 33*(4), 604-610. doi: 10.1080/10402009008981995

Ödfalk, M., & Vingsbo, O. (1992). An elastic-plastic model for fretting contact. *Wear, 157*(2), 435-444. doi: http://dx.doi.org/10.1016/0043-1648(92)90080-R

Olsson, H., Astrom, K. J., De Wit, C. C., Gafvert, M., & Lischinsky, P. (1998). Friction models and friction compensation. *European Journal of Control, 4*(3), 176-195.

Ozaki, S., & Hashiguchi, K. (2010). Numerical analysis of stick-slip instability by a rate-dependent elastoplastic formulation for friction. *Tribology International, 43*(11), 2120-2133. doi: 10.1016/j.triboint.2010.06.007

Pesheck, E., Boivin, N., Pierre, C., & Shaw, S. (2001). Nonlinear Modal Analysis of Structural Systems Using Multi-Mode Invariant Manifolds. *Nonlinear Dynamics, 25*(1-3), 183-205. doi: 10.1023/a:1012910918498

Price, S. J. (1995). A Review of Theoretical Models for Fluidelastic Instability of Cylinder Arrays in Cross-Flow. *Journal of Fluids and Structures, 9*(5), 463-518. doi: http://dx.doi.org/10.1006/jfls.1995.1028

Rao, M., Gupta, G., Eisinger, F., Hibbitt, H., & Steininger, D. (1987). *Flow Induced Vibrations.* Paper presented at the Flow Induced Vibrations: proceedings of the 1st international conference: Bowness-on-Windermere, England, 12-14 May, 1987.

Reynolds, O. (1886). On the Theory of Lubrication and Its Application to Mr. Beauchamp Tower's Experiments, Including an Experimental Determination of the Viscosity of Olive Oil. *Proceedings of the Royal Society of London, 40*(242-245), 191-203.

Rogers, R. J., & Pick, R. J. (1977). Factors associated with support plate forces due to heat-exchanger tube vibratory contact. *Nuclear Engineering and Design, 44*(2), 247-253. doi: 10.1016/0029-5493(77)90031-0

Rosenberg, R. M. (1966). On Nonlinear Vibrations of Systems with Many Degrees of Freedom. In H. L. D. P. G. L. H. W. O. W. P. R. F. P. G.G. Chernyi & H. Ziegler (Eds.), *Advances in Applied Mechanics* (Vol. Volume 9, pp. 155-242): Elsevier.

Sauve, R. G., & Teper, W. W. (1987). Impact simulation of process equipment tubes and support plates - a numerical algorithm. *Journal of Pressure Vessel Technology, Transactions of the ASME, 109*(1), 70-79.

Shaw, S. W., & Pierre, C. (1992). *On nonlinear normal modes.* Paper presented at the Winter Annual Meeting of the American Society of Mechanical Engineers, November 8, 1992 - November 13, 1992, Anaheim, CA, USA.

Stachowiak, G. W., & Batchelor, A. W. (2005). *Engineering tribology* (3rd ed.). Amsterdam ; Boston: Elsevier Butterworth-Heinemann.

Stevens, A. B., & Hrenya, C. M. (2005). Comparison of soft-sphere models to measurements of collision properties during normal impacts. *Powder Technology, 154*(2-3), 99-109. doi: 10.1016/j.powtec.2005.04.033

Stribeck, R., & Schröter, M. (1903). *Die wesentlichen Eigenschaften der Gleit-und Rollenlager: Untersuchung einer Tandem-Verbundmaschine von 1000 PS*: Springer.

Swevers, J., Al Bender, F., Ganseman, C. G., & Prajogo, T. (2000). Integrated friction model structure with improved presliding behavior for accurate friction compensation. *IEEE Transactions on Automatic Control, 45*(4), 675-686. doi: 10.1109/9.847103

Toorani, M., Pan, L., Li, R., Idvorian, N., & Vincent, B. (2009). Advanced nonlinear flow-induced vibration and fretting-wear analysis capabilities *6th CNS International Steam Generator Conference*. Ontario

Weaver, D. S., & Schneider, W. (1983). The effect of flat bar supports on the crossflow induced response of heat exchanger U-tubes [nuclear power stations]. *Transactions of the ASME. Journal of Engineering for Power, 105*(4), 775-781.

Xi, T., & Rogers, R. J. (1996). *Dynamic friction modelling in heat exchanger tube simulations.* Paper presented at the Proceedings of the 1996 ASME Pressure Vessels and Piping Conference. Part 1 (of 2), July 21, 1996 - July 26, 1996, Montreal, Can.

Yi-Ti, S., & An-Chen, L. (2003). Survey on modeling and control for motion systems with friction. *Journal of the Chinese Society of Mechanical Engineers, 24*(4), 337-352.

Zeng, H. (2013). *Polymer adhesion, friction, and lubrication*.

ANNEXE A - LES MODÈLES DE FROTTEMENT

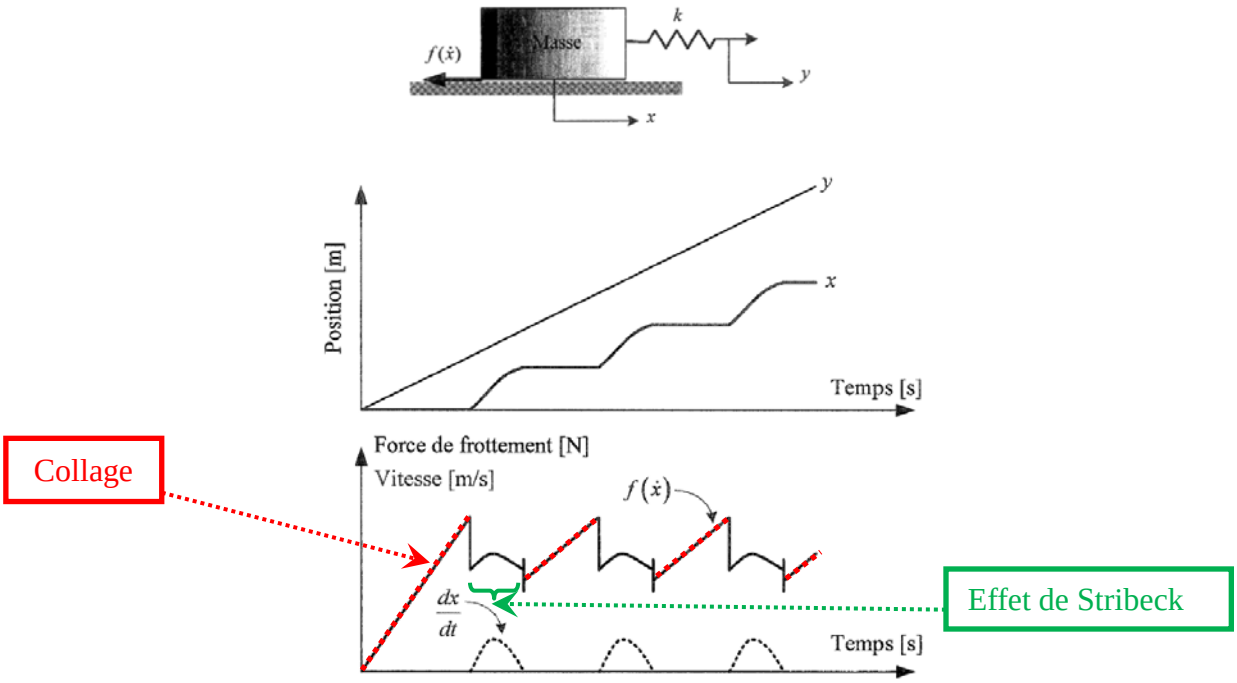

Figure 8-1 : Simulation de l'effet de broutage (Stribeck effect) (Aizel, 2005)

Tableau 8-1 : Bilan des modèles de frottement selon leurs propriétés et leur domaine d'application (Nuninger et al., 2006)

		Number of parameters	Static mode	Coulomb	Viscous mode	Stribeck effect	dwell-time	friction memory	hysteresis	stick-slip	Hybrid model form	Linear model form	for vehicles	for systems like manipulators	for no continuous contact	Simulation / Design	Compensation / Control	Observation / Diagnosis	
Macro-modèles																			*Global Mouvement*
Global Model (Maron)	3/4	X	X	X								X	X		X				Static,Coulomb,Viscous
Lorentzien Model	4	X	X	X	X							X	X		X				Hyperbolic approximation
Tustin Model (exp.)	4	X	X	X	X							X	X		X				form factor =1
Exponential Model	5	X	X	X	X							X	X		X				form factor
Karnopp Model	3+1	X	X	X								X	X	X	X				bound dead-zone
Uncertain Model (k.dx/dt)	1	X	X	X							X	X			X			X	function of sliding
Micro-modèles																			*Tribology properties*
Dahl Model	3	X	X			X	X	X		?			X		X	X			Static
Bliman et al. Model	3/5	X	X		X	X	X	X	X	?	X		X		X	X	X		block models
Armstrong-Helouvry Model	7	X		X	X	X	X	X	X	X			X		X	X			Viscosity
Reset integrator Model	3	X	X	X	X	X		X	X				X		X	X	X		Viscosity
LuGre Model	7	X	X	X	X	X		X	X				X		X	X	X		Viscosity
Lueven et Swevers Model	7/+	X	X	X	X	X	X	X	X				X		X	X	X		Simulation tools
Stramigioli Model	2	X	X				X		X			X		X	X	X			Energy/Walking robot

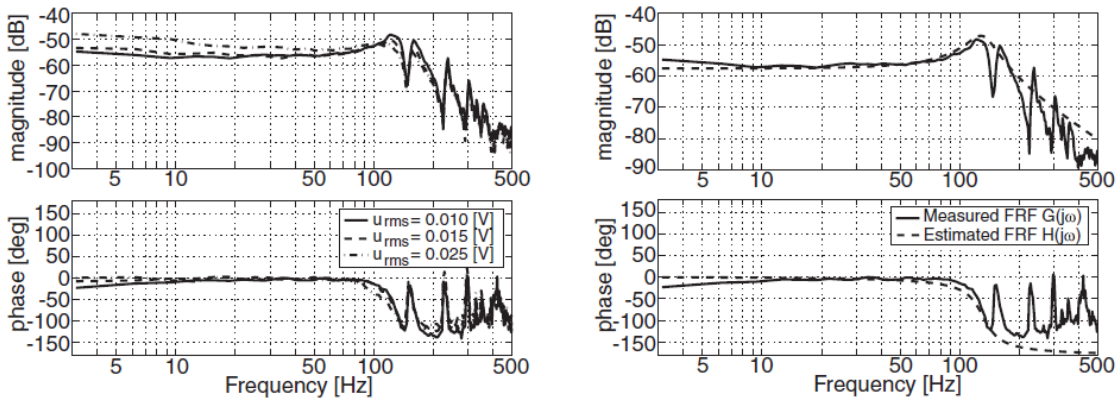

a) Stiffness nonlinearity. b) Measured and estimated FRF.

Figure 8-2 : Fonctions de réponse en fréquence (FRF) comportement de préglissement (Ron H. A. Hensen et al., 2002)

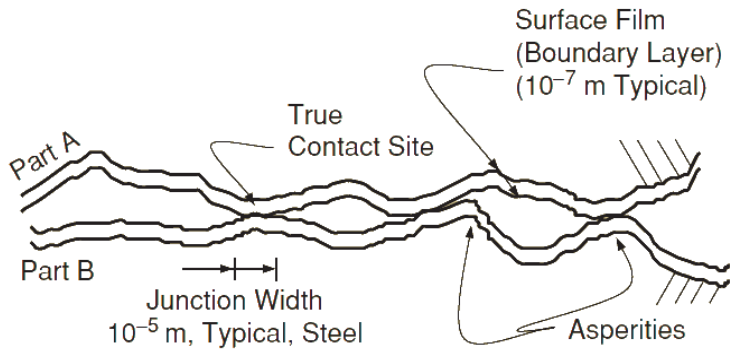

Figure 8-3 : Exemple schématique de la zone de contact d'un contact métal-métal avec lubrification (Armstrong & Qunyi, 2008).

Les contacts qui se produisent entre les aspérités peuvent constituer une petite fraction de la surface totale.

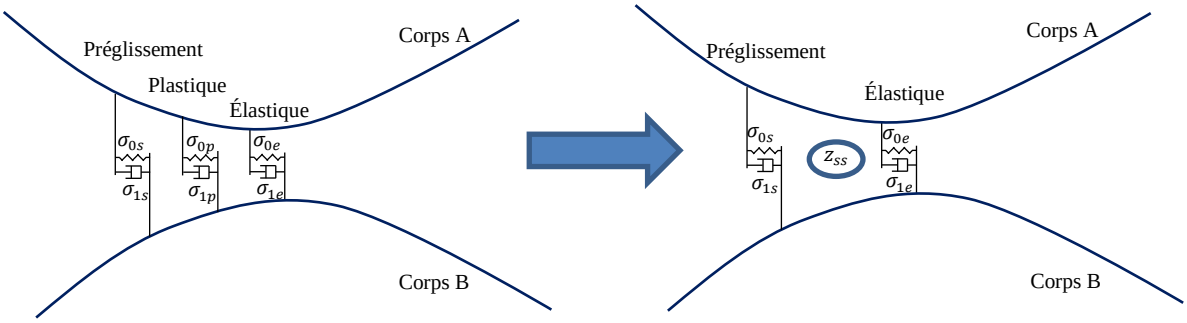

Figure 8-4 : La dynamique de brins (Bristles) dans le test de Cattaneo-Mindlin.

Autres modèles de frottement :

Les modèles de frottement utilisés pour modéliser l'interaction tube-support citée par Hassan et Rogers (M. Hassan & Rogers, 2005) :

1- **Le modèle de frottement à vitesse limitée VLFM** (Velocity-Limited Friction model)

$$\begin{aligned} \left|F_f\right| &= \mu_c N \qquad si \quad \left|V_t\right| > V_0 \\ \left|F_f\right| &= \frac{\left|V_t\right|}{V_0}\mu_c N \qquad si \quad \left|V_t\right| \le V_0 \end{aligned} \tag{A-1}$$

Avec :

μ_c est le coefficient dynamique de frottement,

N est la force normale.

2- **Le modèle de frottement à force équilibrée FBFM** (Force balance Friction model)

$$F_f = Ku - F_e \tag{A-2}$$

Dans le cas de collage, la force de frottement F_f doit respecter la condition suivante:

$$\left|F_f\right| < \mu_s F_n \tag{A-3}$$

Avec :

Ku représentation symbolique de la force interne au point de contact.

F_e est la force externe,

μ_s est le coefficient statique de frottement.

3- Le modèle de frottement à amortisseur-ressort SDFM (Spring damper Friction model)

$$\begin{aligned} F_f &= \mu F_n && \text{glissement} \\ F_f &= K_a(u_c - u_0) + C_a V_t && \text{collage} \end{aligned} \qquad \text{(A-4)}$$

Avec :

K_a est la raideur d'adhérence,

C_a est l'amortissement d'adhérence,

u_c est le déplacement tangentiel actuel.

u_0 : est le déplacement tangentiel à la vitesse zéro.

Les modèles de frottement utilisés par Azizian (Azizian, 2012) pour les comparer par son modèle :

4- **Le modèle de frottement d'Ozaki** (Ozaki & Hashiguchi, 2010)

$$\begin{aligned} \dot{\mu} &= -k\left(\frac{\mu}{\mu_c} - 1\right)\left\|\bar{v}^p\right\| + \xi\left(1 - \frac{\mu}{\mu_s}\right) \\ \bar{v}^p &= -\frac{(\alpha_n R\mu\hat{n} - \alpha_t\hat{t})\bullet\bar{v} - \xi R(1-\mu/\mu_s) f_n}{\alpha_t + r(\ln R)\mu f_n - Rk(\mu/\mu_c - 1) f_n}\hat{t} \end{aligned} \qquad \text{(A-5)}$$

Avec :

μ_c est le coefficient dynamique de frottement,

μ_s est le coefficient statique de frottement.

K, ξ et r sont des constantes de matériau influant sur variation du coefficient de frottement,

$\bar{v}^p$ est la vitesse de glissement plastique.

5- **Le modèle de frottement de Lim** (Lim & Kan, 1998)

$$\mu(\phi,\dot{x}) = A\,\mathrm{sgn}(\dot{x})\sinh^{-1}\left\{\frac{1}{2}\exp\left[\frac{\bar{\mu}}{A}\right]\right\} + \eta\dot{x}$$

$$\bar{\mu} = a_v + b_v \ln\frac{\phi V_0}{D_0} + A\ln\frac{\phi|\dot{x}|}{D_0} \qquad \text{(A-6)}$$

$$\dot{\phi}(t) = 1 - \frac{|\dot{x}|\phi}{D_0}$$

Avec :

ϕ est un variable d'état,

a_v, b_v, A, D_0 sont des constants,

V_0 est un échelle de vitesse arbitraire.

ANNEXE B – ARTICLE 3: NONLINEAR NORMAL MODES AND THE DAHL FRICTION MODEL PARAMETER IDENTIFICATION

Hadji, A., & Mureithi, N. (2014)

Paper presented at the ASME 2014 Pressure Vessels and Piping Conference, Anaheim, California, USA. DOI:10.1115/PVP2014-28733

ABSTRACT

Fretting wear of steam generator tubes due to vibration induced by fluid flow remains a serious problem in the nuclear industry. Azizian and Mureithi (Azizian & Mureithi, 2013) have recently developed a hybrid friction model to simulate the friction behavior of tube-support interaction. However, identification of the model parameters remains unresolved.

To identify the parameters of the friction model, the following quantities are required: contact forces (tangential force (friction) and normal force (impact)), the slip velocity and displacement in the contact region. Direct measurement of these quantities by using a steam generator tube interacting with its supports is difficult. To simplify the problem, a beam, clamped at one end and simply supported with consideration of friction effect at the other is used. The beam acts as a mechanical amplifier of the friction effects at the microscopic level. Using this simple setup, the contact forces, the sliding velocity and the displacement can be indirectly obtained from the beam's vibration response measurements.

A new method based on nonlinear modal analysis was developed to calculate the contact forces. This method is based on the modal superposition principle and Fourier series expansion. The nonlinear normal modes (NNMs) and the generalized coordinates (GCs) have been identified experimentally as functions of the excitation level, the frequency, the preload in the contact area, with and without lubrication.

Three hypotheses and related analyses to identify the NNMs and GCs were tested; the analysis based on the harmonic balance method gives the best results for reconstructing the accelerometer

signals with an error less than 2% for all excitation levels compared to more than 2% for other methods.

The successful signal reconstruction makes it possible to accurately identify the parameters of the Dahl friction model. This is also the first step to identify the parameters of the hybrid friction model.

INTRODUCTION

The fretting wear of steam generator tubes due to vibration remains an important problem in the nuclear industry. The friction models used to model the tube-support interaction cited by (M. Hassan & Rogers, 2005) are special cases of static friction models. The velocity limited friction model (VLFM) (Rogers & Pick, 1977) is a continuous Coulomb model without Stribeck effects. However, the other two models, the force balance friction model (FBFM) (Xi & Rogers, 1996) and the spring damper friction model (SDFM) (Antunes et al., 1988) are based on the modeling of friction by springs and dampers. The principle of Karnopp friction model (Karnopp, 1985) is used in the FBFM model. The newest model of friction designed to model the tube-support interaction is the hybrid friction model (Azizian, 2012; Azizian & Mureithi, 2013), the authors used the dynamics of Dahl model (Dahl, 1976), the principle of LuGre model (Canudas et al., 1995) with consideration of stress distributions in the contact area in accordance with the principle of Cattaneo-Mindlin (Kenneth Langstreth Johnson, 1985).

The nonlinear normal modes have increasingly been used in the analysis of nonlinear systems, as demonstrated by the works of Rosenberg (Rosenberg, 1966) and Pierre and co-workers (Boivin et al., 1994; Pesheck et al., 2001; Shaw & Pierre, 1992). There are also other methods used for analyzing nonlinear systems, for example the method of harmonic balance (HB) (Gilmore & Steer, 1991) which is widely used in the electronic field. HB method will be used for the first time to experimentally determine the NNMs in the current work.

The realization of a test bench able to acquire all of the following quantities: friction force, impact force, slip velocity and displacement, is vital since all these quantities are necessary to study the phenomenon of steam generator tube fretting wear. It is for this reason that we are inspired by the test bench conceived by Jalali et al. (2011).

NOMENCLATURE

A	Area of the cross section of the beam
E	Youngs modulus
F	Excitation force by a shaker
F	Kinetic friction force
I	Quadratic bending moment
L	Length of the beam
N	Resultant of the normal force
P	Static load to ensure permanent contact between the beam and support
R	Support reaction (impact force)
T	Frictional force
X_f	Position of the excitation point
c_p	Plastic damping
c_s	Pre-sliding damping
c_z	Stribeck damping
e	Thickness of the beam
$g(\dot{x})$	Stribeck function
k_e	Elastic stiffness
k_{ep}	Elastic-plastic stiffness
k_{ps}	Plastic-pre sliding stiffness
q_i	Linear generalized coordinates
$\tilde{q}_i$	Nonlinear generalized coordinates
r	Radius of the contact element (half-cylinder)
(t)	Time dependence
u	Displacement at the contact zone
(x)	Position dependence
z_e	Elastic slip relative displacements

z_p Plastic slip relative displacements

z_s Partial slip relative displacements

ϕ_i Linear normal modes

$\tilde{\phi}_i$ Nonlinear normal modes

μ_c Kinetic friction coefficient

μ_s Static friction coefficient

ρ Density of the beam

σ_0 Stiffness coefficient

v Velocity at the contact area

v_s Stribeck velocity

THE TEST RIG AND THEORETICAL CONSIDERATION

The test rig was designed as shown in Figure B–1. It is a simple concept in which the specimen is a simply supported beam on one side (friction effect not-neglected) and clamped on the other. All the forces applied at the contact point are represented in Figure B–2. The beam is excited by a shaker and its response measured by accelerometers as shown in Figure B–3.

The beam is modeled by the theorem of Euler-Bernoulli. The equation of motion is:

$$\rho A\ddot{y}(x,t) + EIy''''(x,t) - T(t)\,y''(x,t) = F(t)\,\delta\left(x - X_f\right) \quad (1)$$

with the following boundary conditions :

At $x = 0$: $y(0,t) = 0$ and $y'(0,t) = 0$ (2,3)

and at $x = L$: $EIy''(L,t) = \left(r + e/2\right)T(t)$ (4)

and $EIy'''(L,t) = -N(t) + m\ddot{y}(L,t) + T(t)\,y'(L,t)$ (5)

Jalali et al. (2011) considered the effect of $y'(L,t)$ in Eq. (5) to be negligible. In contrast, all terms were used in the present model so as to obtain more accurate results with a simple analysis of experimental data. Since the beam is excited at its first natural frequency (resonance), adequate modal analysis is necessary.

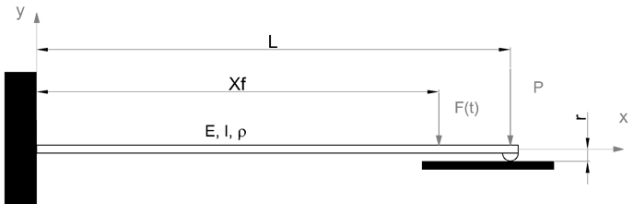

Figure B–1 : Schematic of a nonlinear beam

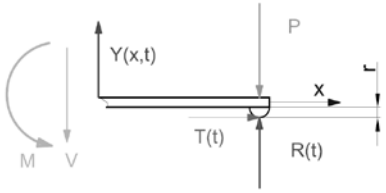

Figure B–2 : Direction of forces applied at the contact point

The assembly is designed in such a manner that the geometry and material of the contact zone can be changed easily. It is even possible to modify the contact environment (with or without lubrication).

The characteristics of the beam are as follows: length L = 606 mm, width b = 38.88 mm, thickness e = 4.76 mm and the radius r = 5 mm. The six accelerometers used in the test were positioned at 0.083 m, 0.153 m, 0.268 m, 0.408 m, 0.499 m and 0.555 m, respectively, and the driving point at 0.555 m from the clamped end.

$$y_j(x_j,t)=\sum_{i=1}^{n}\phi_i(x_j)\,q_i(t) \qquad (6)$$

where:

$q_i(t)$ (i=1,2,...n) are the generalized coordinates

$\phi_i(x)$ (i=1,2,...n) are the normal modes of the system

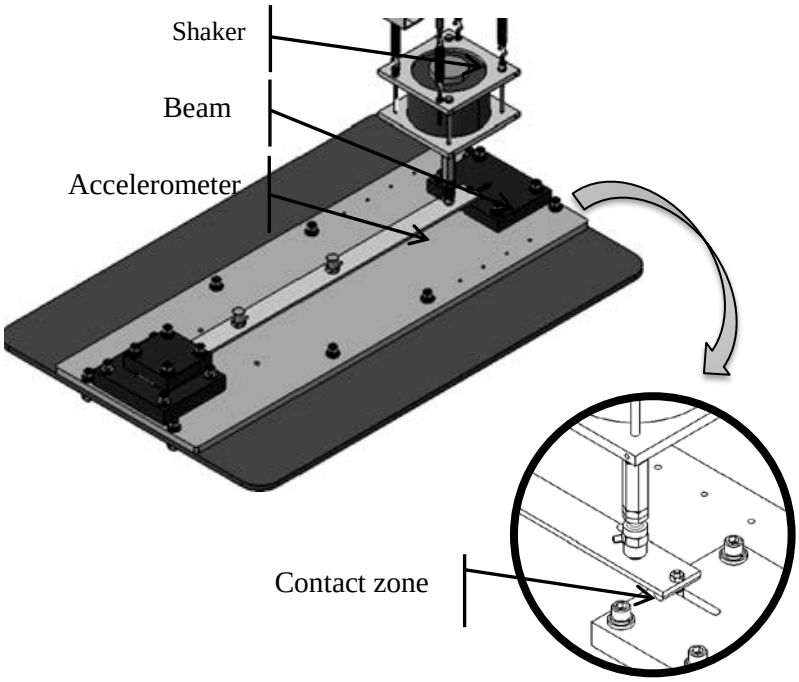

Figure B–3 : Schematic of the test rig

The response of the system may be written in the following form:

Using the modal superposition principle (Eq. (6)) and the Galerkin method, Eq. (1) can be rewritten as follows:

$$\ddot{q}_i(t)+\omega_i^2 q_i(t)-F(t)\tilde{\phi}_i\left(X_f,a\right)=-N(t)\tilde{\phi}_i(L,a)+$$
$$\left[r\tilde{\phi}_i{}'(L,a)+\sum_{j=1}^{n}q_j(t)\left(\int_0^L\tilde{\phi}_j''(x,a)\tilde{\phi}_i(x,a)dx-\tilde{\phi}_i'(L,a)\tilde{\phi}_j(L,a)\right)\right]T(t),\quad i\text{=1-}n \qquad (7)$$

where:

$N(t)=P-R(t)$ is the impact force (or the normal force in the zone of contact), with the following terms of modal orthogonality:

$$\rho A\int_0^L\tilde{\phi}_i(x,a)\tilde{\phi}_j(x,a)\,dx+m\tilde{\phi}_i(L,a)\tilde{\phi}_j(L,a)=\delta_{ij} \qquad (8)$$

$$EI\int_0^L\tilde{\phi}_i^{"}(x,a)\tilde{\phi}_j^{"}(x,a)\,dx=\omega_i^2\delta_{ij} \qquad (9)$$

The displacement and velocity in the contact area can be calculated by the following equations:

$$u(t) = -\frac{1}{2}\int_0^L \left(\frac{\partial y(x,t)}{\partial x}\right)^2 dx + r\left.\frac{\partial y(x,t)}{\partial x}\right|_{x=L} + \frac{T(t)L}{AE} \tag{10}$$

$$u(t) = -\frac{1}{2}\sum_{i=1}^{n} q_i^2(t)\int_0^L \left(\frac{\partial \phi_i(x)}{\partial x}\right)^2 dx + r\sum_{i=1}^{n} q_i(t)\phi_i'(L) + \frac{T(t)L}{AE} \tag{11}$$

$$v(t) = -\frac{1}{2}\sum_{i=1}^{n} \dot{q}_i^2(t)\int_0^L \left(\frac{\partial \phi_i(x)}{\partial x}\right)^2 dx + r\sum_{i=1}^{n} \dot{q}_i(t)\phi_i'(L) + \frac{\dot{T}(t)L}{AE} \tag{12}$$

THE NONLINEAR NORMAL MODES

The definition of nonlinear normal modes (NNMs) was introduced for the first time in the literature by Rosenberg (1966). This definition is applicable only for a discrete and conservative system. However, the NNMs description as proposed by Shaw & Pierre (Boivin et al., 1994; Jiang et al., 2005; Pesheck et al., 2001; Shaw & Pierre, 1992) is the most general and applicable to all systems. Other researchers have attempted to identify the NNMs of a beam experimentally. For example, Jalali et al. (2011) have used basic linear normal modes to build the NNMs of a clamped-simply supported beam with friction.

In the literature, there are two assumptions used to model non-linear dynamic systems. The first uses the linear normal modes and nonlinear generalized coordinates (LNMs-NGCs) while in the other, nonlinear normal modes and the linear generalized coordinates (NNMs-LGCs) are used. The LNMs-NGCs hypothesis is the assumption most commonly used, which the linear normal modes are only used, and the nonlinearity effect is lumped in the generalized coordinates. The second, NNMs-LGCs hypothesis is to consider the effect of non-linearity as manifested only in the deformation of the normal modes. Jalali et al. (2011) proposed an approach to identify NNMs experimentally. They considered the first three harmonics of the response as generalized coordinates.

We represent the main steps used to determine nonlinear normal modes according to the approach proposed in (Jalali et al., 2011) (the NNMs-LGCs hypothesis):

The nonlinear response of the system can be written in the following form:

$$y_j\left(x_j,t\right)=\sum_{i=1}^{n}\tilde{\phi}_i\left(x_j\right)\tilde{q}_i\left(t\right) \tag{13}$$

$\tilde{q}_i\left(t\right)$ (i=1,2,...n) are the NGCs

$\tilde{\phi}_i\left(x\right)$ (i=1,2,...n) are the NNMs of the system.

The quantities $q_i\left(t\right)$ and $\phi_i\left(x\right)$ are known, however, $\tilde{q}_i\left(t\right)$ and $\tilde{\phi}_i\left(x\right)$must be determined. The *n* generalized coordinates can be determined from the following equation:

$$\ddot{q}\left(t\right)=\begin{Bmatrix}\ddot{q}_1\left(t\right)\\ \ddot{q}_2\left(t\right)\\ \vdots\\ \ddot{q}_n\left(t\right)\end{Bmatrix}=\begin{bmatrix}\varphi_1\left(x_1\right) & \varphi_2\left(x_1\right) & \cdots & \varphi_n\left(x_1\right)\\ \varphi_1\left(x_2\right) & \varphi_2\left(x_1\right) & \cdots & \varphi_n\left(x_2\right)\\ \vdots & \vdots & \ddots & \vdots\\ \varphi_1\left(x_n\right) & \varphi_2\left(x_n\right) & \cdots & \varphi_n\left(x_n\right)\end{bmatrix}^{-1}\begin{Bmatrix}\ddot{y}_1\left(x_1,t\right)\\ \ddot{y}_2\left(x_2,t\right)\\ \vdots\\ \ddot{y}_n\left(x_n,t\right)\end{Bmatrix} \tag{14}$$

$\ddot{y}_i=\left(x_i,t\right)$ being the system response at the measurement point *i*. A Fourier series is used to represent the signal of the generalized coordinates.

$$\ddot{q}_i\left(t\right)=\sum_{j=1}^{M}\left(A_{ji}\cos\left(j\omega t+\psi_{ji}\right)\right) \tag{15}$$

On integration, we obtain the equations of the generalized coordinates as:

$$q_i\left(t\right)=\sum_{j=1}^{M}\left(\frac{A_{ji}}{\left(j\omega\right)^2}\cos\left(j\omega t+\psi_{ji}\right)\right) \tag{16}$$

Substituting Eq. (16) into Eq. (13) yields:

$$y\left(x,t\right)=-\sum_{i=1}^{n}\left(\phi_i\left(x\right)\sum_{j=1}^{M}\left(\frac{A_{ji}}{\left(j\omega\right)^2}\sin\left(j\omega t+\psi_{ji}\right)\right)\right) \tag{17}$$

Assuming the system response to be dominated by the first mode and the ψ_{j1} equal $\psi_j=\psi_{j1}$, the above equation can be rewritten as follows:

$$y(x,t) \cong -\sum_{j=1}^{n}\left[\sum_{i=1}^{n}\left(\frac{A_{ji}\phi_i(x)}{|A_j|(j\omega)^2}\right)|A_j|\sin(j\omega t+\psi_j)\right] \tag{18}$$

with

$$|A_j| = \sqrt{\sum_{i=1}^{n} A_{ji}^2} \tag{19}$$

The NNMs are then defined as:

$$\tilde{\phi}_j(x, F_{\max}) \cong -\frac{1}{|A_j|}\sum_{i=1}^{n}\left(\frac{A_{ji}\phi_i(x)}{(j\omega)^2}\right) \tag{20}$$

where $F_{\max}$ is the maximum amplitude of excitation force.

According to Ewins (2000) the modal analysis of a nonlinear system is performed for a constant level of response (approach used by Jalali et al. (2011)) or a constant level of excitation force. The latter approach is the most relevant for displaying the non-linearity effect. Since the level of excitation of the fluid force in practice is known and the final objective is to determine the work rate corresponding to each force level, the latter approach is used in the current work.

In this paper, a new approach for calculating the NNMs based on the principal of modal superposition and utilizing all the harmonics that appear in the system response signal is proposed.

In the new approach the NNMs are calculated in the following manner:

STEP 1

The Fourier series of the response signal is written as follows:

$$y_j(x_j,t) = \sum_{i=1}^{n} A_{ij}\cos(i\cdot\omega_{ext}t+\varphi_{ij}) \tag{22}$$

STEP 2

This equation can also be written as:

$$y_j\left(x_j,t\right)=\sum_{i=1}^{n}\tilde{\phi}_i\left(x_j\right)C_i\cos\left(i\cdot\omega_{ext}t+\varphi_i\right) \tag{23}$$

$$\begin{cases}\tilde{\tilde{q}}_i\left(t\right)=C_i\cos\left(i\cdot\omega_{ext}t+\varphi_i\right)\\ \tilde{\phi}_i\left(x_j\right)=\dfrac{A_{ij}}{C_i}\end{cases} \tag{24}$$

Where x_j is the position of the accelerometer *j*,

The transition from Eq. (23) to Eq. (24) requires the calculation of φ_i by the minimization of the error in the reconstruction of the accelerometer signals (or φ_{ij} optimal) and C_i by the normalization of $\tilde{\varphi}_i\left(x_j\right)$ from A_{ij}.

STEP 3

$\tilde{\phi}_i(x)$ are fitted using a series of trigonometric functions, Eq. (25). To reduce the smoothing error, an intermediate step must be used (natural smoothing spline) to predict the natural deformed form of the beam and improve the fitting result.

$$\begin{aligned}\tilde{\phi}_i(x)=&\,a_{11}\sin\left(\beta_1x\right)+a_{12}\cos\left(\beta_1x\right)+a_{13}\sinh\left(\beta_1x\right)+a_{14}\cosh\left(\beta_1x\right)\\&+a_{21}\sin\left(\beta_2x\right)+a_{22}\cos\left(\beta_2x\right)+a_{23}\sinh\left(\beta_2x\right)+a_{14}\cosh\left(\beta_2x\right)\end{aligned} \tag{25}$$

EXPERIMENTAL RESULTS AND DISCUSSION

In this section, some experimental results are represented, including the detection of different slip regimes and non-linear friction effects.

1. Slip regimes

To detect the different slip regimes at constant frequency, several tests were performed. The results are represented in the form of the beam excitation force as a function of the excitation voltage of the shaker or the sensitivity to the shaker slip speed. Figure B–4 represents the results of such a test conducted at 50 Hz. The different zones can be identified in the figure:

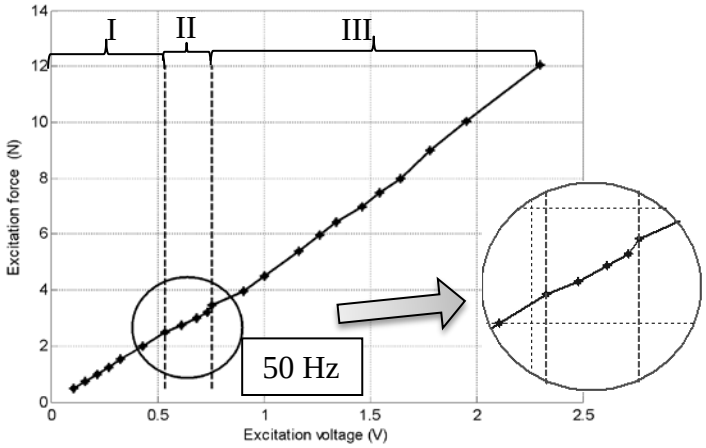

Figure B–4 : The effect of slip regime on the shaker (the sensitivity of the shaker slip regime)

Zone I: Stable (pre-sliding), Zone II: unstable slip (stick-slip) and Zone III: stable sliding regime.

The variation of the reaction force of the vibrating beam is linear in both stable regimes (pre-sliding and stable sliding) but with two different slopes. This variation is, however, non-linear in the regime of unstable slip (stick-slip regime).

2. The non-linear effects of friction

The non-linear effects of friction are illustrated next. Firstly the FFT of the response at the driving point of the same test shown in Figure B–4 is computed. Next the frequency response of the system (FRF) near the first harmonic is obtained.

As shown in Figure B–5 several harmonics appear in the response and their amplitudes change according to the level of excitation. The amplitude of the third harmonic is greater than the second and the higher harmonics. This is because this harmonic is close to the second natural frequency of the system. The harmonics are therefore caused by the coupling between the first mode and the higher modes.

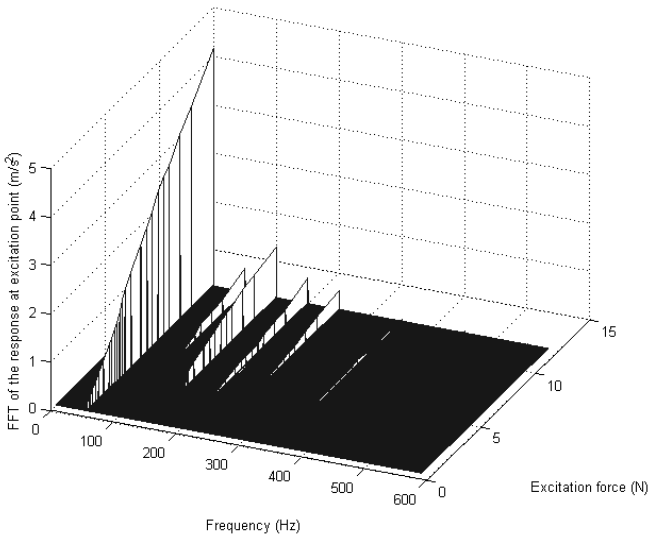

Figure B–5 : FFT of the system response at the drive point (at 50Hz)

The frequency response of the system is obtained by a manual sweep with the excitation force values of 1 N, 3 N, 6.5 N and 8 N. In Figure B–6 we can clearly see the effect of the non-linearity in the change of the first natural frequency and the damping depending on the excitation level (see also Table B–1). Figure B–6 will also be useful for the identification of the Hybrid friction model (Azizian & Mureithi, 2013) parameters.

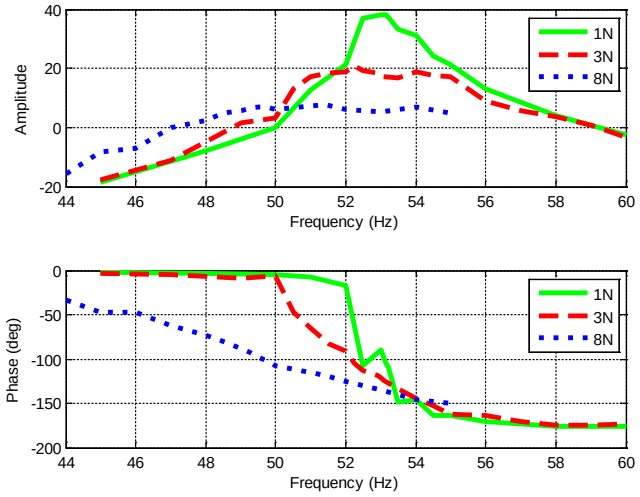

Figure B–6 : The frequency response (FRF) of the system (first harmonic)

Table B–1 : 1st natural frequency

excitation F_{max} *(N)*	***1st natural frequency (Hz)***
1	53
3	52
6.5	50
8	49.1

3. Nonlinear normal modes versus linear normal modes

The first deformed mode varies depending on the excitation level, and may be represented in several harmonic forms. Figure B–7 represents the first harmonic form for two different levels of excitation. In general, the form is between that of a clamped-clamped beam and a simply-supported beam. The shape is closer to a clamped-simply supported beam for very high excitation levels, and closer to a clamped-clamped beam for low excitation levels. This is due to the normal force applied at the contact point and the friction force. It can also be seen in this graph that the approach proposed by Jalali et al. (2011) cannot accurately represent the deformation in the experimental beam contrary to the approach represented here. These features can also be seen in other harmonic forms (see Figure B–14) Appendix A)

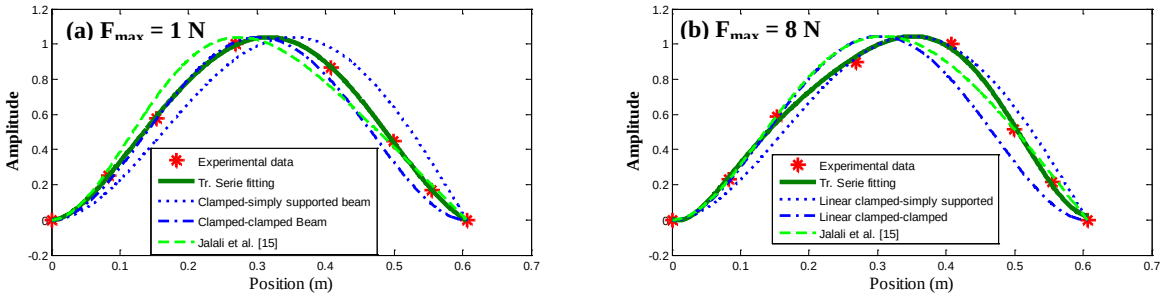

Figure B–7 : The first non-linear mode depending on the level of excitement

Figure B–8 shows the error (difference) between the first experimental normal modes, the NNMs calculated using three methods and the linear normal modes (clamped-simply supported beam and clamped-clamped beam). This graph confirms that NNMs with the approach of harmonic forms (spline fitting and Trigonometric series fitting) better represent the experimental beam deformation and the spline fitting approach gives the best results. The approaches with perfect boundary conditions (LNMs) give poor results as expected.

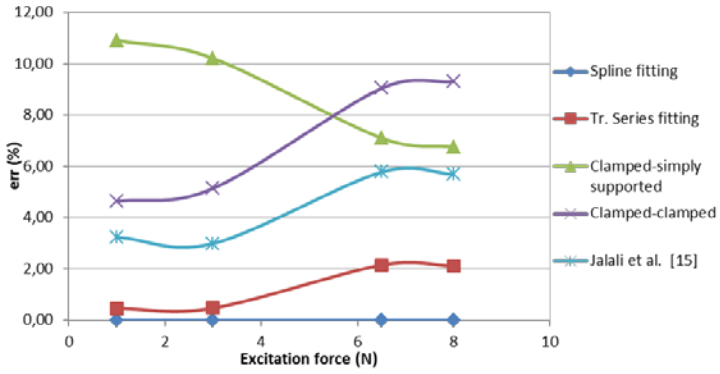

Figure B–8 : The error between the first experimental NM, the NNMs and LMs

4- Reconstruction of accelerometer signals

Using normal modes and the generalized coordinates it is possible to rebuild the accelerometer signals. Figure B–9 shows the response of the beam and the reconstruction of the signals at the driving point. Compared to the approach proposed by (Jalali et al., 2011) the present approach rebuilds the accelerometer signals at all levels of excitation.

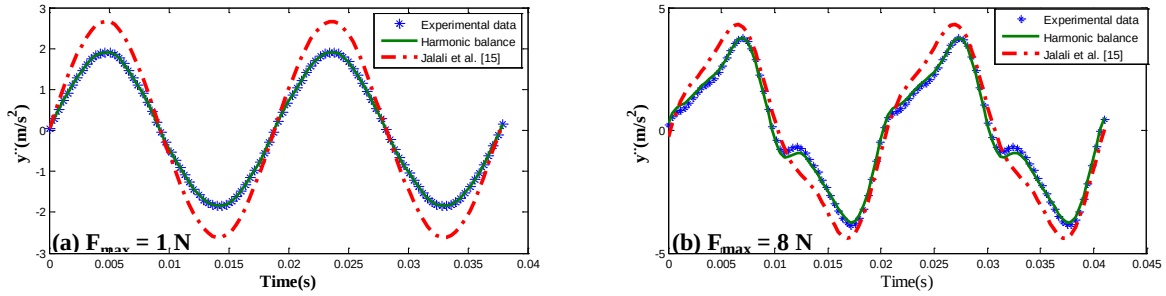

Figure B–9 : The accelerometer signals reconstruction

Figure B–10 confirms these observations, where we see that the reconstruction error of accelerometer signals with the approach proposed by (Jalali et al., 2011) is greater than 16%. However, the reconstruction error of the accelerometer signals by NNMs-NGCs with the approach of harmonic forms is less than 2%.

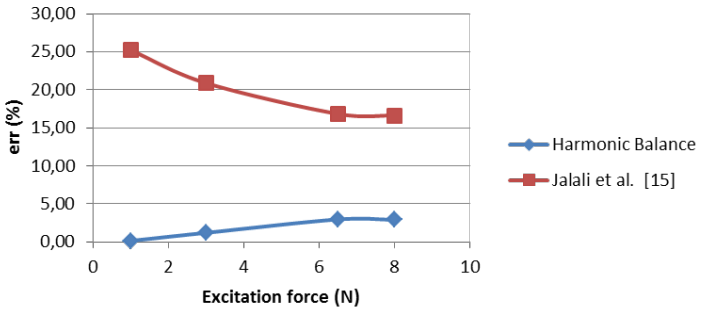

Figure B–10 : The accelerometer signals reconstruction error

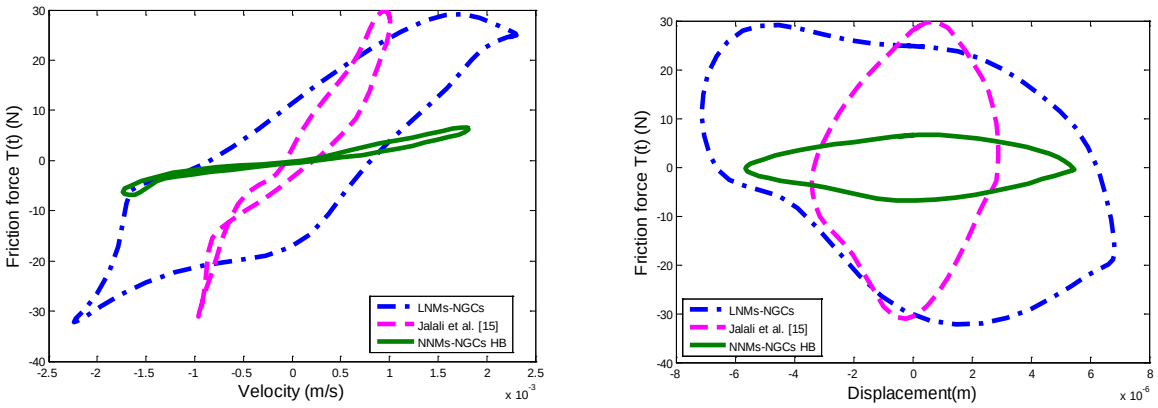

Figure B–11 : Friction force

5. Friction force

Using the results of the NNMs (Figure B–7 and Figure B–14) and generalized coordinates (Eqs. 13, 16 and 24) together with Eqs (7, 11 and 12) the friction force, velocity and the displacement at the contact point can be calculated. It is noteworthy that Jalali et al.(Jalali et al., 2011) used only the first harmonic ($i=1$ in Eq. (7)) in their calculations while in the present case, all the harmonics have been used ($i=$1-n in Eq. (7)).

Figure B–11 represents the friction force as a function of the speed and displacement of the contact point for 6.5 N excitation level (at a frequency of 50 Hz). The level of friction force calculated by the conventional approach (LNMs-NGCs) and the approach proposed by (Jalali et al., 2011) give almost the same level of friction force ≅ 30 N. However the new approach, NNMs-NGCs, gives a much lower force level of approximately 3 N. This is because the first two approaches underestimate some details (the deformed modes in the first approach, the effect of other harmonics and error in calculated deformed harmonics in the second approach) resulting in large errors in the final results.

6. Friction model parameters identification

The hybrid friction model (Azizian, 2012; Azizian & Mureithi, 2013) recently developed to model tube-support interaction is based on the principle of the LuGre model. All properties and benefits of other friction models are included, namely the dynamics of the Dahl model (Dahl, 1976) (i.e. hysteresis effect), the dynamics of bristles (Haessig Jr & Friedland, 1991) and the Stribeck effect (Stribeck & Schröter, 1903). This model has also taken into account the distribution of the stresses in the contact area according to the principle of Cattaneo-Mindlin (Mindlin & Deresiewicz, 1953).

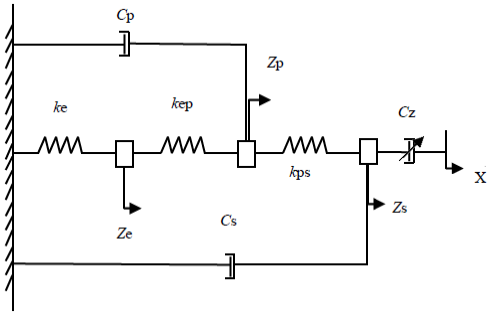

Figure B–12 : Schematic of the hybrid friction model (Azizian, 2012)

The formulation of the Hybrid friction model (Azizian & Mureithi, 2013) is represented in the following equations:

$$T = k_e z_e + c_p \dot{z}_p + c_s \dot{z}_s \qquad (26)$$

$$z = z_e + z_p + z_s \tag{27}$$

$$k_e z_e + k_{ep}(z_e - z_p) = 0 \tag{28}$$

$$k_{ep}(z_p - z_e) + k_{ps}(z_p - z_s) + c_p \dot{z}_p = 0 \tag{29}$$

$$k_{ps}(z_p - z_s) + c_z(\dot{z}_s - \dot{x}) + c_s \dot{z}_s = 0 \tag{30}$$

Where z_e, z_p and z_s are, respectively, the elastic, plastic and partial slip relative displacements. k_e, c_p and c_s are respectively the coefficients of the elastic stiffness, plastic damping and pre-sliding damping. They authors considers two transition stiffness coefficients: elastic-plastic k_{ep} and plastic-pre sliding k_{sp},. c_z is the Stribeck damping which is given by:

$$c_z = \frac{\sigma_0 g(\dot{x})}{\dot{x}} \tag{31}$$

$$\sigma_0 g(\dot{x}) = N\left(\mu_C + (\mu_s - \mu_C)e^{-(\dot{x}/v_s)^2}\right) \tag{32}$$

where

$g(\dot{x})$ is Stribeck function (or Stribeck friction model (Stribeck & Schröter, 1903))

μ_c is kinetic friction coefficient

μ_s is static friction coefficient

v_s is Stribeck velocity

The Dahl model (Dahl, 1976) was the first dynamic friction model. We will use this model to identify two hybrid friction model (Azizian & Mureithi, 2013) parameters, k_e (the equivalent of the σ_0 in Dahl friction model) and μ_c. This model can be written as:

$$\frac{dT}{dt} = \sigma_0 \dot{x} - \frac{T}{F_c}\sigma_0 |\dot{x}| \tag{33}$$

$$F_c = \mu_C \times R \tag{34}$$

$$R = N + P \tag{35}$$

where

F_c is kinetic friction force.

N is a resultant of the normal forces

P is static load to ensure permanent contact between the beam and support

R is support reaction (impact force)

Figure B–13 shows the experimental friction force $T(t)$ calculated using the method proposed in this paper (Figure B–11 NNMs-NGCs HB) and the equivalent force generated by Dahl model after identifying their parameters using two methods. In the first method (Simulation by Dahl model l Figure B–13), the slope σ_{01} is calculated directly from Figure B–13 (the method proposed by (Dahl, 1976)) and F_c is determined using the Matlab® Optimization function FMINSEARCH, we found $\sigma_{01} = 1.19e+6$ N/m and $\mu_c = 0.55$. In the second method (Simulation by Dahl mode 2 Figure B–13), the Matlab®Optimization function FMINCON it used to identify the two parameters at the same time, we got $\sigma_{02} = 1.202e+6$ N/m and $\mu_c = 0.562$. In both methods the objective function is represented as in Eq. (36). The value of μ_c is not far from the normal value of kinetic friction coefficient of steel-steel contact ($\mu_{c\,steel-steel} = 0.56$). Since the Dahl model is the simplest dynamic model it fails to accurately model the behavior of the friction force. However, we were able to find a value of μ_c almost equal to the measured value of the friction coefficient. The identification of other parameters of hybrid friction model (Azizian & Mureithi, 2013) is expected to yield better representation of the friction phenomenon.

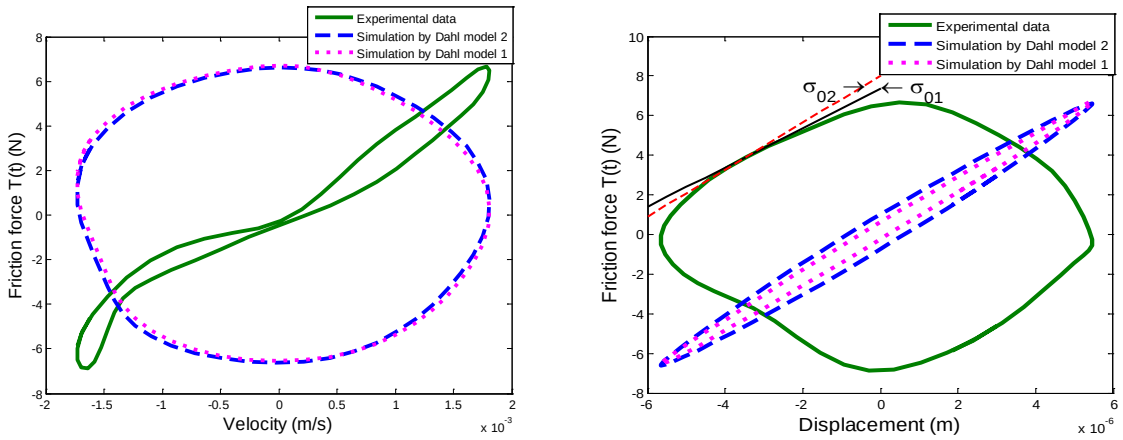

Figure B–13 : Friction force and Dahl model

$$Obj = \left(\left| \max\left(T_{\text{exp.}}\right) - \max\left(T_{suml.}\right) \right| + \left| \min\left(T_{\text{exp.}}\right) - \min\left(T_{suml.}\right) \right| \right) / 2 \qquad (36)$$

where

Obj is objective function,

$T_{\text{exp.}}$ is experimental friction force,

$T_{suml.}$ is simulated friction force using Dahl friction model.

CONCLUSION

Accurate prediction of the dynamics of a structure requires accurate modeling of its boundary conditions. The present work demonstrated that the classical approach to modeling the actual boundary conditions (approach with perfect boundary conditions (LNMs)) gives poor results or fails to represent the actual behaviour of the deformed beam therefore giving poor results.

A new method based on nonlinear modal analysis has been developed to calculate the contact forces. This method is based on the principle of modal superposition and Fourier series expansion.

Three approaches have been developed to identify the normal modes and the generalized coordinates; the NNMs approach with harmonic forms represents the experimental beam deformation better than the approach of Jalali et al. (2011). The assumption used in the method of harmonic balance gives the best result for reconstructing signals from accelerometers for all excitation levels.

For the harmonic balance method, there are two approaches. The first approach is harmonic forms which was represented in this paper, the second, sub-harmonic forms, will be represent in future work.

Although the Dahl model (Dahl, 1976) fails to accurately represent the real behavior of friction force, we managed to find a value of kinetic friction coefficient very close to experimental value. This is an important confirmation of the validty of the the new method represented in this paper for calculating friction force.

REFERENCES

Antunes, J., Axisa, F., Beaufils, B., & Guilbaud, D. (1988). Coulomb friction modelling in numerical simulations of vibration and wear work rate of multispan tube bundles. Paper presented at the International Symposium on Flow-Induced Vibration and Noise: Flow-Induced Vibration in Heat-Transfer Equipment - 1988, November 27, 1988 - December 2, 1988, Chicago, IL, USA.

Azizian, R. (2012). Dynamic Modeling of Tube-Support Interaction in Heat Exchangers. (1027 Ph.D.), Université De Montréal, École Polytechnique De Montréal (Canada), Canada. Available from publications.polymtl.ca & Mémoires et thèses

Azizian, R., & Mureithi, N. (2013). A hybrid friction model for dynamic modeling of stick-slip behavior. Paper presented at the Proc. ASME-PVP Conference, Paris.

Canudas, C. d. W., Olsson, H., Astrom, K. J., & Lischinsky, P. (1995). New model for control of systems with friction. IEEE Transactions on Automatic Control, 40(3), 419-425.

Dahl, P. R. (1976). Solid friction damping of mechanical vibrations. AIAA Journal, 14(12), 1675-1682.

Ewins, D. J. (2000). Modal testing : theory, practice, and application (2nd ed.). Baldock, Hertfordshire, England ; Philadelphia, PA: Research Studies Press.

Gilmore, R. J., & Steer, M. B. (1991). Nonlinear circuit analysis using the method of harmonic balance. A review of the art. Part I. Introductory concepts. International journal of microwave and millimeter-wave computer-aided engineering, 1(1), 22-37.

Haessig Jr, D., & Friedland, B. (1991). On the modeling and simulation of friction. Journal of Dynamic Systems, Measurement and Control, Transactions of the ASME, 113(3), 354-362.

Hassan, M., & Rogers, R. J. (2005). Friction modelling of preloaded tube contact dynamics. Nuclear Engineering and Design, 235(22), 2349-2357.

Jalali, H., Ahmadian, H., & Pourahmadian, F. (2011). Identification of micro-vibro-impacts at boundary condition of a nonlinear beam. Mechanical Systems and Signal Processing, 25(3), 1073-1085.

Johnson, K. L. (1985). Contact mechanics. Cambridge [Cambridgeshire] ; New York: Cambridge University Press.

Karnopp, D. (1985). Computer simulation of stick-slip friction in mechanical dynamic systems. Journal of Dynamic Systems, Measurement and Control, Transactions of the ASME, 107(1), 100-103.

Mindlin, R. D., & Deresiewicz, H. (1953). Elastic spheres in contact under varying oblique forces. American Society of Mechanical Engineers -- Transactions -- Journal of Applied Mechanics, 20(3), 327-344.

Nicholas, B., Christophe, P., & Steven, S. (1994). Non-linear modal analysis of structural systems using multi-mode invariant manifolds. Paper presented at the Dynamics Specialists Conference. http://dx.doi.org/10.2514/6.1994-1672

Pesheck, E., Boivin, N., Pierre, C., & Shaw, S. (2001). Nonlinear Modal Analysis of Structural Systems Using Multi-Mode Invariant Manifolds. Nonlinear Dynamics, 25(1-3), 183-205.

Rogers, R. J., & Pick, R. J. (1977). Factors associated with support plate forces due to heat-exchanger tube vibratory contact. Nuclear Engineering and Design, 44(2), 247-253

Rosenberg, R. M. (1966). On Nonlinear Vibrations of Systems with Many Degrees of Freedom. In H. L. D. P. G. L. H. W. O. W. P. R. F. P. G.G. Chernyi & H. Ziegler (Eds.), Advances in Applied Mechanics (Vol. Volume 9, pp. 155-242): Elsevier.

Shaw, S. W., & Pierre, C. (1992). On nonlinear normal modes. Paper presented at the Winter Annual Meeting of the American Society of Mechanical Engineers, November 8, 1992 - November 13, 1992, Anaheim, CA, USA.

Stribeck, R., & Schröter, M. (1903). Die wesentlichen Eigenschaften der Gleit-und Rollenlager: Untersuchung einer Tandem-Verbundmaschine von 1000 PS: Springer.

Xi, T., & Rogers, R. J. (1996). Dynamic friction modelling in heat exchanger tube simulations. Paper presented at the Proceedings of the 1996 ASME Pressure Vessels and Piping Conference. Part 1 (of 2), July 21, 1996 - July 26, 1996, Montreal, Can.

Appendix A

HARMONIC FORMS

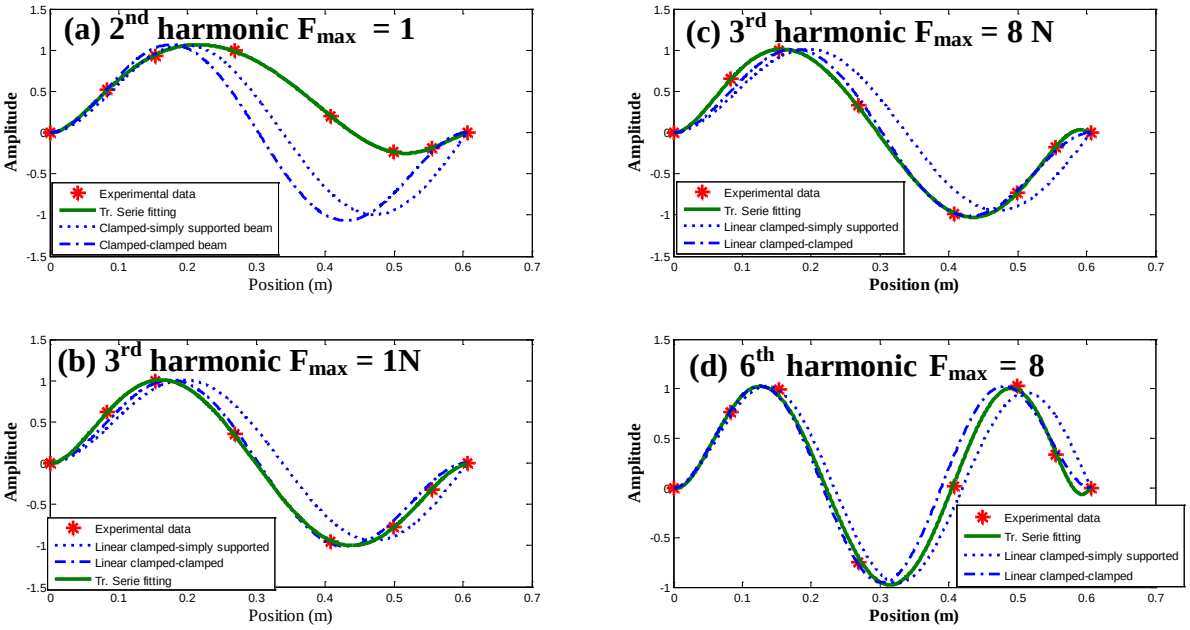

Figure B–14 : The first non-linear mode depending on the level of excitement

ANNEXE C – ARTICLE 4: NONLINEAR NORMAL MODES AND THE LUGRE FRICTION MODEL PARAMETER IDENTIFICATION

Hadji, A., & Mureithi, N. (2014)

Paper presented at the Proc. ASME-IMAC Conference, Montreal, Quebec, Canada.
DOI:10.1115/IMECE2014-38997

ABSTRACT

A Hybrid friction model has recently been developed by Azizian and Mureithi (Azizian & Mureithi, 2013) to simulate the general friction behavior between surfaces in contact. However, identification of the model parameters remains an unresolved problem.

To identify the parameters of the friction model, the following quantities are required: contact forces (friction and impact forces), the slip velocity and displacement in the contact region. Direct measurement of these quantities is difficult. In the present work, a beam clamped at one end and simply supported with the consideration of friction effect at the other is used as a mechanical amplifier of the friction effects at the microscopic level. Using this simplified approach, the contact forces, the sliding velocity and the displacement can be indirectly obtained by measuring the beam vibration response.

A new method based on nonlinear modal analysis to calculate the contact forces is developed in the present work. The method is based on the modal superposition principle and Fourier series expansion.

For the harmonic balance method, two approaches were tested. The approach based on sub-harmonic forms gave the best results.

Signal reconstruction made it possible to accurately identify the parameters of the hybrid friction model with a multiple step approach.

INTRODUCTION

The fretting wear of steam generator tubes due to vibration remains an important problem in the nuclear industry. The tube-support interaction friction models cited by (M. Hassan & Rogers,

2005) are special cases of static friction models. The velocity limited friction model (VLFM) (Rogers & Pick, 1977) is a continuous Coulomb model without Stribeck effects. The force balance friction model (FBFM) (Xi & Rogers, 1996) and the spring damper friction model (SDFM) (Antunes et al., 1988) are based on the modeling of friction by springs and dampers. The principle of the Karnopp friction model (Karnopp, 1985) is used in the FBFM friction model. A H Hybrid friction model (Azizian, 2012; Azizian & Mureithi, 2013) has recently been developed. The authors used the basic approach of the Dahl (1976) and LuGre (Canudas et al., 1995) models with additional consideration of the stress distribution in the contact area in accordance with the principle of Cattaneo-Mindlin (Kenneth Langstreth Johnson, 1985).

To identify the model parameters, the system nonlinear modes are needed. Nonlinear normal modes (NNMs) have increasingly been used in the analysis of nonlinear systems, as revealed by the works of Rosenberg (1966) and Pierre and co-workers (Boivin et al., 1994; Pesheck et al., 2001; Shaw & Pierre, 1992). Other methods used in the analysis of nonlinear systems include the harmonic balance (HB) method (Gilmore & Steer, 1991) which is also widely used in the electronics field. The HB method was used for the first time to experimentally determine the NNMs in our previous work (Hadji & Mureithi, 2014a).

The realization of a test bench able to acquire all of the following quantities: friction force, impact force, slip velocity and displacement, is vital since these provide the parameters needed for friction modeling. The present test bench is based on the apparatus of Jalali et al. (2011).

NOMENCLATURE

A	Area of the cross section of the beam
E	Youngs modulus
F	Excitation force by a shaker
F_c	Kinetic friction force limitation
F_s	Static friction force limitation
I	Quadratic bending moment
L	Length of the beam
N	Resultant of the normal force
P	Static load to ensure a permanent contact between the beam and support
R	Support reaction (impact force)

T	Frictional force
X_f	Position of the excitation point
c_p	Plastic damping
c_s	Pre-sliding damping
c_z	Stribeck damping
e	Thickness of the beam
$g(\dot{x})$	Stribeck function
k_e	Elastic stiffness
k_{ep}	Elastic-plastic stiffness
k_{ps}	Plastic-pre sliding stiffness
q_i	Linear generalized coordinates
$\tilde{q}_i$	Nonlinear generalized coordinates
r	Radius of the contact element (half-cylinder)
(t)	Time dependence
u	Displacement at the contact zone
(x)	Position dependence
z_e	Elastic slip relative displacements
z_p	Plastic slip relative displacements
z_s	Partial slip relative displacements
ϕ_i	Linear normal modes
$\tilde{\phi}_i$	Nonlinear normal modes
μ_c	Kinetic friction coefficient
μ_s	Static friction coefficient
ρ	Density of the beam material
σ_0	Stiffness coefficient (Stiffness of the Bristlls)
σ_1	Damping coefficient of the Bristlls

σ_2 Viscous friction coefficient

v Velocity at the contact area

v_s Stribeck velocity

THE TEST RIG AND THEORETICAL CONSIDERATION

The test rig (Figure C–1) is based on a simple concept. The specimen is a simply supported beam on one side (but also including friction effects) and clamped on the other. Figure C–2 represents all the forces acting at the contact point. The beam is excited by a shaker and its response measured by accelerometers; for more details see (Hadji & Mureithi, 2014a).

The beam equation of motion is:

$$\rho A\ddot{y}(x,t)+EIy''''(x,t)-T(t)y''(x,t)=F(t)\delta(x-X_f) \qquad (1)$$

with the following boundary conditions :

At $x=0$: $y(0,t)=0$ and $y'(0,t)=0$ (2,3)

and at $x=L$: $EIy''(L,t)=\left(r+e/2\right)T(t)$ (4)

and $EIy'''(L,t)=-N(t)+m\ddot{y}(L,t)+T(t)y'(L,t)$ (5)

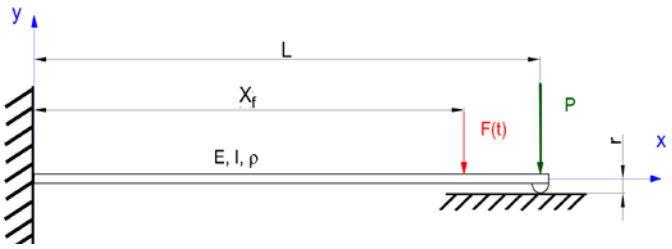

Figure C–1 : Schematic of a nonlinear beam

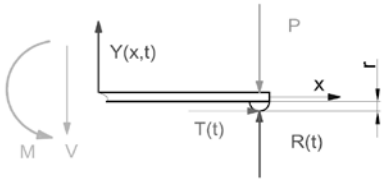

Figure C–2 : Direction of forces applied at the contact point

The characteristics of the beam are as follows: length L = 606 mm, width b = 38.88 mm, thickness e = 4.76 mm and the radius r = 5 mm. The six accelerometers (3 acc. PCB 352C33, 2 acc. PCB 353B33 and an impedance head PCB 288D01) used in the test were positioned at 0.083 m, 0.153 m, 0.268 m, 0.408 m, 0.499 m and 0.555 m, respectively, and the driving point (impedance head) at 0.555 m from the clamped end.

The response of the system may be written in the following form, based on modal superposition:

$$y_j\left(x_j,t\right)=\sum_{i=1}^{n}\phi_i\left(x_j\right)q_i\left(t\right) \tag{6}$$

where:

$q_i\left(t\right)$ (i=1,2,...n) are the generalized coordinates

$\phi_i\left(x\right)$ (i=1,2,...n) are the normal modes of the system.

Using the modal superposition principle, Eq. (6), the boundary conditions equations, Eqs. (2-4) and the Galerkin method, Eq. (1) can be rewritten as follows:

$$\ddot{q}_i\left(t\right)+\omega_i^2q_i\left(t\right)-F(t)\tilde{\phi}_i\left(X_f,a\right)=-N(t)\tilde{\phi}_i\left(L,a\right)+$$
$$\left[r\tilde{\phi}_i{}'\left(L,a\right)+\sum_{j=1}^{n}q_j\left(t\right)\left(\int_0^L\tilde{\phi}_j''\left(x,a\right)\tilde{\phi}_i\left(x,a\right)dx-\tilde{\phi}_i'\left(L,a\right)\tilde{\phi}_j\left(L,a\right)\right)\right]T(t),\quad i\text{=1-}n \tag{7}$$

where:

$N(t)=P-R\left(t\right)$ is the impact force (or the resultant of the normal force in the contact zone). Modal orthogonality may be expressed as follows:

$$\rho A\int_0^L\tilde{\phi}_i\left(x,a\right)\tilde{\phi}_j\left(x,a\right)dx+m\tilde{\phi}_i\left(L,a\right)\tilde{\phi}_j\left(L,a\right)=\delta_{ij} \tag{8}$$

$$EI\int_0^L\tilde{\phi}_i^{"}\left(x,a\right)\tilde{\phi}_j^{"}\left(x,a\right)dx=\omega_i^2\delta_{ij} \tag{9}$$

The reader is referred to (Jalali et al., 2011) for the derivation of Eq.(7). In the analysis the term $\tilde{\phi}_i'\left(L,a\right)\tilde{\phi}_j\left(L,a\right)$ is considered negligible. The displacement and velocity in the contact area can be calculated as follows. The displacement:

$$u\left(t\right)=-\frac{1}{2}\int_0^L\left(\frac{\partial y\left(x,t\right)}{\partial x}\right)^2dx+r\left.\frac{\partial y\left(x,t\right)}{\partial x}\right|_{x=L}+\frac{T\left(t\right)L}{AE} \tag{10}$$

This equation can be rewritten as:

$$u(t) = -\frac{1}{2}\sum_{i=1}^{n} q_i^2(t)\int_0^L \left(\frac{\partial \phi_i(x)}{\partial x}\right)^2 dx + r\sum_{i=1}^{n} q_i(t)\phi_i'(L) + \frac{T(t)L}{AE} \qquad (11)$$

By differentiating Eq.(11) we obtain the following velocity equation:

$$v(t) = -\frac{1}{2}\sum_{i=1}^{n} \dot{q}_i^2(t)\int_0^L \left(\frac{\partial \phi_i(x)}{\partial x}\right)^2 dx + r\sum_{i=1}^{n} \dot{q}_i(t)\phi_i'(L) + \frac{\dot{T}(t)L}{AE} \qquad (12)$$

Since the beam is excited at its first natural frequency (resonance), adequate modal analysis is necessary.

THE NONLINEAR NORMAL MODES

Nonlinear normal modes (NNMs) were first introduced by Rosenberg (1966). However, the NNMs description proposed by Pierre and co-workers (Boivin et al., 1994; Jiang et al., 2005; Pesheck et al., 2001; Shaw & Pierre, 1992) is the most general and applicable to all systems. Researchers have also attempted to identify the NNMs of a beam experimentally. For example, Jalali et al. (2011) used basic linear normal modes to rebuild the NNMs of a clamped-simply supported beam with friction effect.

In our recent work (Hadji & Mureithi, 2014a), we presented the different approaches used to model non-linear dynamical systems. In the modal analysis of a nonlinear system, the nonlinear effects may be accounted for either in the normal modes, in the generalized coordinates, or in both the normal modes and the generalized coordinates. The assumption most commonly used is the linear normal modes and nonlinear generalized coordinates (LNMs-NGCs). Jalali et al. (2011) proposed the second assumption: the nonlinear normal modes coupled with linear generalized coordinates (NNMs-LGCs). In the newest assumption (Hadji & Mureithi, 2014a), nonlinear normal modes and nonlinear generalized coordinates (NNMs-NGCs) are used. The NNMs are computed based on the harmonic form approach (or average phase approach) as described next.

The harmonic form approach is based on the principal of modal superposition and utilizes all the harmonics that appear in the system response signal. The NNMs are calculated in the following manner :

STEP 1

The Fourier series of the response signal is written as follows:

$$y_j(x_j, t) = \sum_{i=1}^{n} A_{ij}(x_j)\cos\left(i\cdot\omega_{ext}t + \psi_{ij}(x_j)\right) \qquad (14)$$

STEP 2

This equation can also be written as:

$$y_j\left(x_j,t\right)=\sum_{i=1}^{n}\tilde{\phi}_i\left(x_j\right)C_i\cos\left(i\cdot\omega_{ext}t+\psi_i\right) \tag{15}$$

$$\tilde{\ddot{q}}_i\left(t\right)=C_i\cos\left(i\cdot\omega_{ext}t+\varphi_i\right) \tag{16}$$

where x_j is the position of the accelerometer *j*,

The transition from Eq. (15) to Eq. (16) requires the calculation of ψ_i by the minimization of the error in the reconstruction of the accelerometer signals (or ψ_{ij} optimal) and C_i by the normalization of $\tilde{\phi}_i(x_j)$ from $A_{ij}\left(x_j\right)$.

STEP 3

$\tilde{\phi}_i(x)$ are represented by a series of trigonometric functions, Eq. (17). To reduce the smoothing error, an intermediate step must be used (natural smoothing spline) to predict the natural deformed form of the beam and improve the fitting result.

$$\tilde{\phi}_i(x)=\sum_{k=1}^{n}\begin{pmatrix}a_{ik1}\sin\left(\beta_{ik}x\right)+a_{ik2}\sinh\left(\beta_{ik}x\right)\\+a_{ik3}\cos\left(\beta_{ik}x\right)+a_{ik4}\cosh\left(\beta_{ik}x\right)\end{pmatrix} \tag{17}$$

n equal to 3 minimizes the fitting error.

In this paper, a new approach for calculating the NNMs based on the assumption NNMs-NGCs is used.

In this approach the NNMs are calculated in the following manner:

STEP 1

The Fourier series of the response signal is written as follows:

$$y_j\left(x_j,t\right)=\sum_{i=1}^{n}\alpha_{ij}\left(x_j\right)\cos\left(i\cdot\omega_{ext}t\right)+\sum_{i=1}^{n}\beta_{ij}\left(x_j\right)\sin\left(i\cdot\omega_{ext}t\right) \tag{18}$$

STEP 2

This equation can also be written as:

$$y_j\left(x_j,t\right)=\sum_{i=1}^{n}\tilde{\phi}_{i1}\left(x_j\right)\gamma_{i1}\cos\left(i\cdot\omega_{ext}t\right)+\sum_{i=1}^{n}\tilde{\phi}_{i2}\left(x_j\right)\gamma_{i2}\sin\left(i\cdot\omega_{ext}t\right) \tag{19}$$

$$\begin{cases} \tilde{\ddot{q}}_{i1}(t) = \gamma_{i1}\cos(i\cdot\omega_{ext}t) \\ \tilde{\ddot{q}}_{i2}(t) = \gamma_{i2}\sin(i\cdot\omega_{ext}t) \end{cases} \tag{20}$$

$$\begin{cases} \tilde{\phi}_{i1}(x_j) = \dfrac{\alpha_{ij}(x_j)}{\gamma_{i1}} \\ \tilde{\phi}_{i2}(x_j) = \dfrac{\beta_{ij}(x_j)}{\gamma_{i2}} \end{cases} \tag{21}$$

where x_j is the position of the accelerometer j, $\tilde{\phi}_{i1}(x_j)$ is the first sub-harmonic form (or cosine sub-harmonic form) and $\tilde{\phi}_{i1}(x_j)$ is the second sub-harmonic form (or sine sub-harmonic form). The modal equation of motion (Eq. (7)) becomes:

$$\begin{aligned} &\left(\ddot{q}_{ik}(t) + a_{il}\ddot{q}_{il}(t)\right) + \omega_i^2\left(q_{ik}(t) + b_{il}q_{il}(t)\right) - F(t)\tilde{\phi}_{ik}(X_f) = \\ &-N(t)\tilde{\phi}_{ik}(L) \\ &+\left(\begin{array}{l} \left(\sum_{i=1}^{n} q_{i1}(t)\int_0^L \tilde{\phi}_{i1}''(x)\tilde{\phi}_{jk}(x)dx + \sum_{i=1}^{n} q_{i2}(t)\int_0^L \tilde{\phi}_{i2}''(x)\tilde{\phi}_{jk}(x)dx\right) \\ -\left(\sum_{i=1}^{n}\tilde{\phi}_{i1}'(L)\tilde{q}_{i1}(t) + \sum_{i=1}^{n}\tilde{\phi}_{i2}'(L)\tilde{q}_{i2}(t)\right)\tilde{\phi}_{jk}(L) \\ +\left(r + e/2\right)\tilde{\phi}_{ik}'(L) \end{array}\right) T(t) \end{aligned} \quad , \ i\text{=1-}n; \tag{22}$$

with k and l chosen as follows (k=1, l=2 or k=1, l=2). In the present work, k=1 and l=2 were chosen. The modal orthogonality equations (Eqs. (8 and 9)) become:

$$\begin{cases} \rho A\int_0^L \tilde{\phi}_{ik}(x)\tilde{\phi}_{jk}(x)dx + m\tilde{\phi}_{ik}(L)\tilde{\phi}_{jk}(L) = \delta_{ij} \\ \rho A\int_0^L \tilde{\phi}_{il}(x)\tilde{\phi}_{jk}(x)dx + m\tilde{\phi}_{ik}(L)\tilde{\phi}_{jk}(L) = a_{ij} \end{cases} \tag{23}$$

$$\begin{cases} EI\int_0^L \tilde{\phi}_{ik}''(x)\tilde{\phi}_{jk}''(x)dx = \omega_i^2\delta_{ij} \\ EI\int_0^L \tilde{\phi}_{il}''(x)\tilde{\phi}_{jk}''(x)dx = \omega_i^2 b_{ij} \end{cases} \tag{24}$$

Equations (20-21) are used to calculate γ_{i1} and γ_{i2} by the normalization of $\tilde{\phi}_{ik}(x_j)$ from $\left(\alpha_{ij}\ or\ \beta_{ij}\right)$.

STEP 3

$\tilde{\phi}_{i1}(x)$ and $\tilde{\phi}_{i2}(x)$ are represented by a natural smoothing spline and a series of trigonometric functions (Eq. (17)).

EXPERIMENTAL RESULTS AND DISCUSSION

In the previous paper (Hadji & Mureithi, 2014a), some experimental results were presented, including the detection of the different slip regimes, non-linear friction effects and the comparison between the nonlinear normal modes and the linear normal modes. In this section, we continue this comparison, by comparing the linear normal modes and the NNMs calculated using the two approaches based on the harmonic balance method.

1. Nonlinear normal modes versus linear normal modes

In the previous work (Hadji & Mureithi, 2014a), we found NNMs to have a form between that of a clamped-clamped beam and a simply-supported beam. For high excitation levels the NNMs approached clamped-pinned mode shapes, while for low excitation, the NNMs were similar to clamped-clamped beam modes.

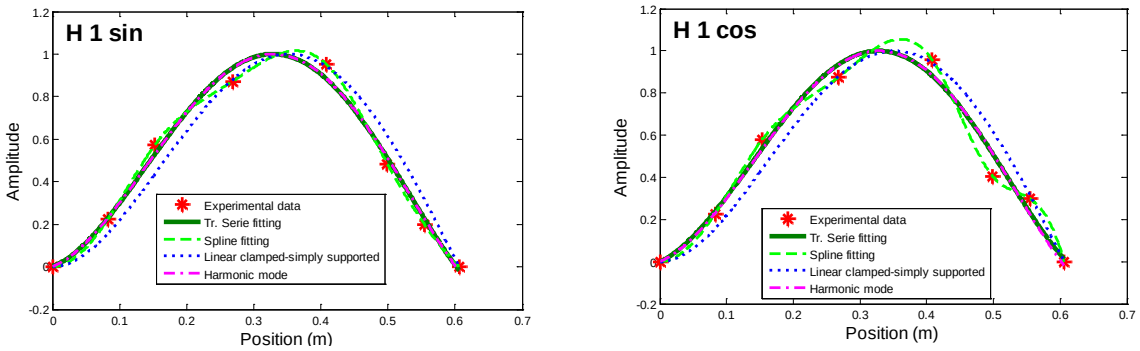

Figure C–3 : The first harmonic and sub-harmonic form at 6.5 N excitation level

Figures (Figure C–3 and Figure C–4) present the first and second harmonic forms and the two sub-harmonic forms at the 6.5 N excitation level fitted using the natural spline and the trigonometry series. In both figures the linear normal modes are also plotted. The fitting using the trigonometric series of the first harmonic gives the same harmonic form and sub-harmonic form, hence cannot accurately represent the experimental data. However, the fitting using the natural spline accurately represents the experimental data.

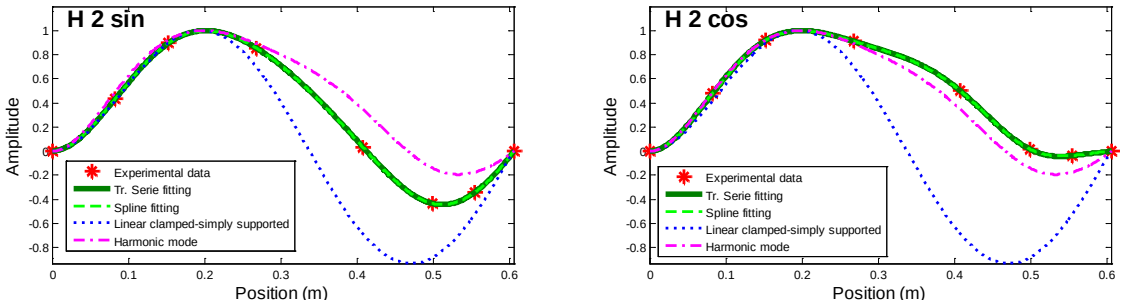

Figure C–4 : The second harmonic and sub-harmonic form at 6.5 N excitation level

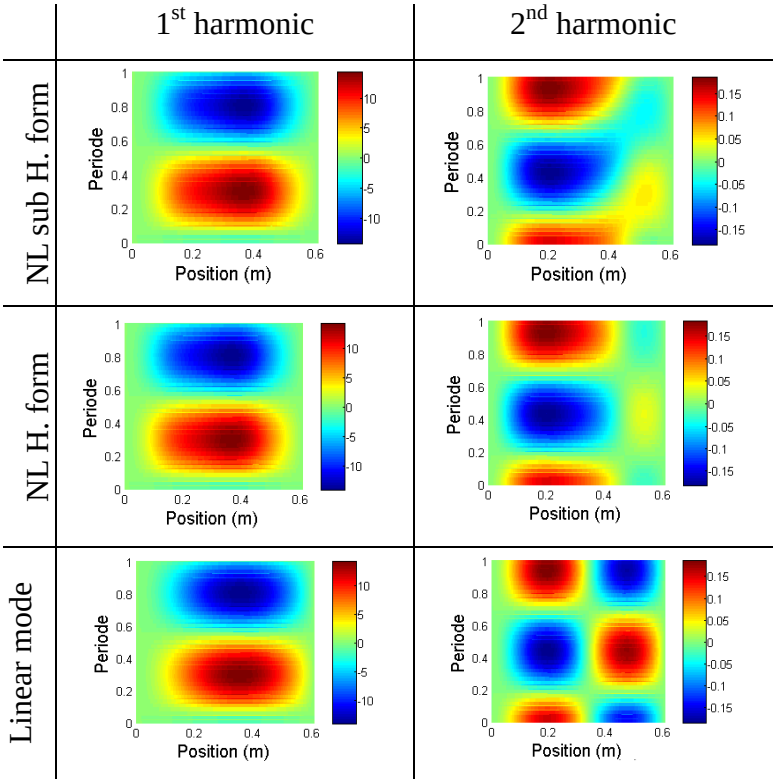

Figure C–5 : The evaluation of the 1st and the 2nd harmonic form in one period

In the second harmonic, Figure C–4, the fitting using the trigonometric series gives the same result as the natural spline fitting. On the other hand, the harmonic form and sub-harmonic form are different, giving two different sub-harmonic forms. We can see similar results in the other harmonics, Figure C–9 Appendix A. In Figure C–9, Appendix A, we can also see that the harmonic form is close to either of the sub-harmonic forms (the two sub-harmonics are equal) if

the harmonic frequencies are close to the natural frequencies, for example (H4= 200Hz and the second natural frequency F_{n2}= 160 Hz, H6= 300Hz and the third natural frequency F_{n3}= 319 Hz)
Figure C–5 presents the first and second harmonic forms in one period. This representation is useful in explaining the nonlinear behavior. For the first harmonic, it is difficult to distinguish the difference between the linear and the nonlinear behaviors. However, for the second harmonic the difference between the linear and the nonlinear behavior is clearly visible.
The evolution of the linear mode in one period is homogeneous and symmetric; conversely, both the nonlinear forms (NL sub H. form, NL H. form) are none homogeneous but have slight symmetry in the time axes (vertical axes) in the harmonic form and asymmetry in the sub-harmonic form.
In the Figure C–10 in Appendix A, same behavior is found for the high harmonics.

2- Reconstruction of accelerometer signals

The accelerometer signals are reconstructed using the normal modes and the generalized coordinates. In our previous work (Hadji & Mureithi, 2014a), the response of the beam and the reconstruction of the signals at the driving point as well as the fitting error were presented as functions of the excitation levels. Table C–1 presents the error of the accelerometer signals reconstruction. The sub-harmonic form approach gives, in general, better results than the harmonic form. The sub-harmonic form approach also gives a small improvement relative to the trigonometry series fit (0.02% less error at the driving point and 0.41% less error of all acceleration signals). However, the sub-harmonic form approach with the spline form improves the reconstruction of the accelerometer signals with an error less than $1e^{-11}$ % (machine error).

Table C–1 : The accelerometer signals reconstruction error

Specification	***Error (%)***	
	Driving point	**All Acc.**
HB Harmonic form with spline fitting	2.96	1.65
HB Harmonic form with Tr. series fitting	7.68	4.72
HB sub-Harmonic form with spline fitting	2.9e-12	2.8e-12
HB sub-Harmonic form with Tr. series fitting	7.66	4.31

3. Friction force

Using the results of the NNMs (Figure C–3, Figure C–4 and Figure C–9) and generalized coordinates (Eqs. 16 and 22) together with Eqs (7 or 22, 11 and 12) the friction force, velocity and the displacement at the contact point can be calculated. This is the primary goal of the foregoing analysis.

Figure C–6 presents the friction force as a function of the velocity and displacement at the contact point for 6.5 N excitation level (at a frequency of 50 Hz). The friction force calculated by the sub-harmonic form with trigonometric series fitting is smaller than the friction force level calculated using the three other approaches. This is due to the inability of the trigonometric series and the harmonic form approaches to represent all the harmonic forms accurately, specifically the first harmonic and sub-harmonic forms. This underestimation leads to poor results for this approach.

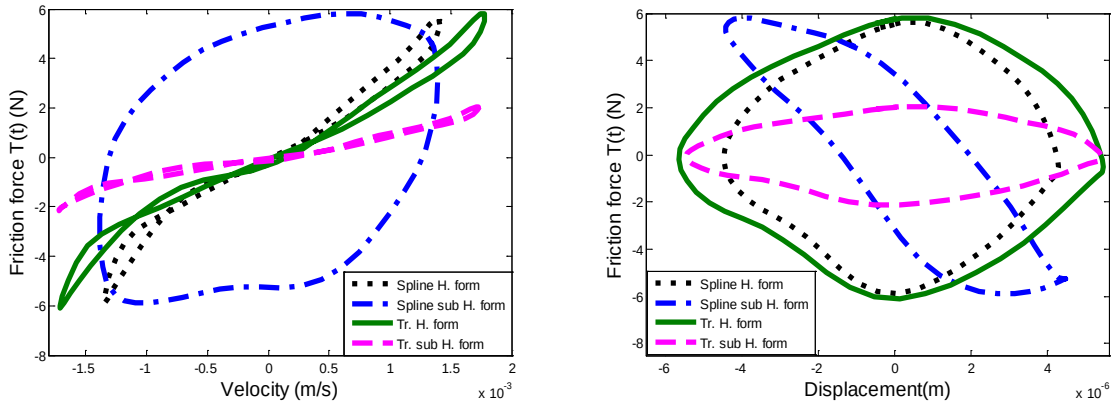

Figure C–6 : Friction force

4. Friction model parameters identification

The hybrid friction model (Azizian, 2012; Azizian & Mureithi, 2013) recently developed to model tube-support interaction is based on the principle of the LuGre friction model (Canudas et al., 1995). All properties and benefits of other friction models are included, namely the dynamics of the Dahl friction model (Dahl, 1976) (i.e. hysteresis effect), the dynamics of bristles (Haessig Jr & Friedland, 1991) and the Stribeck effect (Stribeck & Schröter, 1903). This model also takes

into account the distribution of the stresses in the contact area according to the principle of Cattaneo-Mindlin (1953).

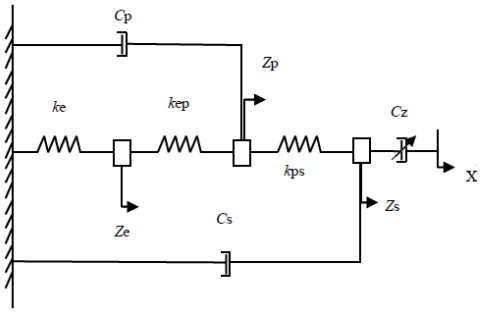

Figure C–7 : Schematic of the hybrid friction model (Azizian, 2012)

The formulation of the Hybrid friction model (Azizian & Mureithi, 2013) is presented in the following equations:

$$T = k_e z_e + c_p \dot{z}_p + c_s \dot{z}_s \quad (24)$$

$$z = z_e + z_p + z_s \quad (25)$$

$$k_e z_e + k_{ep}(z_e - z_p) = 0 \quad (26)$$

$$k_{ep}(z_p - z_e) + k_{ps}(z_p - z_s) + c_p \dot{z}_p = 0 \quad (27)$$

$$k_{ps}(z_p - z_s) + c_z(\dot{z}_s - \dot{x}) + c_s \dot{z}_s = 0 \quad (28)$$

where z_e, z_p and z_s are, respectively, the elastic, plastic and partial slip relative displacements. k_e, c_p and c_s are the coefficients of the elastic stiffness, plastic damping and pre-sliding damping, respectively. The authors considered two transition stiffness coefficients: elastic-plastic k_{ep} and plastic-pre-sliding k_{ps}. c_z is the Stribeck damping which is given by:

$$c_z = \frac{\sigma_0 g(\dot{x})}{\dot{x}} \quad (29)$$

$$\sigma_0 g(\dot{x}) = N\left(\mu_C + (\mu_s - \mu_C)e^{-(\dot{x}/v_s)^2}\right) \quad (30)$$

where:

$g(\dot{x})$ Stribeck function (or Stribeck friction model (Stribeck & Schröter, 1903))

μ_c is kinetic friction coefficient

μ_s is static friction coefficient

v_s is Stribeck velocity

The Dahl friction model (Dahl, 1976) is used to identify two Hybrid friction model (Azizian & Mureithi, 2013) parameters, k_e (the equivalent of the σ_0 in Dahl friction model) and μ_c. This model can be written as:

$$\frac{dT}{dt} = \sigma_0 \dot{x} - \frac{T}{F_c}\sigma_0 \left|\dot{x}\right| \quad (31)$$

$$F_c = \mu_C \times R \quad (33)$$

$$R = N + P \quad (34)$$

where

F_c is kinetic friction force

N is a resultant of the normal forces

P is static load to ensure permanent contact between the beam and support

R is support reaction (impact force)

The LuGre friction model (Canudas et al., 1995), widely used in the control domain, is also based on the principal of the Dahl friction model (Dahl, 1976). This model will be used to identify the three other hybrid friction model (Azizian & Mureithi, 2013) parameters. k_e and c_s are the equivalent of σ_0 and σ_1 in the LuGre friction model (Canudas et al., 1995) respectively. μ_c, μ_s and $v_{\underline{s}}$ are used to identify c_z. This model can be expressed as:

$$F = \sigma_0 z + \sigma_1 \frac{dz}{dt} + \sigma_2 \dot{x} \quad (35)$$

$$\frac{dz}{dt} = \dot{x} - \frac{\left|\dot{x}\right|}{g(\dot{x})} z \quad (36)$$

where σ_0 and σ_1 are respectively, stiffness and damping coefficients of the bristles, σ_2 is the viscous friction coefficient and $g(\dot{x})$ is defined in Eq. (30).

Figure C–8 shows the experimental friction force $T(t)$ calculated using the method proposed in this paper (Figure C–6 Tr. H. Form) and the equivalent force generated by the Dahl friction model (Dahl, 1976) (with the best result presented in the previous paper (Hadji & Mureithi, 2014a)) and by LuGre friction model (Canudas et al., 1995) after identifying their parameters using two approaches. In the first approach (simulation by LuGre model l Figure C–8), the static friction coefficient μ_s is fixed at $\mu_s = 0.74$ (Jalali et al., 2011). The other parameters are then determined using the Matlab® Optimization function FMINSEARCH. In the second approach (simulation by LuGre model 2 Figure C–8), the static and the dynamic friction coefficients (μ_s and μ_c) are set at the measured values ($\mu_s = 0.74$, $\mu_c = 0.56$) (Jalali et al., 2011) and the other parameters determined using the same Matlab® function FMINSEARCH and the results presented in Table C–2. The viscous friction coefficient is supposed to be equal to zero because of non-lubrication assumed at the contact area in both the approaches and the coefficient σ_0 of Dahl friction model (Dahl, 1976) is used as an initial value to identify the σ_0 of LuGre friction model (Canudas et al., 1995).

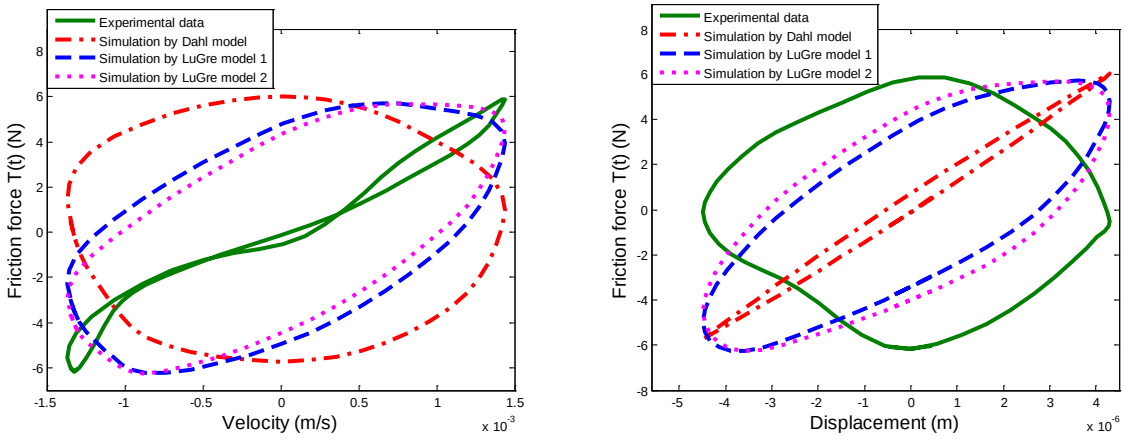

Figure C–8 : Friction force and LuGre model

In both methods the objective function is that given in Eq. (37). From Figure C–8, the LuGre friction model (Canudas et al., 1995) better represents the behavior of the friction force. The second approach, (fixed μ_s and μ_c by its measured value), gives the best results.

$$Obj = \left(\left| \max\left(T_{\exp.}\right) - \min\left(T_{\exp.}\right) \right| - \left| \max\left(T_{suml.}\right) - \min\left(T_{suml.}\right) \right| \right) / 2 \quad (37)$$

where

Obj is objective function,

$T_{\exp.}$ is experimental friction force,

$T_{suml.}$ is simulated friction force using Dahl or LuGre friction model.

Table C–2 : LuGre and Dahl friction model parameters

parameter	***LuGre friction model***		***Dahl friction model***
	*approach **1***	*approach **2***	
μ_c	0.657	0.56	0.56
μ_s	0.74	0.74	-
v_s (m/s)	3.164e-3	3.397e-3	-
σ_0 *(N/m)*	1.159e+6	1.062e+6	1.202e+6
σ_1 *(N.s/m)*	2.619e+3	3.063e+3	-
σ_2 *(N.s/m)*	0	0	-

CONCLUSION

A new approach based on the nonlinear modal analysis has been developed to calculate the contact forces. This method is based on the principle of modal superposition and Fourier series expansion.

The approaches developed to identify the normal modes and the generalized coordinates based on sub-harmonic forms (presented in the present work) represent the experimental beam deformation better than the approach based on harmonic forms (Hadji & Mureithi, 2014a); and using the spline fitting gives better results than the fitting using the trigonometric series. The assumption of NNMs-NGCs using the harmonic balance method with spline fitting approach gives the best results for reconstructing signals from accelerometers for all excitation levels.

Five parameters (k_e, c_s and c_z (μ_s, μ_c and v_s)) of the Hybrid friction model (Azizian & Mureithi, 2013) have been determined using Dahl (1976) and LuGre (Canudas et al., 1995) friction models, the three other parameters (c_p, k_{ep} and k_{ps}) will be determined in future work.

The present work demonstrates that the LuGre friction model is capable of simulating friction behavior better than Dahl friction model.

REFERENCES

Antunes, J., Axisa, F., Beaufils, B., & Guilbaud, D. (1988). Coulomb friction modelling in numerical simulations of vibration and wear work rate of multispan tube bundles. Paper presented at the International Symposium on Flow-Induced Vibration and Noise: Flow-Induced Vibration in Heat-Transfer Equipment - 1988, November 27, 1988 - December 2, 1988, Chicago, IL, USA.

Azizian, R. (2012). Dynamic Modeling of Tube-Support Interaction in Heat Exchangers. (1027 Ph.D.), Université De Montréal, École Polytechnique De Montréal (Canada), Canada. Available from publications.polymtl.ca & Mémoires et thèses

Azizian, R., & Mureithi, N. (2013). A hybrid friction model for dynamic modeling of stick-slip behavior. Paper presented at the Proc. ASME-PVP Conference, Paris.

Canudas, C. d. W., Olsson, H., Astrom, K. J., & Lischinsky, P. (1995). New model for control of systems with friction. IEEE Transactions on Automatic Control, 40(3), 419-425.

Dahl, P. R. (1976). Solid friction damping of mechanical vibrations. AIAA Journal, 14(12), 1675-1682.

Gilmore, R. J., & Steer, M. B. (1991). Nonlinear circuit analysis using the method of harmonic balance. A review of the art. Part I. Introductory concepts. International journal of microwave and millimeter-wave computer-aided engineering, 1(1), 22-37.

Hadji, A., & Mureithi, N. (2014). Nonlinear normal modes and the Dahl friction model parameter identification. Paper presented at the Proc. ASME-PVP Conference, Anaheim, California, USA.

Haessig Jr, D., & Friedland, B. (1991). On the modeling and simulation of friction. Journal of Dynamic Systems, Measurement and Control, Transactions of the ASME, 113(3), 354-362.

Hassan, M., & Rogers, R. J. (2005). Friction modelling of preloaded tube contact dynamics. Nuclear Engineering and Design, 235(22), 2349-2357.

Jalali, H., Ahmadian, H., & Pourahmadian, F. (2011). Identification of micro-vibro-impacts at boundary condition of a nonlinear beam. Mechanical Systems and Signal Processing, 25(3), 1073-1085.

Johnson, K. L. (1985). Contact mechanics. Cambridge [Cambridgeshire] ; New York: Cambridge University Press.

Karnopp, D. (1985). Computer simulation of stick-slip friction in mechanical dynamic systems. Journal of Dynamic Systems, Measurement and Control, Transactions of the ASME, 107(1), 100-103.

Mindlin, R. D., & Deresiewicz, H. (1953). Elastic spheres in contact under varying oblique forces. American Society of Mechanical Engineers -- Transactions -- Journal of Applied Mechanics, 20(3), 327-344.

Nicholas, B., Christophe, P., & Steven, S. (1994). Non-linear modal analysis of structural systems using multi-mode invariant manifolds. Paper presented at the Dynamics Specialists Conference.

Pesheck, E., Boivin, N., Pierre, C., & Shaw, S. (2001). Nonlinear Modal Analysis of Structural Systems Using Multi-Mode Invariant Manifolds. Nonlinear Dynamics, 25(1-3), 183-205.

Rogers, R. J., & Pick, R. J. (1977). Factors associated with support plate forces due to heat-exchanger tube vibratory contact. Nuclear Engineering and Design, 44(2), 247-253.

Rosenberg, R. M. (1966). On Nonlinear Vibrations of Systems with Many Degrees of Freedom. In H. L. D. P. G. L. H. W. O. W. P. R. F. P. G.G. Chernyi & H. Ziegler (Eds.), Advances in Applied Mechanics (Vol. Volume 9, pp. 155-242): Elsevier.

Shaw, S. W., & Pierre, C. (1992). On nonlinear normal modes. Paper presented at the Winter Annual Meeting of the American Society of Mechanical Engineers, November 8, 1992 - November 13, 1992, Anaheim, CA, USA.

Stribeck, R., & Schröter, M. (1903). Die wesentlichen Eigenschaften der Gleit-und Rollenlager: Untersuchung einer Tandem-Verbundmaschine von 1000 PS: Springer.

Xi, T., & Rogers, R. J. (1996). Dynamic friction modelling in heat exchanger tube simulations. Paper presented at the Proceedings of the 1996 ASME Pressure Vessels and Piping Conference. Part 1 (of 2), July 21, 1996 - July 26, 1996, Montreal, Can.

APPENDIX B

HARMONIC FORMS

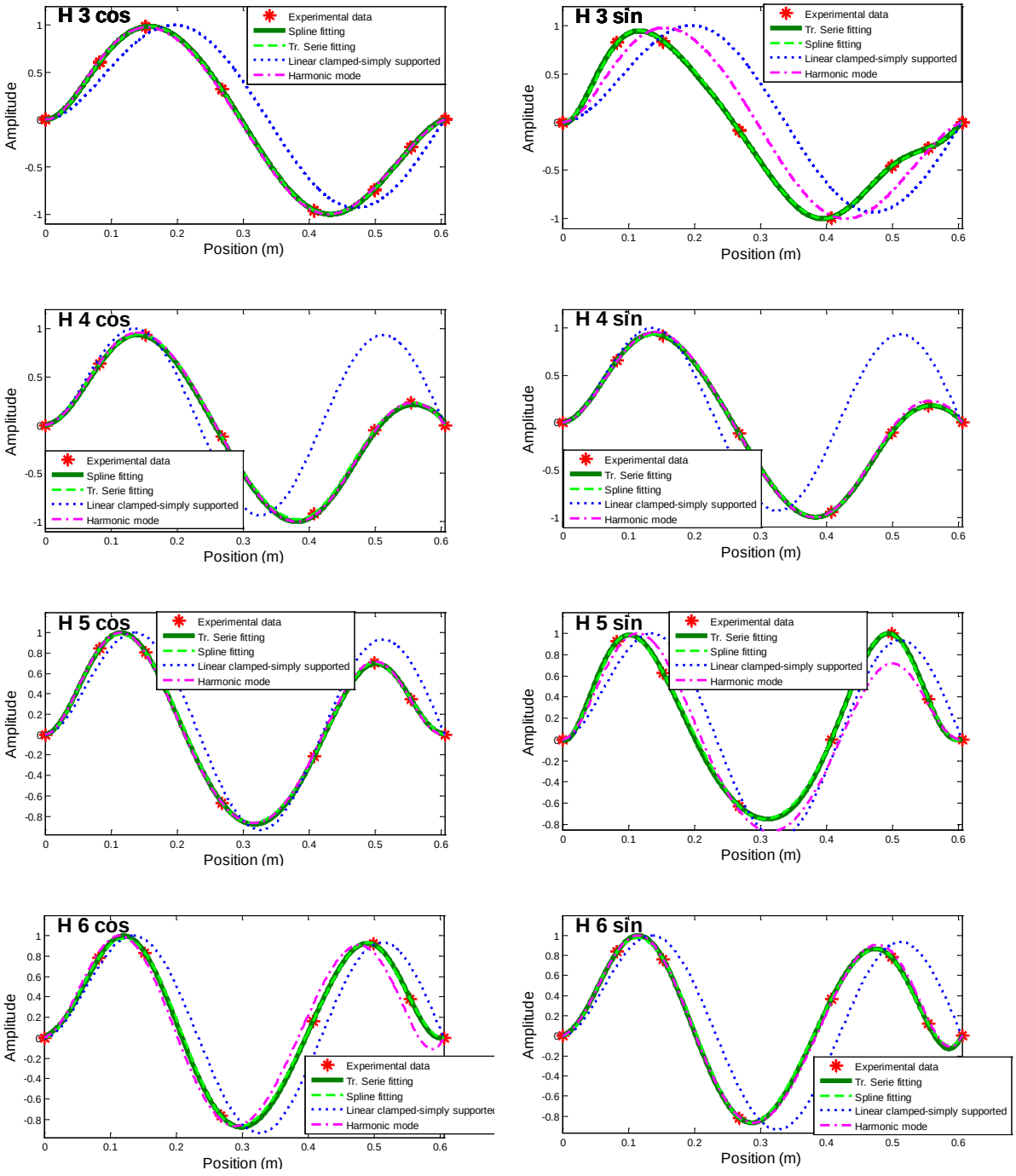

Figure C–9 : The high harmonic and sub-harmonic form at 6.5 N excitation level

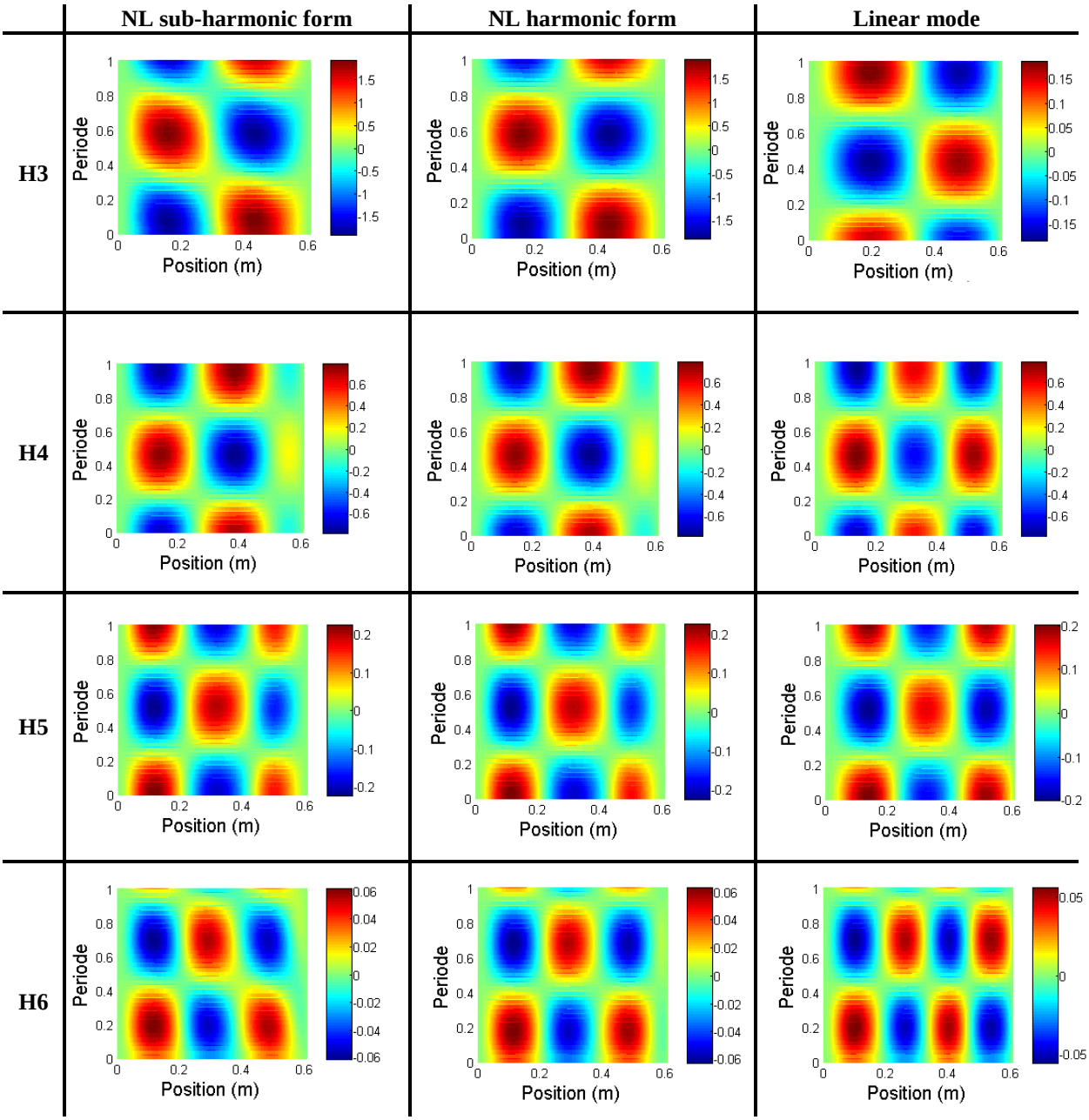

Figure C–10 : The evaluation of high harmonic form in one period

ANNEXE D – ARTICLE 5: VALIDATION OF A FRICTION MODEL PARAMETERS IDENTIFIED USING THE INVERSE HARMONIC BALANCE METHOD

Hadji, A., & Mureithi, N. (2015)

Paper presented at the ASME 2015 Pressure Vessels and Piping Conference, PVP 2015, July 19, 2015 - July 23, 2015, Boston, Massachusetts, United states. DOI:10.1115/PVP2015-45627

ABSTRACT

A hybrid friction model was recently developed by Azizian and Mureithi (Azizian & Mureithi, 2013) to simulate the friction behavior of tube-support interaction. However, identification of the model parameters remains unresolved.

In previous work, the friction model parameters were identified using reverse the harmonic method, where the following quantities were indirectly obtained by measuring the vibration response of a beam: friction force, sliding speed of the force of impact and local displacement at the contact point.

In the present work, the simulation by the finite element method (FEM) of a beam clamped at one end and simply supported with the consideration of friction effect at the other is conducted. This beam is used to validate the inverse harmonic balance method and the parameters of the friction models identified previously.

Two static friction models (the Coulomb model and Stribeck model) are tested. The two models produce friction forces of the correct order of magnitude compared to the friction force calculated using the inverse harmonic balance method. However, the models cannot accurately reproduce the beam response; the Stribeck friction model is shown to give the response closer to experiments.

The results demonstrate some of the challenges associated with accurate friction model parameter identification using the inverse harmonic balance method. The present work is an intermediate step toward identification of the hybrid friction model parameters and, longer term, improved analysis of tube-support dynamic behavior under the influence of friction.

INTRODUCTION

The friction model is an essential element in the detailed analysis of the dynamics of steam generator tubes in the nuclear industry. Most of the friction models currently used to simulate tube-support interaction are cited by (M. Hassan & Rogers, 2005). These are special cases of static friction models. The velocity limited friction model (VLFM) (Rogers & Pick, 1977) is a continuous Coulomb model without Stribeck effects (Stribeck & Schröter, 1903). The force balance friction model (FBFM) (Xi & Rogers, 1996) and the spring damper friction model (SDFM) (Antunes et al., 1988) are two models based on springs and dampers. The principle of the Karnopp friction model (Karnopp, 1985) is used in the FBFM friction model. Recently a hybrid friction model (Azizian, 2012; Azizian & Mureithi, 2013) has been developed to model tube-support interaction. In the hybrid model the all properties and benefits of other friction models are included, namely the dynamics of the Dahl model (Dahl, 1976) (i.e. hysteresis effect), the dynamics of bristles (Haessig Jr & Friedland, 1991) and the Stribeck effect (Stribeck & Schröter, 1903) (transition from the static friction limitation to the kinetic friction limitation). This model also takes into account the distribution of the stresses in the contact area according to the principle of Cattaneo-Mindlin (1953) to model the pre-sliding phenomenon.

In finite element modeling (FEM) codes, the Coulomb friction model and the decay friction model are widely used; these are combined with the principle of the velocity limit (Rogers & Pick, 1977) to model the pre-sliding (stick) regime (ABAQUS-User's-Manual, 2013). Most of the numerical algorithms for analyzing dynamic friction in FEM codes are presented by Oden and Martins (1985). Diehl (1995) has also numerically investigated the friction effect of a circular rigid body in sliding contact with a flexible beam.

In this paper, we validate the friction coefficient identified experimentally in previous work (Hadji & Mureithi, 2014a, 2014b) using the finite element method (FEM) by Abaqus Software.

Traditionally friction model parameters have been identified by direct friction force measurement. In the present ongoing work an indirect approach, based on acceleration measurement, has been proposed (Hadji & Mureithi, 2014a, 2014b). To identify the friction model parameters experimentally using this indirect method, accurate nonlinear normal modes are needed. Nonlinear normal modes (NNMs) and the principle of inverse harmonic balance

(IHB) based on the harmonic balance (HB) method (Gilmore & Steer, 1991) were developed and presented in previous work (Hadji & Mureithi, 2014a, 2014b).

In the previous work (Hadji & Mureithi, 2014a, 2014b), the parameters of the Dahl (1976) and LuGre (Canudas et al., 1995) friction models, which are respectively based on Coulomb and Stribeck friction models were reported. In this paper, therefore, we analyze these two friction models to validate their friction coefficients.

NOMENCLATURE

A	Area of the cross section of the beam
E	Youngs modulus
F	Excitation force by a shaker
F_c	Kinetic friction force limitation
F_{ex}	Excitation force amplitude
F_f	Slip tolerance (fraction of characteristic contact surface length)
F_s	Static friction force limitation
I	Quadratic bending moment
L	Length of the beam
N	Resultant of the normal force
Obj	Optimization objective function
P	Static load to ensure a permanent contact between the beam and support
R	Support reaction (impact force)
RT	Resultant of the force at the contact point in the sliding direction
T	Frictional force
T_{crit}	Critical friction force
$T_{\text{exp.}}$	Experimental friction force
$T_{suml.}$	Simulated friction force
X_f	Position of the excitation point
$\dot{W}$	Work rate

c_p Plastic damping

c_s Pre-sliding damping

c_z Stribeck damping

e Thickness of the beam

$g(\dot{x})$ Stribeck function

k_e Elastic stiffness

k_{ep} Elastic-plastic stiffness

k_{ps} Plastic-pre sliding stiffness

$\bar{l}_i$ Characteristic contact surface length

m Half cylinder mass (contact element)

n Mode index

q_i Linear generalized coordinates

$\tilde{q}_i$ Nonlinear generalized coordinates

r Radius of the contact element (half-cylinder)

(t) Time dependence

u Displacement at the contact zone

u_{crit} Elastic slip

x_j Position of the accelerometer j

(x) Position dependence

y System response (beam deflection)

y_j System response of the accelerometer j

z_e Elastic slip relative displacements

z_p Plastic slip relative displacements

z_s Partial slip relative displacements

α Proportional mass damping

α_n Proportional mass damping of mode n

δ Stribeck exponent

ϕ_i Linear normal modes

$\tilde{\phi}_i$ Nonlinear normal modes

μ_c Kinetic friction coefficient

μ_s Static friction coefficient

ρ Density of the beam material

v Velocity at the contact area

ω_n Naturel pulsation of mode n

ζ Damping ratio

ζ_n Damping ratio of mode n

PRINCIPLE OF THE INVERSE HARMONIC BALANCE METHOD

Figure D–1 shows a schematic of the test specimen used to extract the contact force (friction and impact) and displacement. The specimen is a beam simply supported at one end (but allowing sliding hence friction effects) and clamped at the other. In Figure D–2 all the forces applied at the contact point are represented; for more details see (Hadji & Mureithi, 2014a, 2014b).

The beam equation of motion is:

$$\rho A\ddot{y}(x,t)+EIy''''(x,t)-T(t)y''(x,t)=F(t)\delta\left(x-X_f\right) \tag{1}$$

with the following boundary conditions :

$$\text{At } x=0: \quad y(0,t)=0 \text{ and } y'(0,t)=0 \tag{2,3}$$

$$\text{and at } x=L: \quad EIy''(L,t)=\left(r+e/2\right)T(t) \tag{4}$$

$$\text{and } EIy'''(L,t)=-N(t)+m\ddot{y}(L,t)+T(t)y'(L,t) \tag{5}$$

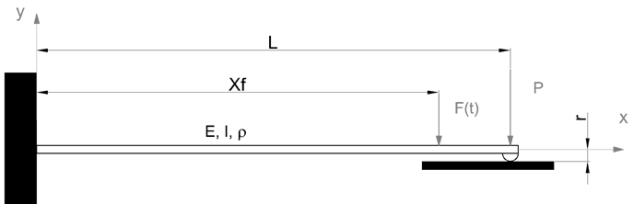

Figure D–1 : Schematic of a nonlinear beam (Hadji & Mureithi, 2014a)

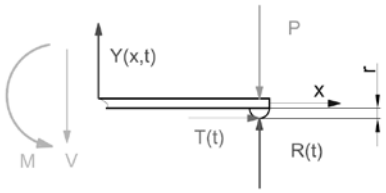

Figure D–2 : Forces acting at the contact point (Hadji & Mureithi, 2014a)

The characteristics of the beam are presented in Table D–1 below. The beam response is measured by six accelerometers (3 acc. PCB 352C33, 2 acc. PCB 353B33 and an impedance head PCB 288D01) used in the tests are positioned at 0.083 m, 0.153 m, 0.268 m, 0.408 m, 0.499 m and 0.555 m, respectively. The beam is excited by a shaker with the driving point (impedance head) positioned at 0.555 m from the clamped end.

Based on modal superposition, the response of the system may be written in the following form:

$$y_j\left(x_j,t\right)=\sum_{i=1}^{n}\phi_i\left(x_j\right)q_i\left(t\right) \tag{6}$$

where:

$q_i\left(t\right)$ (i=1,2,...n) are the generalized coordinates

$\phi_i\left(x\right)$ (i=1,2,...n) are the normal modes of the system.

Using the modal superposition principle, Eq. (6), the boundary conditions equations, Eqs. (2-4) and the Galerkin method, Eq. (1) can be rewritten as follows:

$$\ddot{q}_i(t)+\omega_i^2 q_i(t)-F(t)\tilde{\phi}_i\left(X_f,a\right)=-N(t)\tilde{\phi}_i(L,a)+$$
$$\left[r\tilde{\phi}_i{}'(L,a)+\sum_{j=1}^{n}q_j(t)\left(\int_0^L\tilde{\phi}_j''(x,a)\tilde{\phi}_i(x,a)dx-\tilde{\phi}_i'(L,a)\tilde{\phi}_j(L,a)\right)\right]T(t),\quad i\text{=1-}n\ (7)$$

where:

$N(t)=P-R(t)$

Modal orthogonality may be expressed as follows:

$$\rho A\int_0^L\tilde{\phi}_i(x,a)\tilde{\phi}_j(x,a)dx+m\tilde{\phi}_i(L,a)\tilde{\phi}_j(L,a)=\delta_{ij} \quad (8)$$

$$EI\int_0^L\tilde{\phi}_i^{"}(x,a)\tilde{\phi}_j^{"}(x,a)dx=\omega_i^2\delta_{ij} \quad (9)$$

and *m*is the half cylinder mass (contact element)

The displacement and velocity in the contact area (axial displacement and velocity of the beam end) can be calculated as follows:

$$u(t)=-\frac{1}{2}\sum_{i=1}^{n}q_i^2(t)\int_0^L\left(\frac{\partial\phi_i(x)}{\partial x}\right)^2dx+r\sum_{i=1}^{n}q_i(t)\phi_i'(L)+\frac{T(t)L}{AE} \quad (10)$$

$$v(t)=-\frac{1}{2}\sum_{i=1}^{n}\dot{q}_i^2(t)\int_0^L\left(\frac{\partial\phi_i(x)}{\partial x}\right)^2dx+r\sum_{i=1}^{n}\dot{q}_i(t)\phi_i'(L)+\frac{\dot{T}(t)L}{AE} \quad (11)$$

In our previous work, two new methods were proposed to identify the nonlinear normal modes (NNMs). Here, we present only a summary of the first method, where the NNMs are computed based on the harmonic form (or average phase) approach. The NNMs are calculated in the following manner:

STEP 1

The Fourier series of the response signal is written as follows:

$$y_j\left(x_j,t\right)=\sum_{i=1}^{n}A_{ij}\left(x_j\right)\cos\left(i\cdot\omega_{ext}t+\psi_{ij}\left(x_j\right)\right) \quad (12)$$

STEP 2

This equation can also be written as:

$$y_j\left(x_j,t\right)=\sum_{i=1}^{n}\tilde{\phi}_i\left(x_j\right)\tilde{\tilde{q}}_i\left(t\right) \quad (13)$$

$$\tilde{\tilde{q}}_i\left(t\right)=C_i\cos\left(i\cdot\omega_{ext}t+\psi_i\right) \quad (14)$$

Where x_j is the position of the accelerometer *j*,

The transition from Eq. (12) to Eq. (13) requires the calculation of ψ_i (Eq. (14)) by the minimization of the error in the reconstruction of the accelerometer signals and C_i by the normalization of $\tilde{\phi}_i(x_j)$ from $A_{ij}\left(x_j\right)$.

STEP 3

$\tilde{\phi}_i(x)$ are represented by a series of trigonometric functions as

$$\tilde{\phi}_i(x)=\sum_{k=1}^{n}\begin{pmatrix}a_{ik1}\sin\left(\beta_{ik}x\right)+a_{ik2}\sinh\left(\beta_{ik}x\right)\\+a_{ik3}\cos\left(\beta_{ik}x\right)+a_{ik4}\cosh\left(\beta_{ik}x\right)\end{pmatrix} \quad (17)$$

n =3 reduces the fitting error to an acceptable level.

NUMERICAL SIMULATION

Coulomb and decay friction models are widely used in the finite element method software. In this work, we analyze these two friction models and validate the friction coefficient identified experimentally in the previous works (Hadji & Mureithi, 2014a, 2014b). Firstly, we present the principles of these two models.

Coulomb friction model

In the Coulomb friction model the friction force is computed as (analytical formulation):

$$T = \begin{cases} \mu_c N\left(-sig\left(v\right)\right) & if \quad v \neq 0 \\ RT & if \quad v = 0 \end{cases} \tag{18}$$

where

μ_c is kinetic friction coefficient

N is a resultant of the normal forces at the contact point

v velocity at the contact point

RT is the resultant of the tangential force at the contact point in the sliding direction.

Generally, in the sticking regime, the resultant of the tangential force RT is less than the kinetic friction force $\mu_c N$. The sliding regime begins when the resultant of the tangential force reaches this limit ($RT >= \mu_c N$). But in the (ABAQUS) FEM code the formulation of the Coulomb friction model is similar in form to the Karnopp friction model (Karnopp, 1985) or the velocity-limited friction model (Rogers & Pick, 1977). The latter is used to model the sticking (or pre-sliding) regime (called the "elastic slip" regime in Abaqus (ABAQUS-User's-Manual, 2013)). The Coulomb friction model FEM formulation is given by:

$$T = \begin{cases} k_s u & if \quad u \leq u_{crit} \\ \mu_c N\left(-sig\left(v\right)\right) & if \quad u > u_{crit} \end{cases} \tag{19}$$

and

$$k_s = \frac{T_{crit}}{u_{crit}} \tag{20}$$

$$T_{crit} = \mu_c N \tag{21}$$

where

T_{crit} is critical friction force

u_{crit} is critical elastic slip

In general k_s or u_{crit} is defined by the user in most of FEM software. However in Abaqus there are two option to define the limiting values: Abaqus uses the same option (k_s or u_{crit} is defined by the user) in the Lagrange method. Alternatively, in penalty method, u_{crit} is calculated automatically during the simulations using the formula:

$$u_{crit} = F_f \bar{l}_i \tag{22}$$

where

$\bar{l}_i$ is characteristic contact surface length

F_f is the slip tolerance (default value, $F_f = 0.005$ (ABAQUS-User's-Manual, 2013))

The slip tolerance F_f is the maximum allowable 'elastic slip' (pre-sliding displacement), expressed as a fraction of a characteristic length. The characteristic length is the average length of the contact surface elements. The value of 0.5% is considered typical and used by default in the code. Alternatively, an absolute value (e.g. based on known experimental values) of the characteristic length may be specified. Note that 'elastic slip' is, strictly, not slip at all but rather refers to pre-sliding relative displacement between the contact surfaces. The relative surface displacement is possible due the contact area asperities which deform elastically without breaking. Gross slip occurs when the asperities break.

Decay friction model (Stribeck friction model)

The decay friction model is a special case of the Stribeck friction model (Stribeck & Schröter, 1903) (Eq. 23), with the exponent δ equal to one. Equation 23 represents the general Stribeck friction model (Stribeck & Schröter, 1903) in the slip regime. However, in the pre-sliding (or elastic slip) regime, the friction force takes the same value in the Eqs. 19 to 21 with the replacement of μ_c by μ_s in Eq. 21.

$$T = N\left(\mu_C + (\mu_s - \mu_C)e^{-(v/v_s)^{\delta}}\right)\left(-sig\left(v\right)\right) \tag{23}$$

where

μ_s is static friction coefficient

v_s is Stribeck velocity

δ is Stribeck exponent

To validate the friction model parameters using the FEM code, we must validate the other parameters used as well as the contact algorithms (surface to surface or nodes to surface) and the slip tolerance F_f . In the present work the surface-to-surface contact algorithm with the hard contact model is considered. One of the important parameters investigated is the slip tolerance F_f .

Finite element modeling

The beam of Figure D–1 is modelled by FEM, in conjunction with the friction models presented above. The beam is discretized using Timoshenko beam elements (1D elements). The 1D model is, however, validated using 3D solid elements (3D elements). The characteristic of the finite elements are presented in Table D–1.

Table D–1 : Finite element model

Property	***Symbol***	***Quantity***	***units***
Young's modulus	E	210	GPa
Density	ρ	7800	kg/m^3
Length	L	606	mm
Width	l	38.88	mm
Thick	e	4.78	mm
Radius	r	5	mm
Damping ratio	ζ_1	0.01	%
Proportional mass damping	α_1	0.06	
Normal force	N	83	N
Excitation force amplitude	F_{ex}	6.5	N
Kinetic friction coefficient	μ_c	0.56	-
Static friction coefficient	μ_s	0.74	-
Stribeck velocity	v_s	1.154e-3	m/s

The friction model parameters are presented in Table D–1. The parameters μ_c , μ_s and v_s were identified experimentally using the Dahl friction model (Dahl, 1976) and LuGre friction model (Canudas et al., 1995). These models are detailed in the previous works (Hadji & Mureithi,

2014a, 2014b). The objective function previously used for parameter identification is that given in Eq. (24). Optimization based on an objective function is used to validate the simulation results here as well.

All the results are obtained at the excitation force amplitude of 6.5 N.

$$Obj = \left(\left| \max\left(T_{\exp.}\right) - \min\left(T_{\exp.}\right) \right| - \left| \max\left(T_{suml.}\right) - \min\left(T_{suml.}\right) \right| \right) / 2 \qquad (24)$$

where

Obj is objective function,

$T_{\exp.}$ is experimental friction force,

$T_{suml.}$ is simulated friction force.

In addition to direct parameter validation, further computations are done to investigate the problem of energy dissipation; specifically the difference between experiments and simulations. In the model, proportional (Rayleigh) damping is introduced to simulate energy dissipation due to friction. The mass proportional mass damping coefficient α_n is given by the following equation:

$$\alpha_n = 2\omega_n\zeta_n \qquad (25)$$

where

ω_n is the natural frequency of mode n,

ζ_n is the damping ratio of mode n.

The value of the damping ratio ζ in Table D–1 is identified experimentally using the impact test and the logarithmic decrement method.

SIMULATION RESULTS

All the results of the simulation are obtained using Abaqus software version 6.12-3, with 5 sec simulation time, 0.8 ms fixed time step using the implicit integration method. We begin by presenting the modal analysis results.

Table D–2 presents the first resonance frequency. The simulation of our numerical model with Coulomb and decay friction models give approximately equal first resonance frequencies

(difference of 0.85 Hz). However, these are slightly lower than the experimental resonance frequency, with decay friction model's resonance frequency being the nearest to the experimental value (a difference of 0.2 Hz).

Table D–2 : 1st resonance frequency

test	***1st resonance frequency(Hz)***
Experimental	50
Coulomb	48.95
Decay	49.80

Figure D–3 presents the first nonlinear normal mode (NNM). The simulated results of both friction models have approximately the same NNMs; where their form is between the NNM identified experimentally using the inverse harmonic balance method (IHB) (Hadji & Mureithi, 2014a, 2014b) and the linear normal mode (LNM) of the clamped-simply supported beam. However, the NNM of the simulated results using Coulomb friction model is close to the LNM. The decay friction model is found to yield modal parameters including resonance frequency and the nonlinear normal modes (NNMs) very close to the experiments.

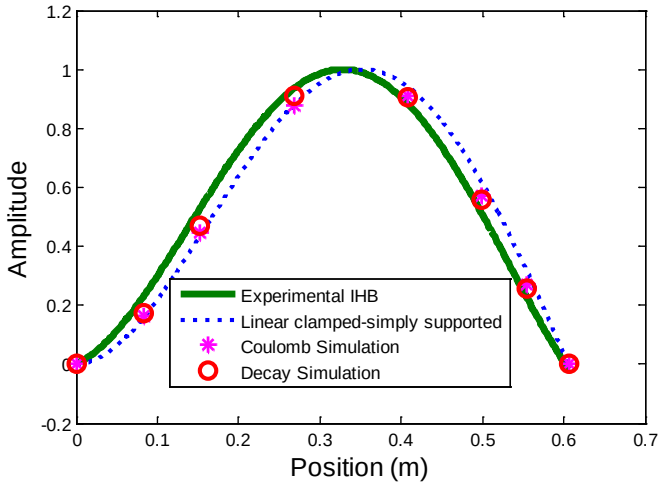

Figure D–3 : 1st nonlinear normal mode

Note that while the nonlinear (NNM) mode appears similar to the linear (LNM) mode, the small difference is important; the mode spatial derivatives are particularly critical for accurate determination of the friction dynamics at the contact point; this is evident in Eq.(7). The

difference is evident when one compares the experimental and numerical FRFs in Figure D–4 and Figure D–5. The predicted vibration response using the Coulomb model is much higher than the response obtained experiments. Whereas the vibration response using Coulombs friction model is more than eighteen times larger than the experimental value, that of the decay friction model is eight times larger. Furthermore, the experimental response occurs over a wider frequency bandwidth. The large response predicted by the model shows that the models do not correctly capture the energy dissipation due to friction. This is partly expected due to the known inadequacies of the Coulomb and decay friction models. Note, however, that there is gradual improvement in the predictive behavior between the more basic Coulomb and the improved decay friction model. The decay friction model peak frequency is close to 50 Hz, which is the correct experimental value. Modeling the Stribeck effect also significantly improves the response amplitude estimation. The next step involves moving next to more sophisticated models – the Dahl, LuGre and eventually the Hybrid friction models. Prior to this, the role played by the numerical implementation of these models in the FEM code needed to be verified. This is important because the implementation of the friction models in FEM codes is not mathematically trivial and involves adjustments and additional parameters. The effect of numerical model parameters, e.g. the slip tolerance, is investigated next.

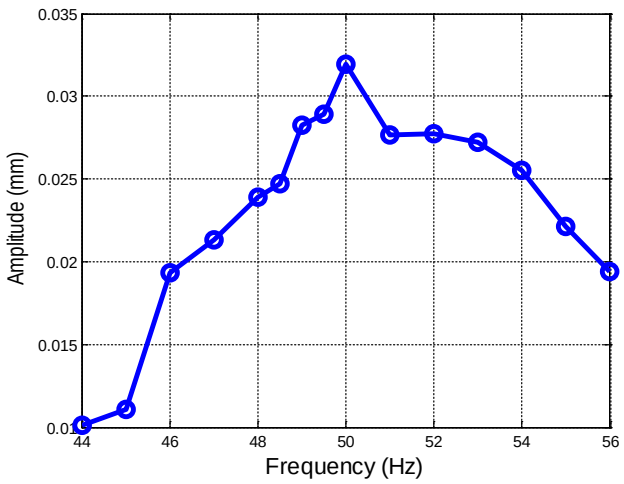

Figure D–4 : FRF at driving point experimental result

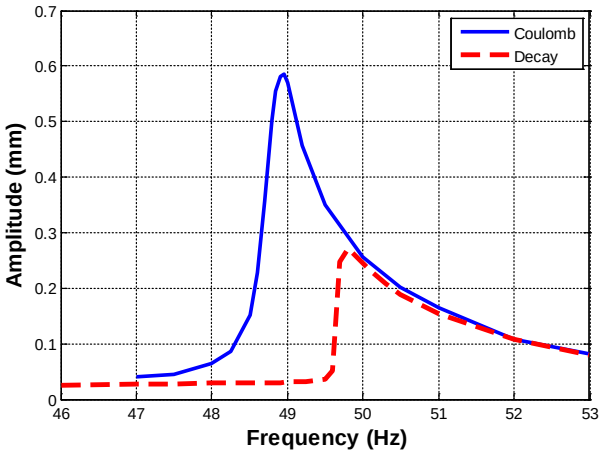

Figure D–5: FRF at driving point simulation results

Figures (Figure D–6 and Figure D–7) present the Slip tolerance $\left(F_f\right)$ (Eq. 22) effect on the friction force. In the same figures, mean (mean max, mean min) represent the value of the objective function Eq. 24 used to identify the friction parameters (Hadji & Mureithi, 2014a, 2014b). Their values are different from the maximum values due to appearance of a beating phenomenon in the response. This behavior is seen in Figures (Figure D–8 to Figure D–12). Further, the beating phenomenon is reduced at the slip tolerance $\left(F_f = 1\%\right)$ in both models; meaning that 50 Hz is the resonance frequency of the system using this value of slip tolerance. The friction forces generated by both friction models are larger than the experimental result when the default value of the slip tolerance $\left(F_f = 0.5\%\right)$ is used. The decay friction model, however, generate a larger friction force. More importantly, the model is more sensitive to variations in F_f. The Coulomb friction model only yields rms values closer to experimental results using for very large values of the slip tolerance $\left(F_f = 70\%\right)$. Similarly the decay friction model yields the same rms values again for very high slip tolerance $\left(F_f = 90\%\right)$. These values are too high and not physically realistic. Using the objective function of Eq. 24 and the default value of F_f, both models are unable to generate the same values as the experimental result. Numerically, the models do show robustness with respect to the slip tolerance for physically realistic values of the parameter.

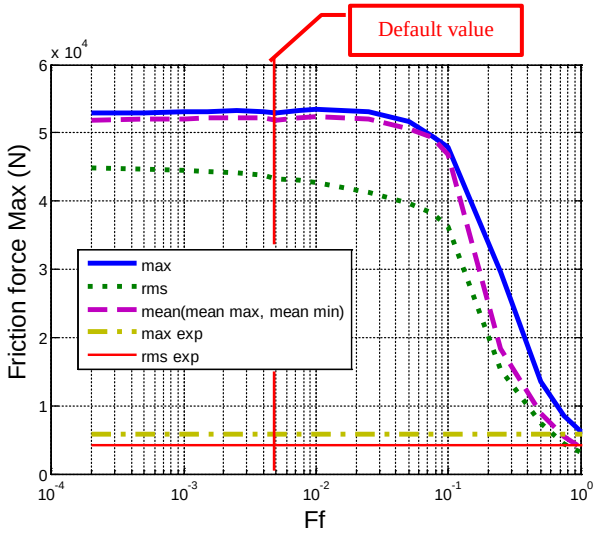

Figure D–6: Slip tolerance (fraction Ff) effect on the friction force (Coulomb)

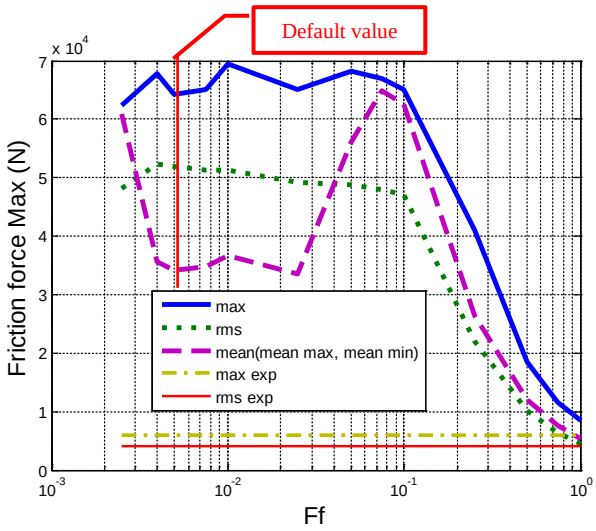

Figure D–7 : Slip tolerance (fraction Ff) effect on the friction force (decay)

We can therefore conclude that the Coulomb and decay friction models are unable to reproduce the friction forces obtained in the experimental result independently of the slip tolerance (F_f).

Figures (Figure D–8 and Figure D–9) present the slip tolerance (F_f) effect on the system response which supports the conclusion above. However, the decay friction model does yield driving point response values close to experimental values for small slip tolerances near 0.25%; this is slightly below the recommended value of 0.5%.

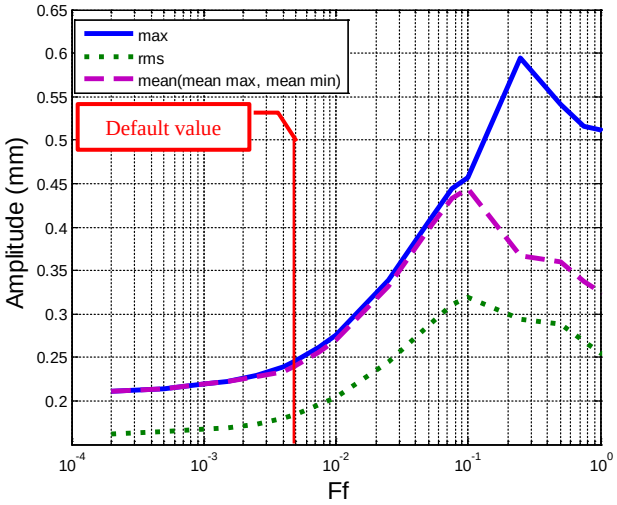

Figure D–8 : Slip tolerance (fraction Ff) effect on the system response at the driving point (Coulomb)

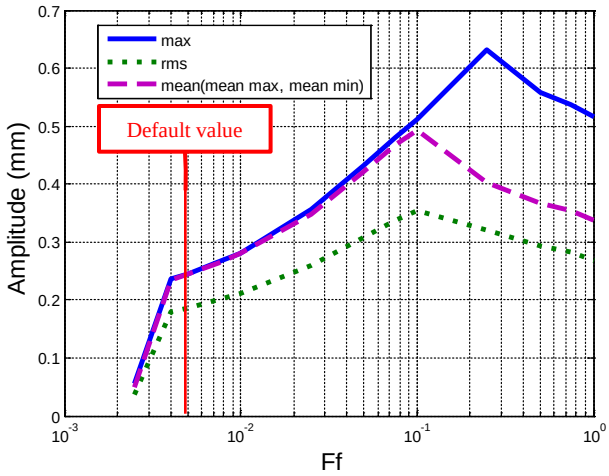

Figure D–9 : Slip tolerance (fraction Ff) effect on the system response at the driving point (decay)

Both numerical models yield a beating-response which was not observed in experiments. To better account for the experimental friction damping and eliminate the beating phenomenon we have analyzed the effect of adding damping to the system in the form of proportional (Rayleigh) damping; here considering only proportionality with the mass. We do this analysis for the decay friction model only, simply because the behavior of decay friction model is better and nearer to the experimental result than Coulomb friction model. The results of this analysis are presented in the Figures (Figure D–10 and Figure D–11). For all mass proportional damping factor α values

considered, there is no significant effect on the friction force generated using decay friction model; and the friction force stay bigger than the experimental values. However, the level of the system response decreases with a reduction of the beating effect. For proportional damping coefficient values up to $\alpha_1 = 40$ (approximately $\zeta = 0.064$) there is only a weak beating effect and the system response is equal to the experimental value.

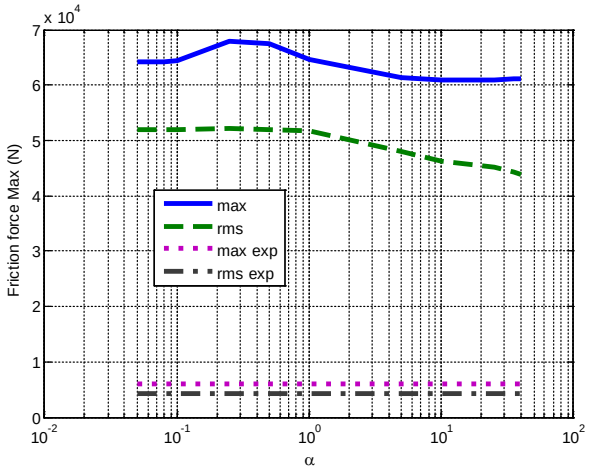

Figure D–10 : Added proportional mass damping effect on the friction force (decay)

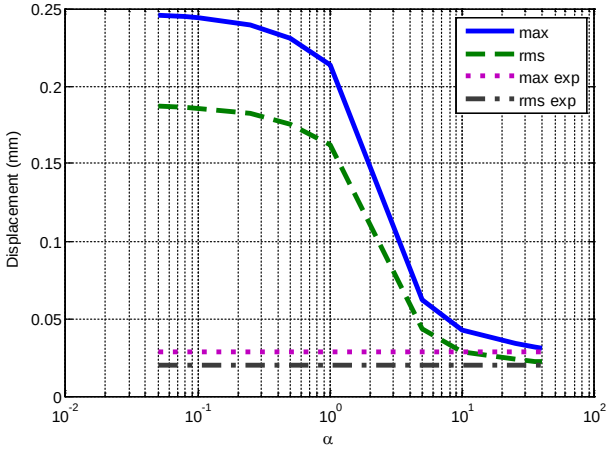

Figure D–11 : Added proportional mass damping effect on the system response at the driving point (decay)

Finally, a word about consider the slip displacement. This displacement is an important quantity used to calculate the work rate, Eq. 26. The slip displacement value at the contact point is plotted versus the fraction F_f in Figure D–12 for the Coulomb model. The values of the slipping

displacement generated by the Coulomb friction model (not shown) are larger than the values generated using decay friction model. However, values from both models are smaller than the experimental values (4E-3 mm). This leads to smaller computed work rates compared to the experimental values.

$$\dot{W} = \frac{\int_0^t N(t).\dot{u}(t)dt}{\int_0^t dt} \tag{26}$$

where

$\dot{W}$ is work rate,

$N(t)$ is normal force,

$\dot{u}(t)$ is sliding velocity,

t is duration of contact.

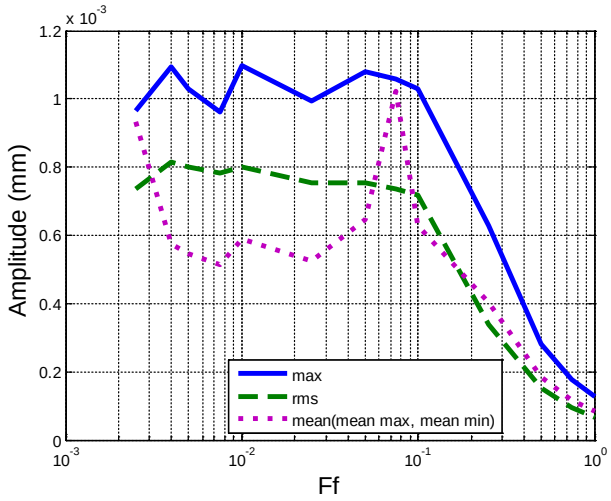

Figure D–12 : Slip tolerance (fraction Ff) effect on the slipping displacement (decay)

CONCLUSION AND DISCUSSION

This paper presents intermediate results in a longer term project on hybrid friction model parameter identification and validation using the friction models used to create this friction model.

As presented in the previous works (Hadji & Mureithi, 2014a, 2014b), five parameters of the hybrid friction model are identified using Dahl (1976) and LuGre friction models (Canudas et al., 1995). Some of these parameters are the same as those of the Coulomb and decay (Stribeck) friction model. Starting then with these simpler models, some of the challenges associated with FEM based parameter identification have been highlighted. Importantly, it is clear that friction models, as implemented in commercial FEM codes, should be used with caution. When quantities intimately related to the details of the friction model are considered, the resulting physical outputs maybe significantly affected and far from true values. The slip tolerance is an adjustable parameter that is found in the numerical friction models. This parameter has, however, been found to have little effect on the computed friction force and displacement when physically realistic values are used. The vibration response was found to be sensitive to this parameter in the range 0.2% - 0.5%. The poor performance of the Coulomb and Stribeck models was largely expected. These models are only an intermediate step toward the general hybrid friction model developed by the authors for which parameter identification is the ultimate goal.

The Hybrid friction model (Azizian, 2012; Azizian & Mureithi, 2013) is based on the principle of the LuGre model (Canudas et al., 1995). All properties and benefits of other friction models are included, namely the dynamics of the Dahl model (1976) (i.e. hysteresis effect), the dynamics of bristles (Haessig Jr & Friedland, 1991) and the Stribeck effect (Stribeck & Schröter, 1903). This model also takes into account the distribution of the stresses in the contact area according to the principle of Cattaneo-Mindlin (1953) to model the pre-sliding phenomenon.

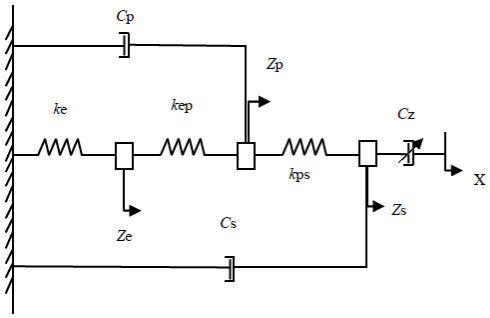

Figure D–13 : Schematic of the hybrid friction model (Azizian, 2012)

The formulation of the hybrid friction model (Azizian & Mureithi, 2013) is represented in the following equations:

$$T = k_e z_e + c_p \dot{z}_p + c_s \dot{z}_s \tag{27}$$

$$z = z_e + z_p + z_s \tag{28}$$

$$k_e z_e + k_{ep}(z_e - z_p) = 0 \tag{29}$$

$$k_{ep}(z_p - z_e) + k_{ps}(z_p - z_s) + c_p \dot{z}_p = 0 \tag{30}$$

$$k_{ps}(z_p - z_s) + c_z(\dot{z}_s - \dot{x}) + c_s \dot{z}_s = 0 \tag{31}$$

where z_e, z_p and z_s are, respectively, the elastic, plastic and partial slip relative displacements. The pre-sliding or the sticking regime is modeled by elastic stiffness k_e, plastic damping c_p and pre-sliding damping c_s and two transition stiffness coefficients: elastic-plastic k_{ep} and plastic-pre sliding k_{ps}. The slip regime is modeled by the coefficients of the Stribeck damping c_z which is given by:

$$c_z = \frac{\sigma_0 g(\dot{x})}{\dot{x}} \tag{32}$$

$$\sigma_0 g(\dot{x}) = N\left(\mu_C + (\mu_s - \mu_C)e^{-(\dot{x}/v_s)^2}\right) \tag{33}$$

where

$g(\dot{x})$ Stribeck function (or Stribeck friction model (Stribeck & Schröter, 1903))

μ_c is kinetic friction coefficient

μ_s is static friction coefficient

v_s is Stribeck velocity

From Figures (Figure D–4 and Figure D–5) we see that the two friction model tested in this paper yield large beam response amplitudes. This is related to the simplification of the sticking regime modeling where only the elastic stiffness is used without any damping consideration. This damping weakness is represented by two damping elements in the hybrid friction model, Figure D–13. An attempt to account for this damping in the decay model was done by introducing the mass proportional damping.

This paper presents the first step to validate the parameters identified in the previous works (Hadji & Mureithi, 2014a, 2014b) using the finite element method and two static friction models (Coulomb friction model and decay friction model).The present work demonstrates that both static friction models: Coulomb friction model and decay friction model are incapable of accurately representing all the behaviors of friction, ultimately leading to incorrect work rate estimates.

The Coulomb and decay friction models yield modal parameters (resonance frequency and NNMs) that are close to those of the experiments, but their FRFs bandwidth values are significantly far from the experimental results. decay friction model yields the closest to the experimental result for the NNMs and resonance frequency. The experimental response level of the system is lower than that of the simulations. The values of the slip displacement generated by the decay friction model and Coulomb friction model are small compared to the experimental values leading to small work rates. In future work, the parameters of the two dynamic friction models, Dahl and LuGre models, will be validated followed by the identification and validation of the hybrid friction model.

REFERENCES

Antunes, J., Axisa, F., Beaufils, B., & Guilbaud, D. (1988). Coulomb friction modelling in numerical simulations of vibration and wear work rate of multispan tube bundles. Paper presented at the International Symposium on Flow-Induced Vibration and Noise: Flow-Induced Vibration in Heat-Transfer Equipment - 1988, November 27, 1988 - December 2, 1988, Chicago, IL, USA.

Azizian, R. (2012). Dynamic Modeling of Tube-Support Interaction in Heat Exchangers. (1027 Ph.D.), Université De Montréal, École Polytechnique De Montréal (Canada), Canada. Available from publications.polymtl.ca & Mémoires et thèses

Azizian, R., & Mureithi, N. (2013). A hybrid friction model for dynamic modeling of stick-slip behavior. Paper presented at the Proc. ASME-PVP Conference, Paris.

Canudas, C. d. W., Olsson, H., Astrom, K. J., & Lischinsky, P. (1995). New model for control of systems with friction. IEEE Transactions on Automatic Control, 40(3), 419-425.

Dahl, P. R. (1976). Solid friction damping of mechanical vibrations. AIAA Journal, 14(12), 1675-1682.

Diehl, T. (1995). Methods of Improving ABAQUS/Standard Predictions for Problems Involving Sliding Contact. Paper presented at the ABAQUS User's Conference Proceedings, Paris, France.

Gilmore, R. J., & Steer, M. B. (1991). Nonlinear circuit analysis using the method of harmonic balance. A review of the art. Part I. Introductory concepts. International journal of microwave and millimeter-wave computer-aided engineering, 1(1), 22-37.

Hadji, A., & Mureithi, N. (2014a). Nonlinear Normal Modes and the Dahl Friction Model Parameter Identification. Paper presented at the ASME 2014 Pressure Vessels and Piping Conference.

Hadji, A., & Mureithi, N. (2014b). Nonlinear normal modes and the LuGre friction model parameter identification. Paper presented at the Proc. ASME-IMAC Conference, Montreal, Quebec, Canada.

Haessig Jr, D., & Friedland, B. (1991). On the modeling and simulation of friction. Journal of Dynamic Systems, Measurement and Control, Transactions of the ASME, 113(3), 354-362.

Hassan, M., & Rogers, R. J. (2005). Friction modelling of preloaded tube contact dynamics. Nuclear Engineering and Design, 235(22), 2349-2357.

Karnopp, D. (1985). Computer simulation of stick-slip friction in mechanical dynamic systems. Journal of Dynamic Systems, Measurement and Control, Transactions of the ASME, 107(1), 100-103.

Manual, A. U. s. (2013). Version 6.12. Abaqus Inc, 5.

Mindlin, R. D., & Deresiewicz, H. (1953). Elastic spheres in contact under varying oblique forces. American Society of Mechanical Engineers -- Transactions -- Journal of Applied Mechanics, 20(3), 327-344.

Oden, J. T., & Martins, J. A. C. (1985). Models and computational methods for dynamic friction phenomena. Computer Methods in Applied Mechanics and Engineering, 52(1–3), 527-634.

Rogers, R. J., & Pick, R. J. (1977). Factors associated with support plate forces due to heat-exchanger tube vibratory contact. Nuclear Engineering and Design, 44(2), 247-253.

Stribeck, R., & Schröter, M. (1903). Die wesentlichen Eigenschaften der Gleit-und Rollenlager: Untersuchung einer Tandem-Verbundmaschine von 1000 PS: Springer.

Xi, T., & Rogers, R. J. (1996). Dynamic friction modelling in heat exchanger tube simulations. Paper presented at the Proceedings of the 1996 ASME Pressure Vessels and Piping Conference. Part 1 (of 2), July 21, 1996 - July 26, 1996, Montreal, Can.

ANNEXE E – THESIS PRESENTATION

(Cette annexe est une traduction anglaise de la présentation de la thèse présentée dans Chapitre 3)

The content of the work done during the doctorate is presented in the following chapters as articles. The test rig was designed, manufactured, tested and improved to reduce the interaction with the excitation system (shaker) firstly. The idea and some details on the test rig were presented in Chapitre 4. Then, experimental data obtained with this test rig were used to get all the results in the five articles exposed in this thesis. The chronological order and the articles' content are presented as follows:

In the first article realized (Article 3), as presented in Annexe B, we find the first formulation (harmonic form) of the new method of inverse harmonic balance (IHB) with the first smoothing method (trigonometric series) and orthogonal harmonic approach. In this article, two parameters of a Hybrid friction model were identified using the Dahl friction model.

The first improvement of the IHB method is presented in the second realized article (Article 4 presented in Appendix (Annexe C), the introduction of the second formulation (sub-harmonic form) and the second smoothing method (natural Spline). In this article, five parameters of a Hybrid friction model were identified using the LuGre friction model.

Then, the parameters of Hybrid friction model identified in the first and second realized articles, Article 3 (Annexe B) and Article 4 (Annexe C), were validated by the Coulomb model and Stribeck model using the finite element method by a 1D model (beam element) to model our beam and the contact elements in the Abaqus software. This work is presented in the third realized article (Article 5) presented in Annexe D.

The second improvement of the IHB method is presented in the fourth realized article (Article 1 presented in Chapitre 5). The latter relates to the use of the non-orthogonality harmonic approach in the friction calculation. In this paper, we also present the approach, multi-step approach, used to identify the five parameters of the Hybrid friction model, which were identified using the Coulomb, Stribeck, Dahl and LuGre friction models.

Finally, the parameters of Hybrid friction models identified in the fourth realized article (Article 1 presented in Chapitre 5) were validated by the Coulomb model and the Stribeck model (preliminary results) using the finite element method with a 2D model (Shell element with plane strain) under the Abaqus software. This work is presented in the fifth realized article (Article 2) presented in Chapitre 6.

In addition, some results and further discussion of Chapitre 5 (article 1) are shown in Chapitre 7 with the general discussion. The conclusions and recommendations for future works will be presented in Chapitre 8. Some graphics and additional information from literature reviews (related to Chapitre 2) are shown in Annexe A.

An English translation of the thesis presentation presented in the Chapitre 3, general discussion (Chapitre 7) and the conclusion (Chapitre 8) is provided in Annexes E, F and G, respectively.

ANNEXE F – GENERAL DISCUSSION

(Cette annexe est une traduction anglaise de la discussion générale Chapitre 7)

In this chapter, we present some results and further discussion of Chapitre 5. Indeed, we present the new results obtained following the improvement of the inverse harmonic balance method (IHB) using the non-orthogonal shape and form sub-harmonic approach. In the end, we present some remarks with the general discussion.

CHAPITRE 5 ADDITIONAL RESULTS

In Chapitre 5 (article 1), we present the first three harmonic forms (Figure 5-9 and Figure 5-10) and evaluations in one period (Figure 5-11) for the excitation level of 8N used in the calculation of the friction force shown in Figure 5-15 and Figure 5-16.

From Figure 7-1, we can see similar results to the first three harmonic forms (Figure 5-9 and Figure 5-10), where the harmonic form is close to either of the sub-harmonic forms (the two sub-harmonics are equal) if the harmonic frequencies are close to the natural frequencies, e.g. (H4= 200Hz and the second natural frequency F_{n2}= 160 Hz, H6= 300Hz and the third natural frequency F_{n3}= 319 Hz). The evolution of linear modes in one period (Figure 7-4) is homogeneous and symmetrical, contrary to the two forms harmonics for non-linear response. The harmonic and sub-harmonic forms are not homogeneous, but have slight symmetry in the time axes (vertical axes) in the harmonic form and asymmetry in the sub-harmonic form.

This behavior is the same as the harmonic forms (Figure 7-1) and their assessment in one period (Figure 7-2) for the excitement level of 6.5N is presented in Annexe C. Thus, we can conclude that, this behavior is general for all non-linear responses independent of the excitation levels.

For the excitement level of 6.5N, the frictional force depending on the velocity and the displacement presented in Figure C–7 Annexe C (obtained using IHB method with the decoupled harmonic forms approach) were recalculated using decoupled harmonic forms approach of IHB

method. The new result is shown in Figure 7-2 and Figure 7-3 and was used for the re-identification of the friction model parameters shown in Table 5-7.

FFT analyzed results are presented in Table 5-3, Table 5-4 and Table 5-5 for 6.5N excitation level. To complement and extend this analysis, the results for the 8N excitation level are presented in Tableau 7-1, Tableau 7-2 and Tableau 7-3. We can say that, the amplitude error is around 0.1% for the first harmonic and less than 3% for the third and the forth harmonics. However, for the other harmonics the average amplitude error is larger than 8 %. The FFT phase errors are of the same order as the FFT amplitude errors. This explains the harmonic number effect (error) presented previously in figures (Figure 5-13 and Figure 5-14).

AECL VIBIC code (Rogers & Pick, 1977) is based in the superposition modal method using the linear (Linear approach) or the experimental modes. Those assumptions are the most commonly used in the industry. From the figures (Figure 5-8 and Figure B–7 (Annexe B)), we found that etch assumption lead to get different nonlinear normal modes. The nonlinear normal mode forms are also depending on excitation level and all this lead to get a completely different system response. Furthermore, from Figure 5-15, the level of the friction force calculated by the conventional approach (LNMs) is too higher than the other approaches and led to get the higher friction coefficient bigger than the commonly used value $(\eta_c = 0.74)$.

The 1st natural frequency values, presented in Table 5-1, were obtained from the phase graph not from the amplitude graph (the peak), where the 1st mode phases are equal to -90 degree.

Figure 5-20 presents the simulation results of the Stribeck friction model (Stribeck & Schröter, 1903) using an equivalent model 1 DOF. This result is considered as the first step to validate the friction model parameters identified in this work. Furthermore, the of the predicted displacement amplitude using Coulomb and Dahl models are almost three times larger than that predicted by using LuGre model, where the LuGre model result is closest to experience. This means that a realistic friction model leads to product the closest system response to the experience, even using a simple approximation of the system as 1 DOF equivalent model.

MULTI-STEP APPROACH

The multi-step approach is an approach that has been used to identify the parameters of complex friction model. In each step, the parameters of the basic models for the complex friction models are identified.

For example, for our problem, Hybrid friction model parameters identification was performed as follows:

Step 1 : the frictional force, the normal force, the sliding movement and sliding velocity are calculated using the inverted harmonic balance method.

Step 2 : using the results of the first step to identify the kinematic friction coefficient μ_c using the Coulomb friction model Eq. (5.42).

Step 3 : using the kinematic friction coefficient as an initial value to identify two parameters (μ_c and σ_0 equivalent of k_e in the Hybrid friction model) of Dahl friction model (1976) by minimizing the error of friction force T eq. (5.51) using Matlab FMINSEARCH ® function Eq.(5.46).

Step 4 : Then, using the parameters of Dahl friction model (1976) as initial values to identify the parameters of the Stribeck friction model (Stribeck & Schröter, 1903), Eq. (5.47) and (5.48). The Dahl friction model parameters μ_c and σ_0 are equivalent to μ_s and k_s (Eq. (5.48)), respectively.

Step 5 : After, the parameters of Stribeck friction model (Stribeck & Schröter, 1903) will be used as initial values to identify the parameters of the LuGre friction model (Canudas et al., 1995) Eqs. (5.49) and (5.50).

Step 6 : Finally, parameters of the LuGre friction model (Canudas et al., 1995) will be used to identify the remaining hybrid friction model (Azizian & Mureithi, 2013) parameters.

CONCLUSION

The inverse harmonic balance (IHB) method is a new method based on nonlinear modal analysis developed to calculate the contact forces (friction and impact). A coupled harmonic form was also introduced to improve the IHB method. The improvement of this method using the non-orthogonal form approach on the one hand and the sub-harmonic form on the other hand makes the method more accurate and more robust, thus it can be used with different levels of excitation.
The friction force calculation using IHB method made it possible to accurately identify five parameters (k_e, c_s and c_z(μ_s, and v_s)) of the Hybrid friction model (Azizian & Mureithi, 2013). These parameters have been identified with a multi-step approach precisely. Where, these parameters were validated by the Coulomb friction model using the finite element method.

ANNEXE G – CONCLUSION AND RECOMMENDATIONS

(Cette annexe est une traduction anglaise du Chapitre 8 (conclusion et recommandations))

Accurate prediction of the dynamics of a structure requires accurate modeling of its boundary conditions. The most important effects of non-linearity, non-comparability and non-reproducible of the results come from imperfect boundary conditions. The present work demonstrated that the classical approach to model the actual boundary conditions (approach with perfect boundary conditions and linear normal modes (LNMs)) fails to represent the actual behaviour of the deformed beam therefore giving poor results.

With a low excitation level, the real boundary condition elements (e.g. friction) are not provoked, so the system response is linear. Contrary, for higher excitation level, the non-linear elements of system cause a divergence between reality and the simulation.

In this project, the behavior of the steam generator tube interaction with its supports was studied, which is a good example of nonlinear boundary conditions effects with contact (friction and impact). This problem has been simplified by using a beam with frictionnel support.

The inverse harmonic balance (IHB) method is a new method based on nonlinear modal analysis developed to calculate the contact forces and the displacement at the contact point between two bodies. In this work, six approaches to identify the nonlinear normal modes have been compared, namely: the classical approach using the basic linear normal modes (LNMs), the approach proposed by Jalali et al. (2011) and the four possible combinations of the inverse harmonic balance method (two formulations and two smoothing methods). The IHB method using the approach based on sub-harmonic forms coupled with spline fitting gave the best results for the accelerometer signal reconstruction. Contrary, the classical approach using LNMs gives poor results.

The friction force calculation using IHB method made it possible to accurately identify five parameters (k_e , c_s and c_z (μ_s , and v_s)) of the Hybrid friction model (Azizian & Mureithi, 2013). Those parameters have been identified with a multiple step approach using Coulomb,

Stribeck (1903), Dahl (1976) and LuGre (Canudas et al., 1995) friction models. The three other parameters (c_p , k_{ep} and k_{ps}) will be determined in future work.

A coupled harmonic form was also introduced to improve the IHB method. A harmonic number analysis has been proposed to enable the choice of the optimal number of harmonics to accurately calculate the friction force. The approach based on sub-harmonic forms with spline fitting method gave the best results.

Simulation using the finite element method (FEM) of our beam with the 1D element (beam element) and 2D (Shell element with plane strain) is used to validate the parameters of friction models identified using the results of the inverse harmonic balance method. Modeling contact area by beam elements (1D) I thought rather not appropriate for this type of problem.

Two static friction models, the Coulomb model and Stribeck model, are tested. The two models produce friction forces, normal force and slip displacement of the correct order of magnitude compared to the friction force calculated using the inverse harmonic balance method (IHB) at the resonance frequency. However, their FRF bandwidth values are significantly far from the experimental results. Furthermore, Coulomb and decay friction models yield modal parameters (resonance frequency and NNMs) that are close to those of the experiments. The decay (Stribeck) friction model yields the closest result to the experiments for the NNMs and resonance frequency.

This work demonstrates that both static friction models: Coulomb friction model and decay friction model are incapable of accurately representing all the behaviors of friction, especially in the sticking regime, ultimately leading to incorrect work rate estimates for all frequency.

Original contributions

The three most important original contributions of this works are:

1. Development of an inverse harmonic balance method (IHB). The method is applicable in a wide range of domains beyond friction modeling.
2. Development of new multiple step approach for the identification of friction model parameters.
3. Identification of five parameters of the Hybrid friction model considering detailed physics of the friction phenomenon.

Publications

This PhD project has led to three peer reviewed conference articles and two journal papers. The relationships between these articles are presented in the thesis presentation (Annexe E).

A- Papers submitted to journals:

Hadji, A., & Mureithi, N. (2016a). Identification of friction model parameters using the inverse harmonic method. *ASME Journal of Pressure Vessel Technology*. doi: 10.1115/1.4034441 (Paper accepted for publication)

Hadji, A., & Mureithi, N. (2016b). Validation of friction model parameters identified using the IHB method using finite element method. (Paper submitted to) *ASME Journal of Pressure Vessel Technology*.

B- Peer reviewed conference publications:

Hadji, A., & Mureithi, N. (2014a). *Nonlinear Normal Modes and the Dahl Friction Model Parameter Identification.* Paper presented at the ASME 2014 Pressure Vessels and Piping Conference, Anaheim, California, USA.

Hadji, A., & Mureithi, N. (2014b). *Nonlinear normal modes and the LuGre friction model parameter identification*. Paper presented at the Proc. ASME-IMAC Conference, Montreal, Quebec, Canada.

Hadji, A., & Mureithi, N. (2015). *Validation of friction model parameters identified using the inverse harmonic balance method.* Paper presented at the ASME 2015 Pressure Vessels and Piping Conference, PVP 2015, July 19, 2015 - July 23, 2015, Boston, Massachusetts, United states.

Future work:

The inverted harmonic balance method (IHB) is a promising method for the identification of nonlinear normal modes (NNMs) and the friction forces or dynamic elements calculation in an indirect way and less expensive with high accuracy. This method is able to give us information about the real nature of the boundary conditions. It can even be used to extract other useful information for numerical simulations as the normal modes deformation and natural frequencies variation depending on the level of excitement. So this method can find several applications in this study field and also be applied to various fields.

For example, the IBH method can be used to identify not only the normal modes and the model parameters, but also to find the behavior laws (creation of new models) physical phenomena when is combined with the Kriging variogram method.

In recommended future work, more analysis of the Stribeck model behaviour is required to validate their parameters. The parameters of the two dynamic friction models (Dahl and LuGre models) can be validated followed by the validation of the hybrid friction model through their parameters identification.

The work rate formulation (Eq.(6.23)) is developed in base of the Coulomb friction model, for that, a new work rate formulation is necessary for the new friction models in the future works.